

# Strain and electric field mediated manipulation of magnetism in $\text{La}_{(1-x)}\text{Sr}_x\text{MnO}_3/\text{BaTiO}_3$ heterostructures

Von der Fakultät für Mathematik, Informatik und Naturwissenschaften der RWTH Aachen University zur Erlangung des akademischen Grades eines Doktors der Naturwissenschaften

vorgelegt von

Diplom-Physiker

Markus Schmitz

aus Aachen

Berichter: Univ.-Prof. Dr. rer. nat. Thomas Brückel  
Univ.-Prof. Dr. rer. nat. Larissa Juschkina

Tag der mündlichen Prüfung: 16.12.2015

Diese Dissertation ist auf den Internetseiten der Universitätsbibliothek online verfügbar.



## **Eidesstattliche Versicherung**

Ich erkläre hiermit an Eides Statt, dass ich die vorliegende Arbeit ohne unzulässige Hilfe Dritter und ohne Benutzung anderer als der angegebenen Hilfsmittel angefertigt habe. Die aus anderen Quellen direkt oder indirekt übernommen Daten und Konzepte sind unter Angaben der Quelle gekennzeichnet. Die Arbeit wurde bisher weder im In- noch im Ausland in gleicher oder ähnlicher Form einer anderen Prüfungsbehörde vorgelegt.

Ort, Datum

Markus Schmitz



## Zusammenfassung

In dieser Arbeit wurden Heterostrukturen aus ferromagnetischem  $\text{La}_{(1-x)}\text{Sr}_x\text{MnO}_3$  (LSMO) und ferroelektrischem  $\text{BaTiO}_3$  (BTO) hergestellt und deren strukturelle und magnetische Eigenschaften untersucht. Die Kombination dieser ferroischen Eigenschaften kann zu einem künstlichen Multiferroikum führen. Eine mögliche magneto-elektrische Kopplung an der Grenzfläche von LSMO/BTO wurde von Burton *et al.* [1] vorhergesagt. Daher wurde speziell die mögliche Manipulation von magnetischen Eigenschaften durch das Anlegen von elektrischen Feldern untersucht. Eine solche magneto-elektrische Kopplung konnte in der untersuchten Heterostruktur gefunden werden. Die epitaktischen LSMO Dünnschichten wurden mittels einer Oxid-Molekularstrahlepitaxieanlage (OMBE) und einer Sauerstoff-Hochdruckspalteranlage (HOPSS) auf  $\text{BaTiO}_3$  Substraten gewachsen. Stöchiometrische  $\text{La}_{(1-x)}\text{Sr}_x\text{MnO}_3$  Dünnschichten wurden mit einer Dotierung von  $x = 0.5$  und  $x = 0.3$  hergestellt. Eine geringe Rauigkeit sowie eine gute kristalline Struktur der gewachsenen Filme wurde durch Röntgenbeugungsmethoden bestätigt. Die  $\text{BaTiO}_3$  Substrate weisen strukturelle Domänen auf, deren Verhältnis sich durch das Anlegen von elektrischen Feldern verändert. Die epitaktischen LSMO Dünnschichten sind im gesamten Temperaturbereich verspannt. Die Magnetisierung der LSMO Filme wird durch die Veränderung dieser Verspannung modifiziert. Die Änderung der Verspannung wird durch die verschiedenen strukturellen Phasen des  $\text{BaTiO}_3$  Substrates bewerkstelligt. Dadurch werden scharfe Stufen in der Magnetisierung bei den Übergangstemperaturen des BTO beobachtet. Die Auswertung magnetischer Hystereseschleifen zeigt sowohl eine Änderung der magnetischen Anisotropie der LSMO Filme zwischen den jeweiligen Strukturphasen des BTO aber auch innerhalb der orthorhombischen Phase. Besonderer Augenmerk wird auf die Manipulation der magnetischen Eigenschaften durch das Anlegen von elektrischen Feldern gelegt. Durch eine neu etablierte Messmethode ist es möglich, die magnetische Reaktion auf das angelegte elektrische Feld als Funktion der Temperatur und des Magnetfeldes zu bestimmen. Die elektrisch induzierte Manipulation der Magnetisierung ist in der Nähe der strukturellen Phasenübergangstemperaturen besonders ausgeprägt. Mittels elektrischer Hystereseschleifen kann ein detaillierter Einblick in den Einfluss des elektrischen Feldes auf die Magnetisierung gegeben werden. Das magnetische Koerzitivfeld wird durch das angelegte elektrische Feld verschoben, was erneut auf eine Änderung der magnetischen Anisotropie schließen lässt. Das Magnetisierungsprofil der LSMO/BTO Heterostrukturen wurde mittels polarisierter Neutronenreflektometrie untersucht um eine mögliche Begrenzung der gefundenen Effekte auf die Grenzfläche zu klären. Dabei zeigt sich eine verringerte Magnetisierung an der Grenzfläche zwischen LSMO und BTO für die Proben die mittels OMBE gewachsen wurden. Diese Verringerung ist durch eine erhöhte Verspannung des LSMO Films zu erklären und zeigt ein besseres epitaktisches Wachstum mittels der OMBE. Die von der HOPSS hergestellten Proben zeigen eine reduzierte Magnetisierung bei höheren Schichtdicken die durch Sauerstoff-Fehlstellen hervorgerufen sein könnte. Simulationen der polarisierten Neutronenreflektivität für verschiedene elektrische Felder zeigen, dass die beobachteten Unterschiede in der Reflektivität durch eine Veränderung der strukturellen Eigenschaften der Proben erklärbar sind. Verschiedene Mechanismen kommen für die Erklärung der beobachteten Effekte in Frage und werden ausführlich diskutiert. Dabei können Verspannungseffekte der Dünnschichten durch Magnetostriktion

zu einer Drehung der magnetischen Anisotropie, einer Änderung der Orbitalordnung oder der Austauschwechselwirkung führen. Effekte die durch Ladungsträger vermittelt werden müssen ebenso berücksichtigt werden, wie die ferroelektrischen Eigenschaften des  $\text{BaTiO}_3$  Substrates und dessen Reaktion auf das angelegte elektrische Feld, die von entscheidender Bedeutung für die Erklärung der beobachteten Effekt sind.

## Abstract

Heterostructures of ferromagnetic  $\text{La}_{(1-x)}\text{Sr}_x\text{MnO}_3$  (LSMO) and ferroelectric  $\text{BaTiO}_3$  (BTO) were produced and investigated for their structural and magnetic properties. The combination of these ferroic properties can lead to an artificial multiferroic. A possible magneto-electric coupling at the interface was proposed by Burton *et al.* [1]. Thus, special emphasis was given to the manipulation of magnetic properties by applying electric fields. A magneto-electric coupling could be observed in the heterostructures under investigation. Epitaxial LSMO thin films were grown on BTO substrates using a state-of-the-art oxide molecular beam epitaxy (OMBE) and a high oxygen sputtering system (HOPSS). Stoichiometric  $\text{La}_{(1-x)}\text{Sr}_x\text{MnO}_3$  films with doping levels of  $x = 0.5$  and  $x = 0.3$  were produced. The film quality in terms of roughness and crystalline structure was confirmed by X-ray scattering methods. The presence of structural domains in the  $\text{BaTiO}_3$  single crystal substrate, whose proportion could be altered due to the application of electric fields, was shown by X-ray diffraction. Tensile strain is induced into the epitaxial  $\text{La}_{(1-x)}\text{Sr}_x\text{MnO}_3$  films in the whole temperature range under investigation. The magnetization of LSMO alters by the variation of strain induced into the film, generated by the different structural phases of single crystal  $\text{BaTiO}_3$  substrates. The magnetization shows sharp steps at the structural phase transition temperatures of BTO. The evaluation of magnetic hysteresis loops reveals a change of the magnetic anisotropy of LSMO for each structural phase of BTO, but also within the orthorhombic phase. Special focus was given to the manipulation of magnetic properties by the application of electric fields. A newly established measurement option was used to determine the magnetic response to an applied electric field as a function of temperature and magnetic field. The electrically induced modification of the magnetization is profound near the structural phase transition temperatures. Electrical hysteresis loops give a detailed view on the influence of the electric field on the magnetization. The magnetic coercivity field shifts by the application of electric fields giving rise to a change of the magnetic anisotropy. Polarized neutron reflectivity measurements yield the magnetization profiles of the LSMO/BTO heterostructures to clarify a limitation of the effect to the interface. Samples grown by OMBE indicate a better epitaxial crystal structure due to a strain induced reduction in the magnetization at the interface. Samples produced by HOPSS show a reduced magnetization for higher layer thicknesses, which might be related to oxygen vacancies. Simulations of the polarized neutron reflectivity data for different electric field directions reveal that the observed differences in the reflectivity are mostly related to altered structural properties. Several mechanisms, which might be responsible for the observed effects in LSMO on BTO, are discussed. Strain effects via the elastic channel can lead to a rotation of the magnetic anisotropy, a change of the orbital ordering or the exchange interaction. Also carrier-mediated effects and oxygen diffusion under applied electric fields have to be considered. Furthermore, the ferroelectric properties of the  $\text{BaTiO}_3$  substrates and their response to the electric field is of crucial importance to explain the observed effects.



# Contents

<b>1</b>	<b>Introduction</b>	<b>1</b>
<b>2</b>	<b>Theoretical Background</b>	<b>3</b>
2.1	Perovskite Structure and Electronic Configuration . . . . .	3
2.2	Magnetic Ordering in $\text{La}_{(1-x)}\text{Sr}_x\text{MnO}_3$ . . . . .	5
2.3	Ferroelectricity in $\text{BaTiO}_3$ . . . . .	8
2.4	Multiferroics . . . . .	11
<b>3</b>	<b>Scattering Theory</b>	<b>13</b>
3.1	Basic Scattering Theory and Born Approximation . . . . .	13
3.2	X-ray Diffraction . . . . .	16
3.3	Reflectometry . . . . .	17
<b>4</b>	<b>Methods</b>	<b>23</b>
4.1	High Oxygen Pressure Sputtering System HOPSS . . . . .	23
4.2	Oxide Molecular Beam Epitaxy OMBE . . . . .	25
4.3	Low Energy Electron Diffraction LEED . . . . .	26
4.4	Auger Electron Spectroscopy AES . . . . .	27
4.5	Reflection High Energy Electron Diffraction RHEED . . . . .	28
4.6	Rutherford Backscattering Spectrometry RBS . . . . .	29
4.7	X-ray Reflectometer/Diffractometer . . . . .	30
4.8	Atomic Force Microscope AFM . . . . .	31
4.9	SQUID-Magnetometer MPMS . . . . .	32
4.10	Polarized Neutron Reflectometry PNR . . . . .	35
	4.10.1 Magnetic Reflectometer with High Incident Angle, MARIA . . . . .	35
	4.10.2 Magnetism Reflectometer MR . . . . .	37
<b>5</b>	<b>Sample Preparation</b>	<b>41</b>
5.1	Substrate Preparation . . . . .	41
5.2	$\text{La}_{0.5}\text{Sr}_{0.5}\text{MnO}_3$ on $\text{SrTiO}_3$ . . . . .	43
5.3	$\text{BaTiO}_3$ on $\text{SrTiO}_3$ . . . . .	47
5.4	Conclusion . . . . .	53
<b>6</b>	<b>Results I: <math>\text{La}_{0.53}\text{Sr}_{0.47}\text{MnO}_3</math> on <math>\text{BaTiO}_3</math></b>	<b>55</b>
6.1	Structural Analysis . . . . .	55
6.2	Characterization of the Macroscopic Magnetization . . . . .	61

6.2.1	Temperature Dependent Magnetization . . . . .	62
6.2.2	Temperature Dependent Electrical Manipulation of the Magnetization	63
6.2.3	Electrical Hysteresis Loops for Different Temperatures . . . . .	64
6.2.4	Electrical Hysteresis Loops at Different Magnetic Fields . . . . .	67
6.2.5	Electrical Manipulation of the Magnetization at Various Magnetic Fields . . . . .	69
6.2.6	Hysteresis Loops with Applied Electric Fields . . . . .	71
6.3	Analysis of the Magnetic Depth Profile . . . . .	74
<b>7</b>	<b>Results II:La<sub>0.7</sub>Sr<sub>0.3</sub>MnO<sub>3</sub> on BaTiO<sub>3</sub></b>	<b>81</b>
7.1	Structural Analysis . . . . .	81
7.2	Characterization of the Macroscopic Magnetization . . . . .	83
7.2.1	Temperature Dependent Magnetization . . . . .	83
7.2.2	Temperature Dependent Electrical Manipulation of the Magnetization	84
7.2.3	Electrical Hysteresis Loops for Different Temperatures . . . . .	86
7.2.4	Electrical Manipulation of the Magnetization at Various Magnetic Fields . . . . .	89
7.2.5	Hysteresis Loops with Applied Electric Fields . . . . .	92
7.3	Analysis of the Magnetic Depth Profile . . . . .	95
<b>8</b>	<b>Discussion</b>	<b>101</b>
<b>9</b>	<b>Summary and Outlook</b>	<b>111</b>
	<b>Acknowledgments</b>	<b>113</b>
	<b>Bibliography</b>	<b>115</b>
	<b>List of Figures</b>	<b>125</b>
	<b>List of Tables</b>	<b>132</b>
	<b>Fit Parameter</b>	<b>134</b>

# Chapter 1

## Introduction

The understanding and manipulation of highly correlated electron systems in complex oxides has attracted much interest in the broad realm of solid state physics due to the large amount of possible applications [2]. Highly correlated electron systems, like transition metal oxides, have a huge variety of unique properties [3], like superconductivity [4], colossal magnetoresistance CMR [5], magnetocaloric effects [6], multiferroic effects [7] and much more [8]. The control of an ordering parameter with a second different one, e.g. magneto-electric coupling [9], will lead to numerous applications, like magnetic field sensors and data storage devices with a four-state [10] or even an eight-state [11] logic in a single device. For storage devices this can lead to combined advantages of FeRAMs and MRAMs, a non-volatile magnetic storage with bits switched by electric fields [12]. Unfortunately, single-phase magneto-electrics are rare. Ferromagnetism and ferroelectricity normally exclude each other, because empty d-shells are necessary for ferroelectricity, but partially filled d-shells essential for magnetism [13]. Hence other ways to create a multiferroic device have to be developed. Since fabrication techniques like High Oxygen Pressure Sputter Deposition [14], Pulsed Laser Deposition and Oxide Molecular Beam Epitaxy [15] improved in the last decades, thin films and material combinations with an atomically flat surface can be produced. In those artificially fabricated heterostructures further interesting phenomena emerge due to finite size effects or coupling effects at interfaces [16, 17], like superconductivity at the interface between two insulating oxides [18] or magnetism between two non-magnetic oxides [19]. The combination of a strong ferromagnetic and a ferroelectric material can lead to an artificially multiferroic system via the coupling at the common interface. A magneto-electric effect could be observed in previous work for example by Molegraaf *et al.* in a  $\text{La}_{0.8}\text{Sr}_{0.2}\text{MnO}_3/\text{PbZr}_{0.2}\text{Ti}_{0.8}\text{O}_3$  heterostructure [20], but a much more desired non-toxic, lead free system is of great interest due to ecological reasons. Burton *et al.* predict the control of magnetization due to the application of an electric field at the interface between  $\text{La}_{0.5}\text{Sr}_{0.5}\text{MnO}_3$  and  $\text{BaTiO}_3$  [1]. First-principle calculations suggest that a change in the electron population at the interface due to the reversal of the ferroelectric polarization of the  $\text{BaTiO}_3$  leads to a change in the magnetic order at the interface from ferromagnetic to antiferromagnetic. This change of the magnetic order is caused by the manipulation of the  $\text{Mn}^{+3}$  and  $\text{Mn}^{+4}$  concentration, which affects the balance between super-exchange interaction and double-exchange interaction, favoring antiparallel and parallel alignment of neighboring Mn spins, respectively.

In this work heterostructures of  $\text{La}_{(1-x)}\text{Sr}_x\text{MnO}_3$  and  $\text{BaTiO}_3$  are produced by an oxide molecular beam epitaxy and a high pressure oxygen sputtering system. The heterostructures are investigated with respect to the structural properties by several scattering methods and by atomic force microscopy measurements. Macroscopic magnetic properties are determined by the use of a SQUID magnetometer, which was modified to allow for the application of electric fields. Additionally, the magnetic profiles of the samples are characterized by polarized neutron reflectometry measurements. Especially, the manipulation of the magnetization by the application of an external electric field is of great interest to find magneto-electric effects, which are theoretically predicted.

### **Outline of the present work**

A short introduction in the theoretical background of the properties of  $\text{La}_{(1-x)}\text{Sr}_x\text{MnO}_3$  and  $\text{BaTiO}_3$  is given at the beginning of this thesis. The structure of perovskite oxides is introduced, followed by the magnetic properties of  $\text{La}_{(1-x)}\text{Sr}_x\text{MnO}_3$ , ferroelectric properties of  $\text{BaTiO}_3$ , and the combination of both properties to form a multiferroic material. Since scattering methods are used extensively for the investigation of the samples, the theoretical basics of scattering theory are summarized. Experimental methods used to produce and to characterize the system under investigation are described in Chapter 4. Some methods had to be modified e.g. for the ability to apply an electric field, or new options had to be installed. Therefore, those methods will be discussed in much more detail. Since the production of the investigated oxides is a large part of the thesis, Chapter 5 is dedicated to the sample preparation. The results of the magnetic and structural properties of  $\text{La}_{(1-x)}\text{Sr}_x\text{MnO}_3$  on  $\text{BaTiO}_3$ , especially with respect to the application of external electric fields, are presented in Chapter 6 and 7. The observed effects are discussed in Chapter 8. The final chapter will give a summary of the presented work and an outlook for future investigations.

# Chapter 2

## Theoretical Background

Within this chapter the most important properties of the materials used in this thesis are described. Beginning with the structure and the electronic configuration of perovskite oxides and followed by a section handling the magnetism in  $\text{La}_{1-x}\text{Sr}_x\text{MnO}_3$  and ferroelectricity in  $\text{BaTiO}_3$ . This will be concluded with a brief introduction into the multiferroic properties with specific focus on how to combine the aforementioned properties of magnetism and ferroelectricity.

### 2.1 Perovskite Structure and Electronic Configuration

The materials under investigation belong to the class of transition metal oxides [8]. A large amount of these transition metal oxides are stable within the  $\text{ABO}_3$  perovskite structure [21]. The perovskite structure was named after the compound  $\text{CaTiO}_3$  [22] and can be seen in Fig. 2.1. In the perovskite structure, a small  $3d$ -transition metal cation B (e.g.  $\text{Ti}^{4+}$ ) is located at the center of the unit cell which is surrounded by an octahedron of oxygen anions. The larger alkaline earth metal or rare earth cation A (e.g.  $\text{Ba}^{2+}$ ) sits at the corners of the unit cell. The ideal cubic perovskite structure gets distorted due to buckling of the oxygen octahedron [23] depending on the ion sizes of the compound. For  $\text{Ln}_{0.5}\text{Sr}_{0.5}\text{MnO}_3$  ( $\text{Ln} = \text{La}, \text{Pr}, \text{Sm}, \text{Nd}, \text{Gd}$ ) an evolution from  $\text{Pnma}$  (orthorhombic) to  $\text{I4/mcm}$  (tetragonal) is observed, which stabilizes in the rhombohedral symmetry [24].  $\text{La}_{0.5}\text{Sr}_{0.5}\text{MnO}_3$  is stable in  $\text{I4/mcm}$ , but the unit cell can still be described as a pseudocubic unit cell with  $a=b=c=3.86 \text{ \AA}$ , in good agreement with the real structure as indicated in Fig. 2.1.

The properties of transition metal oxides strongly cohere with their electronic configuration. Before taking any exchange mechanisms into account the magnetic moment of the cation is determined by the electronic ground state of the ion in a simple local environment model. As mentioned before the  $3d$ -transition metal ion on the B-site is surrounded by an oxygen octahedron. This environment leads to a crystal field splitting of the 5 degenerate  $3d$ -states into 3 energetically lowered  $t_{2g}$  orbitals and 2 elevated  $e_g$  orbitals, in order to minimize the Coulomb repulsion (as depicted in Fig. 2.2). The  $e_g$  orbitals point towards the negatively charged oxygen ligands while the  $t_{2g}$  orbitals point in between, resulting in the enhancement and lowering of the associated energy level, respectively. The size of

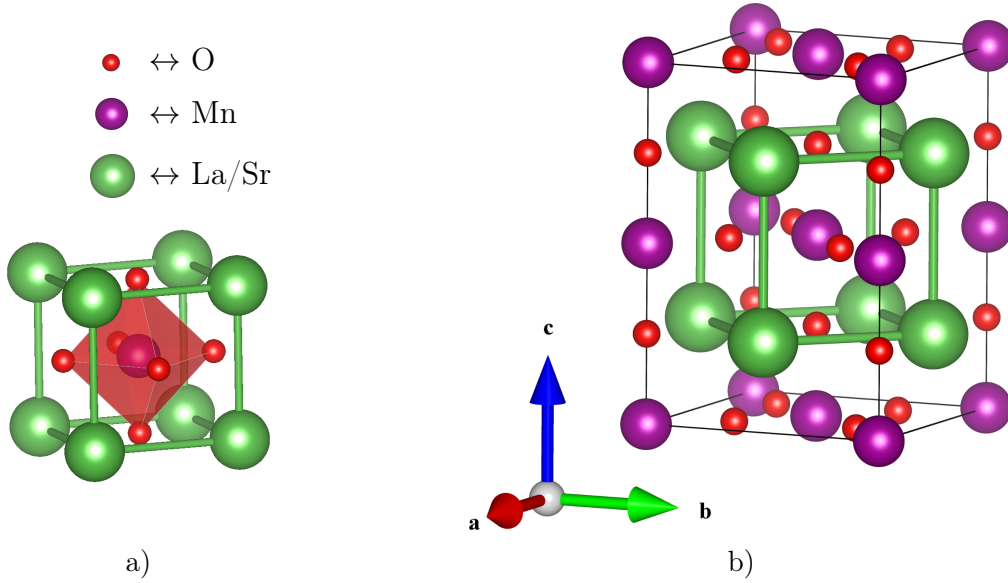


Figure 2.1: *Crystal structure of  $\text{La}_{(1-x)}\text{Sr}_x\text{MnO}_3$  in the a) pseudocubic perovskite structure and in the b) tetragonal structure. The legend applies to both figures.*

the energy gap  $\Delta E_{\text{CF}}$  between those energy levels depends on the distance between the transition metal ion and the oxygen ligand. The degeneracy of the  $t_{2g}$  and  $e_g$  orbitals itself is also lifted in some systems due to the Jahn-Teller effect which leads to a local distortion of the crystal structure [25]. The Jahn-Teller effect can be cooperative, leading to a distortion of the lattice, or fluctuating without any average change of the crystal structure. The splitting of the  $t_{2g}$  and  $e_g$  levels can be supported by strain. The ground state configuration is given by the electronic configuration of the ion and the ratio of the Hund's coupling energy  $\Delta E_{\text{Hund}}$ , which splits the spin- $\uparrow$  and spin- $\downarrow$  state according to Hund's first rule and the crystal field splitting energy  $\Delta E_{\text{CF}}$ . The first three  $d$ -electrons of the ion will occupy the  $t_{2g}$  orbitals while the occupation of the fourth electron will lead to a high spin state if  $\Delta E_{\text{CF}} < \Delta E_{\text{Hund}}$  and a low spin state for  $\Delta E_{\text{CF}} > \Delta E_{\text{Hund}}$ . Manganese has the configuration  $[\text{Ar}] 3d^5 4s^2$  with 4 and 3  $d$ -electrons for the two important oxidation states  $\text{Mn}^{3+}$  and  $\text{Mn}^{4+}$ , respectively. Their ground states according to the usually moderate crystal field splitting is  $t_{2g}^3 e_{g\uparrow}^1$  for  $\text{Mn}^{3+}$  and  $t_{2g}^3$  for  $\text{Mn}^{4+}$ .

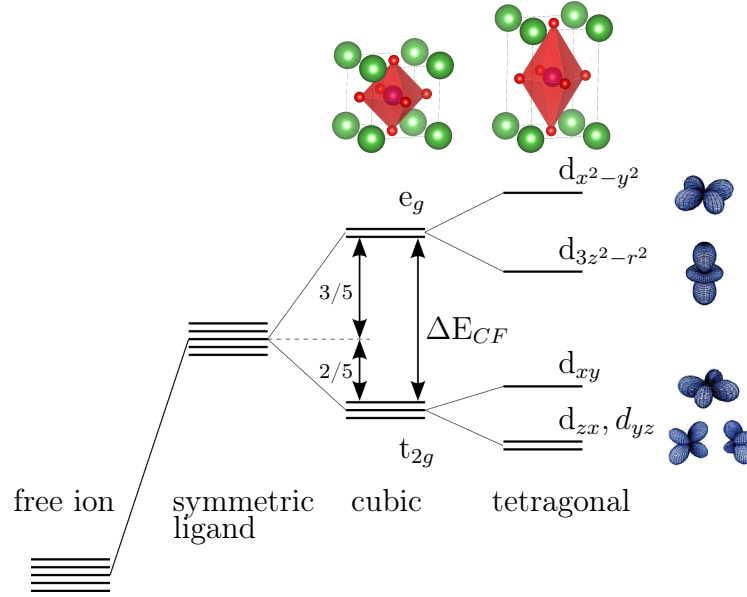


Figure 2.2: *Electronic configuration in 3d-transition metal ions in a local picture. The crystal field and Jahn-Teller effect lead to a splitting in the energy levels.*

## 2.2 Magnetic Ordering in $\text{La}_{(1-x)}\text{Sr}_x\text{MnO}_3$

In order to describe the magnetic ordering in a transition metal oxide one has to consider the exchange interaction between localized electrons. The exchange interaction can be attributed to the Coulomb interaction with the Heisenberg uncertainty principle and the Pauli exclusion principle. The delocalization of two electrons leads to a decrease of their kinetic energy due to the uncertainty principle  $\Delta x \cdot \Delta p \geq \hbar$ . However the Pauli principle forbids that two electrons with the same quantum numbers occupy the same place. This leads to an antisymmetric total wavefunction for the electrons. The exchange mechanism can be described by a Heisenberg-Spin-Hamiltonian [26]:

$$\mathcal{H} = - \sum_{j \neq i, i > j} J_A^{ij} \frac{1}{\hbar^2} \mathbf{S}_i \cdot \mathbf{S}_j, \quad (2.1)$$

with  $\mathbf{S}_i$  and  $\mathbf{S}_j$  as quantum mechanical spin operators and the exchange coupling constant  $J_A$ . For a positive exchange coupling constant  $J_A > 0$  ferromagnetic alignment is favored, while antiferromagnetic alignment is favored for negative  $J_A < 0$ . The Hund's coupling energy  $\Delta E_{\text{Hund}}$  for the manganese ion is higher than the crystal field splitting, so that a high spin state is favored as the ground state. The two most important exchange mechanisms for  $\text{La}_{(1-x)}\text{Sr}_x\text{MnO}_3$  are the super-exchange SE and the double-exchange DE mechanism.

**Super-exchange SE:** The super exchange (following [27]) occurs not directly due to overlapping orbital of the magnetic atoms, but indirectly due to the overlap with an diamagnetic connecting atom, e.g. oxygen. The manganese orbitals overlap with those of the oxygen which makes a hopping of an electron after the Hubbard-model from the oxygen to

the manganese atom possible. This process is virtual, since the gain in kinetic energy due to the hopping process has to overcompensate a high Coulomb-energy. A real hopping process is forbidden, because of the high Coulomb-energy, but the virtual process is still possible within the energy-time uncertainty. Second order perturbation theory shows a negative exchange constant  $J_A < 0$  leading to an antiferromagnetic coupling. The two antiparallel spins of the oxygen 2p-orbital can only hop to the neighboring manganese atoms if the spins of the manganese atoms are aligned antiparallel. For filled or partially filled  $e_g$  orbitals the situation gets more complicated. Whether the SE interaction via the  $e_g$  orbitals favors either an antiferromagnetic or ferromagnetic alignment, can be obtained from the semi-empirical Goodenough-Kanamori rules depending, on the Mn-O-Mn bonding angle and the  $e_g$  occupation [28–30].

**Double-exchange DE:** The double exchange (following [31]) is similar to the super exchange taking atoms with different valencies e.g.  $\text{Mn}^{3+}$  and  $\text{Mn}^{4+}$  into account. If, for example, a spin-up-electron hops from the oxygen to the manganese  $\text{Mn}^{4+}$ -ion with a quasi simultaneous hopping of a spin- $\uparrow$ -electron from the  $\text{Mn}^{3+}$ -ion to the oxygen, the two states are degenerate so that a real hopping process can take place. The electrons can lower their kinetic energy due to delocalization. In this case the exchange constant is positive  $J_A > 0$ . Due to the fact that all spins of the 3d-electrons of the manganese are aligned parallel, because of strong Hund's coupling and the constant  $J_A$ , the manganese atoms align ferromagnetic in the double exchange mechanism.

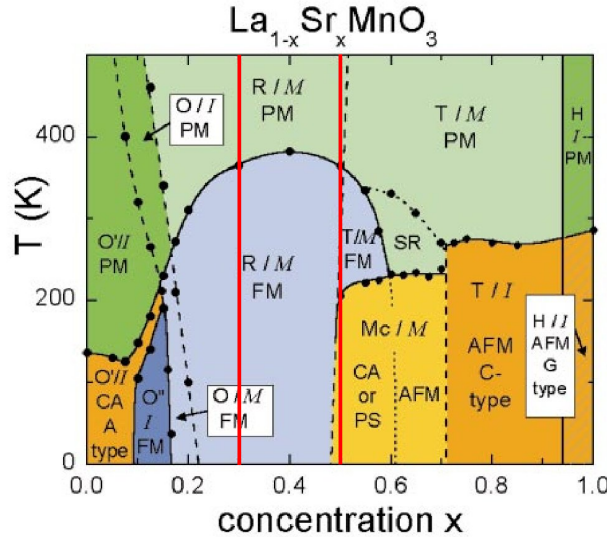


Figure 2.3: *Magnetic temperature-vs.-doping level phase diagram of  $\text{La}_{(1-x)}\text{Sr}_x\text{MnO}_3$  adapted from [32]. Ferromagnetic FM, antiferromagnetic AFM and paramagnetic PM regions are depicted as well as the electronic state (insulating: I, metallic: M) and the crystal structures (orthorhombic O, rhombohedral: R, tetragonal: T, monoclinic: Mc, and hexagonal H) . The stoichiometry used in this work is indicated by a red line.*

Bulk  $\text{La}_{(1-x)}\text{Sr}_x\text{MnO}_3$  has a rich magnetic temperature-vs.-concentration phase diagram (see Fig. 2.3) due to the competition of the SE and DE interaction. These can be tuned by the doping level from pure  $\text{LaMnO}_3$  (with just  $\text{Mn}^{3+}$ ) to pure  $\text{SrMnO}_3$  (with only  $\text{Mn}^{4+}$ ). For low Sr concentrations  $x < 0.1$  an a-type antiferromagnetic ordering occurs below  $\approx 130$  K in  $\text{La}_{(1-x)}\text{Sr}_x\text{MnO}_3$ . Here the SE interaction is dominant, because the major part of manganese atoms have equal valency states. Between  $0.1 < x < 0.17$  a ferromagnetic insulating phase stabilizes. A metal-insulator phase transition occurs at  $x \approx 0.17$  [33], where a sufficient number of  $\text{Mn}^{4+}$  ions are present and the DE interaction becomes dominant up to  $x \approx 0.5$ . For  $x > 0.5$ , again, the SE interaction gets dominant leading to an antiferromagnetic ordering in the  $\text{La}_{(1-x)}\text{Sr}_x\text{MnO}_3$ . Up to  $x \leq 0.7$  the phase is still metallic while for  $0.7 < x \leq 1$  an insulating antiferromagnetic c-type phase is present [34].

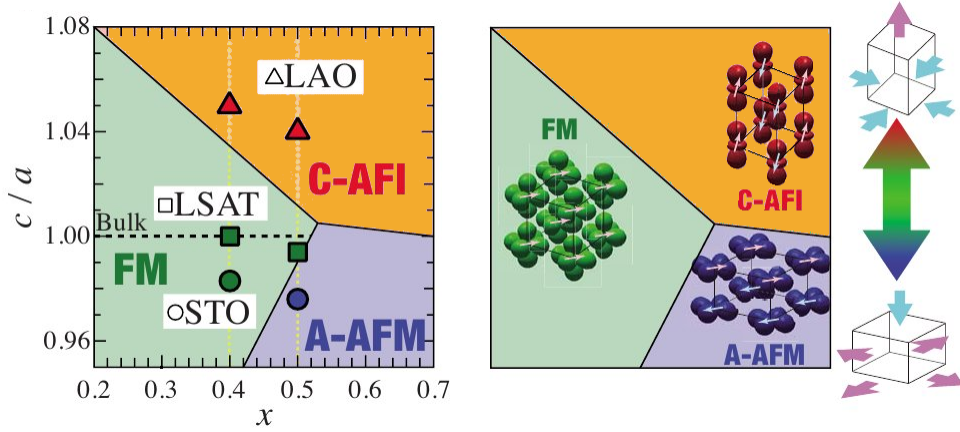


Figure 2.4: *Strain-vs.-doping level magnetic phase diagram of  $\text{La}_{(1-x)}\text{Sr}_x\text{MnO}_3$  adapted from [34, 35].*

There are several other mechanisms to change the magnetic order in  $\text{La}_{(1-x)}\text{Sr}_x\text{MnO}_3$ . Especially the occurrence of strain can lead to different magnetic behavior compared to bulk. The properties of a thin  $\text{La}_{(1-x)}\text{Sr}_x\text{MnO}_3$  layer can be tuned for example by the epitaxial growth on different substrates. Ultra thin epitaxial  $\text{La}_{(1-x)}\text{Sr}_x\text{MnO}_3$  films near half doping show that the ground state changes from FM to AFM due to tensile strain at a critical lattice misfit of about -1% [36]. A strain-vs.-hole concentration phase diagram for epitaxial films of  $\text{La}_{(1-x)}\text{Sr}_x\text{MnO}_3$  can be seen in Fig. 2.4. Compressive in-plane strain in  $\text{La}_{0.5}\text{Sr}_{0.5}\text{MnO}_3$  films leads to a c-type antiferromagnetic insulator behavior, while tensile strain can lead to an a-type antiferromagnetic metallic ordering. Two different stoichiometries of  $\text{La}_{(1-x)}\text{Sr}_x\text{MnO}_3$  compounds were chosen for the investigation of the magneto-electric coupling in this thesis. These are  $\text{La}_{0.5}\text{Sr}_{0.5}\text{MnO}_3$  at the border between ferromagnetism and antiferromagnetism and  $\text{La}_{0.7}\text{Sr}_{0.3}\text{MnO}_3$ , which is ferromagnetic and far away from any magnetic phase transition.

## 2.3 Ferroelectricity in BaTiO<sub>3</sub>

In general, a ferroelectric material is defined as a material which has a spontaneous electric polarization that can be reversed due to the application of an external electric field (see Fig. 2.5). The research of ferroelectric materials began a century ago, as anomalously large piezoelectric constants were found in Rochelle salt. Although the research effort in this field was intense, it was difficult to find a coherent theory of ferroelectricity in this complex structure, with a large number of ions per unit cell [13]. In the 1940s Barium titanate BaTiO<sub>3</sub> was found as ferroelectric material with a much simpler unit cell [37], the perovskite structure (see Fig.2.1). Bulk BaTiO<sub>3</sub> has four structural phases (see Fig. 2.7) with a paraelectric undistorted cubic phase above 393 K and a lattice parameter of 4.01 Å [38]. For lower temperatures it undergoes several ferroelectric phase transitions from cubic to tetragonal (393 K), tetragonal to orthorhombic (278 K) and orthorhombic to rhombohedral (183 K) [39].

Nowadays the most used and studied ferroelectric materials are ABO<sub>3</sub> perovskite structure oxides. With this type of perovskite oxide ferroelectric material, first principle density functional theory calculations lead to the current understanding of the origin of ferroelectricity. In BaTiO<sub>3</sub> the electrical polarization is created by the shift of the positive transition metal ion Ti<sup>4+</sup> away from the center of the negatively charged oxygens. This leads to a net dipole moment per unit volume of 26 μC/cm<sup>2</sup> [41]. A macroscopic electrical polarization is induced if such a shift occurs cooperatively to the same direction in neighboring unit cells. The existence of ferroelectricity within a perovskite oxide material is determined by a sensitive balance between bonding conditions stabilizing the ferroelectric state and short-range repulsion favoring the non-polar state [42]. Even ferroelectric materials have a non-polar symmetric high temperature state where the short-range repulsions are dominant. It was shown that a Ti 3d-O 2p hybridization in BaTiO<sub>3</sub> is essential for the stabilization of the ferroelectric distortion for low temperatures, to overcompensate the short range repulsion [39, 43]. Two different models to explain the ferroelectric structural phase transitions were introduced already more than fifty years ago, the displacive model and order-disorder model. The displacive model [44, 45] describes the stabilization of the B cation in its equilibrium position in the middle of the oxygen octahedron for the cubic phase by the so called soft mode phonon. This phonon becomes softer for lower temperatures until its frequency is zero at the phase transition to the tetragonal structure, where the displacement of the Ti cation occurs spontaneously into the [001] direction [13]. In the orthorhombic and the rhombohedral phase the Ti ion is shifted to the [011] and [111] direction, respectively, leading to a polarization in the direction of this Ti shift. However, in the order-disorder model [46–48] the Ti B-cation is already displaced in the cubic phase. This displacement takes place randomly in all direction along the cube diagonals [111] leading to the absence of a macroscopic net polarization. For lower temperatures an averaged net polarization in the [001] direction is created in the tetragonal phase due to the displacement of the B-cation along the four directions of the diagonals. In the orthorhombic phase just two preferred [111] directions are allowed resulting in a polarization to the [110] direction. The ground state results in a rhombohedral symmetry, where all displacements adopt the same direction and the macroscopic polar-

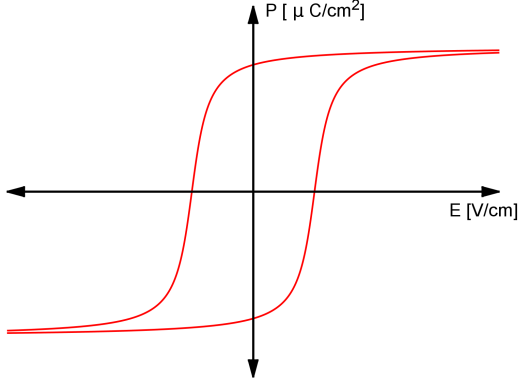


Figure 2.5: *Typical ferroelectric hysteresis loop.*

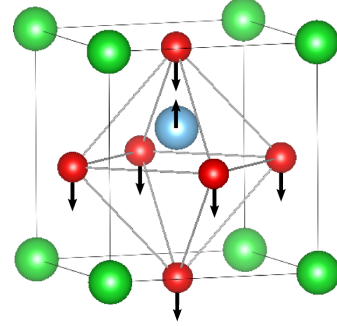


Figure 2.6: *The shift of the Ti-ion with respect to the oxygen octahedron leads to a spontaneous electric polarization in BaTiO<sub>3</sub>.*

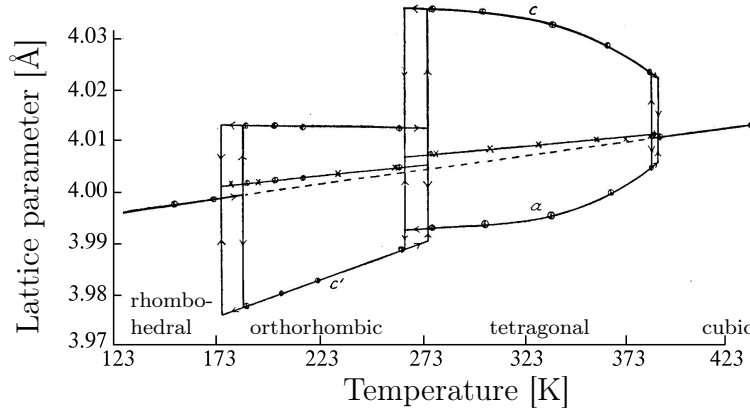


Figure 2.7: *Temperature dependent lattice parameter of bulk BaTiO<sub>3</sub> adapted from [40]. BaTiO<sub>3</sub> undergoes phase transitions from cubic to tetragonal at  $\approx 393$  K, tetragonal to orthorhombic at  $\approx 278$  K and orthorhombic to rhombohedral at  $\approx 183$  K.*

ization is pointing in  $[111]$  direction [13, 39, 49]. Nevertheless, both models fail to explain several things. The displacive model contradicts to X-ray fine structure measurements showing a Ti displacement in the  $[111]$  direction also in the cubic phase [50]. Raman experiments show first-order excitation which should vanish in the cubic phase due to the microscopic inversion symmetry [51]. The order-disorder model cannot describe the soft modes near the cubic-to-tetragonal phase transition which are observed by neutron scattering [52, 53]. Therefore, Girshberg and Yancoby proposed a combination of both models [54] whose intermediate character between the order-disorder and the displacive model could be suggested by Monte Carlo simulations and molecular dynamic studies [55–58]. First principle quantum mechanics calculations by Zhang et al. [59] underline this suggestion by a ferroelectric-antiferroelectric (FE-AFE) model for all four phases of

BaTiO<sub>3</sub>. In this model the cubic phase shows an antiferroelectric (AFE) coupling in [100], [010] and [001] directions resulting in the non-polar state. The structural phase transitions of BaTiO<sub>3</sub> are related to a change from AFE to FE coupling. The AFE coupling in [001] changes to a FE coupling in the tetragonal phase while for the orthorhombic phase AFE coupling is just valid in [100] direction and FE coupling is proposed for all directions in the rhombohedral phase. This FE-AFM model explains all of the puzzling properties of BaTiO<sub>3</sub> and seems to be the origin of the apparent coexistence of the disorder-order and the displacive properties.

The ferroelectric properties of BaTiO<sub>3</sub> can be highly tuned by strain engineering [60]. The epitaxial growth of BaTiO<sub>3</sub> films on different substrates can for example lead to the stabilization of the orthorhombic or tetragonal phase due to tensile or compressive in-plane strain, respectively. It could be shown, that the critical temperature  $T_C$  of the ferroelectric-paraelectric transition can be shifted  $\sim 500$  K by the use of DyScO<sub>3</sub> substrates with a biaxial strain of -1.7 % [61], with a simultaneous increase of the permanent polarization  $P_r$  by a factor 2.7 compared to bulk BaTiO<sub>3</sub>. General boundaries for the strain tuning of the ferroelectric properties are given by the film thickness. Completely relaxed films can lead to a zero strain state with bulk like properties. For BaTiO<sub>3</sub> on SrTiO<sub>3</sub> a relaxation limit of 5 nm was estimated by Suzuki *et al.* [62]. Ferroelectric properties can be reduced for ultra thin films by finite-size effects [63, 64]. A lower limit of six unit cells was suggested by Junquera *et al.* [65] for the presents of ferroelectricity. For lower thicknesses the imperfect screening of depolarization fields leads to the disappearance of the ferroelectric instability. Temperature-strain phase diagrams of BaTiO<sub>3</sub> based on thermodynamic analysis can be found in [61, 66].

## 2.4 Multiferroics

The class of materials which exhibit at least two ferroic properties is named "multiferroics" following Schmid [67]. These properties could be ferroelectricity, ferromagnetism or ferroelasticity. The control of these order parameters and a possible interaction among them is shown graphically in Fig. 2.8. In Chapter 2.2 and 2.3 the magnetic properties of LSMO and the ferroelectric properties of BTO have been described. The existence of a cross-coupling between those properties is of high interest for the application in data storage media [12]. In this work we focus on multiferroics which exhibit ferroelectricity and ferromagnetism.

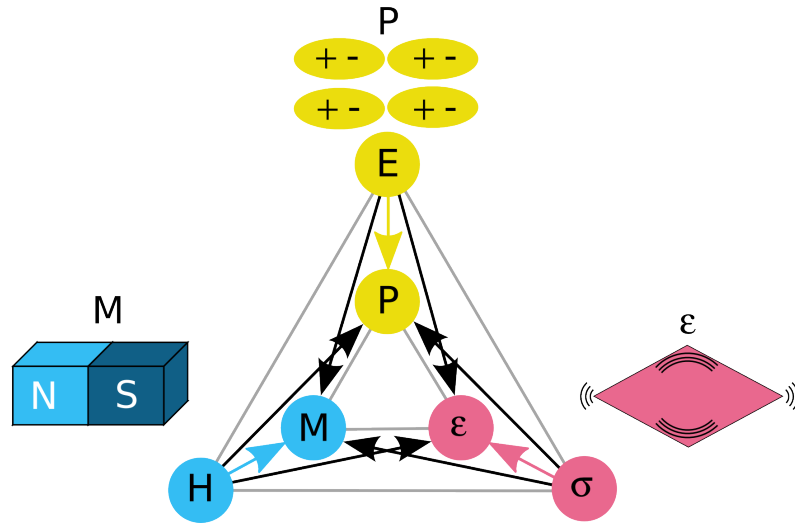


Figure 2.8: *Control of order parameter in ferroics and multiferroics. The stress  $\sigma$ , electric field  $E$  and magnetic field  $H$  controls strain  $\varepsilon$ , magnetization  $M$  and electric polarization  $P$ , respectively. Additional interaction occur at the coexistence of at least two ordering parameter (multiferroicity) adapted from [68].*

The most promising class of materials as multiferroics are transition metal perovskites [69]. A large amount of magnetic and ferroelectric perovskites exist, but the coexistence of ferroelectricity and ferromagnetism is very rare [70]. Unfortunately, these two ferroic properties usually exclude each other, because for magnetism filled d-orbitals are required, while for conventional ferroelectricity empty d-shells are necessary [13]. But several other routes to form ferroelectric/multiferroic materials are described exemplary in the following [7]:

**Lone pairs:**  $\text{BiFeO}_3$  [71] and  $\text{BiMnO}_3$  [72, 73] show multiferroic behavior due to the lone pair mechanism. Here, the ferroelectricity is not induced by the TM ion, but by the A-ions [74], e.g.  $\text{Bi}^{3+}$ . The two outer 6s electrons do not contribute to the chemical bonding, but contribute to an electrical polarization by ordering of those lone pairs, while the TM B-ion provides the magnetic properties. The magneto-electric coupling is expected to be very small due to the spatial distance between magnetic and ferroelectric ions.

**Charge order:** Charge ordering can lead to a ferroelectric polarization especially for materials with different valencies. The coexistence of inequivalent sites with different charges and inequivalent bonds leads to the spontaneous electrical polarization [70]. Charge order was long time proposed for  $\text{LuFe}_2\text{O}_4$  [75, 76].

**Inverse Dzyaloshinskii-Moriya DM interaction:** The DM interaction is a relativistic correction of the SE interaction. Its strength is proportional to the spin-orbit coupling constant. The inverse DM interaction can cause ferroelectricity in spiral magnetic ordered systems resulting from exchange striction. For transition metal oxides the exchange between spins is mediated by oxygen ions. The inverse DM interaction pushes negative oxygen ions in one direction perpendicular to the spin chain inducing a electrical polarization [77]. For example, ferroelectricity is induced by the inverse DM interaction in  $\text{TbMnO}_3$  [78, 79].

**Geometric ferroelectricity:** Ferroelectricity in hexagonal  $\text{RMnO}_3$  (e.g.  $\text{R} = \text{Y}$  or small rare earths) is caused by the tilting of the  $\text{MnO}_5$  block to provide close packing. This leads to a forming of a bipolar Y-O bond and a net polarization since two "up" and one "down" dipole per unit cell is created [80].

The aim of this thesis is to build an **artificial multiferroic heterostructure** of a strong ferromagnetic and ferroelectric perovskite oxide material [81–83]. By the use of thin films one can achieve a multiferroic system on different routes. The magneto-electric coupling in a heterostructure can be induced indirect via the elastic channel. An applied voltage can induce strain due to the electro-strictive effect in the ferroelectric layer which can lead to a change in the magnetic layer via the magneto-strictive coupling. It is also possible to get finite coupling via the interface between to individual layers. Another advantage of thin film structures is that ferroic properties can be stabilized and enhanced in thin films, e.g. due to strain [61]. However the idea of this thesis follows a slightly different route. Following the prediction of Burton *et al.* [1], the change of the polarization of the ferroelectric material tunes the charge carrier concentration at the interface of the magnetic layer. Since the driving force for the magnetic alignment in  $\text{La}_{1-x}\text{Sr}_x\text{MnO}_3$  is the competition between SE and DE interaction, it might be possible to change the magnetic order due to electrostatic screening, especially if the stoichiometry is chosen close to a magnetic phase transition.

# Chapter 3

## Scattering Theory

Scattering methods are widely used as a non-destructive method to study materials in condensed matter physics. In this thesis, neutrons, electrons, and X-rays with their various properties are used as probes for different phenomena. Structural information of the samples under investigation were obtained by X-ray and neutron reflectometry as well as X-ray diffraction. Mesoscopic magnetization measurements were performed by polarized neutron reflectometry to probe the magnetization depth profile of the samples. The basic theoretical concepts of these methods will be introduced in this Chapter. Here the focus is placed on the elastic scattering. For a complete understanding the reader is referred to [84].

### 3.1 Basic Scattering Theory and Born Approximation

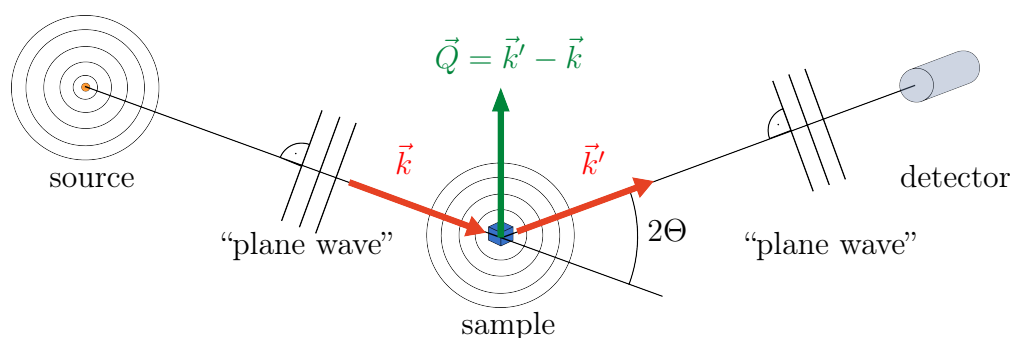


Figure 3.1: *Schematic representation of a scattering experiment within the Fraunhofer approximation. Adapted from [84]*

The description of the elastic scattering process can be done within the Fraunhofer approximation, for which the general geometry of the scattering experiment is shown in Fig. 3.1. The incident particles, produced by a monochromatic source, can be described as plane waves if the distance between radiation source and the sample is much larger than the sample size. The same applies for the scattered beam, since the distance of the sample to the detector is high. The incident and scattered beam can be described by the wave vectors  $\vec{k}$  and  $\vec{k}'$  respectively, leading to the scattering vector

$$\vec{Q} = \vec{k}' - \vec{k}. \quad (3.1)$$

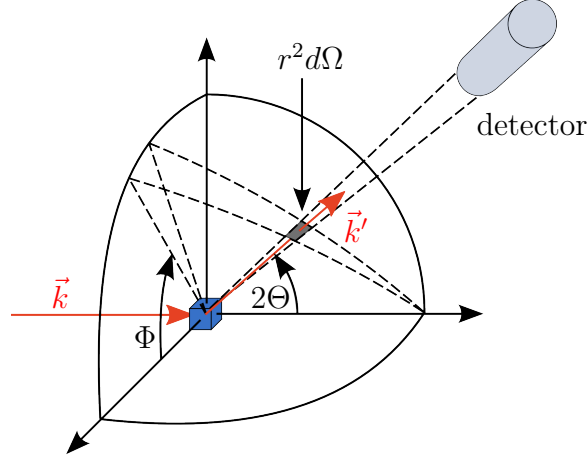


Figure 3.2: *Geometry to derive the scattering cross-section.*

In a scattering experiment, the intensity  $I(\vec{Q})$  is measured as a function of the scattering vector  $\vec{Q}$ . The scattered radiation is detected by a detector which covers the solid angle  $d\Omega = dS/r^2$  with the area  $dS$  of the detector and its distance  $r$  to the sample. The position of the detector is determined by the angles  $\Phi$  and  $\theta$ . The measured intensity is proportional to the scattering cross-section, which corresponds to the probability for an interaction of the incident particles with the matter under investigation. Figure 3.2 shows the geometry which is used to derive the scattering cross section. The differential scattering cross section  $\frac{d\sigma}{d\Omega}$  is proportional to the probability that a particle is scattered into the solid angle  $d\Omega$  by the interaction with the sample. This is given by

$$\frac{d\sigma}{d\Omega} = \frac{dn}{Jd\Omega}, \quad (3.2)$$

with the number of detected particles  $dn$ , normalized to the number of incident particles  $J$ . For the microscopic calculation of the differential scattering cross-section a quantum mechanical consideration of the interaction of the radiation with the sample is necessary. For neutrons, the influence of the interaction on the wave function can be described by the potential  $V(\vec{r})$  and the probability density amplitude  $\psi$  within the Schrödinger equation

$$\hat{H}\psi = \left( -\frac{\hbar^2}{2m}\Delta + V(\vec{r}) \right) \psi = i\hbar\frac{\partial}{\partial t}\psi. \quad (3.3)$$

The solutions of the Schrödinger equation lead to possible states of the system. Since only elastic scattering is considered, the evolution in time can be described within the wave function by the factor  $e^{-\frac{E}{\hbar}t}$ . Thus one can derive a wave equation for the spatial part of the probability amplitude  $\psi$  from Equation 3.3

$$(\Delta + k^2(\vec{r}))\psi = \frac{2m}{\hbar^2}V\psi, \quad (3.4)$$

$$\text{with } k^2(\vec{r}) = \frac{2m}{\hbar^2}(E - V(\vec{r})). \quad (3.5)$$

A solution of this wave equation in vacuum ( $V(\vec{r})=0$ ) within the Fraunhofer approximation is given by plane waves  $\psi = \psi_0 e^{i(\vec{k}\vec{r} - \frac{E}{\hbar}t)}$  with the energy  $E = \frac{\hbar^2 k^2}{2m}$ . For weak interaction potentials, taking only single scattering processes into account, the solution of the wave Equation 3.4 in matter can be derived in the so called Born approximation to

$$\psi(\vec{r}) \stackrel{1.Born}{\approx} e^{i(\vec{k}\vec{r})} + \frac{m}{2\pi\hbar^2} \frac{e^{ikr}}{r} \int V(\vec{r}') e^{i\vec{Q}\vec{r}'} d^3r' \quad (3.6)$$

$$= e^{i(\vec{k}\vec{r})} + f(\vec{Q}) \cdot \frac{e^{ikr}}{r}. \quad (3.7)$$

This is just a superposition of the incident plane wave and the spherical wave emitted from the sample according to Huygens principle. Especially for neutron scattering in which the interaction potential is small, this approximation gives good results. The amplitude of the scattered wave is given according to Equation 3.6:

$$f(\vec{Q}) = \frac{m}{2\pi\hbar^2} \int V(\vec{r}') e^{i\vec{Q}\vec{r}'} d^3r'. \quad (3.8)$$

Mathematically,  $f(\vec{Q})$  is the Fourier transform of the scattering potential. In order to obtain the connection to the differential scattering cross-section, which is defined as the angular dependent scattering probability, it should be noted that in quantum mechanics the probability to find a particle in the volume element  $d^3r$  is given by the absolute square of probability amplitude. Therefore the angular dependent scattering probability is equal to the absolute square of the amplitude of the scattered wave:

$$\left(\frac{d\sigma}{d\Omega}\right)_{\text{neutron}} = |f(\vec{Q})|^2 = \frac{m^2}{4\pi^2\hbar^4} \left| \int V(\vec{r}') e^{i\vec{Q}\vec{r}'} d^3r' \right|^2. \quad (3.9)$$

For X-ray scattering one can derive a similar expression by use of the Maxwell Equations. This leads to a wave equation for the electromagnetic field amplitude, resulting in the scattering probability:

$$\left(\frac{d\sigma}{d\Omega}\right)_{\text{X-ray}} = |f(\vec{Q})|^2 \propto \left| \int \rho_e e^{i\vec{Q}\vec{r}'} d^3r' \right|^2. \quad (3.10)$$

Since X-rays predominantly interact with the electrons of the sample, the amplitude of the scattered wave is proportional to the Fourier transform of the electron density  $\rho_e$ . Generally, the absolute square of the scattering amplitude is measured in a scattering experiment, hence the phase information is lost. Therefore, one cannot calculate the scattering potential from the scattering intensity. But one has to create a model of the investigated structure to calculate the scattering intensities and compare with the experiment. This model is iteratively improved to obtained the best possible correspondence of the simulation and the measured data.

## 3.2 X-ray Diffraction

Since X-ray radiation and moderated neutrons have a wavelength in the Ångström range they are perfect probes to investigate crystal structures. The scattered intensity can be calculated from the Fourier transformation of the scattering potential of the single crystal (see Chapter 3.1). The crystal can be mathematically described as the convolution of the periodic lattice and the unit cell structure. By the use of the convolution theorem, this Fourier transformation  $\mathcal{F}$  can be simplified to the product of the Fourier transformation of the lattice function  $\rho_L$  times the Fourier transformation of the unit cell function  $\rho_{u.c.}$  [84].

$$\mathcal{F}(\rho_L * \rho_{u.c.}) = \mathcal{F}(\rho_L) \cdot \mathcal{F}(\rho_{u.c.}). \quad (3.11)$$

For crystal structures the lattice function  $\rho_L$  along the  $x$ ,  $y$  and  $z$  directions consists of  $N, M$  and  $P$  unit cells with the associated lattice parameters  $\vec{a}$ ,  $\vec{b}$  and  $\vec{c}$ . Hence,  $\rho_L$  is proportional to

$$\rho_L \propto \sum_{n=0}^{N-1} \sum_{m=0}^{M-1} \sum_{p=0}^{P-1} \delta(\vec{r} - (n\vec{a} + m\vec{b} + p\vec{c})). \quad (3.12)$$

The Fourier transformation of Eq. (3.12) leads to the Laue-function Eq. (3.13) for pointlike scatterers by the use of a geometrical series.

$$I(\vec{Q}) \propto \frac{\sin^2(\frac{1}{2}N\vec{Q}\vec{a})}{\sin^2(\frac{1}{2}\vec{Q}\vec{a})} \cdot \frac{\sin^2(\frac{1}{2}M\vec{Q}\vec{b})}{\sin^2(\frac{1}{2}\vec{Q}\vec{b})} \cdot \frac{\sin^2(\frac{1}{2}P\vec{Q}\vec{c})}{\sin^2(\frac{1}{2}\vec{Q}\vec{c})}. \quad (3.13)$$

The Laue function for  $\vec{Q}$  parallel to  $\vec{c}$  is plotted in Fig. 3.3 for different numbers  $P$  of scatterers along  $\vec{c}$ . For  $Q_z = p \cdot \frac{2\pi}{c}$  the function shows main maxima with intensities proportional to  $P^2$ , meaning that the maximum intensity scales with the square of the number of unit cells in the corresponding direction. The width of the main peaks is inversely proportional to the number of unit cells  $\frac{2\pi}{P}$ . Thus the integral intensity is independent of the number of unit cells. It can be easily shown that the Laue conditions for this interference maxima can be transferred to the well known Bragg's law with scattering from different  $(hkl)$ -planes with the interplanar distance  $d_{hkl}$ . There are  $P - 2$  side maxima between the main ones with the distance  $\Delta Q_z = \frac{2\pi}{d}$ . This distance can be used to probe the thickness of the film  $d = P \cdot |\vec{c}|$ , when the out-of-plane direction of the thin film sample is probed. In principle also the width of the main maxima could be used to determine the film thickness, but the finite resolution of the experiment and effects like strain, mosaicity and lattice imperfections also broaden the peaks, which hinder the analysis with respect to the film thickness.

The intensity of the main maxima calculated from Equation 3.13 is modulated by the Fourier transform of the unit cell function  $\mathcal{F}(\rho_{u.c.})$  named the structure factor of the unit cell

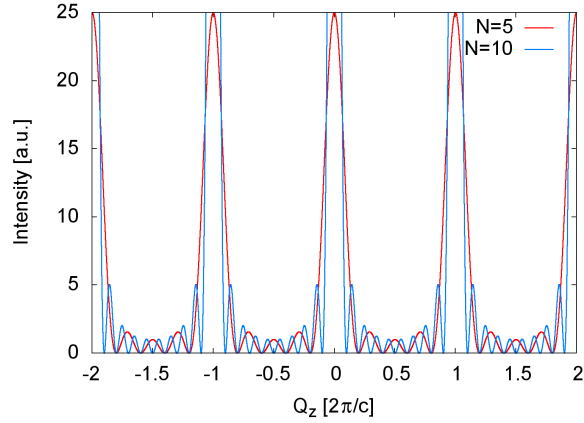


Figure 3.3: Plot of the Laue function for  $P=5$  and  $P=10$ .

$$A_S \propto \sum_j \overbrace{f_j(\vec{Q})}^{\text{unit cell structure factor}} e^{i\vec{Q}\vec{R}_j}, \quad (3.14)$$

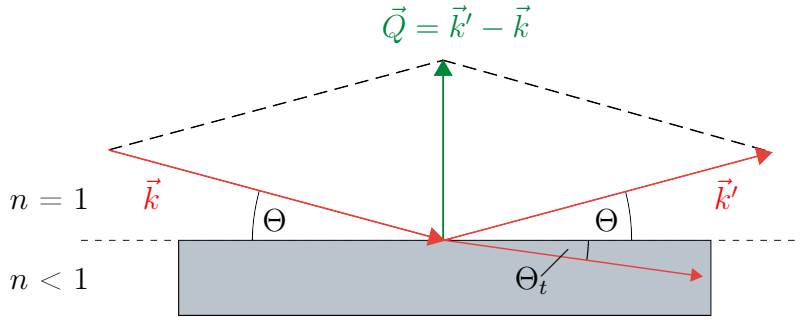
atomic form factor

with the atomic form factor  $f_j(\vec{Q})$ . The atomic form factor corresponds to the scattering potential of a single atom  $j$  and depends on the element and the radiation which is used. The structure factor does not just modulate the intensity of the Bragg reflections, but can even forbid them. In summary, the position of the Bragg peaks give information about the lattice parameters and from the intensity pattern the atom type and position in the unit cell can be deduced. By scanning perpendicular to  $\vec{Q}$  (rocking scan) the mosaicity of the crystal can be probed giving an idea of the film quality.

### 3.3 Reflectometry

Reflectometry is a scattering technique under grazing incidence for the depth-resolved determination of nuclear and magnetic profiles especially for thin film systems. A typical beam path for a grazing incidence experiment is shown in Fig. 3.4. A monochromatic and well collimated beam impinges upon the sample under a well-defined angle  $\alpha_i = \theta$  (usually  $\theta \ll 5^\circ$ ). The beam is partially reflected and partially transmitted into the material. For the so called specular scattering at  $\alpha_f = \alpha_i$  the scattering vector  $\vec{Q}$  is always perpendicular to the sample surface. Depth-resolved information on the laterally averaged order parameters such as layer thickness and roughness can be probed. Furthermore lateral correlations can be probed in off-specular or diffuse scattering at angles  $\alpha_i \neq \alpha_f$ . Here just the case of specular reflectivity will be discussed.

In contrast to diffraction experiments it is no longer possible to describe the scattering process within the Born approximation, which was derived in Chapter 3.2. Multiple scattering events cannot be neglected anymore [85] and the  $\vec{Q}$  region which is covered by reflectivity measurements is not sensitive to atomic structures. Hence, it is possible

Figure 3.4: *Typical scattering geometry under grazing incidence.*

to describe the scattering potential within the continuum approximation and the wave Equation (3.4) can be solved in an optical approach. Since the scattering vector  $\vec{Q}$  is perpendicular to the surface normal (out-of-plane direction), the scattering potential of the material can be simplified to the component  $V(z)$ . For such a one dimensional step potential it is known from quantum physics that the wave is partly transmitted and reflected leading to the reflection and transmission coefficients  $R$  and  $T$  ("Fresnel Equations"):

$$R = \left| \frac{\theta - n\theta_t}{\theta + n\theta_t} \right|^2, \quad (3.15)$$

$$T = \left| \frac{2\theta}{\theta + n\theta_t} \right|^2. \quad (3.16)$$

Here, the complex index of refraction is  $n = 1 - \delta + i\beta$  and the angle of the transmitted beam is  $\theta_t$ . The values for the scattering power  $\delta$  and the absorption  $\beta$ , depend on the material and type of radiation. For most materials the index of refraction for X-rays and neutrons is smaller than one, leading to total reflexion. For incident angles smaller than the critical angle  $\theta_c$  there is no part of the beam, which is transmitted into the material. For larger angles the intensity drops with  $I(Q) \approx Q^{-4}$  assuming a perfect smooth interface. The intensity is additionally decreased by e.g. roughness, which can be described by multiplying  $I(Q)$  with a Debye-Waller type term  $e^{-Q_z^2 \sigma^2}$  with the roughness  $\sigma$  of the surface. For more than one material, e.g. a thin film on a substrate, Parratt [86] introduced an iterative formalism to describe the scattering process in the system by the use of the reflection and transmission coefficient in each material. The interference of the reflected beams of different surfaces/interfaces leads to the typical oscillations of the intensity in the reflectometry curve.

### Polarized neutron reflectometry

By the use of neutrons as probes one can investigate the magnetic structure of matter in addition to the nuclear structure. Due to the dipole-dipole interaction of the magnetic moment of the neutrons with magnetic field  $\vec{B}$  of the sample obtained by the spins of unpaired electrons and magnetic moment generated by the orbital angular momentum, the interaction potential for neutrons can be averaged from the Fermi-pseudo-potential to:

$$V(\vec{r}) = \underbrace{\frac{2\pi\hbar^2}{m_N}\rho_N b}_{\text{nuclear}} - \overbrace{\gamma_n\mu_N\vec{\sigma}\cdot\vec{B}}^{\text{magnetic}}, \quad (3.17)$$

with the neutron mass  $m_N$ , nuclear density  $\rho_N$  and scattering length  $b$ . The magnetic component includes the vector  $\vec{\sigma}$  of the Pauli-matrices, the gyromagnetic factor for neutrons  $\gamma_n = -1.913$ , the nuclear magneton  $\mu_N = 5 \cdot 10^{-27}$  J/T and the magnetic field  $\vec{B}$ . With this potential the differential magnetic scattering cross section can be derived [87] as

$$\frac{d\sigma}{d\Omega} = (\gamma_n r_0)^2 \left| \frac{1}{2\mu_B} \langle \sigma'_z | \vec{\sigma} \cdot \vec{M}_\perp(\vec{Q}) | \sigma_z \rangle \right|^2, \quad (3.18)$$

with the classical electron radius  $r_0 \approx 2.82$  fm. The Fourier transform  $\vec{M}_\perp(\vec{Q})$  of the magnetization component of the sample, which is perpendicular to the scattering vector  $\vec{Q}$ , contributes to the cross section. In general, the magnetic scattering of neutrons is comparable in magnitude to the nuclear scattering.

The effect of magnetic scattering can be used in polarized neutron reflectometry (PNR) to investigate not just the nuclear, but also magnetic profiles of the magnetic thin film samples.

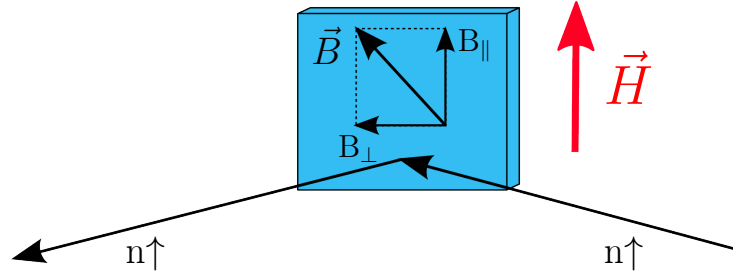


Figure 3.5: *Schematic geometry of a PNR experiment. Neutrons are polarized parallel or antiparallel to the external magnetic field  $\vec{H}$ . This field leads to a magnetic induction  $\vec{B} = \mu_0(\vec{H} + \vec{M})$  in the sample with two in plane components  $\vec{B}_\perp$  and  $\vec{B}_\parallel$ .*

The typical geometry for PNR can be seen in Fig. 3.5. The neutron beam is polarized parallel or anti-parallel to the quantization axis along the external magnetic field  $\vec{H}$ . This magnetic field causes a magnetic induction  $\vec{B} = \mu_0(\vec{H} + \vec{M})$  in the sample with two in-plane components  $\vec{B}_\perp$  and  $\vec{B}_\parallel$ . Regarding Equation 3.18, PNR is just sensitive to the in-plane components. The magnetic induction  $B_0 = \mu_0\vec{H}$  is constant over the sample volume giving a constant contribution to the index of refraction for vacuum and every material involved. Therefore, this contribution cancels out for the calculation of reflectivity and transmission. In total one can distinguish between four spin channels ( $++$ ,  $--$ ,  $-+$ ,  $+-$ ) since the incoming neutron beam, as well as the scattered beam, can be considered polarization dependent.

Here, the polarized neutron beam can be described by plane waves with two spin components  $\psi_+(\vec{r})$  and  $\psi_-(\vec{r})$  for polarization "up" and "down" with respect to the quantization axis. With this assumption and the interaction potential for neutrons (Equation 3.17), the three dimensional Schrödinger equation can be reduced to the following one dimensional coupled equations:

$$\psi_+''(z) + \left[ k_z^2 - 4\pi b\rho_N + \frac{2m\gamma_n\mu_n}{\hbar^2} B_{\parallel} \right] \psi_+(z) + \frac{2m\gamma_n\mu_n}{\hbar^2} B_{\perp} \psi_-(z) = 0, \quad (3.19)$$

$$\psi_-''(z) + \left[ k_z^2 - 4\pi b\rho_N - \frac{2m\gamma_n\mu_n}{\hbar^2} B_{\parallel} \right] \psi_-(z) + \frac{2m\gamma_n\mu_n}{\hbar^2} B_{\perp} \psi_+(z) = 0. \quad (3.20)$$

For the magnetization components  $B_{\parallel}$  these equations are decoupled and lead to nuclear and magnetic scattering in the so called non-spinflip channels. In the  $R_{++}$  channel the contribution of the magnetic scattering is added to the nuclear one while it is subtracted for the  $R_{--}$  channel. The components of the magnetization  $B_{\perp}$  can be observed in the spin-flip channels and contain purely magnetic information. With this polarization analysis it is possible to determine the magnetic profile of the sample.

### Analysis of reflectivity data

The XRR and PNR data is analyzed by simulating the reflectivity using the Parratt formalism [86], within the framework of the program "GenX" [88]. A structural model of the sample under investigation can be defined. The substrate and the required layers are described by their structural properties: nuclear scattering length density, roughness and their thickness. These structural parameters are sufficient to simulate the X-ray reflectivity. Furthermore, for PNR measurements a magnetization model has to be taken into account. This is represented by the magnetic scattering length density (SLD) which is calculated using the density of the material and the magnetization of each layer. The nuclear and magnetic structures of the sample are defined separately, which allows one to define arbitrary magnetic profiles. One can use a magnetic layer model with zero nuclear scattering length or even self defined profiles using analytical functions. Thus, interface effects and magnetization gradients can be simulated independent from the nuclear properties. Finally, the reflectivity of the  $R_{++}$  and  $R_{--}$  channel of PNR is simulated by the combination of the nuclear and magnetic SLD profiles. The SLD profile for the  $R_{++}$  and  $R_{--}$  channel is obtained by the addition and subtraction of the nuclear and magnetic SLDs, respectively. The reflectivity can then be fitted by the use of several free parameters. Fig. 3.6 illustrates the modeling of the SLDs.

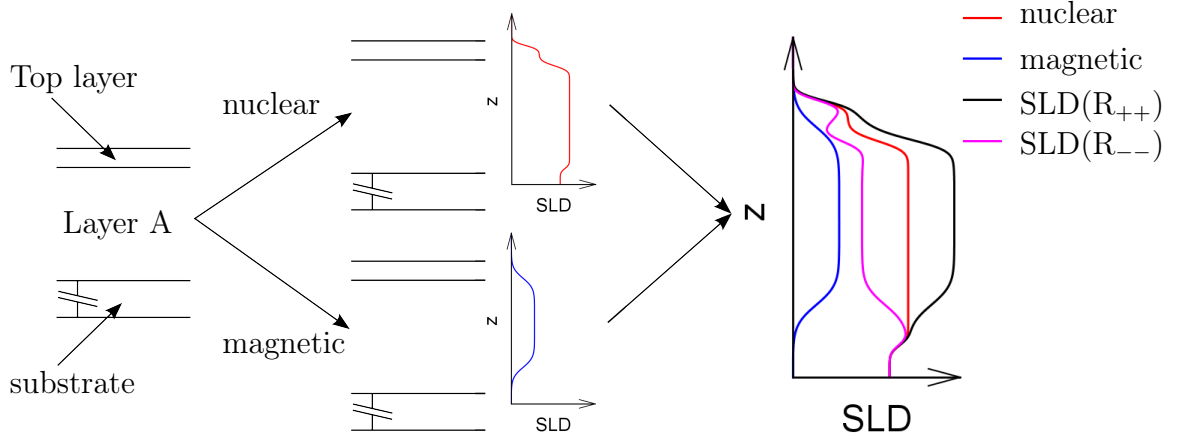


Figure 3.6: *Illustration to describe the modeling of the SLDs. Nuclear and magnetic profiles are separated. The final SLDs to simulate the  $R_{++}$  and  $R_{--}$  reflectivities are calculated by the addition and subtraction of the nuclear and magnetic SLDs, respectively.*

### Figure of Merit

The goodness of fit is determined by a function that compares the simulation with the data that gives a value how well those matches. The Figure of Merit (FOM) used here is calculated by the average of the absolute difference between the logarithms of the data and the simulation:

$$\text{FOM}_{\log} = \frac{1}{(N-1)} \cdot \sum_Q |\log_{10}(Y_Q) - \log_{10}(S_Q)|, \quad (3.21)$$

with the intensity  $Y_Q$  of the measurement and the simulated intensity  $S_Q$  for each Q-point. The error of each parameter of the simulation is also given by the FOM. It is calculated as the value for which the FOM reduces by 5%, starting at the optimum FOM. Since the increasing and decreasing of a value does not result in the same modification of the FOM, the error is asymmetric. Hence, errors are given for both directions.



# Chapter 4

## Methods

In this Chapter the experimental methods for the sample preparation and investigation used in this thesis will be shortly described. A High Oxygen Pressure Sputtering and a Oxide Molecular Beam Epitaxy system were used to produce the samples. Structural and magnetic properties were determined by various methods, which will be described in the following. Several sections will include more detailed information if those methods are of particular importance.

### 4.1 High Oxygen Pressure Sputtering System HOPSS

$\text{La}_{(1-x)}\text{Sr}_x\text{MnO}_3$  and  $\text{BaTiO}_3$  thin films were prepared using a High Oxygen Pressure Sputtering System (HOPSS). Sputtering is a technique where atoms are ejected from a target material by the bombardment of ionized atoms from a process gas. This effect can be used as a thin film deposition technique, if the mean free path of the target particles is larger than the distance to the substrate. The schematic design of the sputtering system can be seen in Fig. 4.1.

In order to remove impurity atoms, a pressure of  $10^{-6}$  mbar can be reached by a Pfeiffer HiPace 80 turbo pump and a backing pump. A sputtering pressure of up to 3 mbar can be stabilized by a MKS mass flow controller and by lowering the pumping cross section via a valve-by-pass system. Pure oxygen is used as process gas in order to avoid oxygen vacancies within the samples. Substrate temperatures required for single crystal growth conditions up to 1270 K can be reached. The substrate position is height adjustable to vary the distance between the sample and the target. The stoichiometry for this technique is predefined by the target. The sputtering system used here can be operated in direct current (DC) and high frequency (HF) sputtering mode using a Heinzinger DC or Hüttinger HF generator, respectively.

**Direct current sputtering:** For the DC sputtering a voltage (typically  $\approx 200$  V) is applied between the target and the anode. A plasma is ignited by impact ionization and the positive charged ions are accelerated towards the target. Due to this permanent bombardment of ions, small particles of the target material are struck out and condense at the substrate. Unfortunately, this method is limited to conducting targets. In the case of

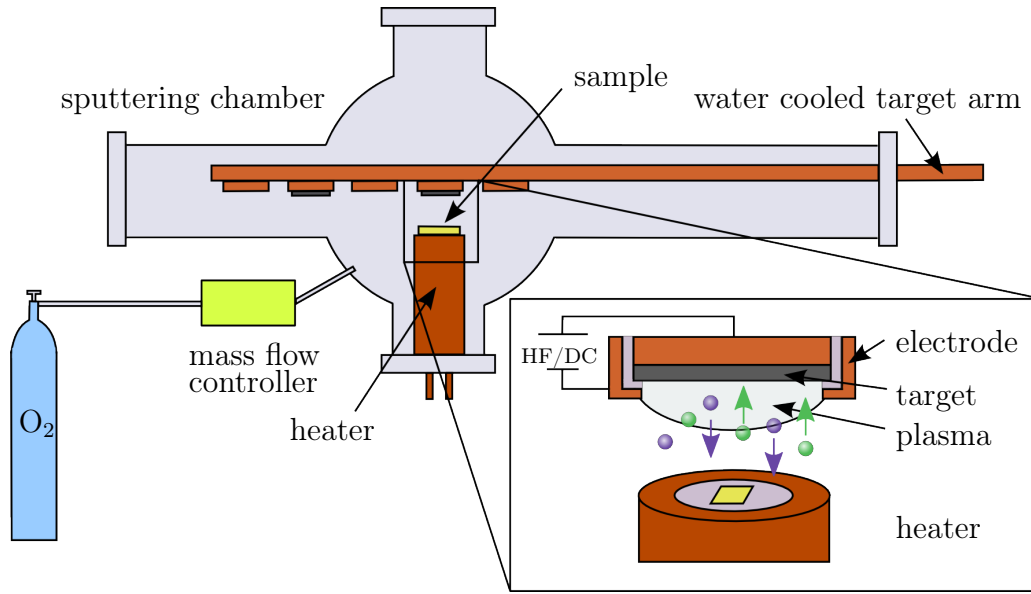


Figure 4.1: *Setup of the High Oxygen Pressure Sputtering System. The mass flow controller and the pumps ensures a stable oxygen pressure in the chamber. Five targets can be mounted on the movable target arm.*

an insulating target, it would be electrical charged due to the constant supply of charge carriers leading to a compensation of the DC electric field. Thus, the sputter process is highly suppressed or even stopped in this case.

**High frequency sputtering:** For insulating targets, like most of the perovskite oxides one can use the HF sputtering mode. A high frequency (13.56 MHz) AC-field is applied between the target and electrode. Due to this electric AC-field the process gas ions and electrons are accelerated. For high frequencies the ions are not able to follow the field anymore, because of their small charge-to-mass ratio. Thus, the cations are accelerated to the target by a superimposed negative DC voltage, while the electrons oscillate in the plasma. This enhances the amount of electrons and ions collisions leading to a higher sputter rate.

Since the high oxygen pressure leads to a drastically reduced sputtering rate it is convenient to use the magnetron sputter method. Here, in addition to the electric field a constant magnetic field is applied by permanent magnets. Due to the Lorentz force the charge carriers travel in a spiral path. This captures the electrons near the target and enlarges the amount of collisions enhancing the sputtering rate.

In this thesis, most materials were deposited with the HF sputtering method using commercial Kurt J. Lesker company targets. The target material is bonded onto a copper plate, which is attached to the magnetron unit. In this geometry the target is only fixed by this bonding. Due to the influence of the thermal radiation from the heater and the plasma, some target materials expand and the bonding can break. Hence the targets fall down and break. To avoid this, a new type of target holder/electrode head was designed.

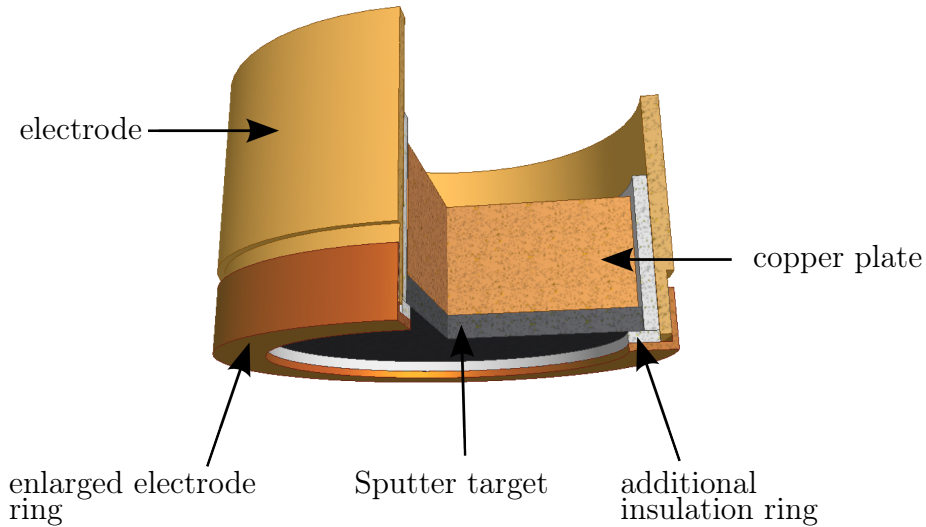


Figure 4.2: *Newly designed sputter target holder/electrode head to avoid target cracking. The electrode ring is enlarged and the use of an additional insulation ring prevents dropping of the target.*

An additional insulating ring was placed between target position and the electrode, which holds the target as one can see in Fig. 4.2. By tightening the lower thread the target is moved up and pressed onto the magnetron device. Additionally, the electrode ring was expanded to cover the whole insulation material to avoid sputtering thereof. The bonding is not necessary and the target cannot fall down anymore. Furthermore the target change is much easier and less time consuming, because the magnetron unit can stay in the sputtering system. No sputtering from the electrode occurs, since no material of the electrode was found by RBS measurement of the samples.

## 4.2 Oxide Molecular Beam Epitaxy OMBE

$\text{La}_{0.5}\text{Sr}_{0.5}\text{MnO}_3$  films were produced by a state-of-the-art Oxygen Molecular Beam Epitaxy (OMBE) system from DCA instruments. The OMBE system is depicted in Fig. 4.3. It is separated into a load-lock, a buffer line and the main chamber. The load-lock is used to introduce substrates into the chamber without breaking the ultra high vacuum (UHV) conditions in the rest of the system. The buffer line contains a LEED (Chap. 4.3) and Auger (Chap. 4.4) system for the in-situ sample characterization. The samples can be annealed at up to 1200 K at the Auger stage under  $\text{O}_2$  atmosphere. The surface of the samples can be investigated during the growth process by a RHEED (Chap. 4.5) unit installed in the main chamber. The main chamber contains six effusion cells and two electron gun (e-gun) evaporator units. Each e-gun has four crucible stations, so that in total 14 materials can be present in the chamber. The growth rate associated with each e-gun is monitored by a quartz micro balance (QMB) and adjusted by a proportional-integral-derivative PID regulation algorithm using the output power. Additionally, a main QMB at the sample position can be used to adjust the rates of the effusion cells before the

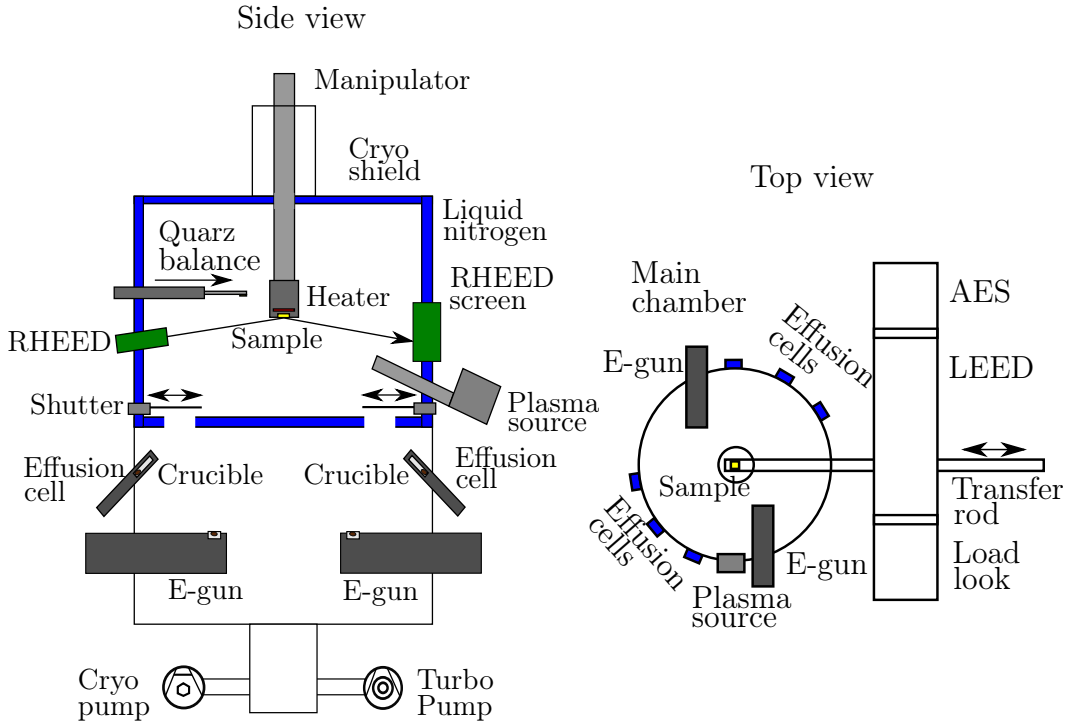


Figure 4.3: Schematic setup of the Oxide Molecular Beam Epitaxy system adapted from [89].

growth process. In the main manipulator the samples can be heated up to temperatures of 1200 K. The rotation of the sample up to 20 rpm yields a better homogeneity of the prepared thin film. To avoid oxygen deficiencies in the films as well as in the substrates, which would highly influence the properties of oxide materials [90], an atomic oxygen plasma source is installed in the main chamber producing a directed atomic oxygen beam onto the sample during growth. The oxygen flux can be controlled by a MKS mass flow controller, while the ratio of the oxygen-to-nitrogen can be monitored by a residual gas analyzer. The main chamber reaches a UHV pressure of  $4 \cdot 10^{-11}$  Torr by a Pfeiffer HiPace 700 Turbo pump and a cryo pump. Additionally, a cryo shielding operated with liquid nitrogen is installed to capture atoms and protect the chamber from heat radiation of the effusion cells. A constant flow of liquid nitrogen is ensured by a phase separator unit. The calibration procedure to find the desired rates and the growth of thin films of good quality will be described in Chapter. 5.2 for the growth of  $\text{La}_{0.5}\text{Sr}_{0.5}\text{MnO}_3$  on  $\text{SrTiO}_3$  substrate.

### 4.3 Low Energy Electron Diffraction LEED

Low Energy Electron Diffraction (LEED) is a method to investigate the crystalline structure of the surface. Electrons with a wavelength in the range of the atomic spacing of the crystal lattice i.e. some Ångstroms are used as probes. The wavelength of the electrons and thus their energy can be changed by the accelerating voltage according to de-Broglie's formula. The small penetration depth of the elastically scattered electrons is the reason

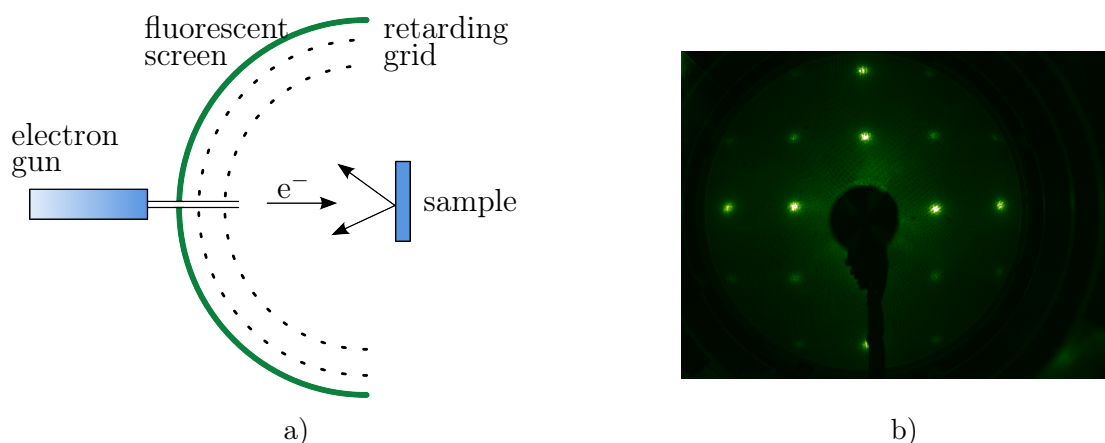


Figure 4.4: a) typical LEED setup. b) LEED pattern of a good quality  $\text{La}_{0.5}\text{Sr}_{0.5}\text{MnO}_3$  layer on a  $\text{SrTiO}_3$  substrate measured at 100 eV.

for the surface sensitivity of this method. UHV is necessary to achieve the required mean free path length of the electrons in order to prevent them from interacting with gas atoms but also to hinder the contamination of the surface by impurity atoms. A typical setup can be seen in Fig. 4.4 a). The electrons emerging from a hot filament are accelerated by a Wehnelt cylinder in the electron gun and focused by an electrostatic lens system onto the sample. There, electrons get backscattered by the interaction with the sample. After passing a retarding grid which filters inelastically scattered electrons, the elastically scattered electrons are accelerated to a fluorescent screen that is biased to high voltage. An example of a LEED pattern from a  $\text{La}_{0.5}\text{Sr}_{0.5}\text{MnO}_3$  layer on a  $\text{SrTiO}_3$  substrate at 100 eV is shown in Fig. 4.4 b). Sharp reflections with a very low background indicate a crystalline thin film of good quality [91]. In this thesis LEED is used to qualitatively verify the quality of substrate and film surfaces although it is a much more powerful tool to e.g. determine lattice parameters. For a detailed theoretical description of the scattering process of electrons in the LEED the reader is referred to dedicated literature [92].

## 4.4 Auger Electron Spectroscopy AES

Auger Electron Spectroscopy (AES) is a surface sensitive method based on the Auger effect to probe the chemical composition of a solid. The Auger effect is schematically shown in Fig. 4.5. An electron beam of 3 kV can remove a core electron. Since this state is energetically unfavorable, an electron from an outer shell will replace it. The energy gain in the amount of the difference between the shell and core level can be coupled to another shell electron. If this energy is bigger than the binding energy, the electron can be emitted with an element specific kinetic energy. With Auger spectroscopy the amount of such Auger electrons with respect to the kinetic energy is measured. The concentration of the element can be determined by the intensity of the associated peak.

The AES setup mainly consists of an e-gun providing electrons with the desired energy,

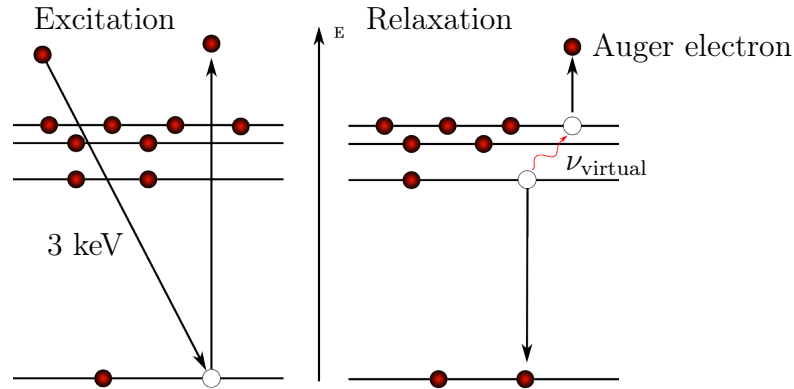


Figure 4.5: *Schematic explanation of the origin of Auger electrons.*

an analyzer for the determination of the kinetic energy of the Auger electrons and a detector. Because of the small signal-to-background ratio, a lock-in technique is required. The system is operated under UHV conditions like in the LEED setup. A list of spectra for most elements can be found in the “Handbook of Auger electron spectroscopy“ [93]. In this thesis AES is used to check for clean surfaces of the substrate, by monitoring the Auger peak corresponding to carbon, and to check for the stoichiometry of the films after the growth process.

## 4.5 Reflection High Energy Electron Diffraction RHEED

Another surface sensitive technique used in this thesis is Reflection High Energy Electron Diffraction (RHEED). It has the advantage that it can be performed in-situ during the growth process due to the specific geometry of RHEED (see Fig. 4.6).

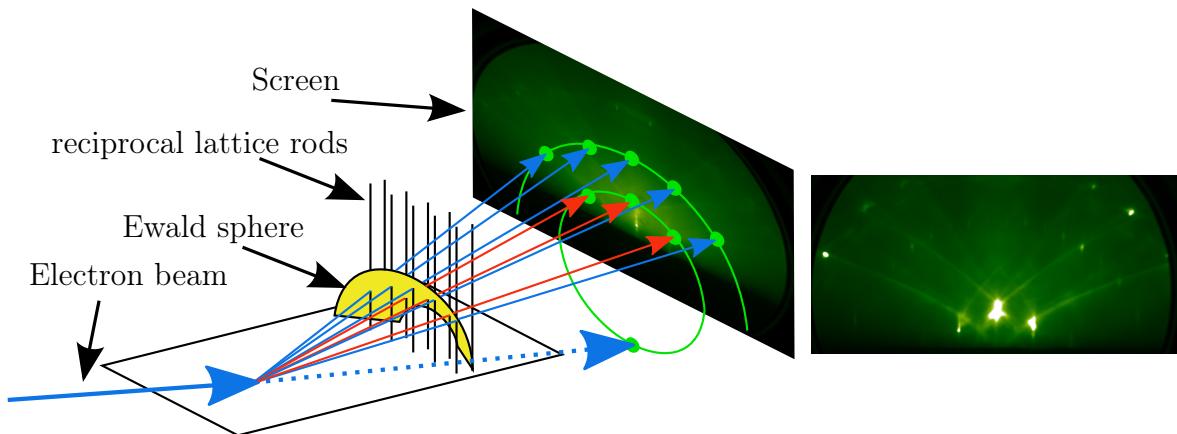


Figure 4.6: *Schematic geometry of RHEED. The electron beam hits the sample under grazing incidence. The surface sensitivity of this technique leads to rods in reciprocal space, since just two Laue equations are valid. The scattering pattern becomes visible on the detector screen. Here a typical pattern for a clean  $\text{SrTiO}_3$  substrate is shown.*

Electrons with an energy of 15 kV are impinging onto the sample under an angle of  $1 - 3^\circ$  by an electron gun. Due to the high interaction of the electrons with the sample and the grazing incidence, the electrons are diffracted only from the surface. The electrons can interfere constructively to form a scattering pattern on the photoluminescent detector screen. Elastic scattering from a three dimensional object can be described in general by the Laue equations. Since the method is very surface sensitive, just two Laue equations are valid, as the system is two dimensional. This leads to rods in reciprocal space (see Fig. 4.6). Each rod will intersect the Ewald sphere in one point leading to reflections on Laue rings of different order on the screen. This is valid for an ideal system without roughness. Roughness will lead to diffuse scattering so that these rods becomes broader. Thus they cross the Ewald sphere not just at one point, but in a small area, leading to a broadening of the scattering pattern. Especially for small orders this effect is pronounced due to the steep slope of the Ewald sphere. This broadening and the peak-to-background ratio are an indication for roughness and quality of the film [94]. Furthermore with RHEED it is possible to identify the growth mode of the thin film. For a Frank van-der-Merwe growth mode (layer-by-layer), the form of the RHEED pattern will stay constant, but the intensity will oscillate with maxima for completed layers and minima for half-completed layers [95–97]. For a Stranski-Krastanov growth mode (3D island) the form of the RHEED pattern changes to the typical pattern for a three dimensional material. More details on RHEED can be found in [95]. In this thesis RHEED was used for the qualitative analysis of the sample surface.

## 4.6 Rutherford Backscattering Spectrometry RBS

Rutherford Backscattering Spectrometry (RBS) is an analytical method to determine the composition of matter by measuring the backscattering of a light projectile, e.g.  $\text{He}^+$  ions, impinging on a sample. The RBS instrument of the Peter Grünberg Institute uses  $\text{He}^+$  ions as probes which are accelerated by a tandetron accelerator to an energy of 1.4 MeV. In first approximation RBS can be described by elastic hard-sphere collision between the  $\text{He}^+$  ion and the stationary atom in the sample. The  $\text{He}^+$  ions lose a specific portion of kinetic energy depending on the mass of the stationary atom. The energy  $E_1$  of the  $\text{He}^+$  ions after the scattering process can be described as [91]

$$E_1 = k \cdot E_0, \quad (4.1)$$

with initial energy  $E_0$  and the kinematic factor,

$$k = \left( \frac{\cos(\Theta) + \sqrt{\left(\frac{m_{\text{At}}}{m_{\text{He}}}\right)^2 + \sin^2(\Theta)}}{1 + \frac{m_{\text{At}}}{m_{\text{He}}}} \right)^2. \quad (4.2)$$

The kinematic factor depends on the mass of the projectile  $m_{\text{He}}$ , the mass of the target atom  $m_{\text{At}}$  and the scattering angle  $\Theta$ . The detector is typically positioned close to  $\Theta \approx 180^\circ$ , because the energy loss for particles detected at this angle is maximum, leading to a maximization of the mass resolution of the measurement. Furthermore, the  $\text{He}^+$  ions lose energy while traveling through matter. Hence the final energy  $E_2$  is

$$E_2 = k \left( E_0 - \int_0^{d_1} \left( \frac{dE}{dz} \right) dz \right) - \int_0^{d_2} \left( \frac{dE}{dz} \right) dz \quad (4.3)$$

where  $d_1$  and  $d_2$  denotes the distance from the sample surface to the scattering event and vice versa ( $d_1 = d_2$  for  $\Theta=180^\circ$ ). The energy loss  $\frac{dE}{dz}$ , can be described by an empirical model using the atomic density of the material [91]. The energy spectra can be modeled to get depth resolved information on the chemical composition. Unfortunately, the method is not sensitive to light elements like oxygen. RBS measurements are used to determine the stoichiometry of the thin films prepared by OMBE and HOPSS. The error on the result of the RBS measurement is roughly 5%.

## 4.7 X-ray Reflectometer/Diffractometer

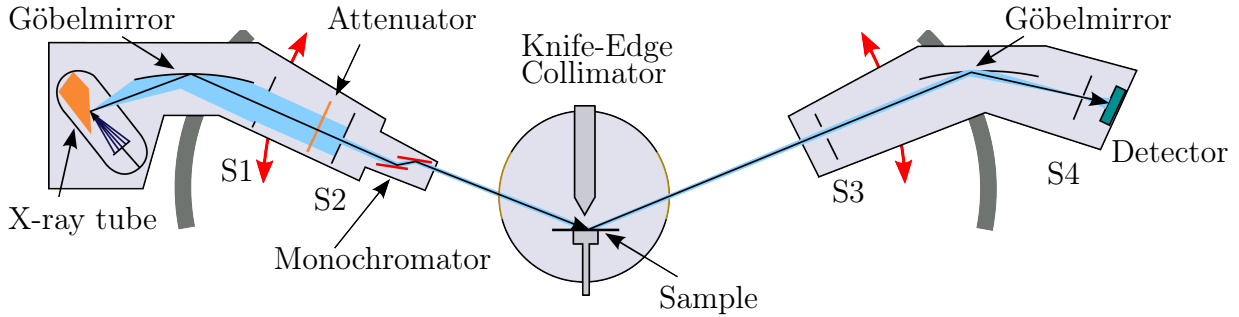


Figure 4.7: Schematic setup of the X-ray diffractometer D8 Advanced. It operates with a copper X-ray source. The flight path is defined by Göbelmirrors and slits. The vacuum sample stage provides a temperature range from 70 to 700 K. Adapted from [98].

The Bruker AXS X-ray diffractometer D8 Advanced is used as reflectometer and diffractometer for the investigation of the prepared thin films. The system operates a  $\text{Cu}_{K\alpha}$  X-ray source with a wavelength of  $\lambda = 1.54 \text{ \AA}$ . The beam path of the experiment is shown in Fig. 4.7. The X-rays are collimated by a Göbel mirror and two slits. A vacuum sample stage with a temperature unit is installed to provide the opportunity to measure within a temperature range of 70-700 K. Additionally a Knife-Edge-collimator is installed to achieve an optimal collimation of the incident beam and for background suppression. Next to the sample position an automated attenuator unit is placed to protect the detector from radiation damage. The degree of absorption can be changed during the measurement. The reflected beam passes a second Göbel mirror and slit combination and the X-ray beam is detected by a point detector. All slits can be changed to adjust the resolution of the experiment. The X-ray diffractometer D8 Advanced is used in reflectometry mode to determine the laterally averaged thickness and roughness of the thin film samples. In order to investigate the crystalline quality and out-of-plane lattice parameter it is used in diffraction mode. Additionally, a channel cut monochromator is mounted for the diffraction measurements to suppress background and to cut off the Bremsstrahlung.

## 4.8 Atomic Force Microscope AFM

An Agilent Technologies 5400 Atomic Force Microscope (AFM) is used to probe the topological properties of the sample surface. The method utilizes the atomic interaction between a measuring tip and the sample surface, which can be described by the Lennard-Jones-potential (see Fig. 4.8 a)). The AFM is used in AC-mode (non-contact mode). In this case the measuring tip, which is fixed to a cantilever, is moved to the sample surface. The cantilever is excited to oscillate close to its resonant frequency. This oscillation is measured by the reflection of a laser beam from the cantilever and probed by a 4-quadrant detector as illustrated in Fig. 4.8 b)). The change in the oscillation amplitude due to the atomic interaction between tip and surface is compensated by a height correction of the cantilever realized by piezocrystals. This correction is interpreted as a topological height profile of the sample. The atomic force microscope is used to probe the surface quality and especially the surface roughness. The average height distribution of the surface is used to calculate the root mean square (rms) roughness.

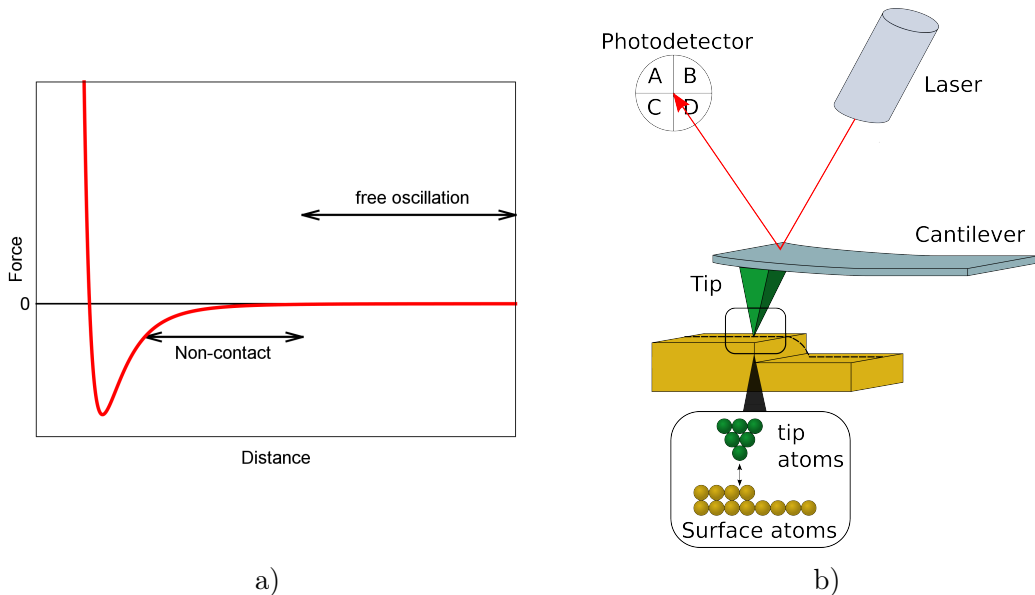


Figure 4.8: a) shows the Lennard-Jones Potential which describes the interaction between the measurement tip and the sample surface. b) shows the AFM-setup, the oscillation of the cantilever is probed by a laser beam which is detected by a 4-quadrant detector.

## 4.9 SQUID-Magnetometer MPMS

The "Magnetic Property Measurement System" (MPMS) from Quantum Design was used to determine magnetic properties. Since the manipulation of the magnetization with respect to an applied electric field is of great interest for magneto-electrics some modifications of the MPMS were done to apply electric fields at the sample and to probe a possible magneto-electric coupling (MEC). In the first part of this section the measurement principle of the standard MPMS will be described, while the modification thereof and the measurement of the magneto-electric coupling will be discussed in the second part.

The MPMS magnetometer utilizes a Superconducting Quantum Interference Device (SQUID), to probe the magnetization very precisely down to  $10^{-11}$  A m<sup>2</sup>. The sample is moved through a second-order gradiometer detection coil, where the magnetic moment of the sample induces an electric current, which is transferred to the SQUID. The rf-SQUID consists of a superconducting ring interrupted by a Josephson tunnel junction that is inductively coupled to a rf-tank circuit. The current induced by the sample causes a magnetic field at the SQUID due to a second coil, which leads to a change of the impedance of the ring causing a change of the voltage of the tank circuit. This change in the voltage amplitude gives the response function with respect to the sample position. The magnetic moment of the sample can be determined from this response signal, using the theoretical signal of a dipole moving through a second-order gradiometer [99]. For details see [100, 101]. The magnetometer used here can reach external magnetic fields of up to  $\pm 7$  T with a field uniformity of 0.01% over a range of 4 cm. The MPMS has a high-precision temperature unit, which covers a temperature range of 1.9 - 400K. An AC-coil at the sample position can provide an AC magnetic field in order to measure the magnetic susceptibility of a sample. Since we are interested in the magneto-electric coupling (MEC) we had to adapt the MPMS to apply electrical contacts at the sample position, which is explained in the following.

### Magneto-electric Setup

The linear magneto-electric effect was measured for the first time by Astrov in 1960 [102]. The measurement principle was picked up by Borisov and improved by the use of the advantages of a commercial SQUID magnetometer [103]. The schematic diagram of the required electrical connections can be seen in Fig. 4.9 a). The connection to the AC-coil has to be disconnected and the coil is short-circuited. A resistance is plugged in instead of the AC-coil, which transforms the driving current  $I = I_{\max} \cos(\omega t)$  (normally used for the AC-coil) into a voltage  $U = RI_{\max} \cos(\omega t)$ . This voltage is increased by a power amplifier (Krohn-Hite Corp., model 7602) up to 200 V and connected to the sample. Fig. 4.9 b) shows the sample mounting on an insulating Vespel rod and the connection of the electrical contacts by silver paste. By monitoring the phase with an oscilloscope it was ensured that there is no phase shift between the driving voltage and the voltage output of the amplifier in the frequency range of  $1 \leq f \leq 10$  Hz. The measurement can be performed with the standard command for the AC-susceptibility measurement, using the advantage of high sensitivity due to a lock-in technique. Here, the sample is not moved through

the pick up coils, so that only the change of the samples magnetization induced by the applied electric AC field is measured. In the case of a magneto-electric effect a AC magnetic moment  $m' \cos(\omega t + \phi) + m'' \sin(\omega t + \phi)$  can be detected by the dual phase lock-in amplifier with the same frequency  $\omega$  as the electric excitation field  $E = E_{AC} \cos(\omega t)$ .

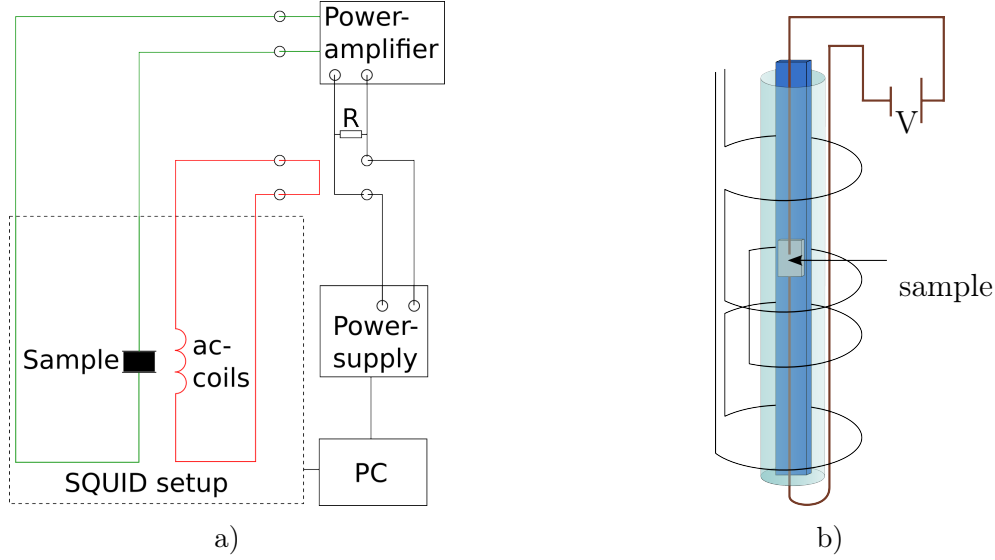


Figure 4.9: a) Diagram of the electrical connections, which are required for the operation of a commercial SQUID magnetometer for MEC measurements. b) Electrical connection to the sample which is fixed at a Vespel rod and covered by a straw. Around the straw the second-order gradiometer pick-up coils are depicted.

In order to interpret the measured quantity we have to consider that the lock-in technique, which uses the frequency of the sinusoidal AC electric field as reference signal, gives the first Fourier coefficient of the input signal as output for two phases shifted by  $90^\circ$  corresponding to  $m'$  and  $m''$ . We interpret the amplitude as half of the change of the magnetization induced by the electric field. For this,  $\frac{1}{2}\Delta m_{E_{AC}}$  is calculated as the absolute square of  $m'$  and  $m''$  in order to avoid complications by the phase. In order to get  $\Delta m_{E_{AC}}$  for electric fields from maximum negative to maximum positive electric field, it has to be multiplied by a factor of two. This interpretation of the measured signal is unlike in Ref. [103], where the measured quantity of this technique is interpreted as a ME susceptibility. However, this is only valid in the case of a linear response. A linear response is given, if one takes a small perturbation, e.g. a small AC electric field, into account. Since here the used AC voltages are quite high this approach is not valid. Furthermore, the interpretation of the signal as  $\Delta m_{E_{AC}}$  is underlined by the comparison to manually taken data points. Constant electric fields up to  $\pm 200$  V can be applied at the sample by the use of external device control programs. Hence, electrical hysteresis loops or standard measurements with applied electric fields can be performed. With this, test measurements of the magnetization with applied electric fields have been performed. Fig. 4.10 a) shows the data taken with the new MEC option and data points taken "manually". The

change of the magnetization  $\Delta m_{T,E_{AC}}(H)$  measurement by the lock-in technique is depicted as function of the external magnetic field. The manually measured difference of the magnetization  $\Delta m_{\text{man.}} = m_{-150\text{V}} - m_{+150\text{V}}$  with respect to the electric field is in a good agreement with the results of the MEC measurement underlining the reliability of the newly installed measurement technique and the interpretation of the data as  $\Delta m_{E_{AC}}$ . The reduced errorbars in the MEC measurement clearly show the advantage of the lock-in technique. A second test measurement can be seen in Fig. 4.10 b). Here, a pure BaTiO<sub>3</sub> substrate with a Au top and bottom contact was measured. The measurement shows that no magnetization appears due to any flowing currents within the substrate from the application of electric fields. Additionally, measurements to check our setup were performed on a Cr<sub>2</sub>O<sub>3</sub> crystal (3mmx3.5mmx0.5mm) and compared with the results of the Kleemann group [103, 104]. For a better comparability, data points are given in units used in [103]. Since these measurements show similar results (see Fig. 4.11), we can be sure that our setup works correctly, although the interpretation of the measured quantity is different.

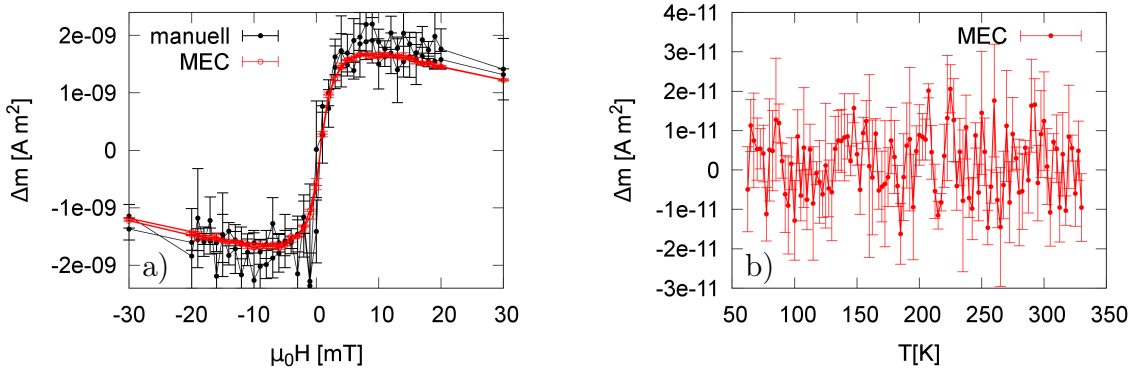


Figure 4.10: a) shows the comparison of a measurement performed by the new installed MEC option ( $\omega = 1$  Hz) and manually taken data points. It shows the change of the magnetization by the application of electric fields with respect to the external magnetic field. Both measurements are in a good agreement. b) shows the temperature dependent MEC measurement for a Au/BaTiO<sub>3</sub>/Au system. No signal is observed, as expected. This gives evidence that no magnetic signal is measured by any flowing currents within the substrate due to application of the electric field.

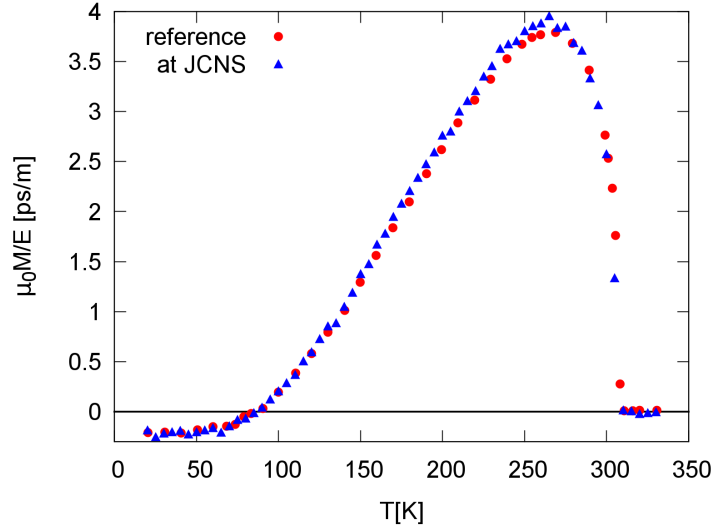


Figure 4.11: *MEC* measurement on a  $\text{Cr}_2\text{O}_3$  crystal vs. temperature at  $\omega = 1$  Hz and  $E = 65.2$  kV/m. Reference data points taken from [103] are in good agreement with the measurement performed with the local setup at the JCNS.

## 4.10 Polarized Neutron Reflectometry PNR

Polarized Neutron Reflectometry (PNR) measurements are performed to probe the magnetic profile of the  $\text{La}_{(1-x)}\text{Sr}_x\text{MnO}_3$  layers. Measurements are done at two different beamlines operating at a continuous neutron source and a spallation source, respectively. Each experiment will be described in the following.

### 4.10.1 Magnetic Reflectometer with High Incident Angle, MARIA

The polarized neutron reflectometer MARIA is operated at the continuous neutron source of the MLZ. The setup of the experiment is schematically shown in Fig. 4.12. The wavelength of the incoming neutrons can be selected by a velocity selector in the range of  $4.5 \text{ \AA} < \lambda < 40 \text{ \AA}$ , with a maximum intensity for a wavelength of  $4.5 \text{ \AA}$ . The velocity selector provides a wavelength distribution of  $\frac{\Delta\lambda}{\lambda} = 0.1$ . Additionally, the neutron beam can be polarized by a double reflection polarizer. Next to the polarizer a slit system collimates the neutron beam and shrinks the beam for an optimal illumination of the sample, leading to a reduction of the background for well chosen slit settings. The setup is optimized for  $1 \times 1 \text{ cm}^2$  samples by a vertical focusing elliptic neutron guide. The sample environment is mounted on a hexapod which provides the movement of the sample. The polarization of the scattered beam can be analyzed by a  $\text{He}^3$  cell for a full horizontal polarization analysis. The scattered neutrons are detected by a  $400 \times 400 \text{ mm}$   $\text{He}^3$  2D Detector. MARIA delivers optimal conditions to probe magnetic interface effects and thin magnetic layers down to sub monolayers. An electromagnet provides an external magnetic field of up to 1.3 T. Temperatures in a range from room temperature to 4 K can be reached by the use of a closed cycle cryostat. A voltage up to 500 V can be applied

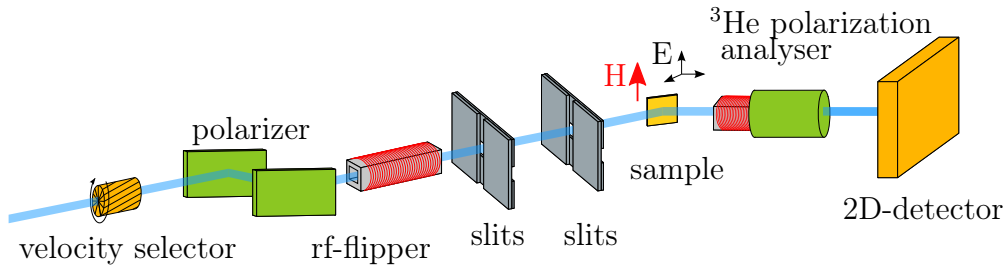


Figure 4.12: *Schematic setup of the polarized neutron reflectometer MARIA. The wavelength can be chosen by the use of a velocity selector. The beam is collimated by a slit system and can be polarized/analyzed by neutron optics. Electric and magnetic fields can be applied at the sample stage.*

at the sample position. A Q-space from  $0.002 \text{ \AA}^{-1}$  to  $3.2 \text{ \AA}^{-1}$  can be probed with MARIA.

Simulations of an ideal system show that a signal-to-noise ratio of 4-5 orders of magnitude is necessary to observe the interface effect predicted by Burton et al. [1]. Hence, a new sample holder (see. Fig. 4.13) was designed to reduce the background of the experiment and to apply the required voltage to the sample. The sample holder is made of aluminum covered with boron, which is highly neutron absorbing. Due to the small beam window, just the sample is illuminated by the neutrons even if the slits are opened too far. The back electrode of the sample is connected to the ground of the cryostat by the aluminum holder. The top electrode is connected by a wire to the electrical feed through of the cryostat. With this setup the required signal-to-noise ratio could be reached and a voltage up to  $\pm 500 \text{ V}$  could be applied.

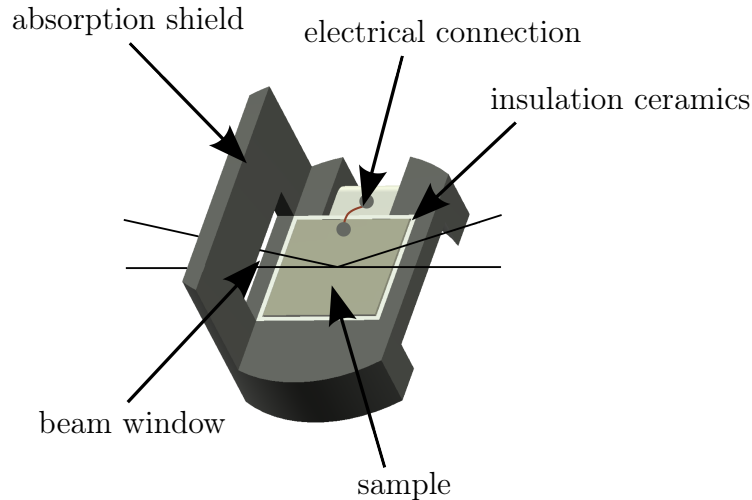


Figure 4.13: *Sample holder used during the scattering experiments, to reduce background and allow connection of the electrodes for application of external electric fields.*

## Data reduction

The instrument saves one detector image for each angle position. A typical detector image can be seen in Fig. 4.14. It shows the reflected peak 2) in the middle of the detector, the tail of the almost blocked direct beam 1) and the background 3).

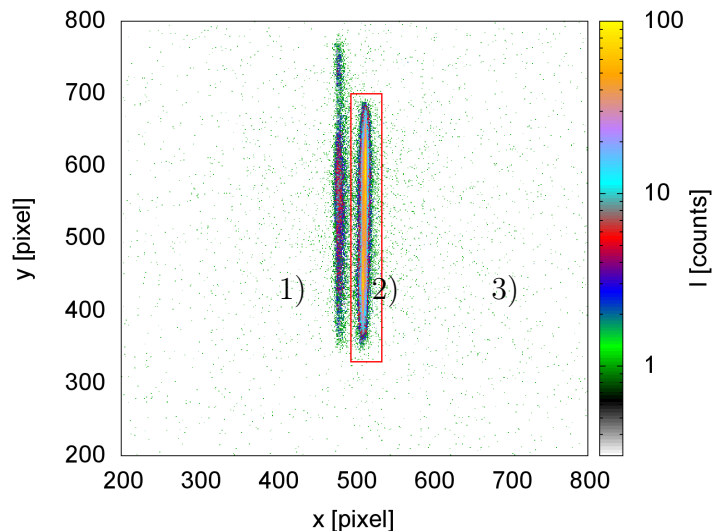


Figure 4.14: *Typical detector image taken at MARIA. The left peak 1) corresponds to the tail of the almost blocked direct beam, the peak in the middle of the detector is the reflected beam 2) and 3) shows the background.*

This data has to be reduced to get the  $Q$ -dependent reflectivity curve. The detector image is integrated vertically in the region of interest, represented by the red box, for each detector position. Background generated by the scattering of neutrons with air, the sample holder, and other components within the neutron beam is angular dependent. Hence, the background has to be subtracted for each detector image. For this, the background is fitted for the vertical integrated intensity and subtracted. The obtained integrated intensities are normalized to the incident neutrons measured by the monitor and sorted by the scattering angle obtained from the detector and sample angle.

### 4.10.2 Magnetism Reflectometer MR

The magnetism reflectometer MR [105] at the beamline 4A operated at the Spallation Neutron Source SNS is dedicated to the study of magnetic thin films. The reflectometer is a Time-Of-Flight (TOF) experiment with a bandwidth of  $\Delta\lambda = 2.74 \text{ \AA}$  and a wavelength range of  $1.8 \text{ \AA} < \lambda < 14.0 \text{ \AA}$ . It operates in a horizontal scattering plane in a  $Q$ -range of  $0 \text{ \AA}^{-1} < Q < 6 \text{ \AA}^{-1}$ . The spin-state of the neutrons can be determined by the polarizer, analyzer and spin-flippers. Scattered neutrons are counted by a position sensitive 2D multidetector. Magnetic fields up to 1.2 T can be applied. The sample can be investigated in a temperature range of 5-750 K. Electric voltages of  $\pm 200 \text{ V}$  can be applied to the sample. MR is one of two SNS neutron reflectometry instruments that can

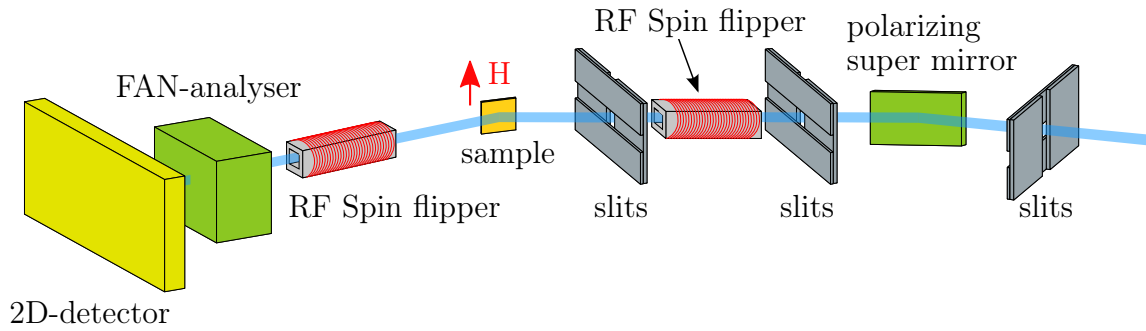


Figure 4.15: *Schematic setup of the time-of-flight reflectometer MR.*

be used for magnetic investigation of thin films and interfaces.

### Data reduction

Since MR is a TOF experiment, a broad  $Q$ -range, depending on the used bandwidth, can be probed within a single scattering angle. A typical detector image of the MR can be seen in Fig. 4.16 a). At the first glance, it does not differ from those taken at MARIA, but it includes additional information about the flight time of the neutrons from the moderator to the detector. Assigning the TOF to each count and integrating along  $y$ -axis within a certain region of interest results in the time dependent scattering intensities like one can see in Fig. 4.16 b). The  $Q$ -dependency of each  $x$ -pixel is calculated by the scattering angle and the time-of-flight for each point. Then, the reflectivity curve is obtained by integrating the intensities along  $x$  within the region of interest. Additionally, background is subtracted from the data. The intensity distribution of the wavelength in the neutron

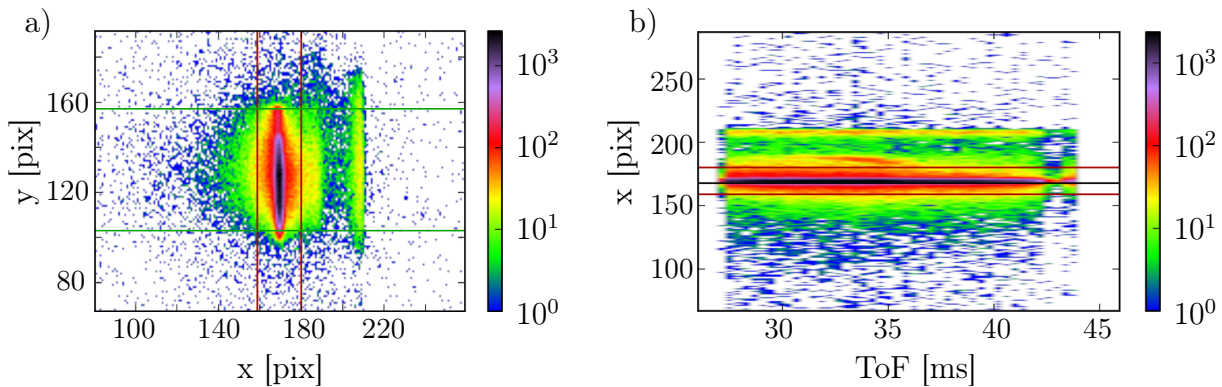


Figure 4.16: *The detector image a) at MR shows the reflected and the tail of the direct beam. Red and green lines indicate the region of interest. b) shows the intensities separated to the flight time of the neutrons.*

pulse is not necessarily homogeneous, hence the intensities are normalized by taking the distribution by a direct beam measurement into account. Additionally, the intensity is normalized to the incoming neutrons by the proton charge of the spallation process. In order to cover the required  $Q$ -range, data have been taken at three different scattering

angles ( $0.35^\circ$ ,  $0.55^\circ$ ,  $1.028^\circ$ ). The lowest angle has been measured by a wavelength band around  $6.1 \text{ \AA}$  and  $4.1 \text{ \AA}$ , higher angles with  $4.1 \text{ \AA}$ . The angles have been chosen in such way that the successive regions slightly overlap. Each region has to be scaled by a factor, beginning with the lowest Q-region. This region includes the plateau of total reflection which has the highest intensity. This has to be scaled to 1, while the rest of the regions are scaled in a such way, that they fit to the region before. All the data reduction can be done within the "quicknxs" software provided by the SNS.



# Chapter 5

## Sample Preparation

In this chapter the fabrication of the functional oxides films is described. A state-of-the-art Oxide Molecular Beam Epitaxy (OMBE) (Chapter 4.2) and a High Oxygen Pressure Sputtering System HOPSS (Chapter 4.1) were used to prepare the thin films. In order to prepare good quality films of the desired stoichiometry using the OMBE a growth process had to be developed. For the preparation by the HOPSS an existing recipe had to be optimized. Since the predicted effect in  $\text{La}_{0.5}\text{Sr}_{0.5}\text{MnO}_3/\text{BaTiO}_3$  heterostructures is strongly related to the interfaces, samples with a well defined, e.g. very smooth interface have to be produced. Furthermore the produced single crystal thin films have to be of high quality with a minimum amount of crystal defects. These defects could lead to different properties of the materials themselves, e.g. the presence of oxygen vacancies leads to an increase of the Curie temperature  $T_C$  in  $\text{LaMnO}_{3-\delta}$  [90]. Beginning with the substrate preparation I will describe, how the films were produced and why we decided to use  $\text{BaTiO}_3$  substrates instead of growing films for the heterostructure.

### 5.1 Substrate Preparation

The main idea is to build a  $\text{La}_{0.5}\text{Sr}_{0.5}\text{MnO}_3/\text{BaTiO}_3$  multilayer stack which can be electrically connected. Niobium doped  $\text{SrTiO}_3$  (Nb:STO) was chosen as substrate, because it is conductive and the lattice parameter allows epitaxial growth of  $\text{BaTiO}_3$  [15, 106]. Additionally, the ferroelectric properties of  $\text{BaTiO}_3$  are strongly enhanced due to strain by the use of  $\text{SrTiO}_3$  substrates [60, 61, 66]. For the growth of high quality epitaxial thin films already the substrate must exhibit a clean, well terminated surface and a good crystalline quality. In order to get rid of organic residuals and to obtain a  $\text{TiO}_2$ -terminated surface a hydrofluoric acid (HF) process was carried out as described following Ref. [107]. Fig. 5.1 shows the topography measured by AFM of the prepared substrates after a annealing process at 1150 K. The roughness is very low in the range of two unit cells given by the atomic steps of the surface. The atomic terraces also indicate a  $\text{TiO}_2$ -termination of the surface. The miscut of the surface to the lattice planes is lower than  $0.3^\circ$  matching the product specifications given by CrysTec GmbH. After loading the etched substrates into the vacuum chamber, the substrates were tempered at high temperatures to remove impurity atoms. First they were heated to 770 K in vacuum over night, afterwards they were heated to 1270 K in oxygen atmosphere at  $9.3 \cdot 10^{-6}$  mbar in the OMBE and at 3

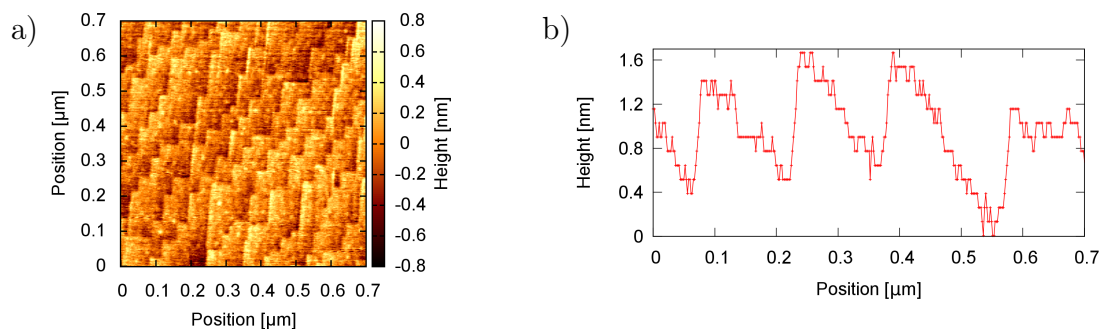


Figure 5.1: a) Topography of a prepared  $\text{SrTiO}_3$  (001) substrate measured with AFM. Atomic flat terraces can be seen indicating a  $\text{TiO}_2$  termination of the surface as expected. b) Line profile of the prepared  $\text{SrTiO}_3$  substrate measured by AFM. The miscut is  $0.3^\circ$ .

mbar in the HOPSS. Fig.5.2 a) shows an AES measurement with an absent carbon peak indicating a clean surface. As shown in Fig. 5.2, the temperature treatment leads to a much sharper LEED pattern with decreased background corresponding to a good crystal quality.

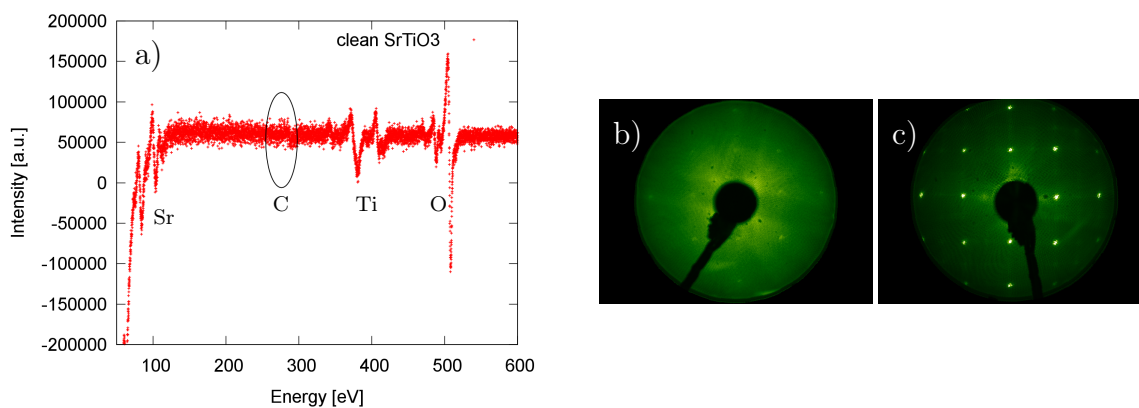


Figure 5.2: a) AES of a  $\text{SrTiO}_3$  substrate after the preparation treatment. The carbon peak vanishes due to the process indicating a clean surface. LEED pattern of a b) untreated and c) prepared  $\text{SrTiO}_3$  substrate at an energy of 100 eV. The pattern gets much sharper with a lowered background due to the substrate preparation confirming the clean surface.

## 5.2 $\text{La}_{0.5}\text{Sr}_{0.5}\text{MnO}_3$ on $\text{SrTiO}_3$

In this section a description is given of how to prepare the magnetic  $\text{La}_{0.5}\text{Sr}_{0.5}\text{MnO}_3$  films. The first part deals with the preparation done by the OMBE while in the second part the preparation by the HOPSS is considered.

### Preparation by Oxide MBE

The preparation of good quality films in the desired stoichiometry by the use of the new installed Oxide MBE is quite challenging. A detailed description of the OMBE system is given in Chapter 4.2. The films are produced by co-deposition, meaning that all elements are evaporated at the same time. Each source has to be calibrated very accurately to achieve the intended stoichiometry. The accurate stoichiometry is very important to prove the effect predicted by Burton et al. [1], but also for a high quality thin film. Quartz micro balances (QMB) are used to determine the growth rates by the change of their frequency due to the deposited mass

$$\Delta f \sim m \cdot \Delta n, \quad (5.1)$$

with the atomic mass  $m$  of the element and the number of the deposited atoms  $\Delta n$ . Regarding the pseudo cubic perovskite structure of  $\text{La}_{0.5}\text{Sr}_{0.5}\text{MnO}_3$ , the number of deposited atoms per time of each material has to be in the correct ratio, namely:

$$n_{\text{Sr}} : n_{\text{La}} : n_{\text{Mn}} = 1 : 1 : 2.$$

The manganese growth rate was chosen as the starting point for the calculations of the required frequency changes  $\Delta f$  for lanthanum and strontium

$$\Delta f_i = \frac{\Delta n_i \cdot m_i}{\Delta n_j \cdot m_j} \cdot \Delta f_j \quad \text{with } j=\text{Mn and } i=\text{La, Sr} . \quad (5.2)$$

In order to achieve constant rates the sources have to be under growth conditions for some time. Particularly the oxygen pressure is a very important parameter, because the oxygen leads also to the oxidation of the evaporation materials in the sources. Thus an equilibrium has to be stabilized which can take some days, before a sample can be grown. Finding the correct stoichiometry is an iterative process, where the samples have to be investigated after the growth process. Due to influences like the sticking coefficient, different absorption and desorption behavior of the QMB compared to the substrate, the calculation of the desired frequency change must be considered as a first approach to determine the correct rates. Rutherford Backscattering (see Chapter. 4.6) is excellent for the determination of the stoichiometry of thin film samples and available at Forschungszentrum Jülich GmbH. However, since the oxygen content of our samples cannot be measured by this technique we have to assume that our samples are completely saturated with oxygen ensured by cooling in oxygen. The summary of good quality samples investigated by RBS can be seen in Fig. 5.3, showing the ratio of La to Mn with respect to the factor  $x = \frac{\Delta f_{\text{La}}}{\Delta f_{\text{Mn}}} \frac{m_{\text{Mn}}}{m_{\text{La}}}$  used for the rate calculation. A linear dependence to the ratio in the stoichiometry was observed for La/Mn as expected according to Equation 5.2, but one can also see that the calculated frequency changes are not very accurate. These calculated  $\Delta f$  seem to be underestimated with respect to the real ratio of elements within the sample. The analysis of

the stoichiometry also shows that the Oxide MBE works reproducibly, if the parameters are chosen equal to previous growth processes. For example, the frequency ratio around  $x \approx 0.7$  always leads to a ratio of La/Mn of  $\approx 0.8$ . The correct rates for the desired stoichiometry can be found by an iterative refinement of the frequency changes according to the results of the RBS analysis. An exemplary RBS measurement including simulation of the final stoichiometry of  $\text{La}_{0.53}\text{Sr}_{0.47}\text{MnO}_3$  on a  $\text{SrTiO}_3$  substrate is presented in Fig. 5.4.

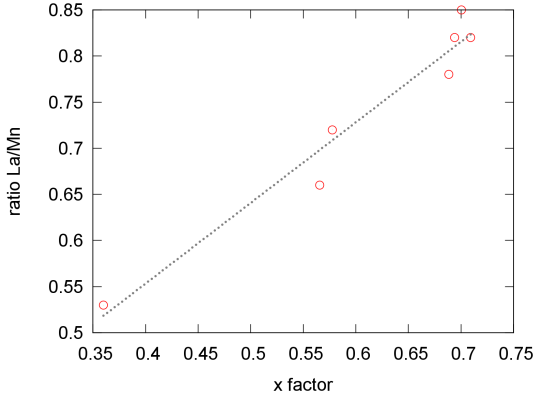


Figure 5.3: *Lanthanum to manganese ratio within the samples measured by RBS. The factor  $x$  corresponds to the ratio of the weighted frequency changes  $x = \frac{\Delta f_{\text{La}}}{\Delta f_{\text{Mn}}} \frac{m_{\text{Mn}}}{m_{\text{La}}}$ . The dotted line is a guide to the eye.*

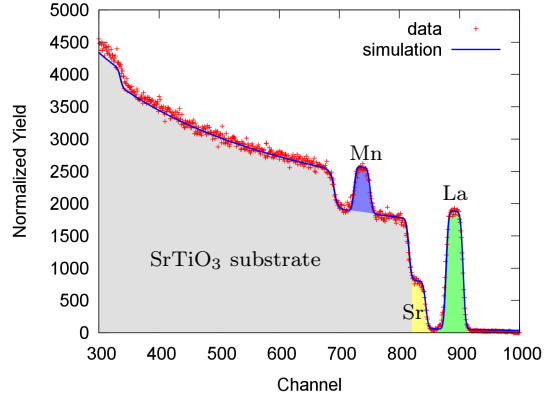


Figure 5.4: *RBS analysis of the final stoichiometry of  $\text{La}_{0.53}\text{Sr}_{0.47}\text{MnO}_3$ . The gray area corresponds to the RBS signal of the substrate and the green, yellow and blue to lanthanum, strontium and manganese of the layer, respectively.*

The best sample quality and the desired stoichiometry of the prepared films was reached at a growth temperature of 1170 K with an oxygen flow of 0.1 sccm and a plasma power of 300 W. A growth rate of one monolayer per minute was used. Substrates were treated as described in the previous chapter. After the growth process the sample was cooled to room temperature within the oxygen plasma.

Temperature [K]	$\Delta f_{\text{Mn}}$ [Hz/s]	$\Delta f_{\text{La}}$ [Hz/s]	$\Delta f_{\text{Sr}}$ [Hz/s]	$\text{O}_2$ -flow [sccm]
1170	0.080	0.0729	0.0465	0.1

Table 5.1: *Optimal parameters for the growth of  $\text{La}_{0.53}\text{Sr}_{0.47}\text{MnO}_3$  films by the OMBE.*

The in-situ RHEED and LEED analysis both indicate a good quality of the  $\text{La}_{0.53}\text{Sr}_{0.47}\text{MnO}_3$  films (see inset of Fig. 5.5) with respect to a smooth surface and a good crystalline structure. The RHEED pattern shows sharp rods even on the first Laue ring and a low background. This also applies for the LEED pattern showing sharp spots and a low background. All prepared samples were investigated by X-ray reflectometry and diffraction measurements in order to obtain the structural information. The reflectometry measurement of the  $\text{La}_{0.53}\text{Sr}_{0.47}\text{MnO}_3$  sample (see Fig 5.5 a)) shows a layer thickness of  $367 \pm 6 \text{ \AA}$  and a smooth surface with a roughness of  $5.7 \pm 0.6 \text{ \AA}$  corresponding to 1.5 unit cells. The

diffraction measurement (see Fig.5.5 b)) on the (001) Bragg-peak indicates a good layer quality. Additionally to the (001) LSMO peak at  $Q_z=1.64 \text{ \AA}^{-1}$ , corresponding to an out-of-plane lattice constant of  $3.83 \text{ \AA}$ , so called thickness oscillations are observed which can only be observed for smooth layers. Additional peaks appear in the diffraction pattern due to a wavelength contamination of the incident beam. Also the Bremsberg produced by the copper tube is visible in the measurement. Both features are not included in the simulation. In conclusion, high quality LSMO films could be produced in the desired stoichiometry.

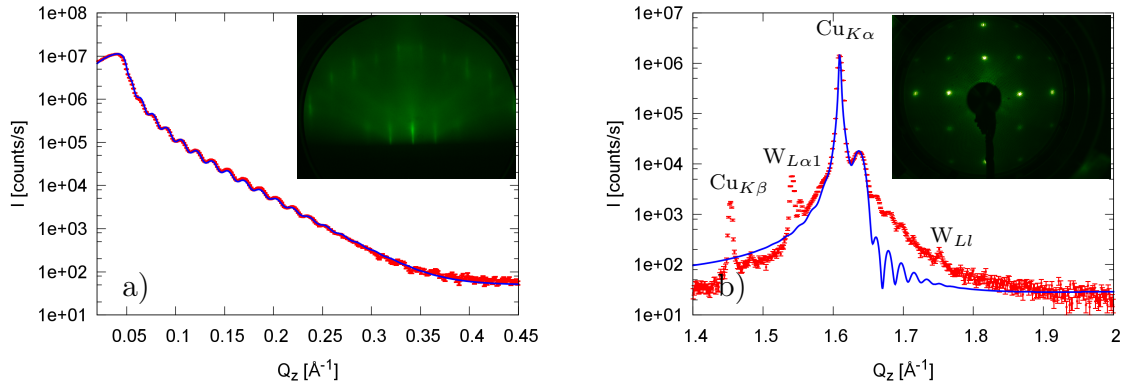


Figure 5.5: *Structural analysis of  $\text{La}_{0.53}\text{Sr}_{0.47}\text{MnO}_3$  film on  $\text{SrTiO}_3$ . a) Shows the XRR data and simulation with a thickness of  $367 \pm 6 \text{ \AA}$  and a roughness of  $5.7 \pm 0.6 \text{ \AA}$ . The (100) reflex b) of the layer corresponds to a lattice parameter of  $3.83 \text{ \AA}$ . Thickness oscillations indicate a very smooth surface. The Bremsberg is not simulated. The inset in a) and b) shows the RHEED and LEED pattern, respectively, indicating a good sample quality.*

## Preparation by HOPSS

$\text{La}_{(1-x)}\text{Sr}_x\text{MnO}_3$  films were also prepared by the HOPSS which is described in Chapter 4.1. After mounting the substrate into the deposition chamber it is pumped to a pressure of  $10^{-6}$  mbar. Afterwards, the substrate is annealed in the same way as described in Chapter 5.1. After the first annealing step the pumping cross section was reduced and an oxygen flow was initiated to a constant pressure of 3 mbar. In this oxygen atmosphere the substrates were annealed at 1270 K for another hour. After the plasma was initiated at the target, the plasma power was slowly increased to obtain an homogeneous plasma at 120 W. The growth process was started by moving the target to the substrate position. The films were grown with a sputtering rate of  $\sim 4 \text{ \AA}/\text{min}$  at a temperature of 1070 K. After reaching the desired film thickness, the sample was cooled down to room temperature with a ramp rate of 5 K/min in oxygen atmosphere (3 mbar) to prevent oxygen from diffusing out of the sample. The stoichiometry of the sample can be slightly influenced by the substrate temperature, sputtering power and the distance from target to substrate. RBS analysis shows that we achieved a perfect  $\text{La}_{0.5}\text{Sr}_{0.5}\text{MnO}_3$  stoichiometry grown on MgO as one can see in Fig. 5.6. MgO was chosen as substrate, since there is no overlap in the expected peaks of the materials of the substrate and the grown film in the RBS spectrum. This leads to a very precise determination of the stoichiometry by RBS. Samples with a smooth layer surface could be grown with a roughness in the range of one atomic unit cell ( $\approx 5 \text{ \AA}$ ) measured by XRR, as presented in Fig. 5.7. The inset shows the (001) diffraction peak confirming a good crystalline quality with thickness oscillations being present.

Temperature [K]	Power [W]	Pressure [mbar]	Distance [cm]
1170	120	3	2

Table 5.2: *Optimal parameters for the growth of  $\text{La}_{0.5}\text{Sr}_{0.5}\text{MnO}_3$  films by the HOPSS.*

In summary, high quality LSMO single crystal thin films could be produced with both systems. The structural properties are comparable in both cases. Due to the time consuming calibration of the sources it is more simple to grow these films using the HOPSS. On the other hand the advantage of the OMBE is the flexibility in the stoichiometry of the films. Additionally, the growth by OMBE leads to an enhanced clamping of the film to the substrate, as will be shown later.

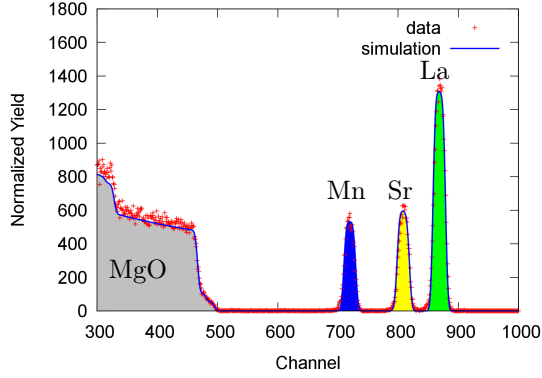


Figure 5.6: *RBS analysis of the stoichiometry of  $\text{La}_{0.5}\text{Sr}_{0.5}\text{MnO}_3$  on  $\text{MgO}$ . The signal caused by the substrate is colored in gray. Lanthanum, strontium and manganese are colored in green, yellow and blue, respectively.*

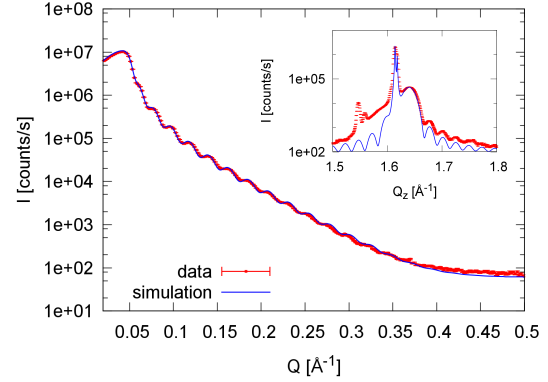


Figure 5.7: *XRR measurement of  $\text{La}_{0.5}\text{Sr}_{0.5}\text{MnO}_3$  on  $\text{SrTiO}_3$  with a layer thickness of  $264 \text{ \AA}$  and a roughness of  $5 \text{ \AA}$ . The inset shows the XRD data of the  $(001)$  Bragg-peak. Thickness oscillations are present confirming a smooth layer.*

### 5.3 BaTiO<sub>3</sub> on SrTiO<sub>3</sub>

Since the magnetic layer could be produced in a good quality, the next step was to fabricate the ferroelectric component of the heterostructure. For the growth of BaTiO<sub>3</sub> films also both systems were available. Once again at first the results achieved by the Oxide MBE are presented, followed by those of the HOPSS.

#### Preparation by Oxide MBE

The procedure to grow BaTiO<sub>3</sub> films by the Oxide MBE is in principle similar to LSMO films described in the previous chapter. The best growth parameters for high quality single crystalline thin films and the correct rates for Ti and Ba to achieve the desired stoichiometry of

$$n_{\text{Ba}} : n_{\text{Ti}} = 1 : 1,$$

had to be found. The required frequency changes can be calculated in first approximation by Equation 5.2 using the masses of barium and titanium. SrTiO<sub>3</sub> substrates were used as mentioned in Chapter 5.1. Since the growth temperature for BaTiO<sub>3</sub> films known from literature is in a large temperature range [97, 108, 109], films were grown with substrate temperatures ranging from 770-1270 K. The growth process was observed with RHEED. Fig 5.8 a) shows the sharp RHEED pattern after the deposition of the first monolayers. For further deposition times, the sharp reflections change to a more stripe like pattern (Fig 5.8 b)) which gets broader with enlarged background due to an increase in the surface roughness (Fig 5.8c)). Unfortunately, additional peaks appear, which are an indication

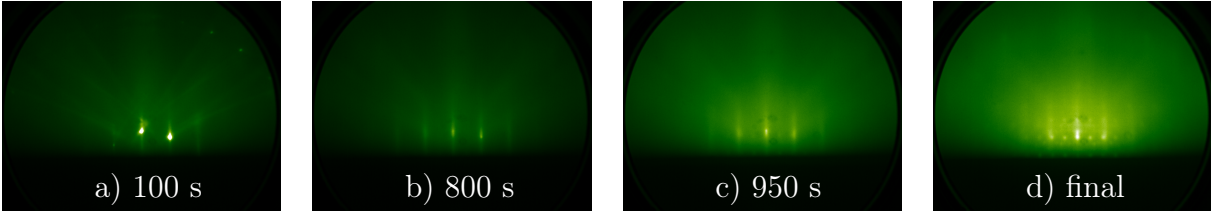


Figure 5.8: *RHEED* study with respect to the deposition time of  $\text{BaTiO}_3$ . The layer-by-layer growth mode a)-c) changes by the deposition time to a 3D like island growth d), indicated by the arising of additional peaks and the high background signal.

for 3D island growth and an elevated surface roughness as one can see in Fig 5.8 d). This change from layer-by-layer to 3D like growth was observed for all samples over the entire temperature range.

XRR measurements were performed to determine the thickness of the films, the roughness of the surfaces and the density profile. The XRR measurement including a simulation of the data can be seen in Fig. 5.9 a). The results of the fit are presented in Figure 5.9 b) in which the scattering length density (SLD) is plotted against the film thickness  $z$ . The gray area indicates the SLD of the  $\text{SrTiO}_3$  substrate, the blue one the SLD of  $\text{BaTiO}_3$  and the green represents a top layer with a reduced SLD. A drastically decrease in the SLD after a film thickness of  $\approx 47 \text{ \AA}$  has to be taken into account to reproduce the data by the fit. The deposition time for each region was calculated. The SLD is directly related to the density of the material and thus the total amount of deposited material is proportional to the integral over the SLD. A linear dependence between time and the amount of deposited material was assumed since the rates of the evaporation sources are constant. Taking additionally the total deposition time and the total thickness into account a deposition time of  $\approx 990 \text{ s}$  was calculated for the first  $\approx 47 \text{ \AA}$  with the density of  $\text{BaTiO}_3$  known from literature [110]. The rest of the material was deposited within  $\approx 250 \text{ s}$  with a reduced density. These results are in good agreement with the RHEED pattern where an enlarged background raises up in the pattern taken after a deposition time of 950 s (see Fig 5.8 c)) resulting in the 3D like pattern in Fig. 5.8 d) after the total deposition time of 1240 s. The scattering length density profile underlines the suggestion of a 3D island growth mode after a certain growth time.

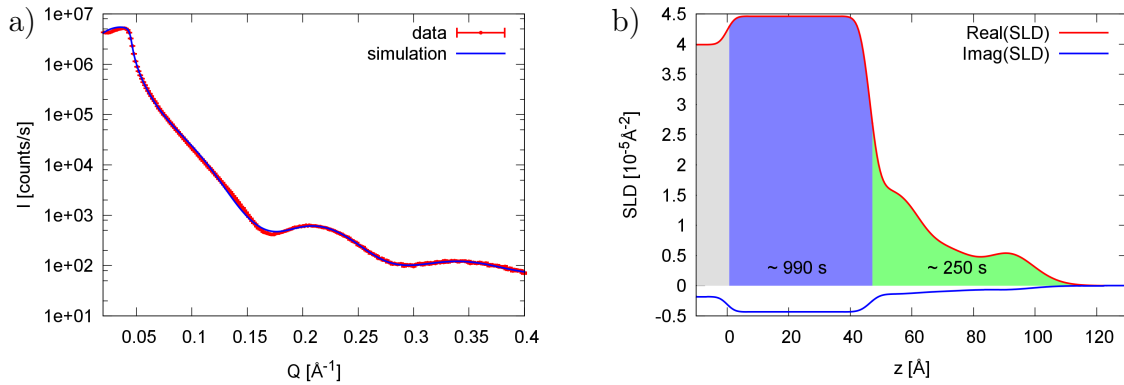


Figure 5.9: a) shows the XRR measurement of a grown Ba:Ti:O layer on SrTiO<sub>3</sub> including the fit of the data. The resulting SLD with respect to the layer thickness is shown in b). A drastically reduction of the density is observed after a thickness of 47 Å corresponding to a deposition time of about 950 s.

The stoichiometry of the samples near the surface was determined by AES in order to study the material composition of those islands. For this purpose a reference measurement of a BaTiO<sub>3</sub> substrate was done for comparison. Auger spectra of the samples were taken under the same parameters as the substrates. After normalization to the oxygen peak of the substrate measurement, the height of the peaks corresponding to Ba and Ti are compared. Fig. 5.10 a) presents exemplary an Auger spectra showing that the peaks corresponding to Ba are elevated while the peaks for Ti are smaller than in the reference measurement. This behavior is valid for all samples under investigation, even for a growth process using a titanium rate which is 10% higher than the calculated rate.

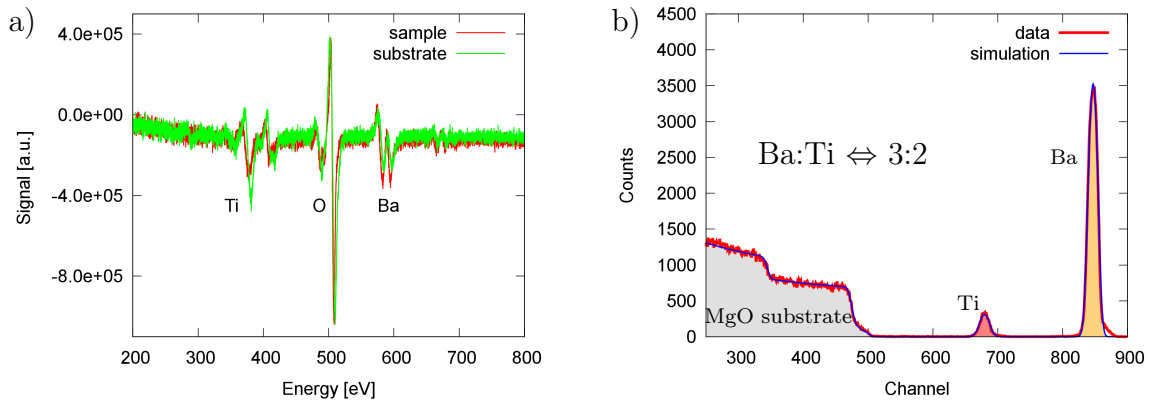


Figure 5.10: Analysis of stoichiometry: a) Comparison of Auger spectra of a grown Ba:Ti:O layer to the reference measurement of a BaTiO<sub>3</sub> substrate. The Ba peak of the sample is enlarged, while the Ti peak is too small. This suggests a Ba rich top layer. b) RBS analysis of a grown Ba:Ti:O layer on MgO substrate with a Ba:Ti ratio of 3:2.

The analysis of the stoichiometry near the surface by AES shows that a Ba rich surface

layer arises which properly favors island growth as it was also shown in previous work from Barbier et al. [109]. Another possibility is that the calculated rates are far of the required ones. Since AES is a surface sensitive method it is still unclear of which composition the layer consists of, hence RBS measurements were performed to determine the depth resolved stoichiometry of the sample. For reasons mentioned before, MgO was used as substrate for the determination of the stoichiometry. Fig. 5.10 b) shows a RBS measurement of a BTO film on MgO including the simulation. All samples under investigation show a Ba content which is much too high (up to  $\approx 64\%$ ). The deviant stoichiometry could be one reason for the insufficient sample quality and the 3D growth mode. In order to improve the stoichiometry one could use RHEED oscillations and a shuttered deposition method in which only one source is opened for the required time. By this method the correct stoichiometry is achieved using the oscillation of the RHEED intensity which should be more accurate. Finding the correct stoichiometry is the first step for the growth of high quality samples. Since it was not possible to achieve samples in a required quality and stoichiometry it was attempted to grow the  $\text{BaTiO}_3$  films by the HOPSS which is presented in the next section.

### Preparation by HOPSS

Since the deviant stoichiometry of the  $\text{BaTiO}_3$  films prepared by the OMBE could be the reason for the island growth,  $\text{BaTiO}_3$  films were also prepared by the HOPSS using a commercial stoichiometric  $\text{BaTiO}_3$  target from Lesker Company. At first the stoichiometry of the  $\text{BaTiO}_3$  layers was checked by RBS, again sputtered on MgO substrates for a better visibility of the elements. The measurement presented in Fig. 5.11 shows a perfect stoichiometry of  $\text{BaTiO}_3$ .

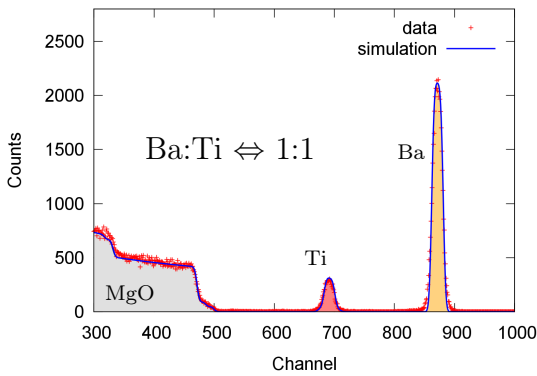


Figure 5.11: RBS measurement including simulation of the data of a  $\text{BaTiO}_3$  sample on MgO substrate showing a perfect stoichiometry.

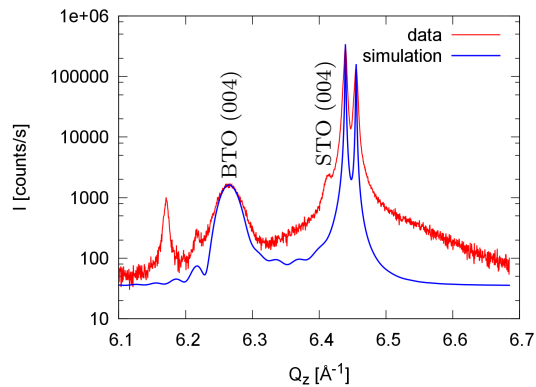


Figure 5.12: Diffraction scan of  $\text{BaTiO}_3$  layer on  $\text{SrTiO}_3$  substrate. The observable (004)- $\text{BaTiO}_3$  reflection indicates a good layer quality.

Afterwards,  $\text{BaTiO}_3$  layers were grown on  $\text{SrTiO}_3$  substrates which were treated as described before. Substrate temperatures in a range from 770 K to 1140 K are used with a

HF power of 100 W, an oxygen pressure of 3 mbar and a target-to-substrate distance of 2 cm. Samples prepared at 1050 K show the best crystalline quality with an observable (004) BTO Bragg-reflection corresponding to a lattice parameter of 4.015 Å as presented in Fig. 5.12 b). XRR measurements show a sharp drop in intensity indicating a high roughness of the surface. Again, a reduced SLD at the top of the  $600_{-14}^{+22}$  Å thick layer (see Fig. 5.13) has to be taken into account to simulate the data.

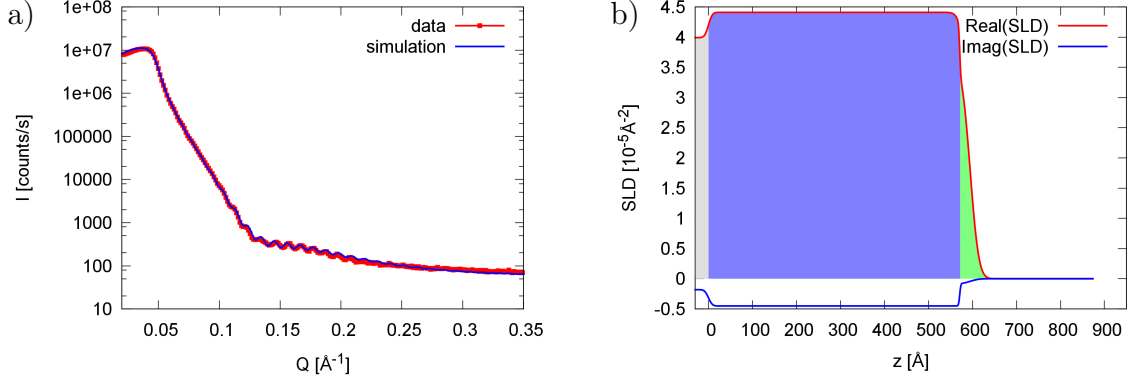


Figure 5.13: *a)* shows the XRR measurement of a grown BaTiO<sub>3</sub> layer on SrTiO<sub>3</sub> including the fit of the data. The resulting SLD with respect to the layer thickness is shown in *b)*. A small top layer with reduced SLD has to be taken into account.

The topography of the surface was probed by AFM to check for islands since a smooth interface is of high importance. The Gaussian distributed roughness is 1.6 nm. Islands on the surface are present as depicted in the topography shown in Fig. 5.14 a). The line scan clearly shows that those islands reach a height of more than 6 nm. Since the island growth mode of BaTiO<sub>3</sub> layers produced by the OMBE starts already for much thinner films also the surface of a 80 Å BaTiO<sub>3</sub> film grown by the HOPSS was investigated. Unfortunately, also for this thinner films the surface shows islands as one can see in the topography pattern and the line profile in Fig. 5.15.

In total, it was not possible within a reasonable time to grow BaTiO<sub>3</sub> layers with a good crystalline quality and a smooth surface, especially, with a certain thickness. The BaTiO<sub>3</sub> films have to have a certain thickness to be ferroelectric (at least 5 nm [111]) and to avoid leakage currents over a large area, as needed for neutron scattering. Also a detailed study to improve the structural properties of BaTiO<sub>3</sub> prepared by the HOPSS did not lead to a satisfactory result [112].

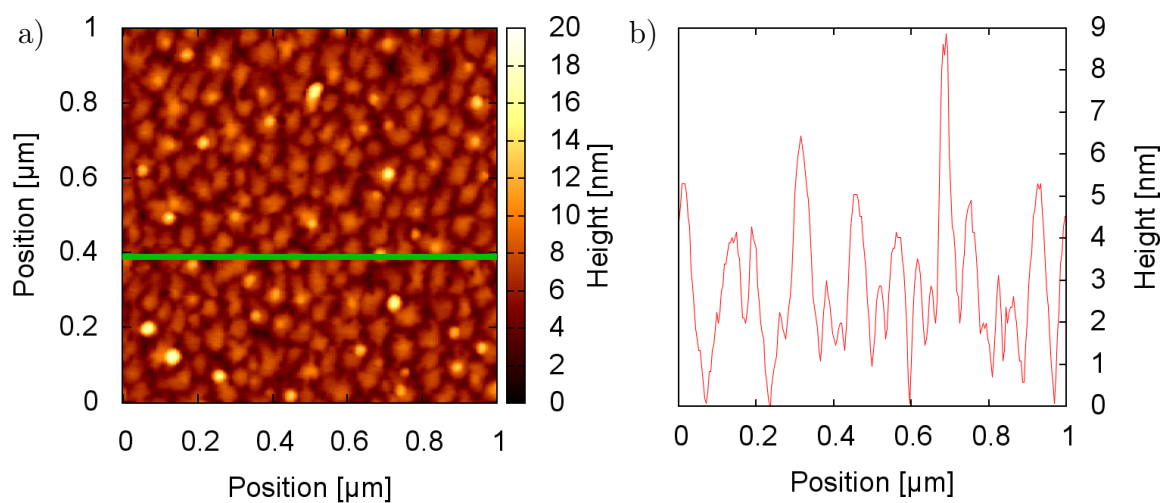


Figure 5.14: a) Topography of a  $600 \text{ \AA}$   $\text{BaTiO}_3$  layer produced by HOPSS and b) a line profile. The position of the extracted line profile is indicated by the green line in a).

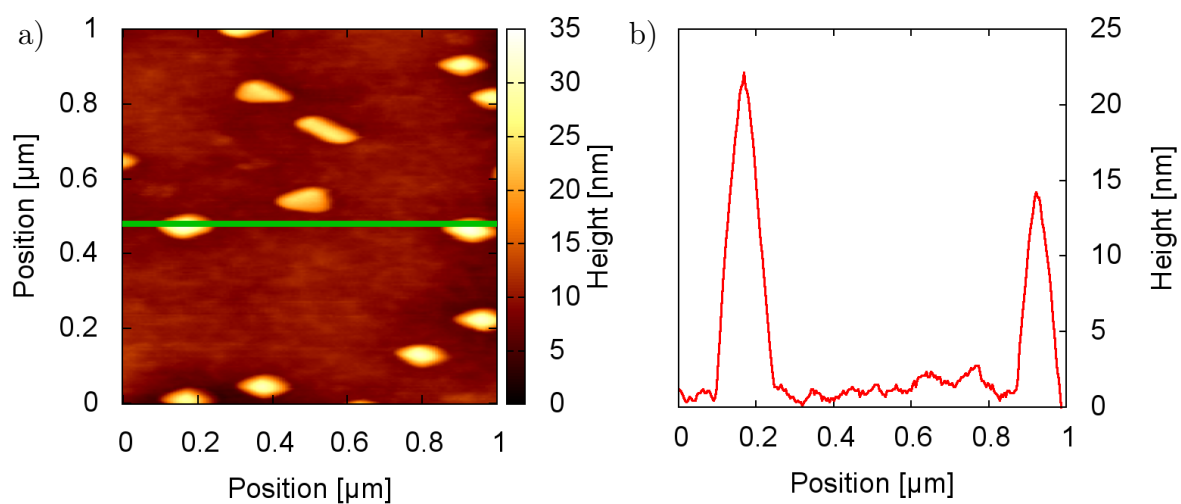


Figure 5.15: a) Topography of a  $80 \text{ \AA}$   $\text{BaTiO}_3$  layer produced by HOPSS and b) a line profile. The position of the extracted line profile is indicated by the green line in a). The surface is not homogeneous flat, but shows islands.

## 5.4 Conclusion

Good quality  $\text{La}_{0.5}\text{Sr}_{0.5}\text{MnO}_3$  single crystalline thin films were successfully prepared by the OMBE as well as with the HOPSS. A recipe for the growth by the OMBE was found by an iterative calibration of the growth rates of each deposition source. The fabrication process of  $\text{La}_{(1-x)}\text{Sr}_x\text{MnO}_3$  by the HOPSS could be optimized. However, neither by OMBE nor by HOPSS was it possible to grow good quality  $\text{BaTiO}_3$  films with a smooth surface. Hence, we decided to use commercially available  $\text{BaTiO}_3$  single crystal substrates, which exhibit a much better quality. Additionally, leakage currents are not a problem due to the thickness of 0.5 mm of the substrates. The  $\text{BaTiO}_3$  substrate is polarizable with an electric field of  $E=4$  kV/cm, which can be reached with an applied voltage of 200 V [113]. Nevertheless, the interface of ferroelectric  $\text{BaTiO}_3$  to ferromagnetic  $\text{La}_x\text{Sr}_{1-x}\text{MnO}_3$  is given by the use of  $\text{BaTiO}_3$  substrates. The developed recipes for the growth of  $\text{La}_x\text{Sr}_{1-x}\text{MnO}_3$  films on  $\text{SrTiO}_3$  substrates was transferred to  $\text{BaTiO}_3$  substrates which lead to reasonable results for the sample quality. The results for the produced samples will be presented in the following chapters.



# Chapter 6

## Results I:

### $\text{La}_{0.53}\text{Sr}_{0.47}\text{MnO}_3$ on $\text{BaTiO}_3$

In this chapter the results of the investigation of  $\text{La}_{0.53}\text{Sr}_{0.47}\text{MnO}_3$  on  $\text{BaTiO}_3$  substrates are presented. This half doped  $\text{La}_{(1-x)}\text{Sr}_x\text{MnO}_3$  is close to the magnetic phase transition from ferromagnetic to antiferromagnetic. At the beginning, the structural properties of the film are given. The main part of this chapter contains the magnetic properties of the system and the manipulation thereof by electric fields. Furthermore, the analysis of the magnetic profile performed by PNR is presented in order to verify a possible limitation of magneto-electric effects to the interface.

#### 6.1 Structural Analysis

$\text{La}_{0.53}\text{Sr}_{0.47}\text{MnO}_3$  layers are grown by OMBE using the process described in Chapter 5.2. LSMO is grown at a substrate temperature of 1150 K and a growth time of 4865 s.  $\text{BaTiO}_3$  is used as substrate to provide the ferroelectric component of the system. The  $\text{BaTiO}_3$  substrates were not treated by HF like  $\text{SrTiO}_3$ , but annealed at 1250 K to get rid of surface contaminations. The LEED pattern measured after the growth process indicates a crystalline order of the LSMO layer on  $\text{BaTiO}_3$  substrates as presented in Fig. 6.1 a). The pattern is blurred compared to those using  $\text{SrTiO}_3$  as substrate (Fig. 5.5) indicating a lower crystalline quality. The increased strain on the LSMO layer due to the enlarged unit cell of  $\text{BaTiO}_3$  compared to  $\text{SrTiO}_3$  could be the reason for the reduced crystalline quality since more defects are formed in the crystal during the relaxation process within the layer. The RHEED pattern in Fig. 6.1 b) shows spots at the Laue ring and a low background both indicating a good surface quality. Since it is essential to apply electric fields at the sample an Au contact was deposited at the reverse side of the substrate. As top contact the metallic LSMO layer itself is used.

Fig. 6.2 shows the topography of the surface measured by AFM and the Gaussian height distribution with a rms roughness of 11 Å confirming a good sample quality. XRR measurements are performed to deduce the layer thickness and roughness. XRR data verify a good layer quality as can be seen in Fig. 6.3 a). The best fit gives a layer thickness

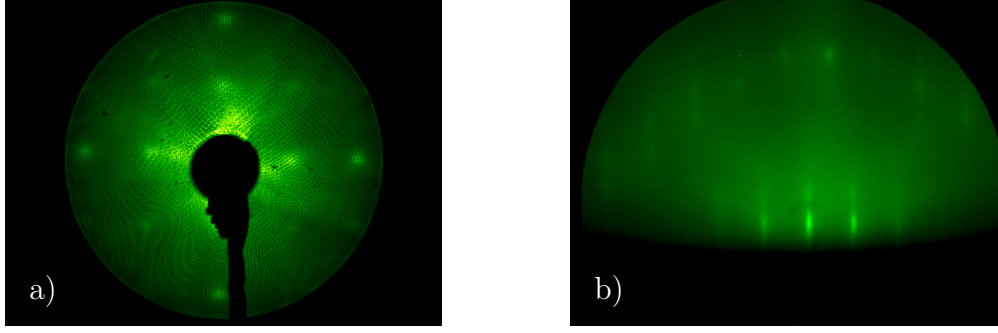


Figure 6.1: a) *LEED pattern of the  $\text{La}_{0.53}\text{Sr}_{0.47}\text{MnO}_3$  film on  $\text{BaTiO}_3$  substrate, taken at 100 eV. The reflexes indicate epitaxial growth. b) The RHEED pattern taken after the growth process shows stripes indicating a smooth layer. Spots at the first Laue ring suggest a good crystalline quality.*

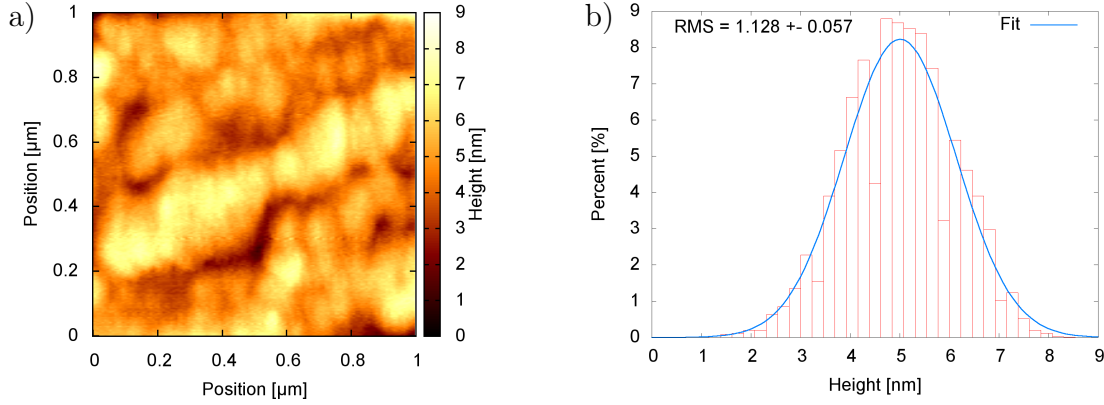


Figure 6.2: a) *Topography of the LSMO layer on  $\text{BaTiO}_3$  measured by AFM and b) the Gaussian height distribution with a rms roughness of less than three unit cells.*

of  $228_{-4}^{+1}$  Å and a surface roughness of  $5.50_{-0.07}^{+0.03}$  Å. The profile of the SLD with respect to the layer thickness  $z$  is depicted in Fig. 6.3 b). The SLD region corresponding to the substrate is colored in gray and the LSMO layer in blue. No additional top layer has to be taken into account to simulate the data accurately. The thickness oscillations are weak due to the low contrast of  $\text{La}_{(1-x)}\text{Sr}_x\text{MnO}_3$  and  $\text{BaTiO}_3$  for X-ray scattering. Hence, the error on the thickness might be underestimated. The roughness obtained by AFM is twice as large as by XRR. The difference between these roughnesses might be due to the different probed areas. The AFM roughness is determined for an area of  $1 \times 1 \mu\text{m}^2$  while the roughness determined by XRR is averaged over the whole sample ( $1 \text{ cm}^2$ ). X-ray diffraction measurements validate the crystalline growth of LSMO on  $\text{BaTiO}_3$  as shown in Fig. 6.4. The (002) substrate peak is doubled indicating a split of the substrate into a-type and c-type domains. Due to heating during the growth process, the substrate undergoes a phase transition at 400 K to the non ferroelectric cubic phase as described in Chapter 2.3. Coming back into the ferroelectric tetragonal (Tet) phase by

cooling without an applied electric field leads to the splitting into domains. The peaks correspond to lattice parameters of  $c_{\text{BTO}} = 4.030 \pm 0.001 \text{ \AA}$  and  $a_{\text{BTO}} = 3.985 \pm 0.001 \text{ \AA}$  for the c-type and a-type domain, respectively, according to literature values [40]. The (002) LSMO Bragg-peak at  $Q_z = 3.27 \text{ \AA}^{-1}$  corresponds to an out-of-plane lattice parameter of  $c_{\text{LSMO}} = 3.850 \pm 0.001 \text{ \AA}$ . The literature value for pseudocubic  $\text{La}_{0.5}\text{Sr}_{0.5}\text{MnO}_3$  is  $a=b=c=3.86 \text{ \AA}$  [24]. Due to the instrumental resolution and the broadening of the peak due to finite size effects it is not clear if the layer is completely relaxed. For this, additional information on the in-plane lattice parameter have to be taken into account. Further peaks in the diffraction measurement are related to wavelength contaminations of the incident beam. The identified wavelengths are depicted in Fig. 6.4.

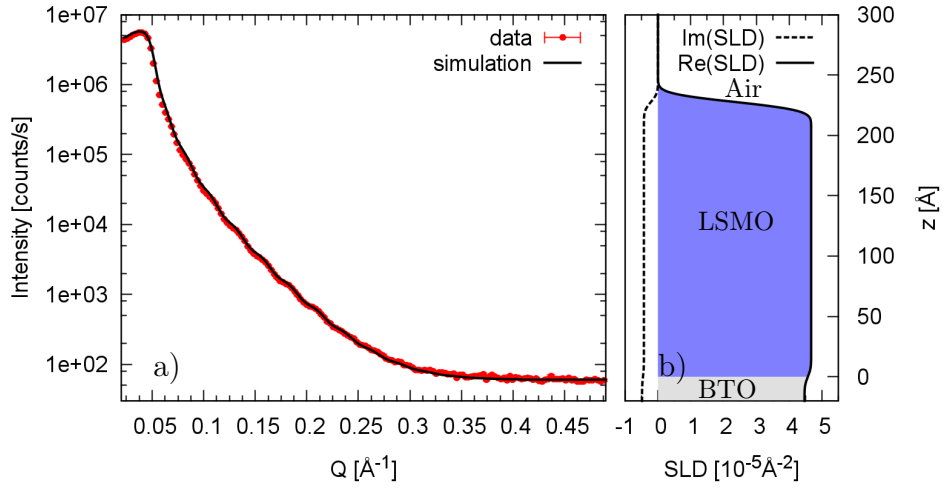


Figure 6.3: a) XRR measurement of the  $228 \text{ \AA}$   $\text{La}_{0.53}\text{Sr}_{0.47}\text{MnO}_3$  layer on  $\text{BaTiO}_3$  substrate. The SLD profile obtained from the fit is shown b). The substrate is indicated by the gray color and the LSMO layer by blue color.

The  $\text{BaTiO}_3$  substrate should be completely polarizable by the application of a sufficiently high electric field. Thus, electrical contacts were connected to the sample by the use of conducting silver paste. X-ray diffraction measurements on the (002) Bragg reflection were performed under the application of an out-of-plane voltage of 400 V. Fig. 6.4 shows the measurement with and without applied voltage. The a-type Bragg peak of the substrates vanishes with the application of the voltage. This is a clear evidence that the substrate is completely polarized to the [001] direction. Additionally the (002) LSMO Bragg peak is slightly shifted to lower  $Q$ , corresponding to an increased lattice parameter. This can be explained by the reorientation of the LSMO unit cells. Since the substrate is now single domain, pure biaxial strain is induced to the LSMO. This leads to purely out-of-plane orientation of the elongated direction of the LSMO.

The formation of domains is also observable at the surface of the samples. A stripe like pattern appears at the surface if no voltage is applied as shown in Fig. 6.5 a). The

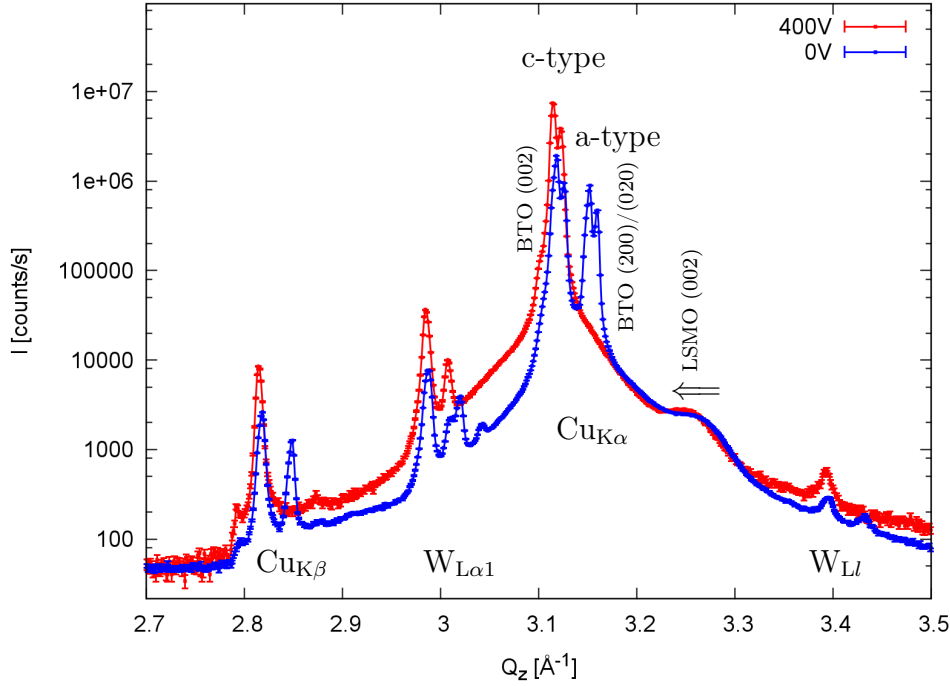


Figure 6.4: XRD measurement on the LSMO/BTO sample at room temperature with and without applied voltage of 400 V. Without electric field the second order  $\text{BaTiO}_3$  Bragg peak splits due to structural domains within the substrate. The  $(002)/(020)$  a-type substrate peak vanishes due to the application of the voltage. A slight shift of the  $(002)$  LSMO Bragg peak is observed. Additional peaks are visible due to a wavelength contamination of the primary beam.

reflection of a laser beam impinging on the sample surface shows a multiple reflection pattern. This pattern vanishes by the application of a critical voltage of about 200 V ( $E=4\text{ kV/cm}$ ) (see Fig. 6.5 b)). Also X-ray rocking scans on the plateau of total reflection ( $2\theta=0.6^\circ$ ) depicted in Fig. 6.6 a) show the distorted sample surface without applied electric field. Nevertheless, the rocking scan with applied voltage of 400 V is sharp with an FWHM of  $0.047^\circ$ . Rocking scans on the  $(200)$  substrate peak were done with the stripe pattern oriented perpendicular and parallel to the scattering plane. The rocking scan for the perpendicular orientation of the stripes shows several peaks as depicted in Fig. 6.6 b). This indicates that the tilted terraces are crystalline ordered. The same rocking scan performed with stripes oriented parallel to the scattering plane shows only one peak as expected. The stripes are formed just in one direction of the substrate. Unfortunately, repeated switching reduces the sample quality.

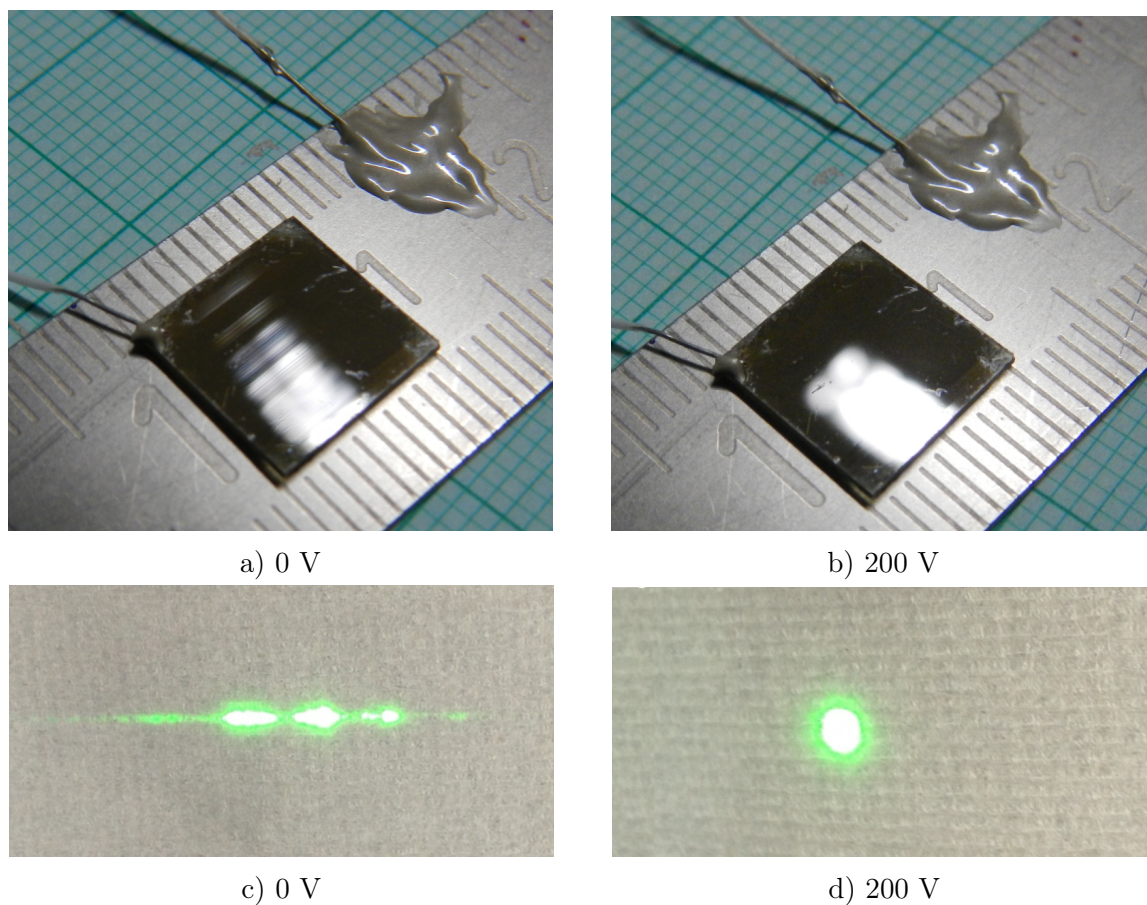


Figure 6.5: a) *Contacted sample without applied voltage. The surface of the sample shows a stripe like pattern.* b) *Sample with applied electric field of 8 kV/cm. The surface becomes completely flat at the critical voltage of about 200 V.* c) and d) *show the corresponding reflection of a laser beam reflected from the sample.*

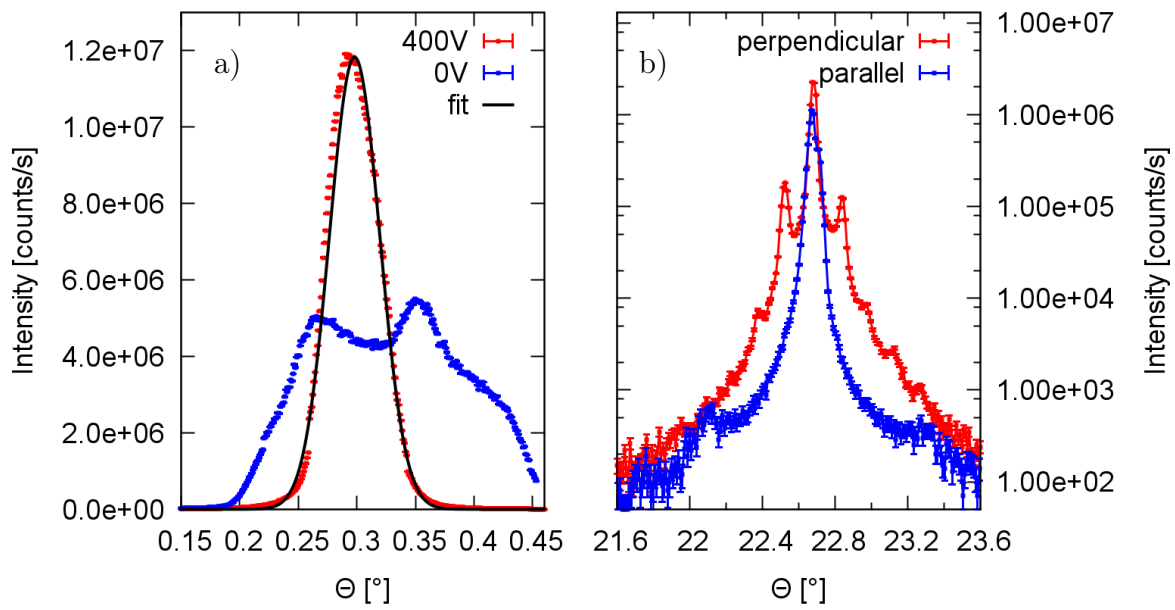


Figure 6.6: *Rocking scan on a) the total plateau of reflection ( $2\Theta = 0.6$ ) with and without applied electric field. The application of the electric field leads to a sharpening of the reflection. b) rocking scan on the BaTiO<sub>3</sub> (002) Bragg Peak. The stripe like pattern is oriented parallel and perpendicular to the scattering plane, both without electric field.*

## 6.2 Characterization of the Macroscopic Magnetization

In the beginning of this section, the measurements which are used to determine the magnetic properties and the manipulation thereof by electric fields, are introduced. Measurements are performed using a SQUID magnetometer, which is described in Chapter 4.9. For all measurements performed with applied electric fields, a special sample rod with electrical feed-through is used. The sample is fixed at a self made Vespel rod and connected with Cu wires using silver paste as shown in Fig. 4.9 b). All parts are mounted symmetrically, so that the pick-up coils do not detect a signal from the wires and other components. A graphically illustration of the measurements is given in Fig. 6.7 and is described in the following:

The temperature dependent magnetization  $m_H(T)$ <sup>1</sup> of the sample is determined by the standard DC option. The magnetization is measured while cooling and warming with an applied magnetic field. Since the manipulation of the magnetization by electric fields is the main interest within this thesis, the so called MEC option is used. For this, the standard AC susceptibility measurement technique is extended as described in Chapter 4.9. With this technique it is possible to apply an AC electric field and measure the magnetic response of the sample by using a lock-in technique. Even very small changes of the magnetization with respect to the applied electric field can be probed. Furthermore, only a change of the magnetization  $\Delta m$  is measured since the sample is not moved through the pick-up coils, hence constant magnetization components are not measured. The MEC measurements are performed in dependence of the temperature and the magnetic field, leading to  $\Delta m_{H,EAC}(T)$  and  $\Delta m_{T,EAC}(H)$ . These values correspond to a change of the magnetization from the maximum negative to positive applied electric field as shown in Chapter 4.9.

In order to obtain absolute values of the magnetization  $m(E)$  in dependence of DC electric fields, the standard DC option of the MPMS is used. All measurements can be performed with electric fields up to  $E = \pm 4$  kV/cm. Thus, electrical hysteresis loops are performed to obtain the electric field dependent magnetization  $m_{T,H}(E)$  at constant temperature and magnetic field. The obtained  $m_{T,H}(E)$  at different electric fields are used to calculate manually the difference  $\Delta m_{\text{man.}}$  of the magnetization for maximum positive and negative electric fields. These values can be compared to  $\Delta m_{H,EAC}(T)$  or  $\Delta m_{T,EAC}(H)$  measured by the MEC option. Furthermore, magnetic hysteresis loops with different applied electric fields are performed to determine  $m_{T,E}(H)$ . Also here, a manually  $\Delta m_{\text{man.}}$  for the magnetization at different electric fields can be calculated to verify  $\Delta m_{T,EAC}(H)$  measured by the MEC option.

---

<sup>1</sup> $m$  is measured in dependency of the temperature  $T$  at a constant magnetic field  $H$

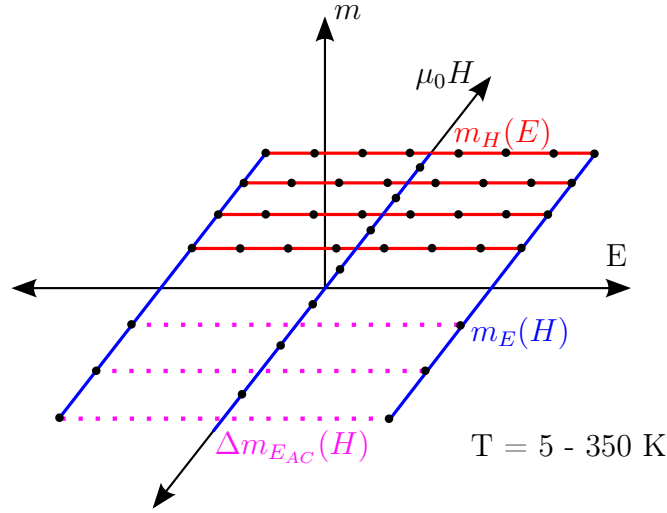


Figure 6.7: *Diagram of the magnetization measurements. The blue lines indicate magnetic hysteresis loops for different applied electric fields. Electrical hysteresis loops at different magnetic field are depicted in red and the magnetization change  $\Delta m_H(T, E)$  performed by the MEC option is drawn in violet. Black dots indicate measurement points. A temperature range from  $T = 5\text{--}350\text{ K}$  can be probed.*

### 6.2.1 Temperature Dependent Magnetization

The temperature dependent magnetization  $m_H(T)$  (see Fig. 6.8) is determined from 50 K to 350 K with an applied magnetic field of  $\mu_0 H = 10\text{ mT}$ . Cooling and warming cycles with a temperature rate of 2 K/min are performed. The Curie temperature  $T_C = 310\text{ K}$  is less than the bulk value given in Hemberger’s phase diagram in Fig. 2.3 [32]. Since LSMO is grown as thin film, the reduction of  $T_C$  is possibly related to strain [114]. The magnetization above  $T_C$  becomes negative due to diamagnetic contributions of the substrate.

The magnetization curve shows sharp steps at temperatures of 278 K and 187 K for cooling and 284 K and 196 K for heating. These temperatures correspond to the structural phase transitions of  $\text{BaTiO}_3$ , as described in Chapter 2.3. This change of the magnetization is forced by the abrupt change of the  $\text{BaTiO}_3$  lattice parameter in the first order phase transition, since no other parameter but the temperature was changed. The temperature of the magnetization steps follows the hysteretic behavior of the temperature of the structural phase transition for cooling and warming as indicated by the gray boxes in Fig. 6.8. Similar behavior could be found for Fe on  $\text{BaTiO}_3$  substrates as investigated in [115–117]. The measurement was performed twice where the abrupt changes of the magnetization seems not to be completely reproducible. The first and second measurement is indicated by the numbers in the plot and show a difference of  $(4.8 \pm 0.2) \cdot 10^{-9}\text{ A m}^2$  at 200 K. Thus, the magnetization of the second measurement is suppressed by 17.3 % compared to the first. The non reproducible behavior is just present in the orthorhombic (Or) phase of  $\text{BaTiO}_3$ . The inset of Fig. 6.8 shows the evolution of the normalized magnetization step

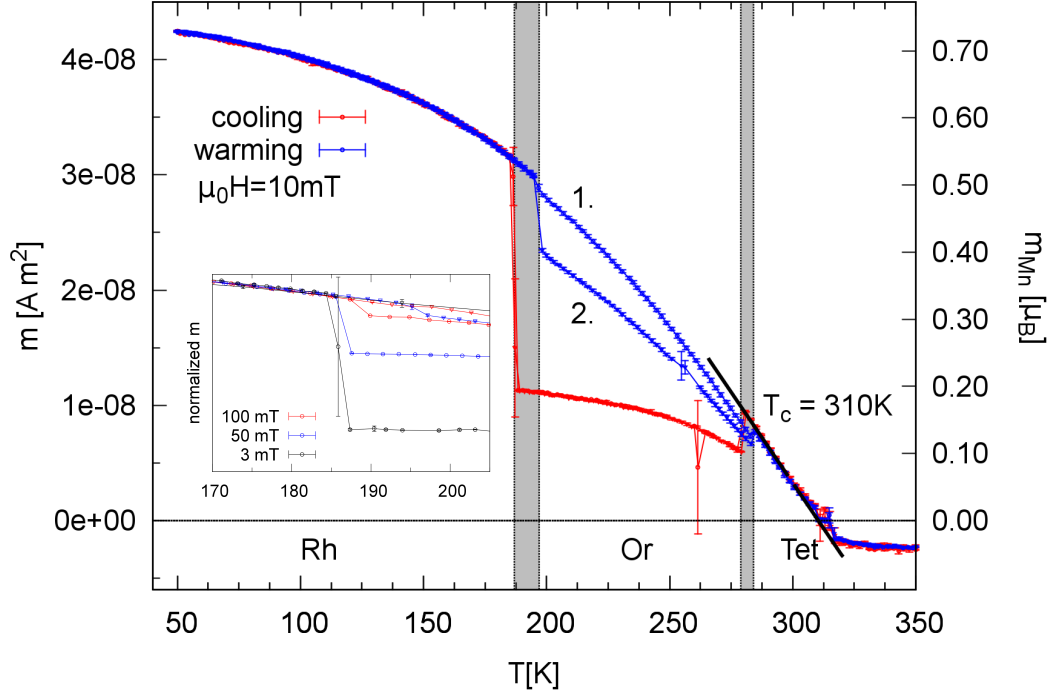


Figure 6.8: *Temperature dependent magnetization measurement at  $\mu_0 H = 10$  mT. Steps in the magnetizations are observed at the structural phase transitions of the  $\text{BaTiO}_3$  substrate. The gray boxes illustrate the temperature region of the phase transitions. The numbers 1. and 2. indicates the repetition of the measurement. The magnetization is additionally given in  $\mu_B$  per Mn atom with an error of approximately 5%. The inset shows the evolution of the magnetization step at the Or  $\leftrightarrow$  Rh phase transition with respect to the external magnetic field. For a better visibility, the magnetization is normalized to that at 180 K.*

at the Or  $\leftrightarrow$  Rh phase transition with respect to the external magnetic field. The size of the step decreases with increasing external magnetic field.

### 6.2.2 Temperature Dependent Electrical Manipulation of the Magnetization

In order to verify the possibility to influence the magnetic moment of the LSMO layer by the application of electric fields, the temperature dependent magnetic response  $\Delta m_{H,EAC}(T)$  to the electric excitation voltage  $U = U_0 \sin(\omega t)$  is measured with a frequency of  $\omega = 1$  Hz and  $U_0 = 160$  V. Fig. 6.9 shows the change of the magnetization  $\Delta m_{H,EAC}(T)$  due to the AC electric field with a constant applied magnetic field of 3 mT while cooling down from 350 K to 25 K with a rate of 2 K/min. The gray boxes illustrate the region of the structural phase transitions known from the field cooled measurement. For temperatures above  $T_C$  the  $\Delta m_{H,EAC}(T)$  signal is at the noise level of  $\approx 1 \cdot 10^{-11}$  A m<sup>2</sup>. A very small change of the magnetization is observed within the tetragonal phase while cooling. A maximum

emerges in the orthorhombic phase near the transition  $\text{Or} \leftrightarrow \text{Tet}$  (280 K). The change of the magnetization due to the electric field slowly decreases with decreasing temperatures. The minimum in the orthorhombic phase is reached at the structural phase transition of the substrate from  $\text{Or} \rightarrow \text{Rh}$ . A second maximum appears at 175 K within the rhombohedral phase ( $T < 190$  K).

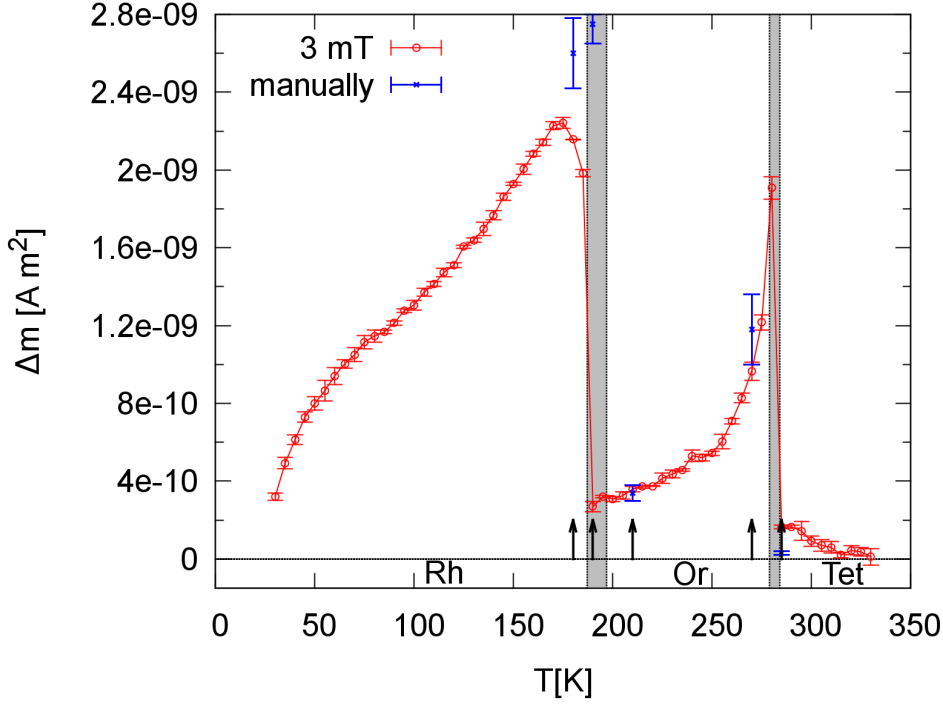


Figure 6.9: *Magneto-electric coupling measured with the MPMS. The temperature dependent change of the magnetizations  $\Delta m_{H,E_{AC}}(T)$  with respect to the applied AC electric field is observed at  $\mu_0 H = 3$  mT. A coupling is observed with maximum values near the phase transitions of the  $\text{BaTiO}_3$  substrate. Arrows indicate temperatures where data points are taken manually (see next section).*

By the use of the new measurement setup it can be shown that the magnetization of the  $\text{La}_{0.53}\text{Sr}_{0.47}\text{MnO}_3$  layer on  $\text{BaTiO}_3$  can be manipulated by the application of an external electric field. Especially, near the structural phase transitions of the  $\text{BaTiO}_3$  substrate the change in the magnetization is pronounced.

### 6.2.3 Electrical Hysteresis Loops for Different Temperatures

In order to clarify the influence of the sign of the applied electric field on the manipulation of the magnetization, the absolute magnetization is determined with respect to the applied electric field at 180 K, 190 K, 210 K, 270 K and 285 K, covering all structural phases of the substrate. The magnetization of the  $\text{La}_{0.53}\text{Sr}_{0.47}\text{MnO}_3$  film is determined

at constant external electric fields up to  $\pm 4$  kV/cm. This corresponds to a voltage of 200 V applied at the 0.05 cm thick substrate, limited by the power supply. The direction of the electric field is shown in Fig. 6.10. For a negative field, the polarization of the  $\text{BaTiO}_3$  points towards the LSMO layer while it points away from the LSMO layer for positive fields. The first data point is taken with  $+4$  kV/cm. To ensure the reproducibility each dataset is measured at least twice. Here, the magnetic moment is determined by the standard DC measurement, in which the sample is moved through the pick-up coils. Hence, the magnetic moment  $m_{T,H}(E)$  of the sample is measured instead of the change of the magnetization  $\Delta m_H(T, E)$  as was done before. However,  $\Delta m_{\text{man.}}$  is calculated by the difference of the magnetization for the maximum positive and negative electric field.

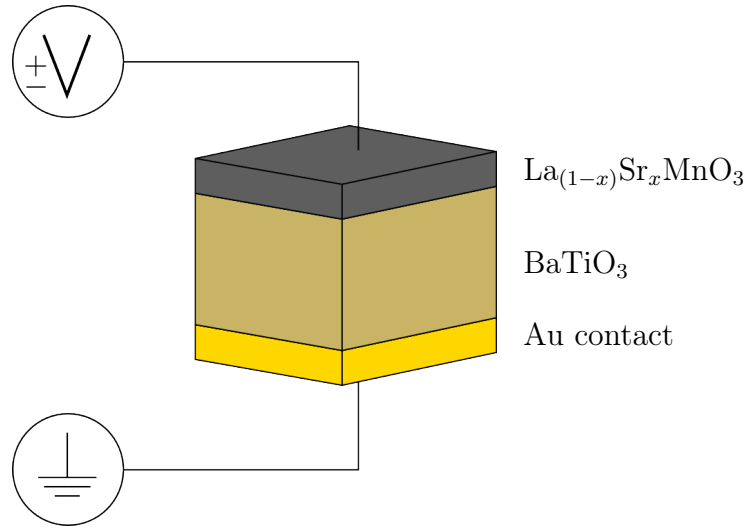


Figure 6.10: *Direction of the applied electric field. For negative applied voltages the electric field points towards and for positive fields away from the  $\text{La}_{(1-x)}\text{Sr}_x\text{MnO}_3$  layer.*

Fig. 6.11 shows the data of the electric field dependent magnetization. For a better comparability the measurement for each temperature is plotted in the same relative scale to visualize the absolute change of the magnetization. Summarized data are presented in Tab. 6.1. In the tetragonal substrate phase, at 285 K (see Fig. 6.11 a)), no change in the magnetization is observed as expected due to the weak signal of the  $\Delta m_H(T, E)$  measurements presented in the chapter before. A moderate effect can be observed at 270 K (Or) (see b)) next to the phase transition from orthorhombic to tetragonal. An absolute increase of the magnetization of  $\Delta m_{\text{man.}} = (1.2 \pm 0.2) \cdot 10^{-9}$  A m<sup>2</sup> and a significant relative change of 43.2% is found for negative applied electric fields. The magnetization stays constant by the application of a positive electric field compared to the neutral state without electric field. The increase of the magnetization could be even larger at this temperature, but in this measurement a maximum electric field of  $\pm 3$  kV/cm was applied. At 210 K (Or) (see c)), next to the Or  $\rightarrow$  Rh substrate phase transition, again a weak increase of  $\Delta m_{\text{man.}} = (3.4 \pm 0.4) \cdot 10^{-10}$  A m<sup>2</sup> for negative electric fields is observed. This corresponds to a relative gain of the magnetization of 7.3% for the absolute magnetic moment of

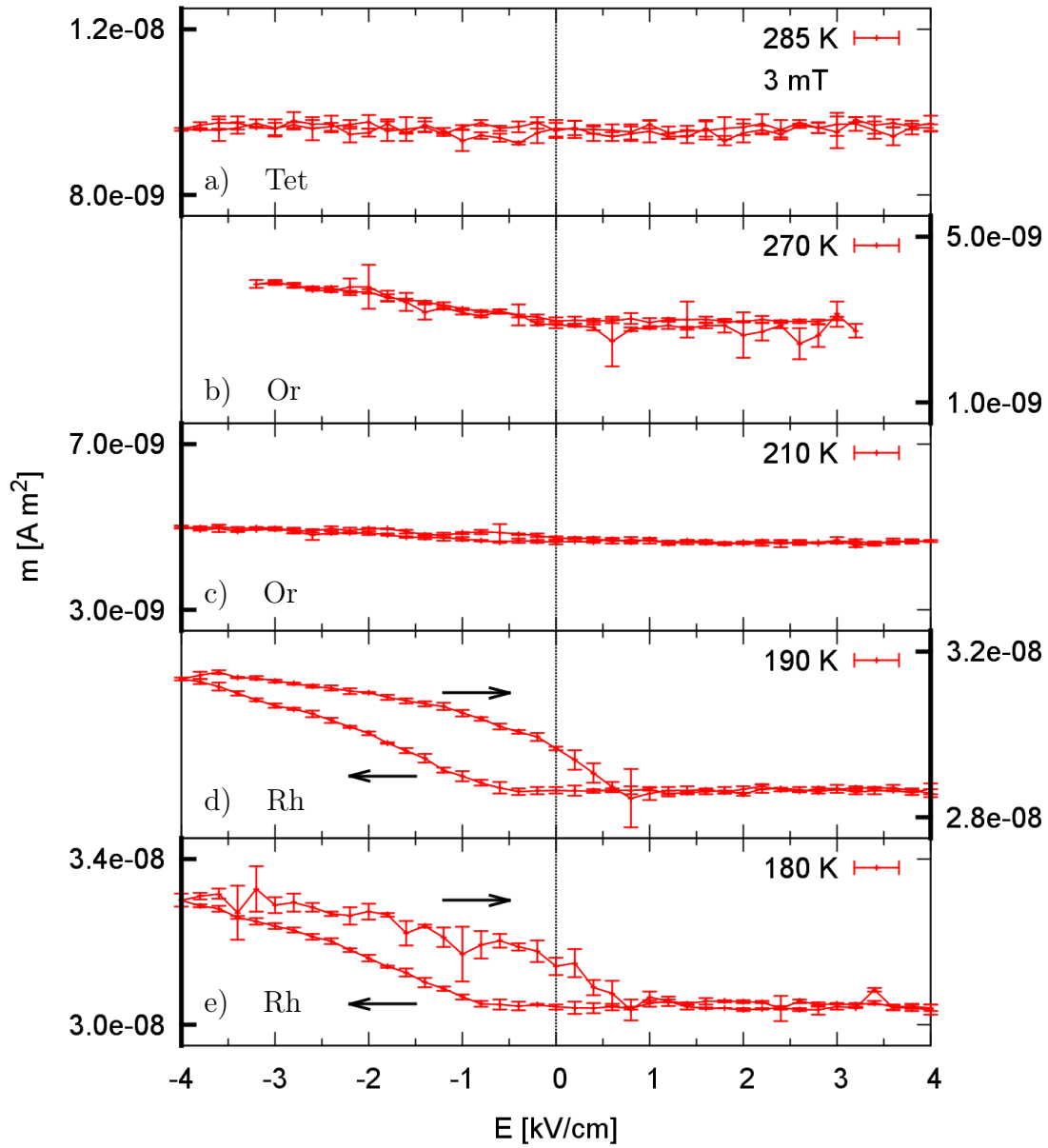


Figure 6.11: Magnetization depending on the applied electric field at various temperatures at  $\mu_0 H = 3$  mT. The arrows show the direction of the increasing or decreasing electric field. An enlarged magnetization is observed for negative electric fields shown in b)-e). The magnetization for positive fields and at 285 K stays almost constant.

$(4.66 \pm 0.03) \cdot 10^{-9}$  A m<sup>2</sup>. For the low temperature region within the rhombohedral phase of the substrate, the magnetization is increased with negative applied electric fields, as one can see in d) and e). Again, the application of a positive electric field does not influence

the magnetization. The magnetization at 180 K increases by  $\Delta m_{\text{man.}} = (2.6 \pm 0.2) \cdot 10^{-9}$  A m<sup>2</sup> and for 190 K by  $\Delta m_{\text{man.}} = (2.8 \pm 0.1) \cdot 10^{-9}$  A m<sup>2</sup>. This corresponds to an increase of 8.5% and 10.8%, respectively. The shape of those curves shows the same behavior, but differs from those of the other phases. Hence, the magneto-electric coupling mechanism seems to be different for the three different substrate phases. A difference in the magnetization remains with vanishing electric field after polarizing the substrate with  $E = -4$  kV/cm. Thus, a small positive electric field is necessary to return to the neutral state. The calculated changes of the magnetization with respect to applied electric fields are in good agreement to the values obtained by the MEC option considering the different electric field values (see Fig. 6.9), presented in the section before.

$\mu_0 H$ [mT]	T [K]	$m \cdot 10^{-9}$ [A m <sup>2</sup> ]	$\Delta m_{\text{man.}} \cdot 10^{-9}$ [A m <sup>2</sup> ]	$\Delta m_{\text{relative}}$ in %
3	180	$30.41 \pm 0.08$	$2.60 \pm 0.18$	8.5
3	190	$28.58 \pm 0.09$	$2.75 \pm 0.10$	10.8
3	210	$4.66 \pm 0.03$	$0.34 \pm 0.04$	7.3
3	270	$2.73 \pm 0.17$	$1.18 \pm 0.18$	43.2
3	285	$9.62 \pm 0.08$	$0.03 \pm 0.01$	0.3

Table 6.1: *Change of magnetization with respect to the applied electric field at  $\mu_0 H = 3$  mT and various temperatures. Additionally, the relative change  $\Delta m_{\text{man.}}$  of the absolute moment is given.*

#### 6.2.4 Electrical Hysteresis Loops at Different Magnetic Fields

The influence of external magnetic fields on the manipulation of the magnetization with respect to electric fields is investigated, since the magnetic field is another quantity in the parameter space. Electrical hysteresis measurements are performed with electric field up to  $E = \pm 3$  kV/cm. A series of measurements are performed with different external magnetic fields of  $\mu_0 H = 0, 3, 6$  and 50 mT at 270 K. The measurement was started with positive applied electric fields and repeated at least twice. The results are presented in Fig. 6.12. Again, all measurements are plotted in the same scale for a better comparability of the data.

All measurements show an increased magnetization for the application of negative electric fields, as expected. Again, there is no difference in the magnetization for positive and zero electric fields. The shape of the electric hysteresis loops slightly differ, depending on the external magnetic field. For low magnetic fields, like in c) and d), loops are closed while they open for  $\mu_0 H \geq 6$  mT as can be seen in a) and b). The absolute and relative changes in magnetization with respect to the electric field are summarized in Tab. 6.2. The absolute increase of the magnetization without an external magnetic field and for 50 mT are in the same order of magnitude. Regarding the absolute magnetic moment, the relative increase of the magnetization with respect to the electric field is high at  $\mu_0 H = 0$  mT with a giant relative change of 46.9 %, whereas the relative increase is moderate with 4.9 % for  $\mu_0 H = 50$  mT. The absolute increase of the magnetization seems

to have a maximum for small magnetic fields, since the highest  $\Delta m_{\text{man.}}$  could be observed for  $H = 6 \text{ mT}$ .

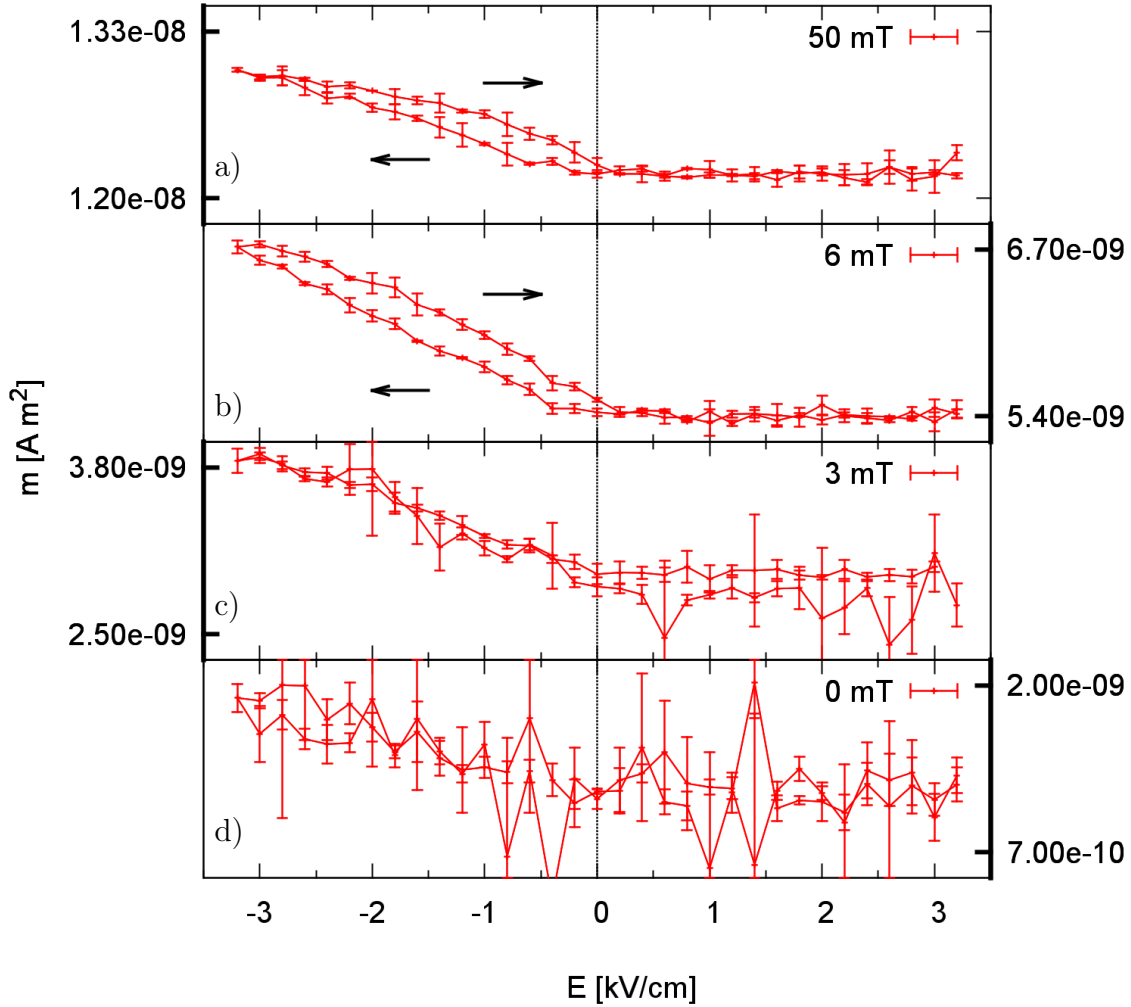


Figure 6.12: *Magnetization as function of the electric field for various external magnetic fields at  $T=270 \text{ K}$ . The application of negative electric field leads to an increase of the magnetization. The shape and size of the modification of the magnetization changes with the external magnetic field.*

Since the magnetic field has a significant influence on the manipulation of the magnetization by electric fields, a more detailed study on the magnetization change  $\Delta m_{T,EAC}(H)$  at various magnetic fields and constant temperatures will be presented in the following.

$\mu_0 H$ [mT]	T [K]	$m \cdot 10^{-9}$ [A m <sup>2</sup> ]	$\Delta m_{\text{man.}} \cdot 10^{-9}$ [A m <sup>2</sup> ]	$\Delta m_{\text{relative}}$ in %
50	270	$12.35 \pm 0.06$	$0.61 \pm 0.06$	4.9
6	270	$5.41 \pm 0.04$	$1.30 \pm 0.06$	24.0
3	270	$2.73 \pm 0.17$	$1.18 \pm 0.18$	43.2
0	270	$1.30 \pm 0.14$	$0.61 \pm 0.18$	46.9

Table 6.2: Summary of the magnetization with respect to the electric field for a series of measurements at 270 K and various magnetic fields.

### 6.2.5 Electrical Manipulation of the Magnetization at Various Magnetic Fields

Measurements of the magnetic field dependency on the manipulation of the magnetization by electric fields are performed. Data are taken at 180 K, 190 K, 210 K, 270 K and 285 K. For this, the MEC option is used to take advantage of the lock-in technique. As mentioned before a maximum electric voltage of 160 V corresponding to  $\pm 3.2$  kV/cm can be applied. Before the measurement, the sample is saturated with a magnetic field of 500 mT at each temperature. First data points are taken at 100 mT, sweeping to -100 mT and backwards. The change of the magnetization  $\Delta m_{T,EAC}(H)$  by the electric field, depending on the external magnetic field can be seen in Fig. 6.13.

Fig. 6.13 a) shows data recorded at 285 K within the tetragonal phase of the substrate. A weak  $\Delta m_{T=285K,EAC}(H)$  is observed as expected from previous measurements, which changes the sign for an inversed magnetic field. A small offset of  $\mu_0 H = 1.3$  mT can be seen for the inversion of the signal. The  $\Delta m_{T=285K,EAC}(H)$  signal does not drop to zero for high fields like one would expect, as high fields could suppress a possible magneto-electric coupling, but stays constant. In Fig. 6.13 b) measurements at 270 K and 210 K are depicted, both in the orthorhombic phase of the substrate. Here, a change of the magnetization  $\Delta m_{T,EAC}(H)$  is present with the expected magnitude. For 270 K, the magneto-electric coupling increases with the magnetic field to a broad maximum at around 7 mT and slightly drops for higher fields. The coupling at 210 K does not show a maximum and the slope around  $\mu_0 H = 0$  mT is less steep. The  $\Delta m_{T,EAC}(H)$  signal slightly splits for the forth and back direction of the measurement in the range of  $-5 \text{ mT} \leq \mu_0 H \leq 5 \text{ mT}$ . Both curves converge to a constant value of  $\Delta m_{T,EAC}(H) = 5 \cdot 10^{-10} \text{ A m}^2$ . Again, in both measurements,  $\Delta m_{T,EAC}(H)$  inverts with inverting magnetic field, but shows an offset of 0.6 mT for the zero crossing. The measurements within the rhombohedral phase are shown in Fig. 6.13 c). The shape of the curve at 180 K is completely different to those of the other phases. A maximum change of the magnetization is observed for 1 mT and 0 mT. The loop shows an asymmetric hysteretic behavior with zero crossing points at  $\mu_0 H = 3.6$  mT and -2.7 mT. An irreversibility like field is reached at 10 mT from which the forth and back direction have same values. For higher fields, the  $\Delta m$  signal converges with increasing magnetic field to  $\Delta m_{T=180K,EAC}(H) = 5 \cdot 10^{-10} \text{ A m}^2$ , as seen before at 210 K and 270 K. The green curve, representing the measurement at 190 K, shows an intermediate state between the measurements done at 180 K and 210 K, related to the

proximity to the structural phase transition of  $\text{BaTiO}_3$ .

In order to clarify whether the observed zero crossing and irreversibility fields for  $\Delta m_{T,EAC}(H)$  correspond to special points in the magnetic ordering, like the coercivity field, hysteresis loop are taken. Especially, in the region of the coercivity field one could expect a high mobility of the spins and thus a high possibility to affect the magnetic moment by the electric field.

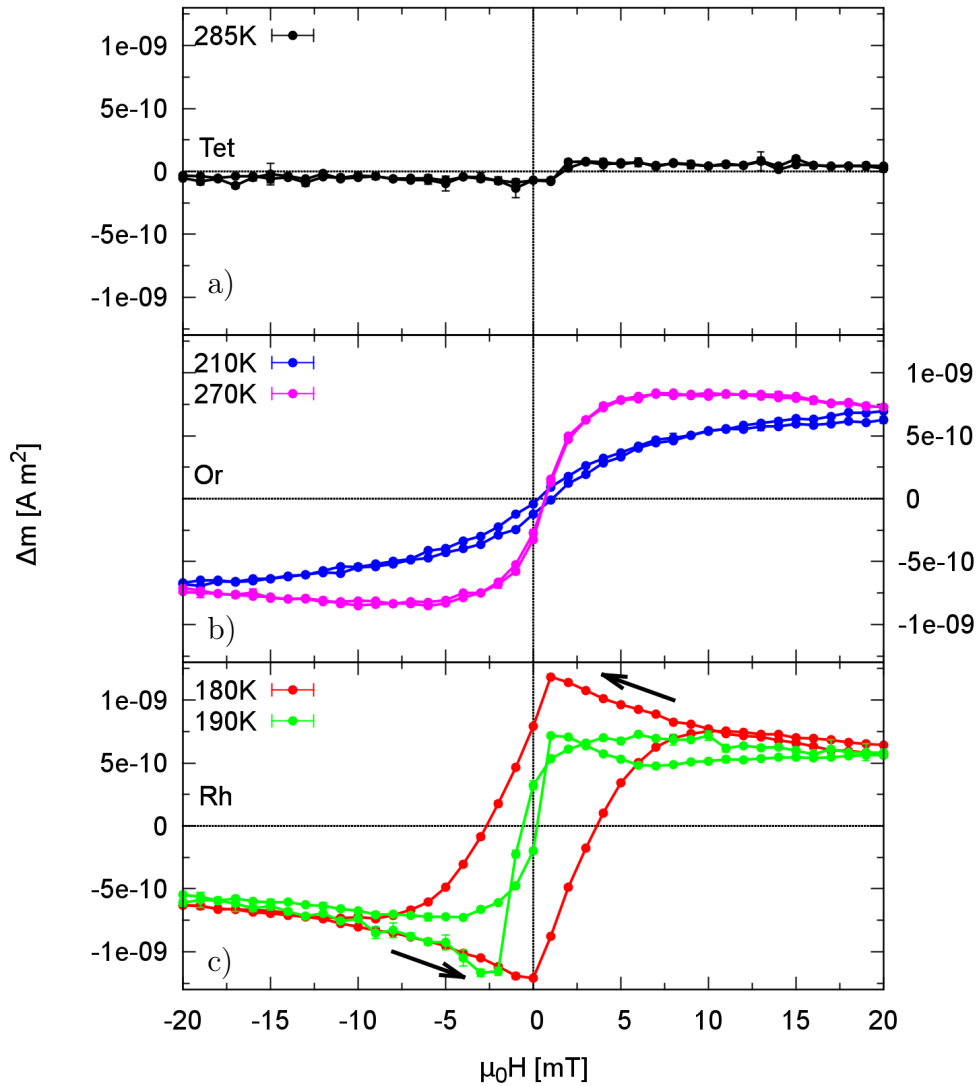


Figure 6.13: Measurement of  $\Delta m_{T,EAC}(H)$  with respect to the external magnetic field for various temperatures. The shape of the curve changes with respect to the temperature. The curve at 180 K completely differs from the others, showing a hysteresis like behavior. The errorbars are smaller than the size of the data points.

### 6.2.6 Hysteresis Loops with Applied Electric Fields

Magnetic field dependent magnetization measurements are performed at the same temperatures as before, using the MPMS. For each temperature, hysteresis loops are measured at  $E = \pm 4$  kV/cm and without electric field. The electric field is switched at the measurement temperature. Data are recorded in a magnetic field range from -60 mT to 60 mT, while saturating to  $\pm 1$  T in between.

Fig. 6.14 shows the hysteresis loops at 285 K, within the tetragonal phase of the substrate, for different applied electric fields. Errorbars are relatively large due to the small magnetization at this temperature, perturbations by the electrical connections and particularly due to the used DC option of the MPMS. Nevertheless, ferromagnetic hysteresis loops with a coercivity field of  $\approx 0.6$  mT are observed. No difference between the measurements at different electric fields can be observed.

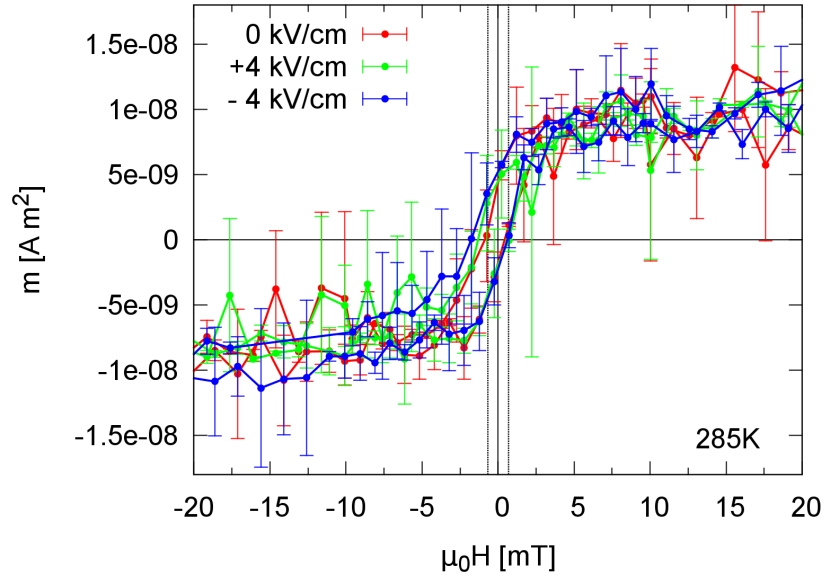


Figure 6.14: *Magnetic hysteresis loops at 285 K for different applied electric fields. No change of the loops can be observed with respect to the applied electric field. The black dashed lines indicate the coercivity field.*

Hysteresis loops performed in the orthorhombic substrate phase, at 210 K and 270 K are depicted in Fig. 6.15. At 270 K, the magnetization loop shows no hysteresis. The application of a negative electric field leads to an increased slope of the magnetization with respect to the external magnetic field. Positive electric fields do not show an influence on the magnetization loop compared to the neutral loop without applied electric field. In general, the magnetization is relatively low as expected from the temperature dependent magnetization curves. However, the measurement at 210 K shows a typically ferromagnetic behavior. The application of positive electric fields leads to a change of

the squareness of the hysteresis loop. The remanent magnetization  $m_r$  is drastically reduced by 45.5% compared to  $m_r$  without electric field. Furthermore, the coercivity field is reduced by 3.2 mT to 10.3 mT. The shift of the coercivity field is indicated by the gray boxes in Fig. 6.15 b). Summarized results of the coercivity field and the remanent magnetization can be found in Tab. 6.3. In comparison to the magnetic field dependent MEC measurement (see Fig. 6.13), the reduction of the remanent magnetization at 210 K is not in agreement with the change of the magnetization  $\Delta m_{T=210\text{K}, E_{AC}}(H = 0 \text{ mT})$ . Furthermore, no distinguished feature is present in the MEC measurement in proximity to the coercivity field.

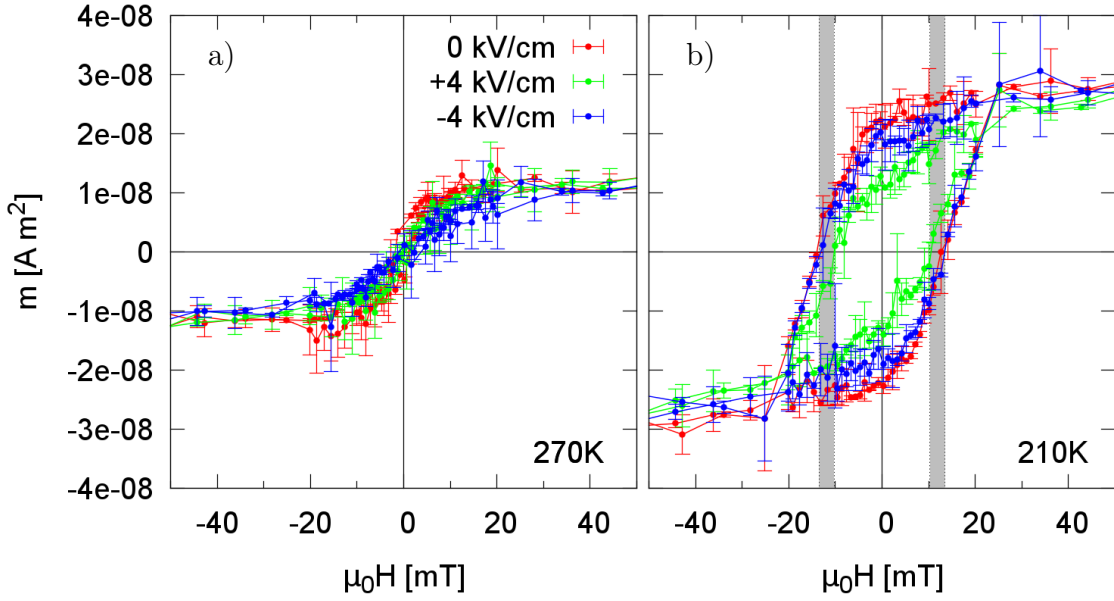


Figure 6.15: *Hysteresis loops of the  $\text{La}_{0.53}\text{Sr}_{0.47}\text{MnO}_3$  layer for different electric fields, taken within the orthorhombic phase of the  $\text{BaTiO}_3$  substrate at a) 270 K and b) 210 K. A shift of the coercivity field is indicated by gray boxes.*

E [kV/cm]	T [K]	$m_r \cdot 10^{-8}$ [A m <sup>2</sup> ]	$\Delta m_r$ [%]	$\mu_0 H_C$ [mT]	$\mu_0 \Delta H_C$ [%]	$m_r/m_s$
0	210	$2.2 \pm 0.2$	-	$13.5 \pm 0.15$	-	0.77
-4	210	$1.9 \pm 0.2$	13.6	$13.5 \pm 0.15$	0	0.67
+4	210	$1.2 \pm 0.1$	45.5	$10.3 \pm 0.15$	23.7	0.42

Table 6.3: *Coercivity field and remanent magnetization at 210 K including relative changes compared to  $E = 0 \text{ kV/cm}$ . The hysteresis loop with  $E = +4 \text{ kV/cm}$  shows a shift of the coercivity field of 3.2 mT and a reduced remanent magnetization of 45.5% compared to the hysteresis at  $E = 0 \text{ kV/cm}$ . The squareness  $m_r/m_s$  is a measure for the anisotropy.*

Hysteresis loops are also performed in the rhombohedral phase at 180 K and 190 K, presented in Fig. 6.16 a) and b), respectively. Both measurements show a typical ferromagnetic behavior as expected for the temperature range. Also in the rhombohedral substrate

phase, a positive applied voltage leads to an increase of the coercivity field by 54.5% at 180 K. The remanent magnetization and coercivity field values are shown in Tab. 6.4. At 190 K (see Fig. 6.16 b)) the shift of the coercivity field is even bigger. The coercivity field is highly enlarged by 144.4% by applying a positive electric field. Most probably, this huge effect is related to the proximity to the structural phase transition (Rh  $\leftrightarrow$  Or), where the structure of the ferroelectric substrate can be highly influenced by the electric field. Here, the change of the magnetization  $\Delta m_{T=180\text{K}, E_{AC}}(H = 0 \text{ mT}) = 1.2 \cdot 10^{-9} \text{ A} \cdot \text{m}^2$  (see Fig. 6.13 c)) measured by the MEC option is in the same order of magnitude as the change of the remanent magnetization of  $\Delta m_r = 4.1 \cdot 10^{-9} \text{ A} \cdot \text{m}^2$  at 180 K and 0 mT. On the other hand, again the MEC measurement shows no special features for magnetic fields in proximity to the coercivity field.

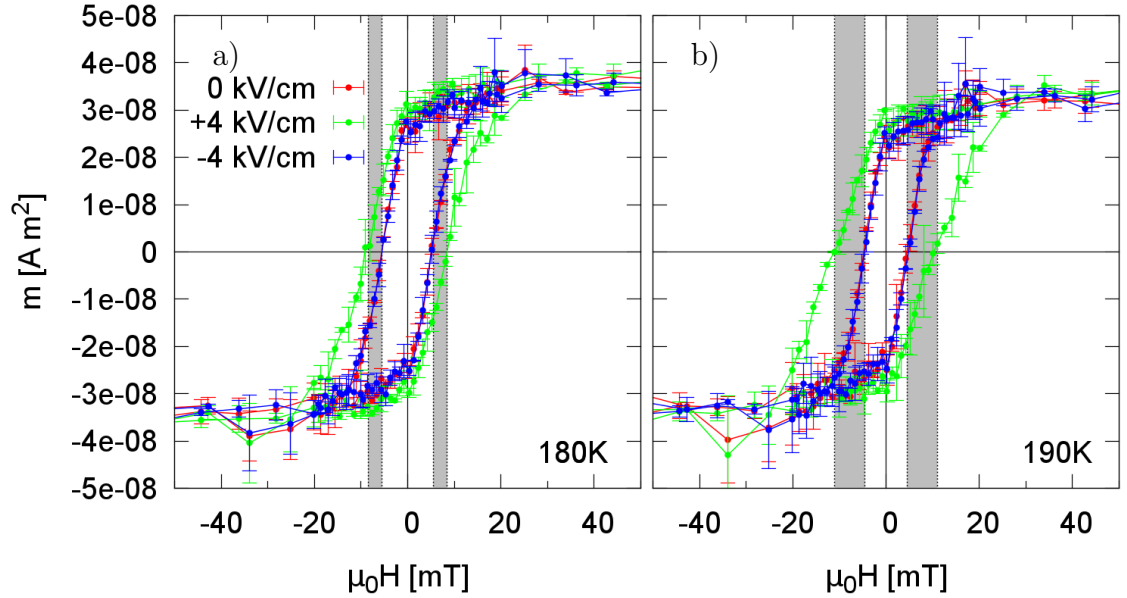


Figure 6.16: *Hysteresis loops of the  $\text{La}_{0.53}\text{Sr}_{0.47}\text{MnO}_3$  layer, performed in the rhombohedral phase of the  $\text{BaTiO}_3$  substrate at a) 180 K and b) 190 K. The gray boxes indicate the shift of the coercivity field.*

In total, no correlation between the coercivity fields of the hysteresis loops and critical fields describing turning points, zero crossings or maxima of the magnetic field dependent  $\Delta m_{T, E_{AC}}(H)$  measurements (Fig. 6.13) could be found. At the saturation field, obtained from the hysteresis loops, the change of the magnetization with applied AC electric field converges to a constant value within the related substrate phase. The magnetic field dependent investigation underlines the asymmetric manipulation of the magnetization by electric fields, since only one electric field direction leads to a change of the hysteresis loop. The observed differences in the remanent magnetization for different applied electric fields is in the same order of magnitude as in the MEC measurement ( $\mu_0H = 0 \text{ mT}$ ) for the rhombohedral substrate phase, but differ in the order of magnitude in the orthorhombic phase.

E [kV/cm]	T [K]	$m_r \cdot 10^{-8}$ [A m <sup>2</sup> ]	$\Delta m_r$ [%]	$\mu_0 H_C$ [mT]	$\mu_0 \Delta H_C$ [%]	$m_r/m_s$
0	180	$2.64 \pm 0.13$	-	$5.5 \pm 0.15$	-	0.73
-4	180	$2.65 \pm 0.14$	0	$5.5 \pm 0.15$	0	0.73
+4	180	$3.05 \pm 0.12$	15.5	$8.5 \pm 0.15$	54.5	0.84
0	190	$2.33 \pm 0.23$	-	$4.5 \pm 0.15$	-	0.71
-4	190	$2.38 \pm 0.15$	0	$4.5 \pm 0.15$	0	0.72
+4	190	$2.78 \pm 0.14$	19.3	$11 \pm 0.15$	144.4	0.84

Table 6.4: Summarized results of the coercivity field, the remanent magnetization and the relative changes compared to  $E = 0$  kV/cm at 180 K and 190 K. Coercivity fields are highly enlarged by the application of positive applied electric fields. The squareness slightly changes.

### 6.3 Analysis of the Magnetic Depth Profile

Polarized neutron reflectometry measurements are performed to deduce the magnetic profile of the La<sub>0.53</sub>Sr<sub>0.47</sub>MnO<sub>3</sub> film. This magnetic profile is of great interest to verify a possible limitation of the manipulation of the magnetization by applied electric fields to the interface, as predicted by Burten et al. [1]. The measurements are performed at MARIA at the MLZ. The instrument and the data reduction is shortly described in Chapter 4.10.1. Furthermore, an introduction on the simulation of the polarized neutron reflectivity is given in Chapter 3.3. PNR measurements are performed at 300 K and 150 K. The temperatures are reached after cooling in a magnetic field of 1 T. The measurement is performed at 70 mT. Thus, the sample is saturated and no spin-flip process is expected. The applied electric field is switched at the measurement temperature from +8 kV/cm to -8 kV/cm. The measurement for  $E=+8$  kV/cm at 300 K had to be remeasured at the end of the beamtime, because in the first measurement the electrical contact was broken and no voltage was applied. Additionally, measurements within the orthorhombic phase of the substrate at 210 K are performed on a La<sub>0.5</sub>Sr<sub>0.5</sub>MnO<sub>3</sub> film, grown by the HOPSS to cover all phases of the substrate.

The PNR measurement performed at 300 K with an applied electric field of +8 kV/cm can be seen in Fig. 6.17 a). The data show thickness oscillations up to the third order. A signal-to-noise ratio of 5 orders of magnitude could be reached using the self designed sample holder and optimized instrument settings. The  $R_{++}$  and  $R_{--}$  reflectivity differ due to the magnetization in the La<sub>0.53</sub>Sr<sub>0.47</sub>MnO<sub>3</sub> layer at 300 K. Fig. 6.17 b) shows a asymmetry plot to visualize the magnetic contribution. The  $R_{++}$  and  $R_{--}$  reflectivities for positive and negative applied electric fields of 8 kV/cm are shown in Fig. 6.18 a) and b), respectively, with the corresponding fit of the data. For a better visibility the  $R_{--}$  reflectivity is divided by a factor of 10. Fig. 6.18 d) shows both data sets for positive and negative applied electric fields. Here, one can clearly see a difference in the reflectivity for both electric field directions. The measurements are well represented by the fit. The SLDs obtained from the fits are plotted in Fig. 6.18 c) with respect to the layer thickness  $z$ . For both a nuclear scattering length density (NSLD) of  $3.44 \cdot 10^{-6} \text{ \AA}^{-2}$  of the  $252^{+3}_3 \text{ \AA}$

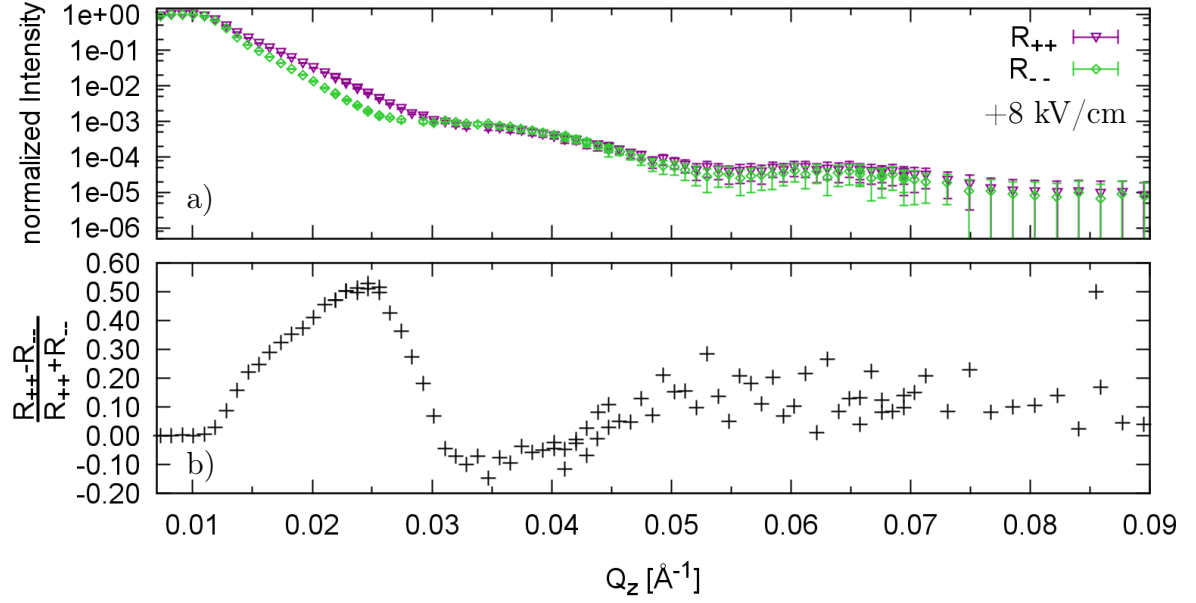


Figure 6.17: a) PNR measurement of the  $\text{La}_{0.53}\text{Sr}_{0.47}\text{MnO}_3$  film at 300 K with an applied electric field of  $+8 \text{ kV/cm}$ . b) asymmetry to visualize the order of the magnetization.

thick LSMO layer was obtained. This NSLD is slightly reduced in comparison to the bulk value of  $3.71 \cdot 10^{-6} \text{ \AA}^{-2}$ . Additionally, a top layer with reduced density has to be taken into account. For the fit of the reflectivity at positive electric field, an enlarged surface roughness has to be taken into account. This leads to the earlier drop in the SLD at the surface as one can see in Fig. 6.18 c). The magnetic scattering length density (MSLD) was calculated by the use of the following model for the magnetization profile:

$$M = \frac{1}{1 + e^{-(z-p_{\text{left}}/\sigma_{\text{left}})}} \cdot m_{\text{LSMO}} \cdot \frac{1}{1 + e^{+(z-p_{\text{right}}/\sigma_{\text{right}})}}. \quad (6.1)$$

The edges of the magnetization profile  $M$  in the LSMO layer are described by two Fermi-Dirac distributions with variable positions  $p_{\text{left}}$  and  $p_{\text{right}}$  and widths  $\sigma_{\text{left}}$  and  $\sigma_{\text{right}}$  as shown in Fig. 6.19.  $m_{\text{LSMO}}$  denotes the magnetic moment of the LSMO given in  $\mu_B$  per Mn atom.

A magnetization of  $0.8_{-0.1}^{+0.1} \mu_B$  per Mn atom is obtained for the positive electric state, while the magnetization of the negative state is  $0.6_{-0.2}^{+0.1} \mu_B$  per Mn atom. Additionally, for both states a reduced MSLD at the interface of the  $\text{La}_{0.53}\text{Sr}_{0.47}\text{MnO}_3$  and  $\text{BaTiO}_3$  has to be taken into account to describe the data accurately.

As mentioned before the measurement at 300 K and positive electric field was remeasured at the end of the beam time, since the electrical contact broke during the first measurement. The aging of the sample due to several switching processes could be the reason for the enlarged roughness of the sample surface. Since MPMS measurements did not show any effect on the magnetization with respect to the applied electric field at 300 K, no effect

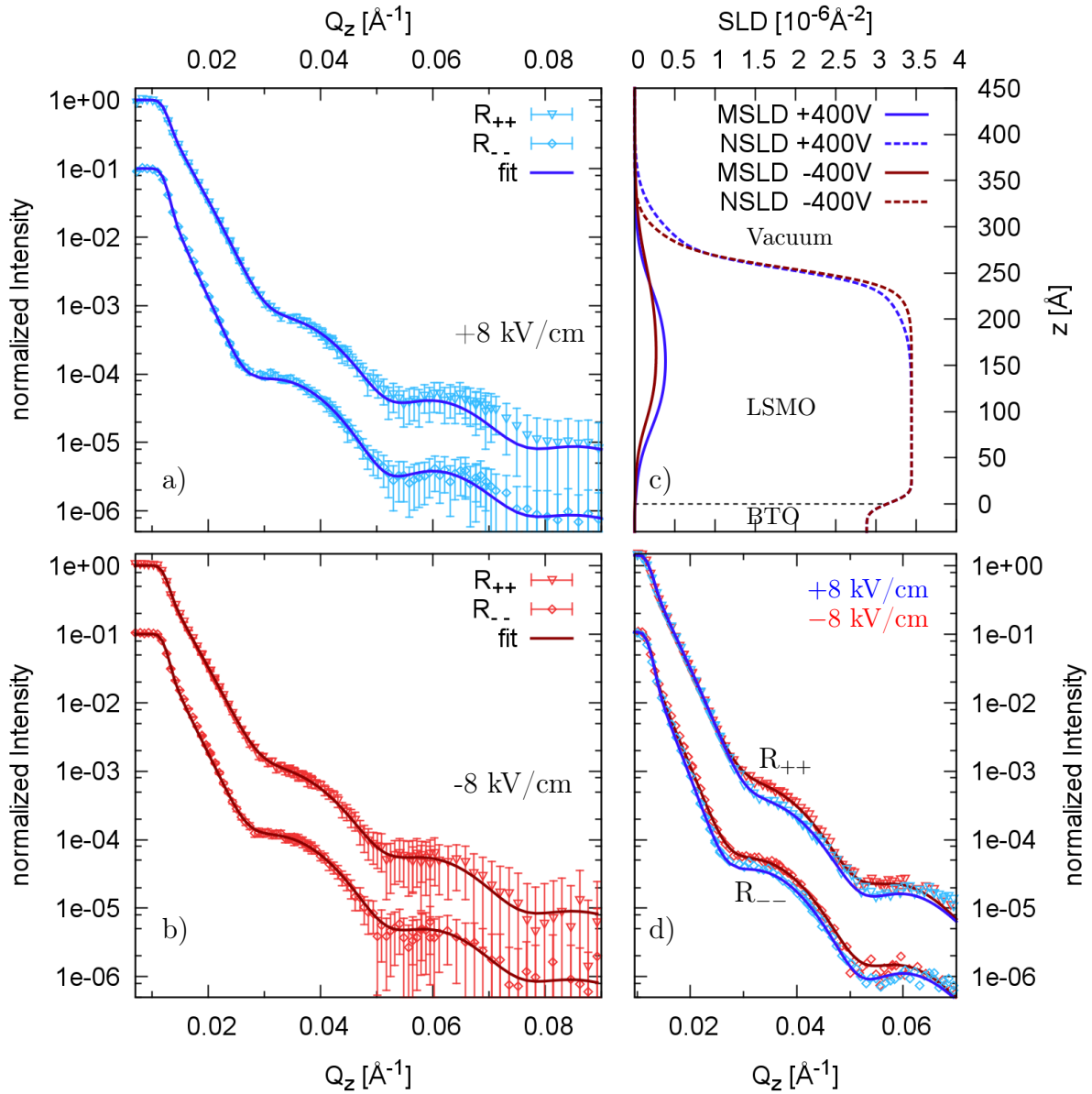


Figure 6.18: Polarized neutron reflectivity data of the  $\text{La}_{0.53}\text{Sr}_{0.47}\text{MnO}_3/\text{BaTiO}_3$  sample at 300 K. The  $R_{--}$  reflectivity is divided by 10 for a better visibility. The reflectivity for electric field of  $+8 \text{ kV/cm}$  and  $-8 \text{ kV/cm}$  including the fit of the data are shown in a) and b), respectively. d) shows both data sets to visualize the difference in the reflectivity with respect to the applied electric field. The SLD profiles obtained by the fits are depicted in c).

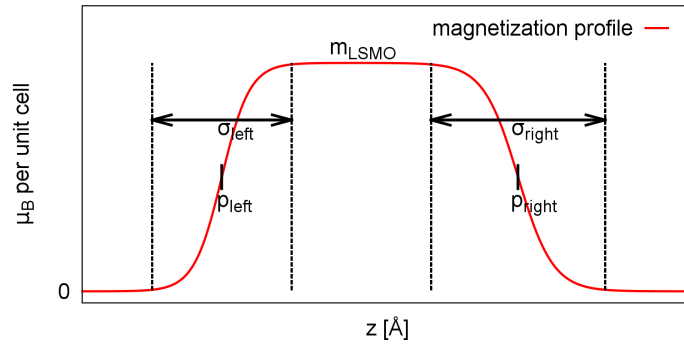


Figure 6.19: *Diagram to illustrate the model of the magnetization profile of the LSMO layer. The edges of the magnetization in the LSMO layer are described by two Fermi-Dirac distributions with variable positions  $p_{\text{left}}$  and  $p_{\text{right}}$  and widths  $\sigma_{\text{left}}$  and  $\sigma_{\text{right}}$ .*

is expected for the PNR measurement. Most probably, the effect seen in the PNR data is not related to a real switching of a magnetic state, but due to the history of the sample since it was heated, cooled and electrically switched for several times during the beamtime.

PNR measurements performed at 150 K, in the rhombohedral substrate phase are depicted in Fig. 6.20. Again, the  $R_{--}$  reflectivity is divided by a factor of 10. No difference in the data for  $\pm 8$  kV/cm could be observed. The thickness oscillations are more pronounced for the  $R_{--}$  channel and less for the  $R_{++}$ . The best fit of the data is plotted as black solid line. The corresponding SLD is presented in Fig. 6.20 b). A top layer with reduced NSLD was assumed. The shape of the magnetic profile stays almost constant compared to the measurement at 300 K, but the magnetization is increased to  $1.9_{-0.1}^{+0.2} \mu_B$  per Mn atom. A reduced MSLD at the interface of  $\text{La}_{0.53}\text{Sr}_{0.47}\text{MnO}_3$  and  $\text{BaTiO}_3$  had to be taken into account.

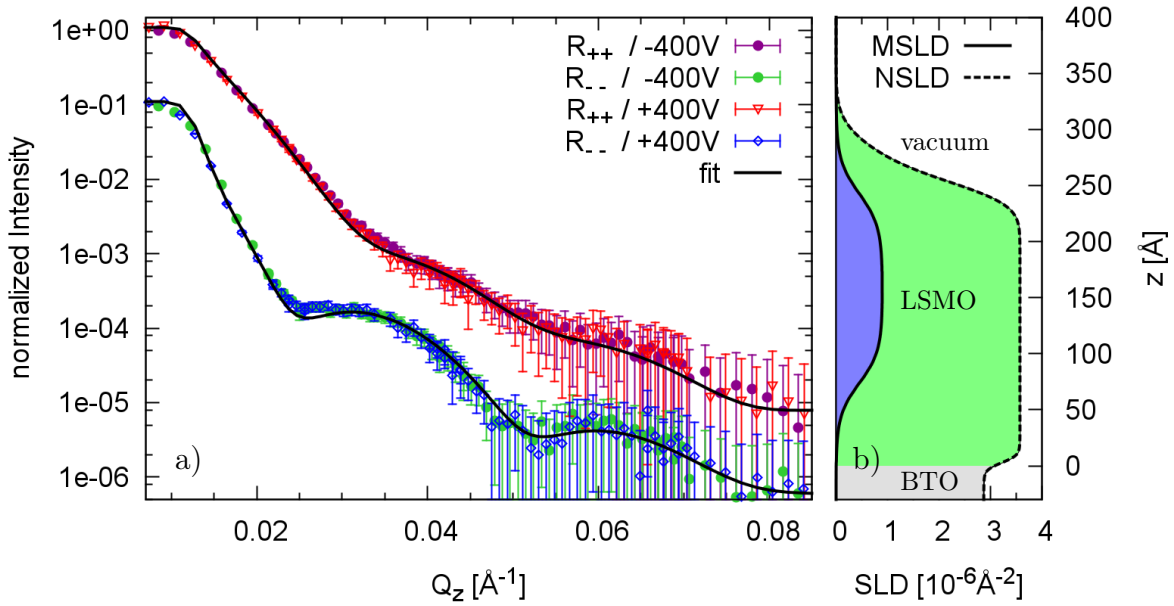


Figure 6.20: *Polarized neutron reflectivity at 150 K, no difference with respect to the electric field direction is observed. b) shows the SLD corresponding to the best fit of the data. The NSLD regarding the substrate is depicted in grey, while the LSMO layer is colored in green. The magnetic SLD is drawn in blue.*

In order to cover each structural phase of the  $\text{BaTiO}_3$  substrate, PNR measurements were performed on a  $\text{La}_{0.5}\text{Sr}_{0.5}\text{MnO}_3/\text{BaTiO}_3$  sample at 210 K. This sample was produced by the HOPSS under the growth conditions mentioned in Chapter 5.2. The investigation by PNR was performed in the same way as before. Only the counting times were increased in order to decrease the errorbars, especially for the higher  $Q$ -range. Fig. 6.21 shows the polarized neutron reflectivity data. The same intensity is observed for the different applied electric fields. The fit shown by the black solid line nicely represents the measured data. The LSMO layer has a thickness of  $270_{-2}^{+4} \text{\AA}$  with a NSLD of  $3.57 \cdot 10^{-6} \text{\AA}^{-2}$ , both a bit larger than for the sample prepared by the OMBE. A  $40 \pm 2 \text{\AA}$  thick top layer with slightly reduced density was fitted. The magnetic profile of the LSMO layer was modeled as before. A magnetization of  $0.8_{-0.1}^{+0.1} \mu_B$  per Mn atom was found. No reduction of the magnetization at the common interface between  $\text{La}_{0.5}\text{Sr}_{0.5}\text{MnO}_3$  and  $\text{BaTiO}_3$  had to be

taken into account. Due to the interface roughness the MSLD seems to extend into the BTO. The magnetization slightly decreases with increasing film thickness. This could be related to oxygen deficiencies, since oxygen can diffuse out of the sample.

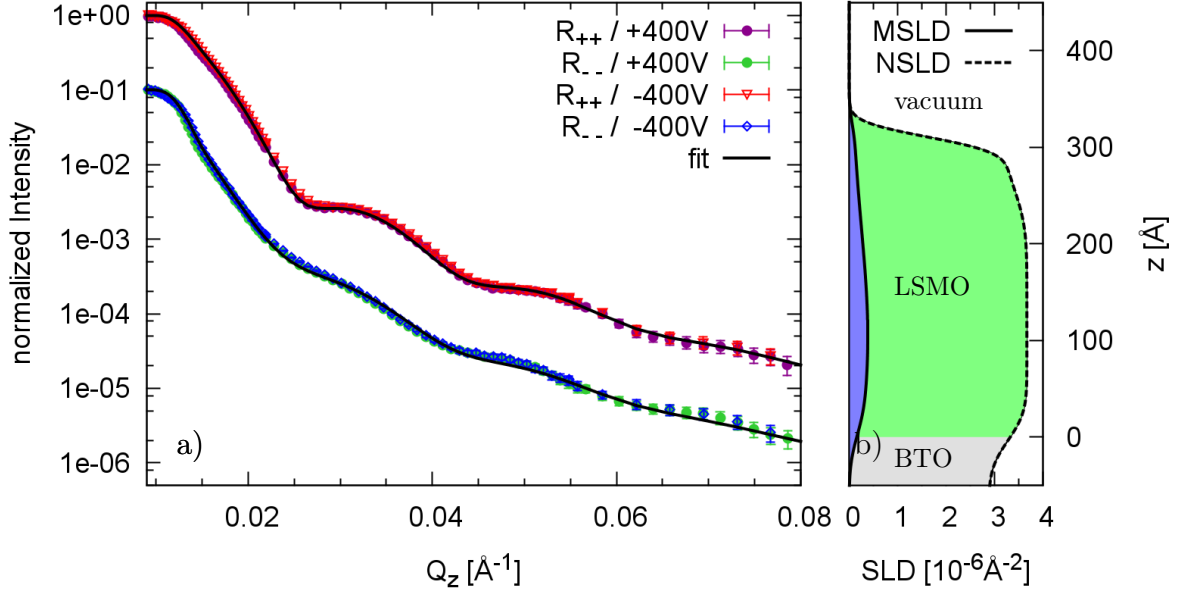


Figure 6.21: Polarized neutron reflectivity data of the  $\text{La}_{0.5}\text{Sr}_{0.5}\text{MnO}_3/\text{BaTiO}_3$  sample at 210 K, in the orthorhombic phase. The  $R_{--}$  reflectivity is divided by 10 for a better visibility. The reflectivity for electric field of  $\pm 8$  kV/cm including the fit are shown in a). b) shows the SLD obtained by the fit of the data.

In summary, the magnetization profiles of the  $\text{La}_{(1-x)}\text{Sr}_x\text{MnO}_3/\text{BaTiO}_3$  were investigated with respect to positive and negative applied electric fields. Measurements were performed in all structural phases of the substrate. For comparison the magnetization profiles are given in Fig. 6.22. A difference in the magnetization with respect to the polarization of the electric field could be observed for the measurement at 300 K. However, this difference is most probably related to the history of the sample. The sample produced by the OMBE shows a reduced magnetization at the common interface of  $\text{La}_{0.53}\text{Sr}_{0.47}\text{MnO}_3$  and  $\text{BaTiO}_3$ . In order to clarify whether the effect predicted by Burton *et al.* is observable by PNR in the samples under investigation, simulations of the polarized neutron reflectivity are done. For this the parameters of the  $\text{La}_{0.53}\text{Sr}_{0.47}\text{MnO}_3/\text{BaTiO}_3$  sample produced by OMBE are taken to simulate realistic structural properties. The magnetization profile is modeled following the prediction of Burton *et al.*. A magnetization of  $2.0 \mu_B$  per Mn is adopted over the whole LSMO layer with an antiferromagnetic alignment of the first two unit cells of the common interface. Fig. 6.23 shows the resulting reflectivities for ferromagnetic and antiferromagnetic alignment at the interface and the corresponding SLDs. The effect should be observable by PNR. Nevertheless, for magnetizations below  $1.0 \mu_B$  per Mn simulations show that the effect is not observable anymore.

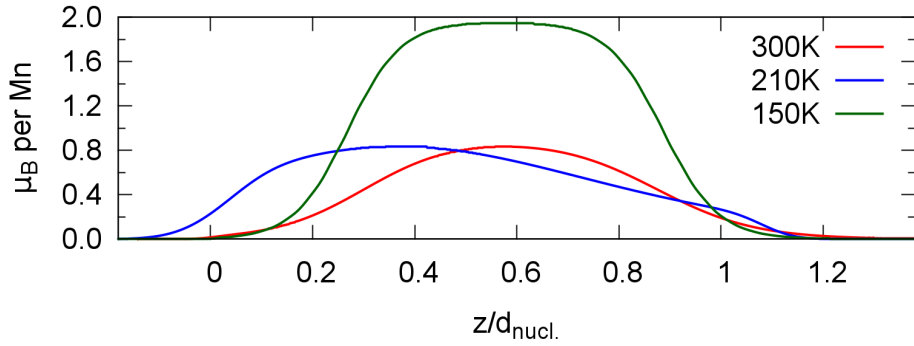


Figure 6.22: *For comparison: Magnetization profiles at various temperatures. The profile thickness is given in units relative to the nuclear layer thickness  $d_{\text{nucl.}}$ .*

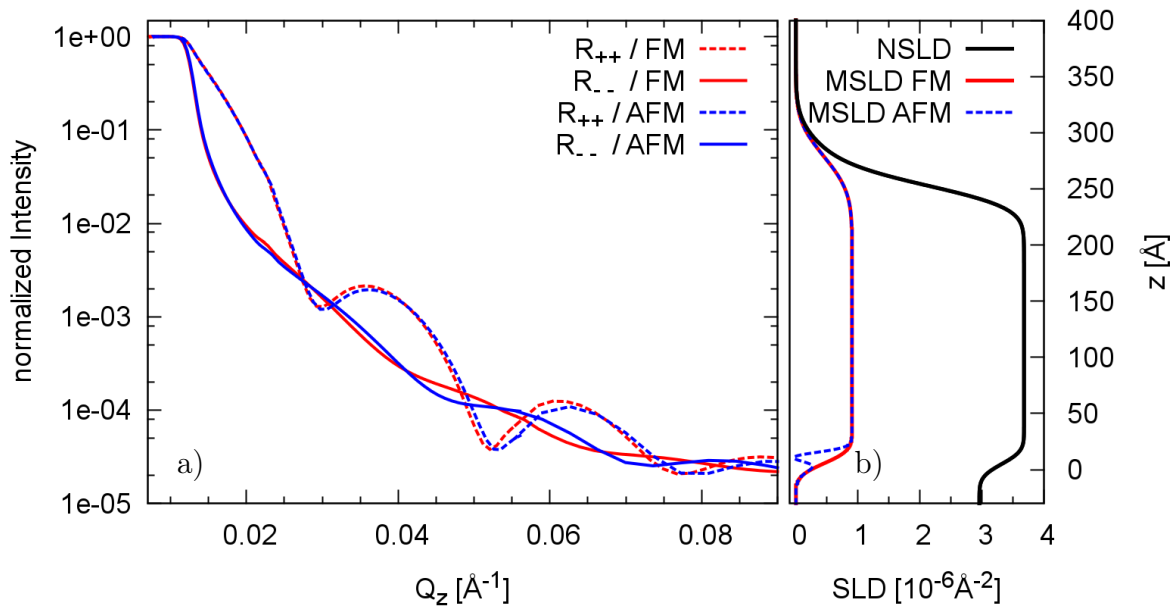


Figure 6.23: *a) Simulation of the polarized neutron reflectivity using the b) magnetization profile for FM and AFM alignment at the interface as predicted by Burton et al. Structural parameters of the  $\text{La}_{0.53}\text{Sr}_{0.47}\text{MnO}_3/\text{BTO}$  sample are used.*

# Chapter 7

## Results II:

### $\text{La}_{0.7}\text{Sr}_{0.3}\text{MnO}_3$ on $\text{BaTiO}_3$

The mechanism of the magneto-electric coupling in  $\text{La}_{0.5}\text{Sr}_{0.5}\text{MnO}_3/\text{BaTiO}_3$ , predicted by Burton et al. [1] is based on the proximity of  $\text{La}_{0.5}\text{Sr}_{0.5}\text{MnO}_3$  to the magnetic phase transition from ferromagnetic to antiferromagnetic. Thus, it is of high interest, whether a similar system without such a phase transition shows similar behavior.  $\text{La}_{0.7}\text{Sr}_{0.3}\text{MnO}_3$  was chosen because no nearby magnetic phase transition is expected [32]. Since the structure of both systems is quite similar,  $\text{La}_{0.7}\text{Sr}_{0.3}\text{MnO}_3$  layers are produced with the same parameters as for  $\text{La}_{0.5}\text{Sr}_{0.5}\text{MnO}_3$ , using the HOPSS. All measurements done for the half doped  $\text{La}_{(1-x)}\text{Sr}_x\text{MnO}_3$  presented in the chapter before are repeated for the doping level of  $x=0.3$ . The structural and magnetic properties of  $\text{La}_{0.7}\text{Sr}_{0.3}\text{MnO}_3$  on  $\text{BaTiO}_3$  are presented in this chapter.

## 7.1 Structural Analysis

$\text{La}_{0.7}\text{Sr}_{0.3}\text{MnO}_3$  films are produced using the HOPSS. A commercial stoichiometric sputter target from Lesker Company is used. The growth process is described in detail in Chapter 5.2. Again,  $\text{BaTiO}_3$  is taken as substrate. The LSMO layer is grown at a substrate temperature of 1150 K for 3915 s. The sputtering process is performed in oxygen atmosphere of 3 mbar and with a sputtering power of 120 W. The sample is cooled down to room temperature in oxygen atmosphere to avoid oxygen vacancies within the oxides. In order to determine the structural properties of the sample, X-ray scattering measurements are performed. Fig. 7.1 a) shows the XRR measurement including the fit of the data. The thickness oscillations correspond to a thickness of  $349^{+5}_{-5}$  Å. Additionally a  $15.3^{+0.6}_{-0.1}$  Å top layer with reduced density has to be taken into account to describe the data accurately. A low surface roughness of  $3.0^{+0.1}_{-0.1}$  Å is obtained. As for the half doped  $\text{La}_{(1-x)}\text{Sr}_x\text{MnO}_3$ , also for  $x = 0.3$  a low contrast is present due to almost equal SLDs of the layer and the substrate. Thus, the oscillations are less pronounced. The SLD profile obtained by the fit is presented in Fig. 7.1 b). The substrate region is marked in gray, LSMO in green and the top layer in blue.

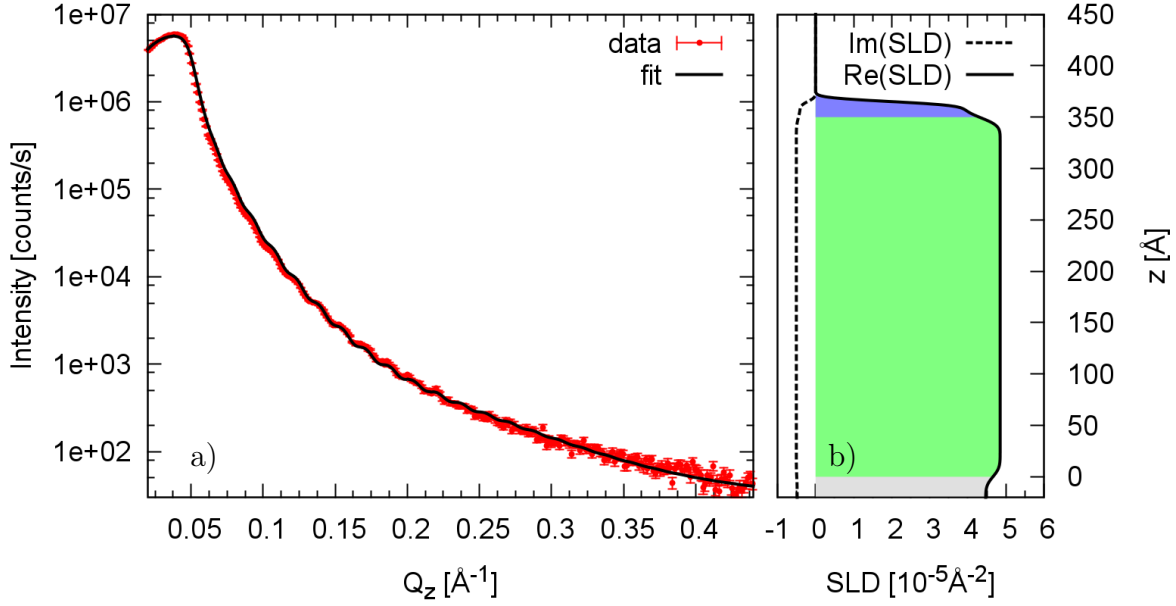


Figure 7.1: a) XRR measurement of the  $\text{La}_{0.7}\text{Sr}_{0.3}\text{MnO}_3$  layer on  $\text{BaTiO}_3$ . The SLD obtained by the fit is shown in b). A top layer with reduced SLD has to be taken into account. The substrate is marked in gray, LSMO in green and the top layer in blue.

X-ray diffraction measurements on the  $\text{La}_{0.7}\text{Sr}_{0.3}\text{MnO}_3$  film on  $\text{BaTiO}_3$  are performed to verify the crystal quality.  $\omega/2\theta$ -scans are shown in Fig. 7.2. The measurement is performed by using a monochromator, thus almost no wavelength contamination of the primary beam is observed apart from  $\text{Cu-K}\alpha_2$ . As seen before, the substrate peak splits into c-type and a-type domains, corresponding to the (002) and (200)/(020) peak. The peaks are fitted by a Gaussian function to determine the peak positions. Both lattice parameters are obtained from the peak positions to  $c_{\text{BTO}} = 4.033 \pm 0.001 \text{ \AA}$  and  $a_{\text{BTO}} = 3.989 \pm 0.001 \text{ \AA}$ . The LSMO (002) peak at  $Q = 3.26 \text{ \AA}^{-1}$  corresponds to an out-of-plane lattice parameter of  $c_{\text{LSMO}} = 3.850 \pm 0.001 \text{ \AA}$ . In summary, the X-ray measurements confirm a good sample quality with a crystalline  $\text{La}_{0.7}\text{Sr}_{0.3}\text{MnO}_3$  layer and a smooth surface.

Additionally, temperature dependent XRD measurements are performed in a  $Q_z$ -range of  $3 \text{ \AA}^{-1} < Q_z < 3.4 \text{ \AA}^{-1}$ . Fig. 7.2 shows the resulting lattice parameter corresponding to the LSMO and BTO Bragg reflections. The LSMO lattice parameter  $c_{\text{LSMO}}$  decreases with decreasing temperature. The largest modification of the lattice parameter is observed between 245 and 270 K. The lattice parameter  $c_{\text{LSMO}}$  decreases from 3.848  $\text{ \AA}$  to 3.841  $\text{ \AA}$ . This change of the lattice parameter is most probably related to the  $\text{BaTiO}_3$  phase transition from Tet to Or. The increase of  $c_{\text{LSMO}}$  from 3.839  $\text{ \AA}$  at 183 K to 3.841  $\text{ \AA}$  at 170 K corresponds to the phase transition of the  $\text{BaTiO}_3$  substrate from Or to Rh. In general, the accessible out-of-plane lattice parameter of the LSMO film is smaller as the bulk value of 3.86  $\text{ \AA}$  over the whole temperature range. Under the assumption, that the unit cell

volume is constant and biaxial strain is induced to the in-plane lattice parameters, the reduced out-of-plane lattice parameter suggests tensile in-plane strain. In order to get the full information of the strain induced into the LSMO layer, diffraction measurements on the in-plane lattice parameter are necessary.

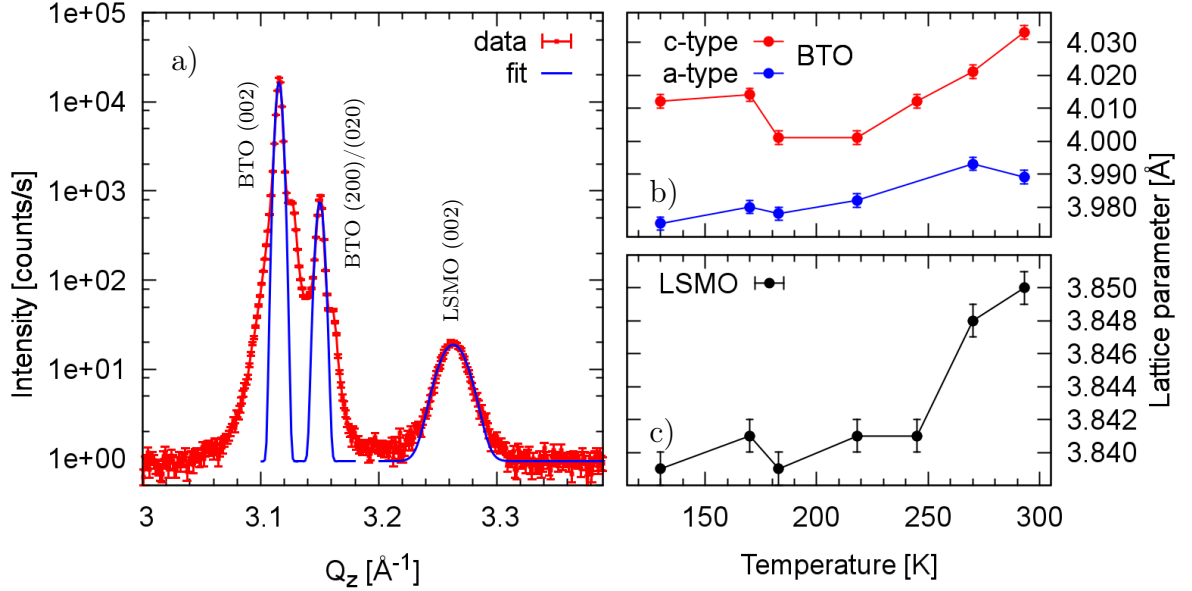


Figure 7.2: a) shows the  $\omega/2\Theta$ -scan of the  $\text{La}_{0.7}\text{Sr}_{0.3}\text{MnO}_3/\text{BaTiO}_3$  sample. The second order Bragg peak of the  $\text{BaTiO}_3$  substrate is split into c-type and a-type domains. The Bragg peak at  $Q = 3.26 \text{ \AA}^{-1}$  corresponds to the lattice parameter of  $c_{\text{LSMO}} = 3.85 \text{ \AA}$  of the crystalline LSMO film. The temperature dependent out-of-plane lattice parameters of the substrate and the LSMO film are depicted in b) and c), respectively.

## 7.2 Characterization of the Macroscopic Magnetization

Within this section the macroscopic magnetic properties of  $\text{La}_{0.7}\text{Sr}_{0.3}\text{MnO}_3$  on  $\text{BaTiO}_3$  and the manipulation thereof by electric fields are presented. The investigation is performed by the MPMS using the measurements introduced in Chapter 6.2.

### 7.2.1 Temperature Dependent Magnetization

The temperature dependent magnetization (see Fig. 7.3) is determined at an external magnetic field of  $\mu_0 H = 10 \text{ mT}$  and a cooling/heating rate of  $2 \text{ K/min}$ . The Curie temperature  $T_C$  of  $326 \text{ K}$  is slightly smaller as the bulk value, as expected for epitaxial grown thin films [114]. A small paramagnetic contribution of the sample holder is observed above  $T_C$ .

In general, the magnetization curve shows a typical ferromagnetic shape, but steps in the magnetization are observable at the structural phase transition temperatures of the substrate as seen before for the half doped  $\text{La}_{(1-x)}\text{Sr}_x\text{MnO}_3$  on  $\text{BaTiO}_3$ . The magnetization

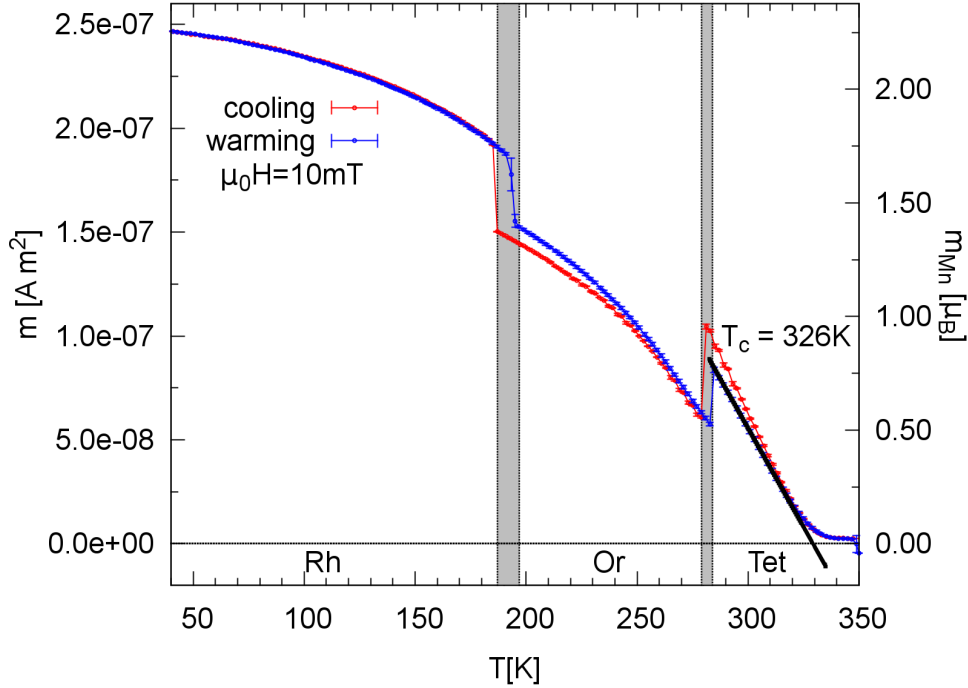


Figure 7.3: *Temperature dependent magnetization measurement at  $\mu_0 H = 10$  mT. Also for the  $\text{La}_{0.7}\text{Sr}_{0.3}\text{MnO}_3$  stoichiometric film, steps in the magnetizations are observed at the structural phase transitions of the  $\text{BaTiO}_3$  substrate. The gray boxes illustrate the temperature region of the supposed phase transitions. The magnetization is additionally given in  $\mu_B$  per Mn atom with an error of approximately 5%.*

decreases for cooling from  $(10.5 \pm 0.1) \cdot 10^{-8}$  A m<sup>2</sup> at 281 K to  $(6.1 \pm 0.1) \cdot 10^{-8}$  A m<sup>2</sup> at 278 K. This corresponds to a decrease of the magnetization by 41.9%. At the second magnetization step, an abrupt increase by 28% from  $(15.0 \pm 0.1) \cdot 10^{-8}$  A m<sup>2</sup> at 187 K to  $(19.2 \pm 0.1) \cdot 10^{-8}$  A m<sup>2</sup> at 185 K is observed. The temperature for the magnetization steps show a hysteretic behavior for cooling and warming, following the temperature behavior of the structural properties of the  $\text{BaTiO}_3$  substrate. In total, the temperature dependent magnetization shows similar behavior for the doping levels of  $x = 0.3$  and  $x = 0.5$  of  $\text{La}_{(1-x)}\text{Sr}_x\text{MnO}_3$ . Thus, it is of great interest, if also the manipulation of the magnetization with respect to applied electric fields is similar.

## 7.2.2 Temperature Dependent Electrical Manipulation of the Magnetization

The manipulation of the magnetization by electric fields is investigated as a function of temperature using the MEC option. The change of the magnetization  $\Delta m_{H,E_{AC}}(T)$  is shown in Fig. 7.4 for  $E_{AC} = 3.2$  kV/cm. The sample is mounted and electrically connected as before (see. Fig. 4.9 b)). The measurement is performed at a frequency of

$\omega = 1$  Hz and a magnetic field of  $\mu_0 H = 3$  mT. The gray boxes illustrate the temperature region of the structural phase transition of the substrate assumed from the temperature dependent magnetization measurement, done before. Above  $T_C$  no  $\Delta m_{H,EAC}(T)$  is observed. For cooling below  $T_C$  a change of the magnetization is observed in the tetragonal phase of the substrate. The change of the magnetization  $\Delta m_{H,EAC}(T)$  abruptly increases at the Tet  $\rightarrow$  Or phase transition. A similar abrupt increase was observed for the half doped  $\text{La}_{(1-x)}\text{Sr}_x\text{MnO}_3$  sample. Further cooling within the orthorhombic phase of the substrate leads to a decrease of  $\Delta m_{H,EAC}(T)$  to  $\sim 240$  K. Most noticeable is the change of the sign of  $\Delta m_{H,EAC}(T)$  in the temperature range between 230 and 240 K. The absolute value increases with decreasing temperature to a maximum value of  $|\Delta m_{H,EAC}(T = 190\text{K})| = (1.90 \pm 0.02) \cdot 10^{-9}$  A m<sup>2</sup> in proximity to the Or  $\rightarrow$  Rh phase transition of the substrate. Here, the sign of  $\Delta m_{H,EAC}(T)$  abruptly inverts, back to positive values. Also in the rhombohedral phase of the substrate,  $\Delta m_{H,EAC}(T)$  decreased by further cooling.

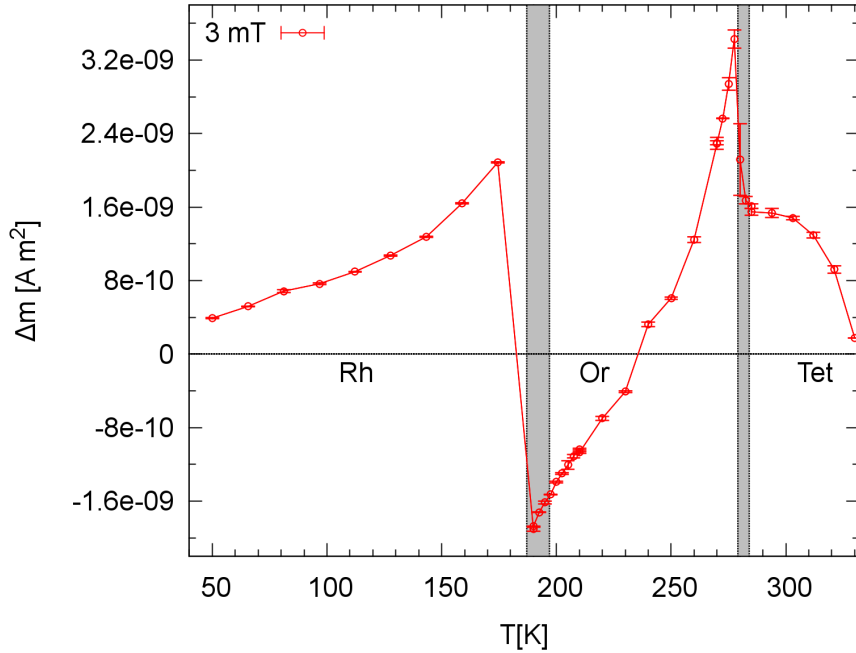


Figure 7.4: *Magneto-electric coupling of  $\text{La}_{0.7}\text{Sr}_{0.3}\text{MnO}_3/\text{BaTiO}_3$  measured by MPMS. The temperature dependent change of the magnetizations  $\Delta m$  with respect to the applied AC electric field is observed at  $\mu_0 H = 3$  mT. A clear coupling is observed with maximum values near the phase transitions of the  $\text{BaTiO}_3$  substrate. A negative change of the magnetization is observed within the orthorhombic phase.*

Since, the largest effects can be expected near the phase transitions and to ensure the possibility to compare the measurements, further investigations on the manipulation of the magnetization of  $\text{La}_{0.7}\text{Sr}_{0.3}\text{MnO}_3$  will be performed at the same temperatures as for  $\text{La}_{0.5}\text{Sr}_{0.5}\text{MnO}_3$ .

### 7.2.3 Electrical Hysteresis Loops for Different Temperatures

The absolute magnetization as a function of applied electric field is determined in each structural phase of the substrate at 285 K, 270 K, 210 K and 180 K. A magnetic field of  $\mu_0 H = 3$  mT is applied during the measurement. The electrical hysteresis loops are measured at least twice, beginning with a positive applied field of  $E = 4$  kV/cm. The electric fields are applied in the same direction as described in Chapter 6.2.2, Fig. 6.10.

Fig. 7.5 shows the absolute magnetization  $m_{T,H}(E)$  as a function of the electric field for selected temperatures. The relative scales of the plots are chosen equal for each temperature, for a better visibility of the magnitude of the effects. At 285 K, the magnetization can be modified by 1.6% by the application of electric fields. Sharp steps in the magnetization curve are observed at  $E = -0.39$  kV/cm and  $E = +0.39$  kV/cm. Apart from those steps the electric field has almost no further influence on the magnetization. At zero electric field the difference in the magnetization is still present after polarizing the substrate by the electric field. At 270 K a similar behavior as for the half doped La<sub>(1-x)</sub>Sr<sub>x</sub>MnO<sub>3</sub> is observed. One direction of the electric field leads to an increase of the magnetization. The application of positive applied fields leads to an increase of 2.8% while the magnetization is almost constant for negative and zero electric fields. At 210 K almost no difference in the magnetization for the maximum positive and negative electric field is observed. Nevertheless, a small step in the magnetization is observed at  $E = -0.5$  kV/cm and  $E=0$  kV/cm. The change of the magnetization is of opposite direction compared to the magnetization step observed at 285 K. This fits to the negative  $\Delta m_{H,EAC}(T)$  in the MEC measurement presented in the section before. Fig. 7.5 d) shows the electric field dependent magnetization at 180 K. Again, the behavior of the magnetization as function of the applied electric field completely differs from that of the other structural phases of the substrate. The magnetization decreases by 1.9% with respect to a negative applied field. At 180 K, a permanent difference of the magnetization is observed at zero electric field after polarizing the sample by  $E = \pm 4$  kV/cm. The difference of the magnetization is  $\Delta m_{\text{man.}} = (1.1 \pm 0.2) \cdot 10^{-9}$  A m<sup>2</sup>. Both, negative and positive electric field lead to a modification of the magnetization.

T [K]	$m(E_{\text{max}}) \cdot 10^{-8}$ [Am <sup>2</sup> ]	$m(E_{\text{min}}) \cdot 10^{-8}$ [Am <sup>2</sup> ]	$\Delta m_{\text{man.}} \cdot 10^{-8}$ [Am <sup>2</sup> ]	$\Delta m_{\text{rel.}}$ in %
180	$16.53 \pm 0.01$	$16.21 \pm 0.01$	$0.32 \pm 0.01$	1.9
210	$19.19 \pm 0.01$	$19.19 \pm 0.02$	—	—
270	$8.37 \pm 0.01$	$8.14 \pm 0.01$	$0.23 \pm 0.02$	2.8
285	$7.10 \pm 0.01$	$6.99 \pm 0.01$	$0.11 \pm 0.01$	1.6

Table 7.1: Magnetization of La<sub>0.7</sub>Sr<sub>0.3</sub>MnO<sub>3</sub> with respect to the applied electric field at  $\mu_0 H = 3$  mT and various temperatures. Additionally, the absolute  $\Delta m$  and relative changes of the magnetization  $\Delta m_{\text{rel.}}$  are given.

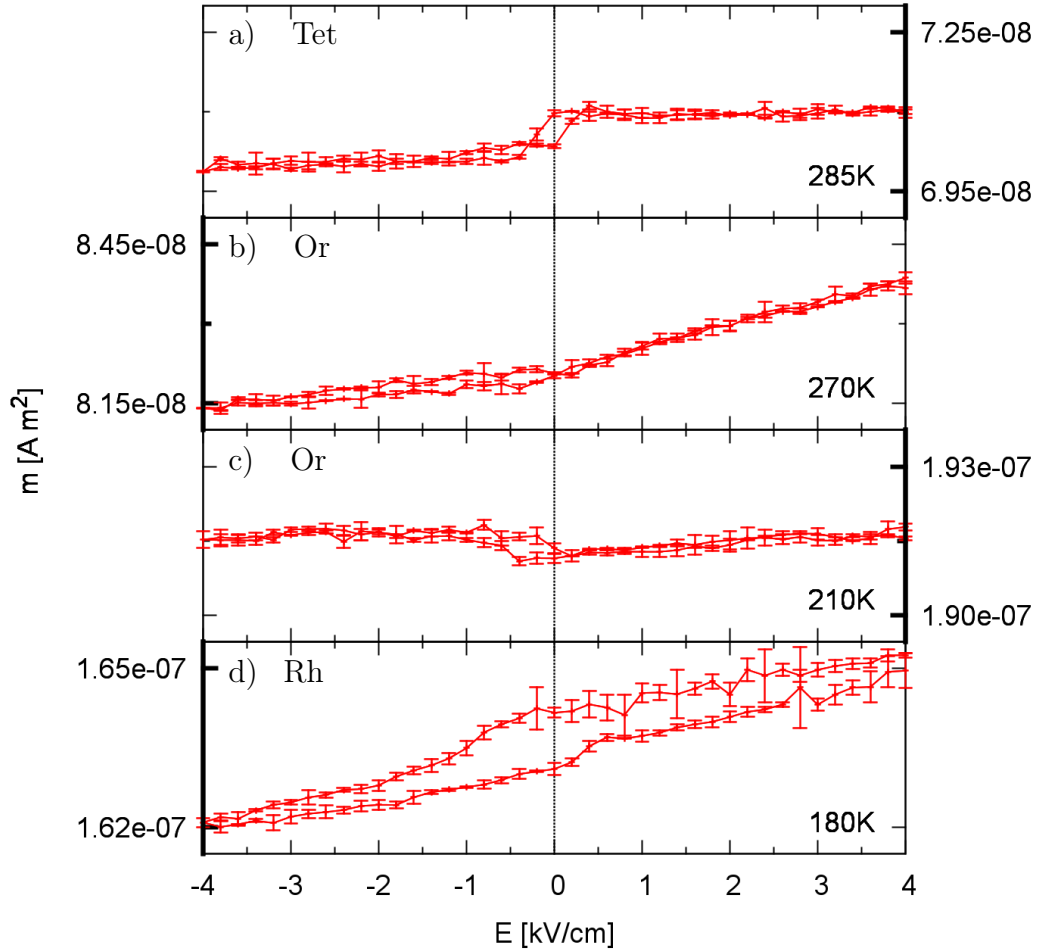


Figure 7.5: Magnetization of the  $\text{La}_{0.7}\text{Sr}_{0.3}\text{MnO}_3$  film depending on the applied electric field at various temperatures at  $\mu_0 H = 3$  mT. It is clearly possible to manipulate the magnetization by an electric field. The effect is maximal at 180 K within the rhombohedral phase of the substrate and at 270 K (orthorhombic). A difference of the magnetization is present also without electric field after polarizing the sample with  $E = +4$  kV/cm and  $E = -4$  kV/cm, at 180 and 285 K.

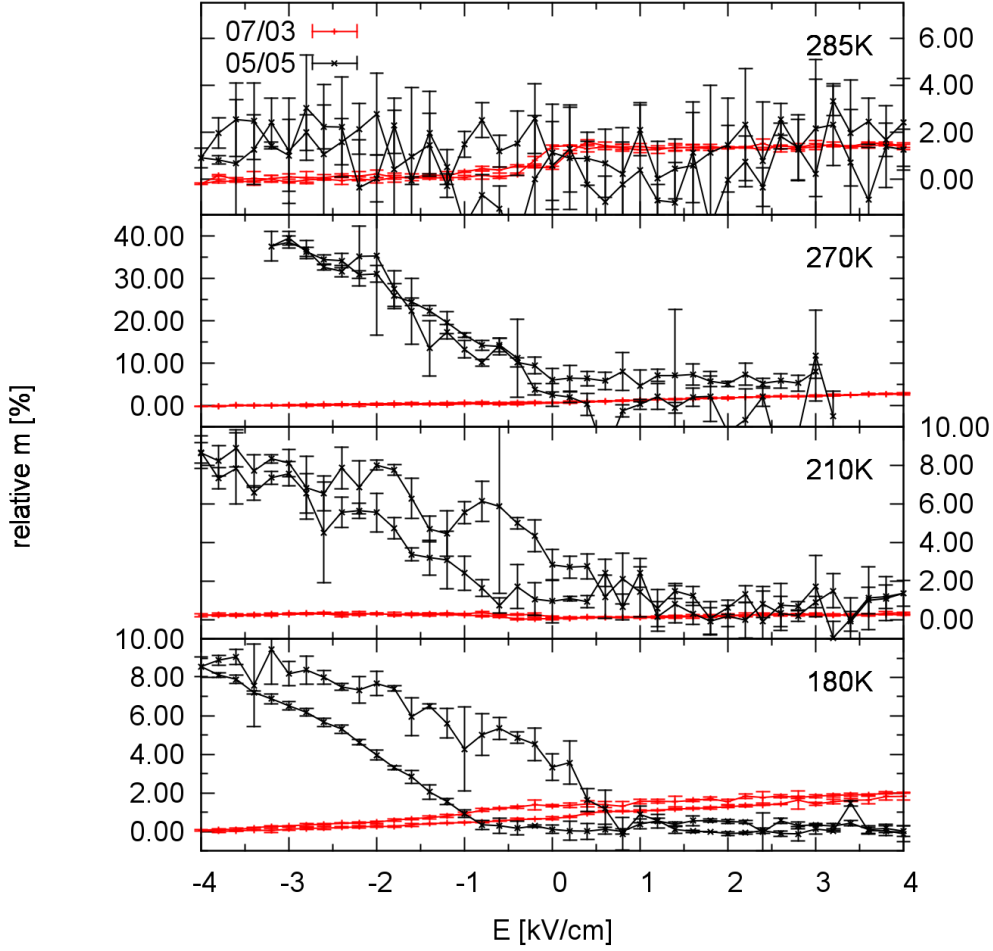


Figure 7.6: Comparison of the relative magnetization of both doping levels depending on the applied electric field at various temperatures.

In summary, it is possible to manipulate the magnetization of La<sub>0.7</sub>Sr<sub>0.3</sub>MnO<sub>3</sub> on BaTiO<sub>3</sub> by applying electric fields. A different behavior was found for each structural phase of the substrate as seen before for half doped La<sub>(1-x)</sub>Sr<sub>x</sub>MnO<sub>3</sub>. The relative changes of the magnetization are significantly smaller for the doping level of  $x = 0.3$  (see Fig.7.6), while the absolute values are comparable in their magnitude. Measurements at 180 K and 285 K show a difference in the magnetization at zero electric field after polarizing the BaTiO<sub>3</sub> with  $E = +4$  kV/cm and  $E = -4$  kV/cm. The calculated changes of the magnetization  $\Delta m_{\text{man.}}$  are in agreement with those measured by the MEC option in the section before.

### 7.2.4 Electrical Manipulation of the Magnetization at Various Magnetic Fields

The manipulation of the magnetization by electric fields, depending on external magnetic fields is probed at 180 K, 210 K, 270 K and 285 K. The MEC option is used to determine the change of the magnetization  $\Delta m_{T,EAC}(H)$ . As mentioned before a maximum electric voltage of 160 V, corresponding to  $\pm 3.2$  kV/cm, can be applied. The sample is saturated with a magnetic field of 500 mT at each temperature before the measurement. The measurement procedure was carried out in the same order as in the chapter before. The results are presented in Fig. 7.7.

The electrically induced change of the magnetization  $\Delta m_{T,EAC}(H)$  at 285 K as function of the magnetic field, within the tetragonal phase of the substrate, is shown in Fig 7.7 a). The magnetic response  $\Delta m_{T,EAC}(H)$  is very low for small magnetic fields, but increases for increasing external magnetic fields up to 50 mT. A constant value of  $(1.48 \pm 0.01) \cdot 10^{-9}$  A m<sup>2</sup> is observed for higher fields as shown in the inset. By inverting the magnetic field, also  $\Delta m_{T,EAC}(H)$  inverts, as expected. Measurements performed in the orthorhombic phase of the substrate are depicted in Fig. 7.7 b). Both curves completely differ from each other, although they are taken in the same phase of the substrate. At 270 K, a hysteretic behavior of  $\Delta m_{T,EAC}(H)$  is observed. Measurements performed at 210 K show also a hysteretic behavior, but the sign of  $\Delta m_{T,EAC}(H)$  is inverted. The inverted sign corresponds to the temperature dependent MEC measurement done before (see Fig. 7.4). Additionally, a minimum and a maximum is observed at 8 mT and -10 mT, respectively. In the rhombohedral phase of the substrate, at 180 K, a similar behavior as at 270 K is observed. A hysteretic loop with asymmetric zero crossing points at -2.8 mT and 5.5 mT can be seen in Fig. 7.7 c). A saturation like field is reached at 12 mT and -8 mT, where forth and back direction have the same value. The centers of the hysteresis loops observed in the MEC measurements are slightly shifted. Those shifts are summarized in Tab. 7.2.

T [K]	180	210	270
shift [mT]	1.35	0.9	0.9

Table 7.2: *Shift of the center of the hysteresis loops in MEC measurement with respect to the external magnetic field.*

Apart from the measurement at 180 K, the magnetic field dependent change of the magnetization by electric fields for the  $\text{La}_{(1-x)}\text{Sr}_x\text{MnO}_3$  doping levels of  $x = 0.3$  and  $x = 0.5$  are different. For better comparison measurements for both doping levels are depicted in Fig.7.8. In order to obtain a better understanding of the magnetic properties additional magnetic hysteresis loops will be presented in the following.

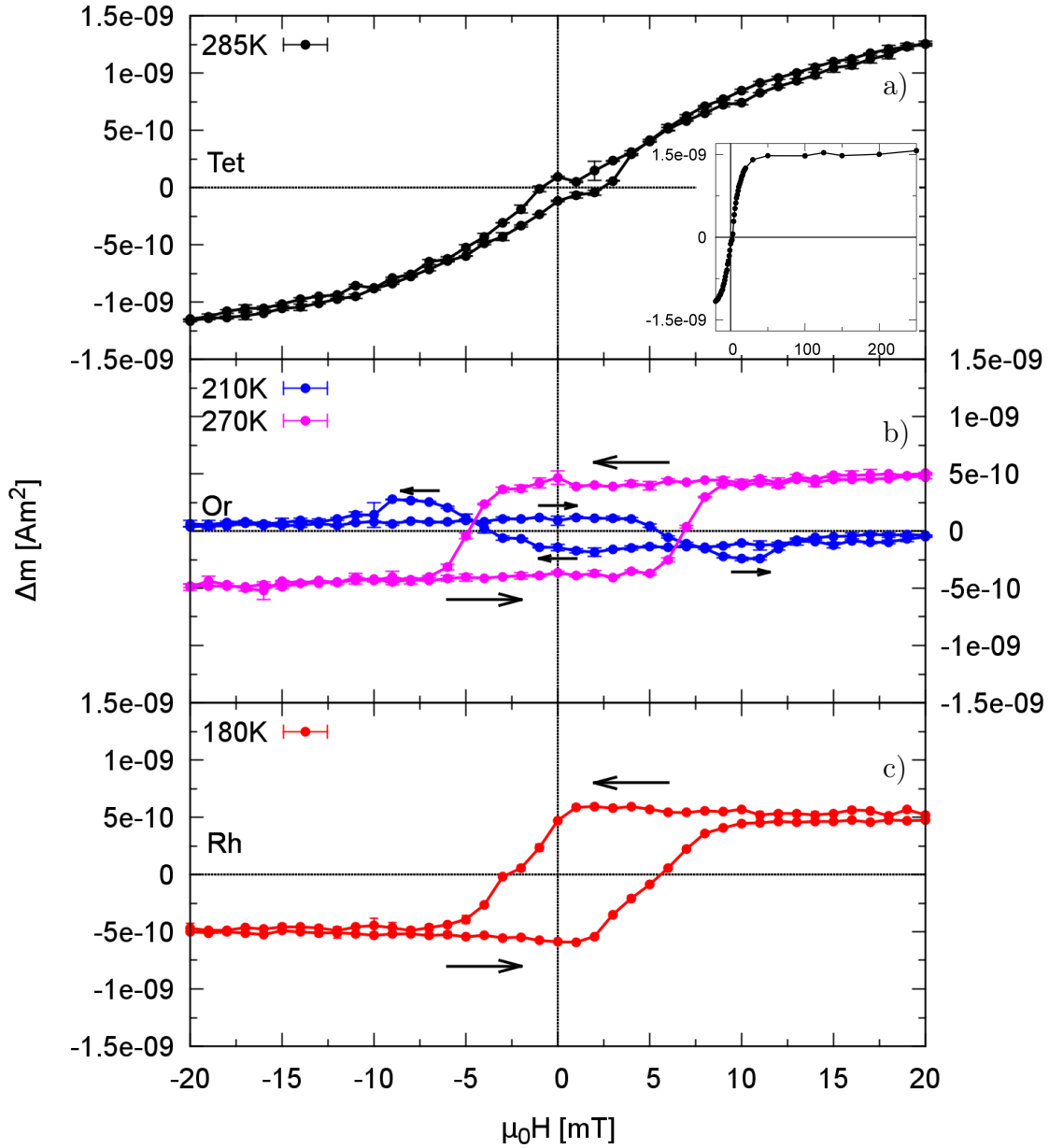


Figure 7.7: MEC measurements of  $\text{La}_{0.7}\text{Sr}_{0.3}\text{MnO}_3$  with respect to the external magnetic field for various temperatures. The arrows indicate the direction of increasing or decreasing magnetic field.

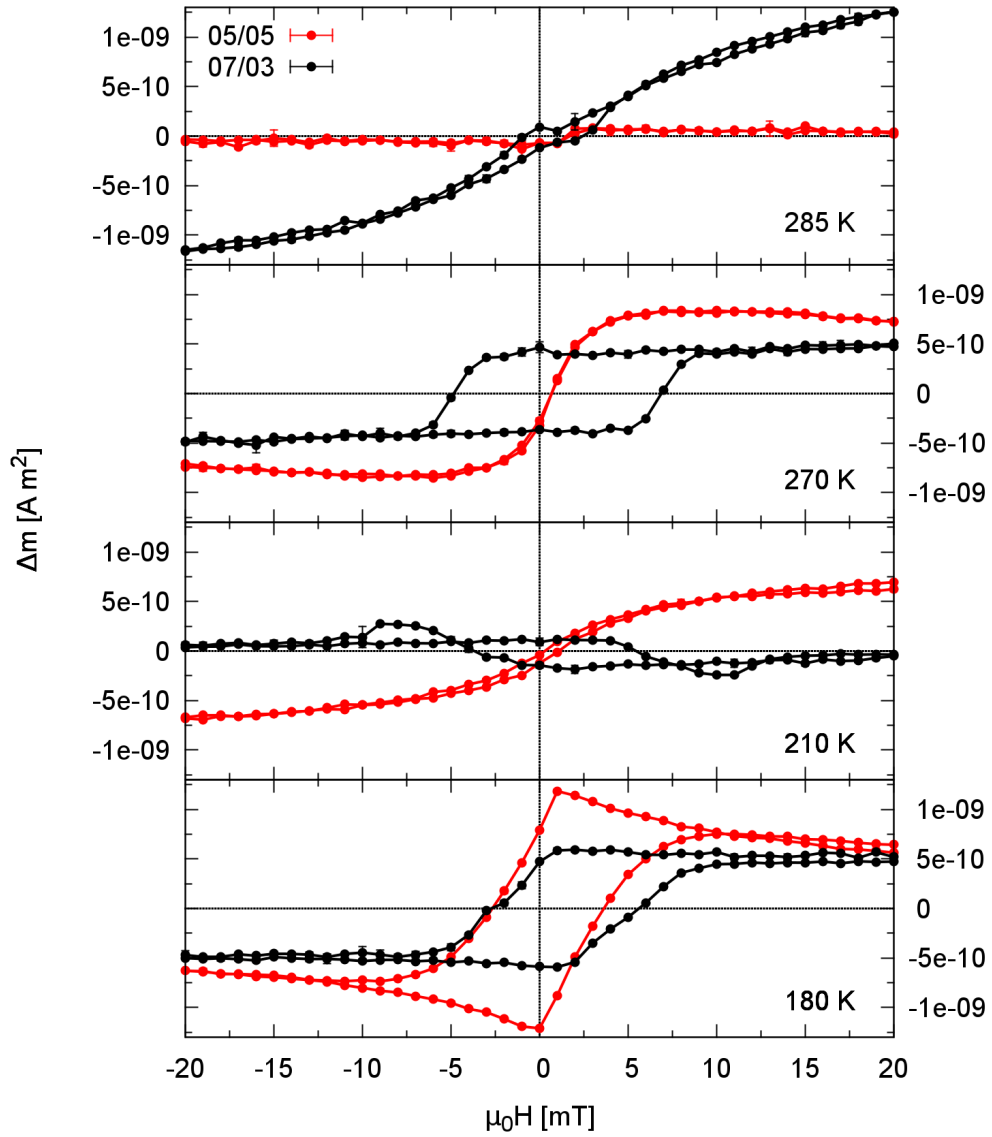


Figure 7.8: *For comparison: MEC measurements of  $\text{La}_{0.7}\text{Sr}_{0.3}\text{MnO}_3$  and  $\text{La}_{0.53}\text{Sr}_{0.47}\text{MnO}_3$  with respect to the external magnetic field for various temperatures.*

### 7.2.5 Hysteresis Loops with Applied Electric Fields

Magnetic hysteresis loops with applied electric fields of  $E = \pm 4 \text{ kV/cm}$  and  $E = 0 \text{ kV/cm}$  are performed using the MPMS. Measurements of the magnetization are done at the same temperatures as before. The electric field is switched at the measurement temperatures which are reached in saturation (1 T). Data are taken in a magnetic field range of -60 mT to 60 mT, while saturating to  $\mu_0 H = \pm 1 \text{ T}$  in between.

Fig. 7.9 shows the hysteresis loops taken at 285 K. Typical ferromagnetic hysteresis loops are observed. A slightly increased magnetization for magnetic fields  $\mu_0 H > 5 \text{ mT}$  can be observed for positive applied electric fields. This corresponds to the electrical hysteresis loops measured before (see Fig. 7.5), in which the positive electric field leads to an increase of the magnetization. Additionally, a small decrease of the coercivity field about  $\mu_0 H_c = 0.3 \text{ mT}$  is found for positive applied electric fields, as can be seen in Fig. 7.9 b).

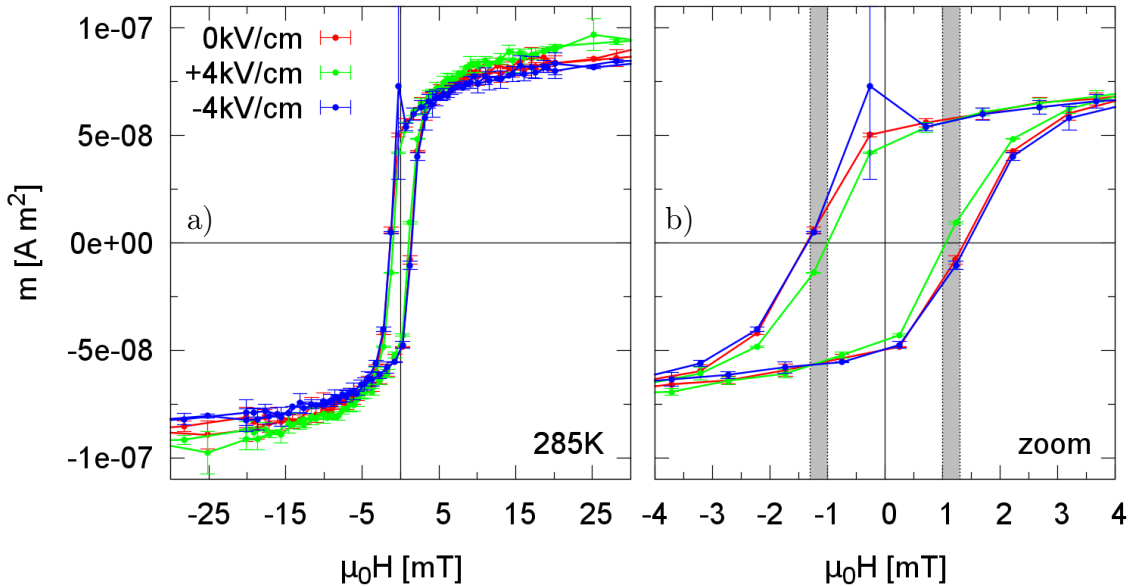


Figure 7.9: *Hysteresis loops of  $\text{La}_{0.7}\text{Sr}_{0.3}\text{MnO}_3$  on  $\text{BaTiO}_3$  for different applied electric fields at 285 K. The magnetization slightly increases with positive applied electric field and  $\mu_0 H > 5 \text{ mT}$ . For a better visibility b) shows the hysteresis plotted in a smaller scale. The gray boxes indicate the modification of the coercivity field.*

The magnetic field dependent magnetization within the orthorhombic phase of the substrate is shown in Fig. 7.10. The shape of the magnetization curve as function of magnetic field at 270 K and 210 K differ, pointing to a change of the anisotropy within this phase. The coercivity field is almost doubled for 210 K in comparison to the hysteresis loop at 270 K. The application of a positive electric field leads to a shift of the coercivity field of 43.3% at 210 K. The coercivity fields and the remanent magnetizations can be found in Tab. 7.3. In comparison to the  $\Delta m_{T,EAC}(H)$  measurement (see Fig. 7.7), one can see that

the coercivity field at 210 K lies close to where a crossing in the MEC measurement of the forth and back direction is observed. Further correlations cannot be found. Especially at 270 K, no correlation can be found for distinguished features in the MEC measurement and the coercivity field or saturation field of the hysteresis loops.

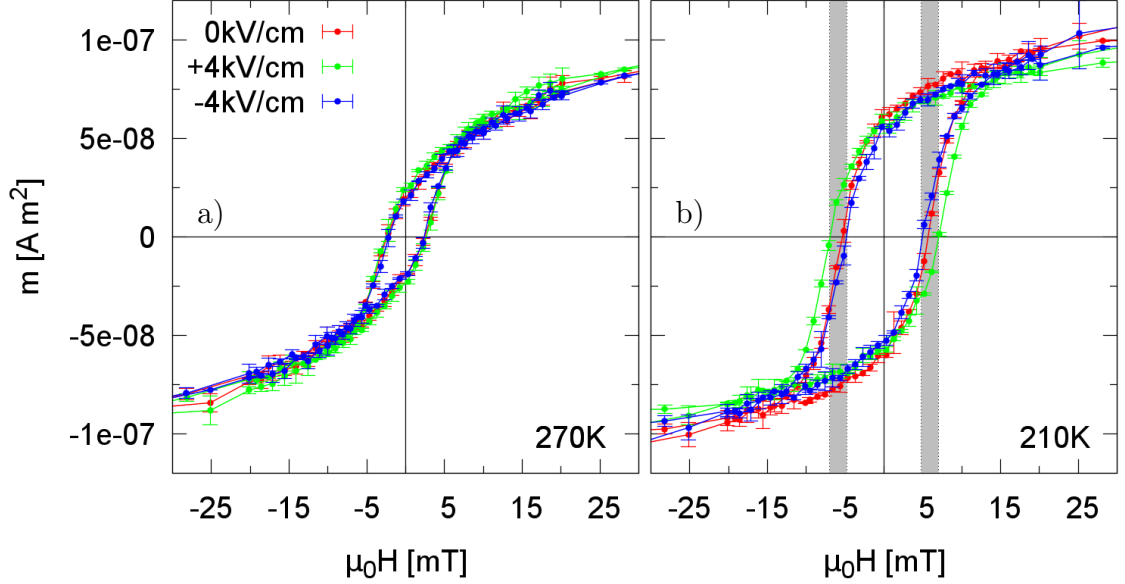


Figure 7.10: *Magnetic field dependent magnetization for different applied electric fields at a) 270 K and b) 210 K. At 210 K the shift of the coercivity field is indicated by the gray boxes.*

E [kV/cm]	Temp [K]	$m_r \cdot 10^{-8}$ [A m <sup>2</sup> ]	$\mu_0 H_C$ [mT]	$\mu_0 \Delta H_C$ [%]	$m_r/m_s$
0	270	$2.03 \pm 0.42$	$2.40 \pm 0.15$	-	0.22
-4	270	$1.89 \pm 0.29$	$2.40 \pm 0.15$	0	0.21
+4	270	$2.49 \pm 0.17$	$2.64 \pm 0.15$	10	0.27
0	210	$6.17 \pm 0.34$	$5.53 \pm 0.15$	-	0.67
-4	210	$5.48 \pm 0.45$	$4.87 \pm 0.15$	11.9	0.60
+4	210	$5.75 \pm 0.37$	$6.98 \pm 0.15$	26.2	0.63

Table 7.3: *Coercivity field and the remanent magnetization at 270 K and 210 K, both within the orthorhombic phase of the BaTiO<sub>3</sub> substrate. Additionally the squareness and the deviation of  $\mu_0 \Delta H_C$  from the neutral state without applied electric field is given.*

Fig.7.11 shows the hysteresis loops at 180 K, in the rhombohedral phase of the substrate. A typical ferromagnetic behavior is observed. No modification of the magnetization with respect to the application of an electric field was found. The coercivity field and the remanent magnetization are 6.1 mT and  $(1.56 \pm 0.02) \cdot 10^{-7}$  A m<sup>2</sup>, respectively.

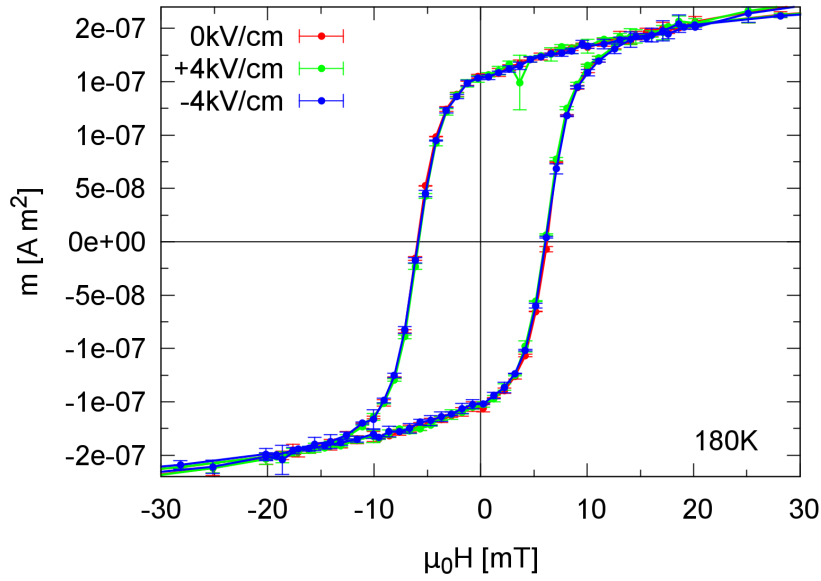


Figure 7.11: *Hysteresis loops performed at 180 K for different applied electric fields. No change in the magnetic behavior is found for the different electric fields at this temperature.*

In summary, the shape and the coercivity fields of the hysteresis loops for each structural phase of the  $\text{BaTiO}_3$  substrate differ, suggesting a change of the anisotropy for the different phases, but also within the orthorhombic phase. A shift of the coercivity fields, with respect to the applied electric field can be observed in the tetragonal and the orthorhombic phase of the substrate. No modification of the hysteresis loops with respect to the applied electric field was found at 180 K, within the rhombohedral phase of the substrate.

## 7.3 Analysis of the Magnetic Depth Profile

The analysis of the magnetization profile of the  $\text{La}_{0.7}\text{Sr}_{0.3}\text{MnO}_3$  film is done at the TOF polarized neutron reflectometer MR at the SNS (see Chapter 4.10.2). Measurements are performed at 285 K and 210 K with applied electric fields of maximum  $E = \pm 4$  kV/cm. The sample was cooled down to the desired temperature within a magnetic field of 1 T. The electric field was set at room temperature and a magnetic field of 10 mT was applied during the measurement. In order to cover the required  $Q_z$ -range, data are taken at incident angles of  $0.35^\circ$ ,  $0.55^\circ$  and  $1.028^\circ$ . The first angle has been measured by a wavelength band of  $\Delta\lambda = 2.74$  Å around 6.1 Å and 4.1 Å, higher angles with 4.1 Å. The data reduction is performed as described in Chapter 4.10.2.

Fig. 7.12 shows the results of the PNR analysis at 285 K with applied electric fields of  $E = +4$  kV/cm and  $E = -4$  kV/cm. Both measurements indicate a present magnetization, due to the difference of the  $R_{++}$  and  $R_{--}$  channels, as expected. A difference in the PNR data with respect to the applied voltage is visible in d). In order to simulate the intensities of the measurement performed with an electric field of  $E = -4$  kV/cm a fixed NSLD of  $3.74 \cdot 10^{-6}$  Å<sup>2</sup> was used for the  $+381_{-4}^{+5}$  Å thick  $\text{La}_{0.7}\text{Sr}_{0.3}\text{MnO}_3$  layer. The magnetization profile is described, by slicing this LSMO layer into three purely magnetic layers. Each of those magnetic layers is described by the magnetic moment per Mn, the magnetic roughness and thickness. The best agreement of the fit with the data is achieved by the SLD profile shown in c). An enlarged magnetization of  $\sim 1.5_{-0.2}^{+0.2}$   $\mu_B/\text{Mn}$  in the first  $\sim 130$  Å of the LSMO layer has to be taken into account. For a higher film thickness the magnetization drops to  $\sim 0.2_{-0.1}^{+0.1}$   $\mu_B/\text{Mn}$ . In the case of a positive electric field, a decreased density at the surface of the LSMO film has to be taken into account. Additionally, the magnetization is slightly different for the first  $\sim 130$  Å of the LSMO layer. In order to justify model 0, which is used for  $E = +4$  kV/cm, several models are compared. The best possible fit achieved for each model is shown in Fig. 7.13, starting with model 0, where the nuclear and magnetic structure is fitted. The reduction of the NSLD at the surface of the sample can also be caused by a reduction of the local oxygen content. For perovskite oxides in general, also for LSMO, it is well known that the application of an electric field lead to the migration of oxygen vacancies [118–120]. Thus, model 02 uses the approach of an oxygen deficient  $\text{La}_{0.7}\text{Sr}_{0.3}\text{MnO}_{3-\delta}$  toplayer with  $\delta = 0.36_{-0.1}^{+0.1}$ . In addition, also the magnetic structure is fitted. The comparison with the data shows that also this fits to the data with slightly worse FOM. In model A, the nuclear structure is fitted while the magnetic structure is kept as for the fit at  $E = -4$  kV/cm (see Fig. 7.12 d)). Also this model fits to the data. For model B, the nuclear structure is kept fixed according to the fit at  $E = -4$  kV/cm while the magnetic structure is fitted. Here, the model does not describe the data properly. The fit using Model C, which assumes a homogeneous magnetization of the LSMO layer, does not fit at all. In Model D, a magnetization of 0.2  $\mu_B/\text{Ti}$  in the  $\text{BaTiO}_3$  is assumed at the interface. The fit is still in a good agreement with the data. Nevertheless, if the magnetization of the  $\text{BaTiO}_3$  is used as a free fit parameter it converges to zero. The models are summarized in Tab 7.4. In total, the reduction of the NSLD at the surface seems to be responsible for the difference of the PNR data at  $E = \pm 4$  kV/cm, while the influence of the difference in the magnetic structure is weak.

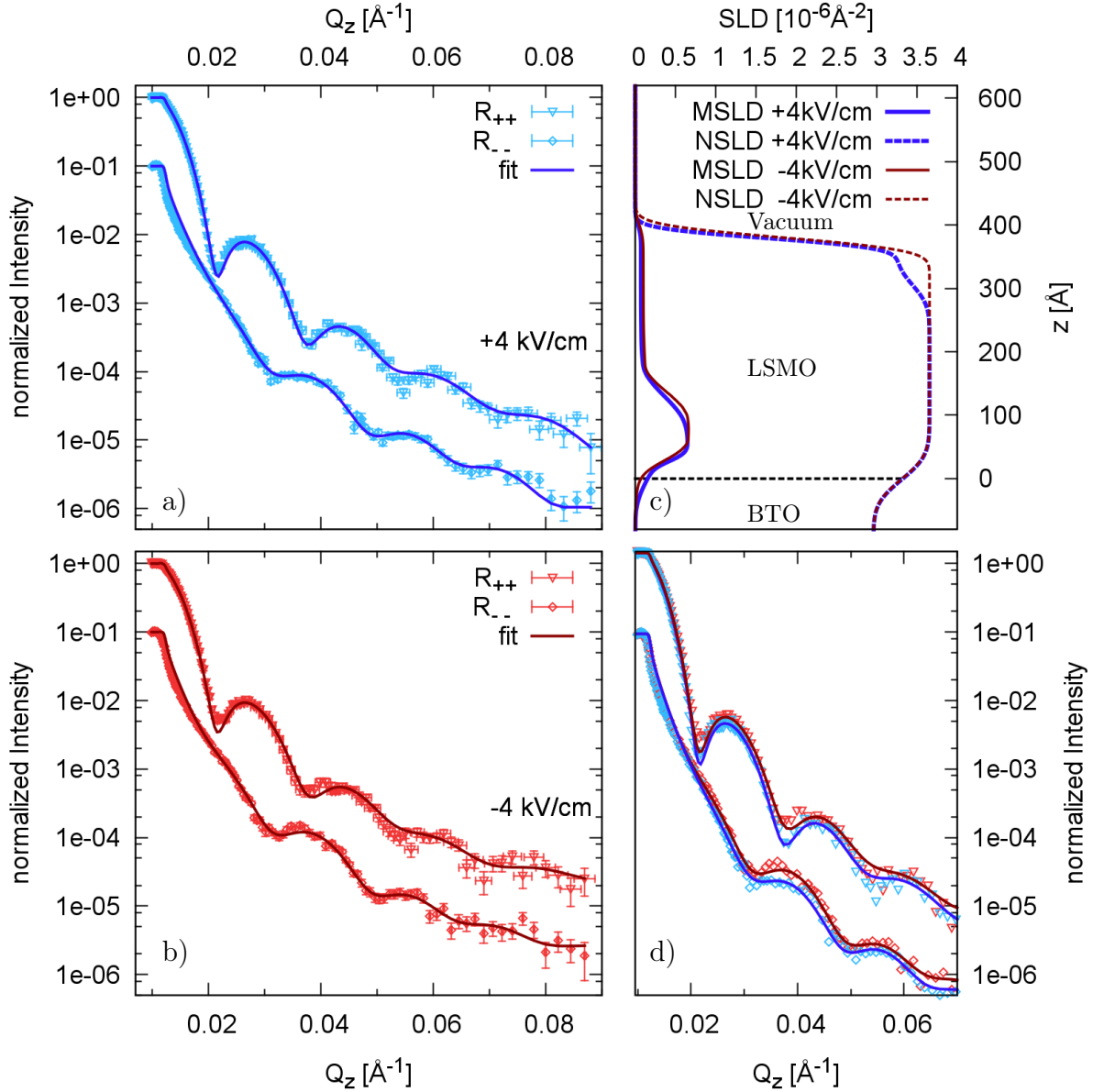


Figure 7.12: Polarized neutron reflectivity data of the  $\text{La}_{0.7}\text{Sr}_{0.3}\text{MnO}_3/\text{BaTiO}_3$  sample at 285 K. The  $R_{--}$  reflectivity is divided by 10 for a better visibility. The reflectivities for electric fields of  $E = \pm 4$  kV/cm including the fit of the data are shown in a) and b), respectively. d) shows both data sets to visualize the difference in the reflectivity with respect to the applied electric field. The SLD profiles obtained by the fits are depicted in c).

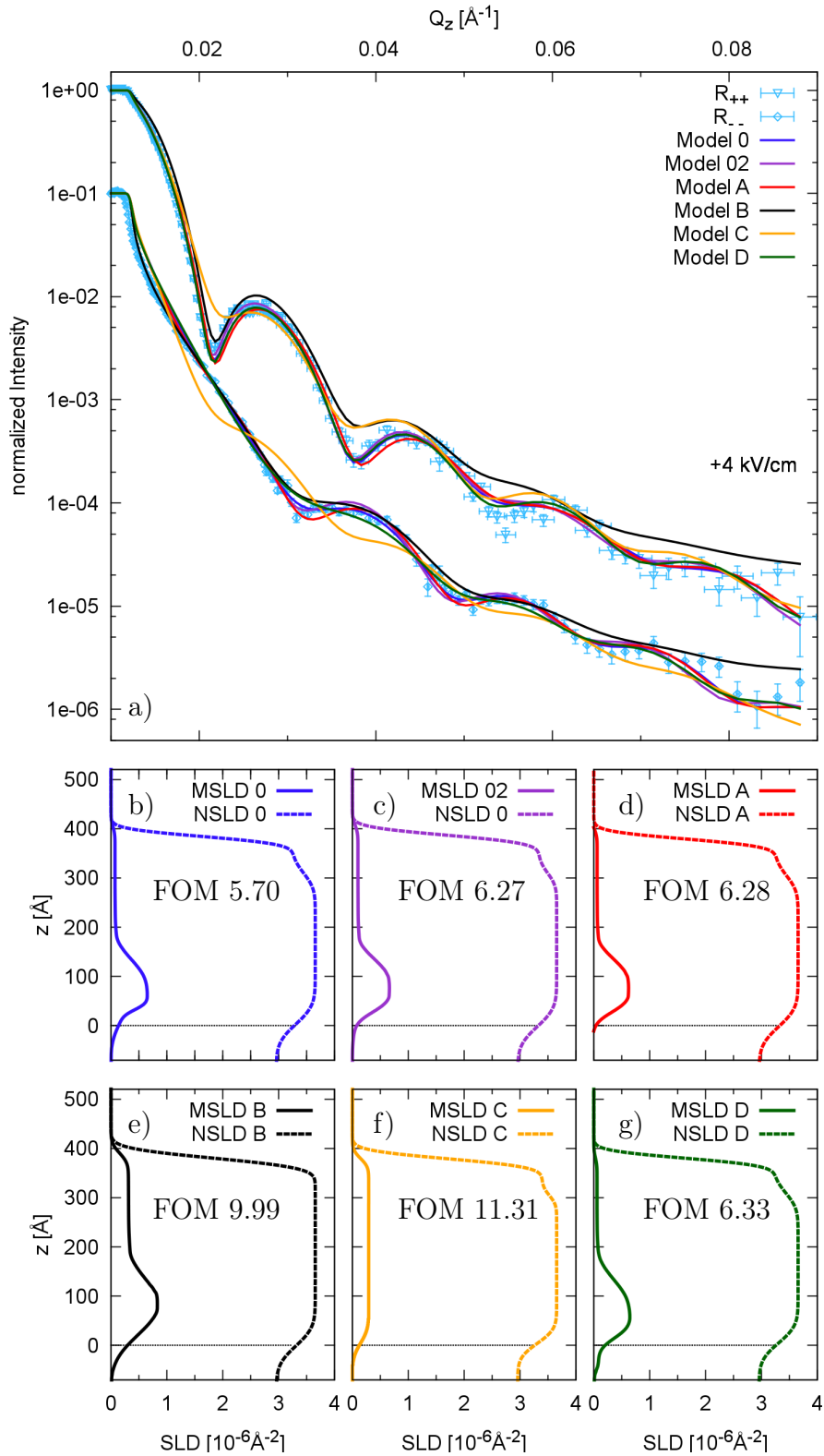


Figure 7.13: a) PNR data of  $\text{La}_{0.7}\text{Sr}_{0.3}\text{MnO}_3$  on  $\text{BaTiO}_3$  at 285 K with the simulated intensities according to different models. The SLDs of the models are presented in b)-g).

	Nuclear	Magnetic	other
Model 0	free	free	—
Model 02	free	free	oxygen deficient toplayer
Model A	free	like $E = -4$ kV/cm	—
Model B	like $E = -4$ kV/cm	free	—
Model C	free	free	homogeneous magnetization
Model D	free	free	magnetization in BaTiO <sub>3</sub>

Table 7.4: *Differences of the compared models to simulate the PNR data at  $E = +4$  kV/cm.*

Additionally, PNR measurements are performed at 210 K, within the orthorhombic phase of the substrate. The macroscopic magnetization, measured by MPMS, shows no difference for positive and negative applied fields, as presented in the section before. But for zero electric field after applying an electric field to one direction a difference of the magnetization is observed. Thus, one PNR measurement is performed at  $E = 0$  kV/cm, after polarizing the sample with an electric field of  $E = +4$  kV/cm, and one at  $E = -4$  kV/cm.

Fig. 7.14 shows the measurements and the corresponding fits of the data at  $E = 0$  kV/cm and  $E = -4$  kV/cm. The SLDs, obtained by the fit, can be seen in c). The application of the negative electric field leads to a decrease of the BaTiO<sub>3</sub> roughness as well as for the layer roughness. No reduction of the NSLD at the LSMO surface has to be taken into account. The magnetization is increased to  $\sim 2.6_{-0.3}^{+0.3} \mu_B/\text{Mn}$  at the first  $\sim 130$  Å of the LSMO layer. As expected, the magnetization of the LSMO film is higher compared to that at 285 K. The magnetization profile at the interface is a bit shifted due to the enlarged BaTiO<sub>3</sub> roughness, but no significant change of the magnetization profile can be observed.

In summary, a difference in the PNR data with respect to the applied voltage could be observed at both temperatures. The change of the intensity is mostly related to an enhanced roughness of the common interface of the BaTiO<sub>3</sub> substrate and the LSMO layer or at the surface of the sample. The different models show that a prediction of the modification of the magnetization is challenging. The shape of the magnetization profile is almost constant within the tetragonal phase and the orthorhombic phase of the substrate with a higher magnetization at 210 K. It is striking that an enhanced magnetization is located in the first  $\sim 130$  Å of the LSMO layer.

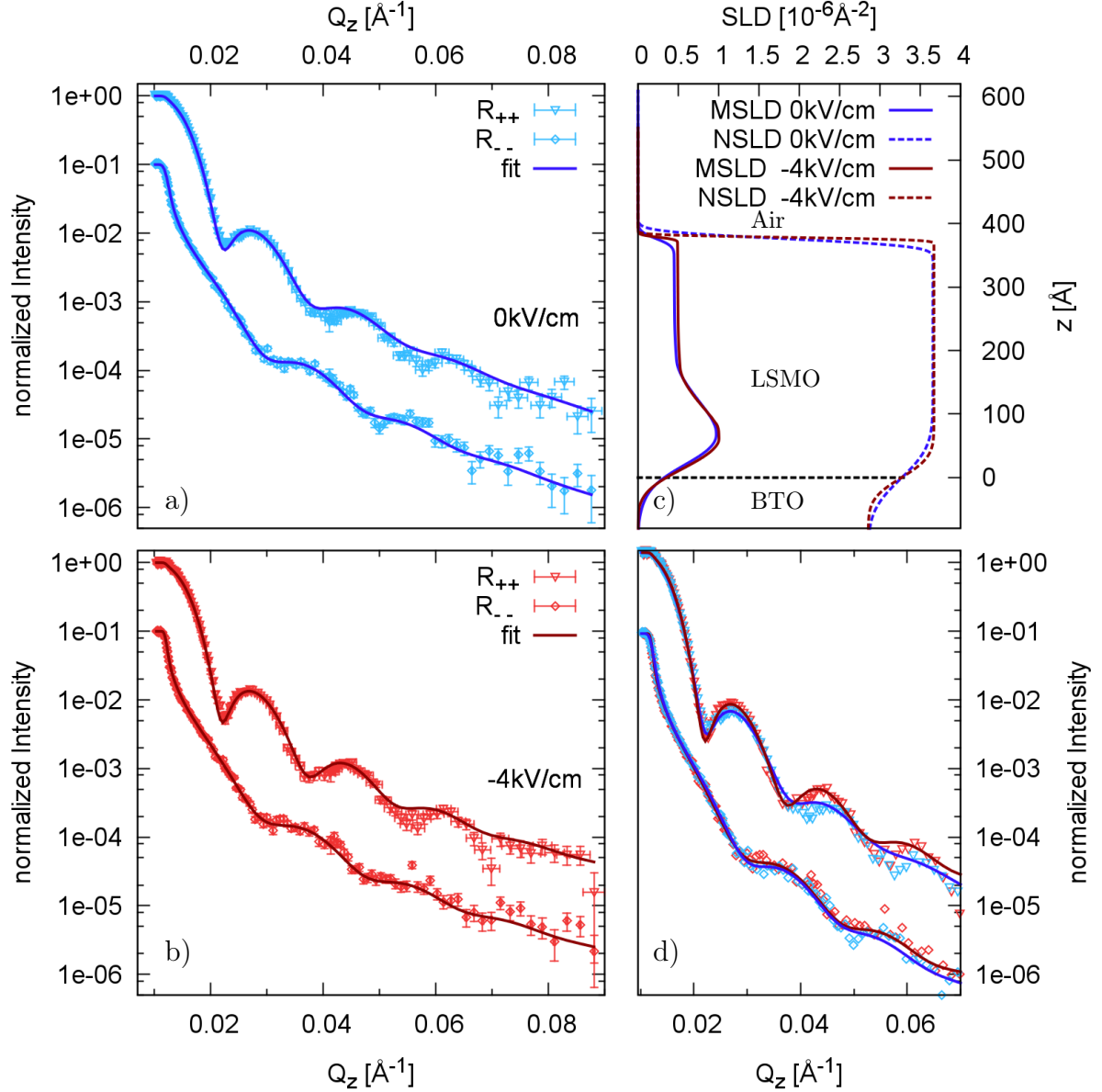


Figure 7.14: Polarized neutron reflectivity data of the  $\text{La}_{0.7}\text{Sr}_{0.3}\text{MnO}_3/\text{BaTiO}_3$  sample in the  $O_r$  phase of the substrate at 210 K. The  $R_{--}$  reflectivity is divided by 10 for a better visibility. The  $Q$ -dependent reflectivity for electric field of 0 kV/cm and -4 kV/cm and the fits are shown in a) and b). The SLD profiles obtained by the fits are depicted in c). d) shows both data sets to visualize the difference in the reflectivity with respect to the applied electric field.



# Chapter 8

## Discussion

The investigation of  $\text{La}_{(1-x)}\text{Sr}_x\text{MnO}_3$  on  $\text{BaTiO}_3$  substrates for the doping levels of  $x = 0.5$  and  $x = 0.3$  show very interesting results. Particularly, the modification of the magnetization with respect to the application of electric fields shows fascinating effects. Now, the question remains: what is the mechanism which is responsible for the observed magneto-electric coupling.

Several mechanisms are possible within the LSMO/BTO heterostructure under investigation. The reversal of the ferroelectric polarization can induce a change in the lattice strain of the ferroelectric material. In a composite of such a piezoelectric and a magneto-elastic compound, a magneto-electric coupling can be established via the elastic channel. The strain in the piezoelectric is induced into the magneto-elastic, leading to a change in the magnetic properties. The strain changes the bonding conditions e.g. bonding angle between Mn and O atoms, leading to a modification of the electron hopping probability of the Mn cations and thus changing the exchange interactions. The strain induced altering of the magnetic properties can also be forced by the structural properties itself, if the lattice parameters in the material are dependent on the temperature [121]. Another mechanism is based on a carrier-mediated effect which might occur in complex oxides. The effect is driven by the accumulation of spin-polarized carriers at the interface of a capacitor consisting of non-magnetic, nonpolar dielectric and a metal with spin polarized carriers at the Fermi level [122]. Molegraaf *et al.* demonstrate a charge-driven coupling effect in  $\text{La}_{0.8}\text{Sr}_{0.2}\text{MnO}_3$  on  $\text{PbZr}_{0.2}\text{Ti}_{0.8}\text{O}_3$  although the observed effect seems to be too large to be explained only by band-filling effects [20]. Furthermore, magneto-electric effects could be related to the bonding at the ferromagnetic/ferroelectric interface. It was predicted that the interface magnetization can be affected due to different bonding length associated with the direction of the ferroelectric polarization [123]. Such an effect was calculated for  $\text{Fe}/\text{BaTiO}_3$  giving rise to a magnetic moment in the Ti [124]. The diffusion of oxygen under the application of electric fields and thus the local variation of the oxygen content could also lead to a modification of the magnetization and to a variation of the NSLD for oxides. It is known that the oxygen content is crucial for magnetic properties in LSMO [90]. Moreover, Burton *et al.* predict a magnetic reconstruction at a ferromagnet/ferroelectric interface induced by switching the electric polarization [1]. Here, not the magnitude of the magnetization is modified but the ordering of the magnetic moments

at the interface for  $\text{La}_{1-x}\text{Sr}_x\text{MnO}_3$  near the doping level of  $x=0.5$  where a magnetic phase transition from ferromagnetic to antiferromagnetic is expected. For a better understanding, the most important properties of the samples will be shortly summarized and compared, for both stoichiometries. Furthermore, possible mechanisms which could be responsible for the observed effects will be discussed.

The temperature dependent magnetization  $m(T)$  shows sharp steps in the magnetization at the structural phase transition temperatures of the  $\text{BaTiO}_3$  substrate independently of the stoichiometry of the  $\text{La}_{(1-x)}\text{Sr}_x\text{MnO}_3$  layer. Since no other parameter apart from the temperature is varied the magnetic properties of the  $\text{La}_{(1-x)}\text{Sr}_x\text{MnO}_3$  film are modulated by the effect of strain in the different phases of the  $\text{BaTiO}_3$  substrate. Additionally, the observed steps in the magnetization follow the hysteretic temperature behavior of the structural phase transition for cooling and warming, emphasizing the relation to lattice distortions. X-ray diffraction measurements (see Fig 7.2) show that the out-of-plane lattice parameter of the LSMO film follows the temperature behavior of the out-of-plane lattice parameter of  $\text{BaTiO}_3$ . Hence, it is reasonable to assume that also the in-plane lattice strain of the film follow those of the substrate. This means, an in-plane lattice clamping of the LSMO film to the  $\text{BaTiO}_3$  substrate is present. The in-plane strain is the driving force for the lattice distortion of the LSMO and lead to the altering of the layer properties. Lee *et al.* [125] show that for a similar system e.g.  $\text{La}_{0.67}\text{Sr}_{0.33}\text{MnO}_3$ , the in-plane lattice parameter at room temperature is  $3.94 \text{ \AA}$ . In our case, this corresponds to a tensile in-plane strain of  $\epsilon = 2.3 \%$  taking the LSMO pseudocubic lattice parameter of  $3.85 \text{ \AA}$  into account. The two strain components  $\epsilon_a = \frac{1}{2}(\epsilon_{xx} + \epsilon_{yy})$  and  $\epsilon^* = \frac{1}{2}(\epsilon_{xx} - \epsilon_{yy})$  denote the in-plane area change and the in-plane distortion away from square symmetry [126]. An expansion of  $\epsilon_a = 0.21\%$  and a distortion by  $\epsilon^* = 0.26\%$  at the Tet  $\mapsto$  Or phase transition is estimated for  $\text{BaTiO}_3$ . The transition from Or  $\mapsto$  Rh is accompanied by an expansion of the area by  $\epsilon_a = 0.10\%$  and distortion of  $\epsilon^* = -0.43\%$ . Hence, tensile in-plane strain is present in the whole temperature range for  $T < 395 \text{ K}$  and the distortion from the square symmetry is increased in the Or phase. The in-plane lattice distortions of (001)  $\text{BaTiO}_3$  are schematically depicted in Fig. 8.1. A similar behavior for the LSMO layer is assumed due to lattice clamping. In-plane shears attributed to the orthorhombic and rhombohedral phases are neglected in this consideration.

The strain in each phase of the substrate, induced to the layer, influences the electronic configuration of the LSMO. The resulting orbital ordering gives rise to the magnetic anisotropy. Furthermore, bonding length and bonding angles of Mn-O-Mn are altered by the strain. Thus a complex magnetic ground state is defined by the DE or SE interaction. Previous studies show the sensitivity of the magnetic properties of  $\text{La}_{(1-x)}\text{Sr}_x\text{MnO}_3$  to strain, resulting in a magnetic phase diagram as function of the doping level  $x$  and the in-plane lattice strain [34, 114]. It shows that a present tensile strain leads to A-type antiferromagnetic properties of  $\text{La}_{1-x}\text{Sr}_x\text{MnO}_3$  with  $d_{x^2-y^2}$  orbital ordering as depicted in Fig. 2.4 [34, 35, 127].

We associate the observed steps in the magnetization  $m(T)$  with the change of the magnetic anisotropy due to the strain induced change of the local environment of the

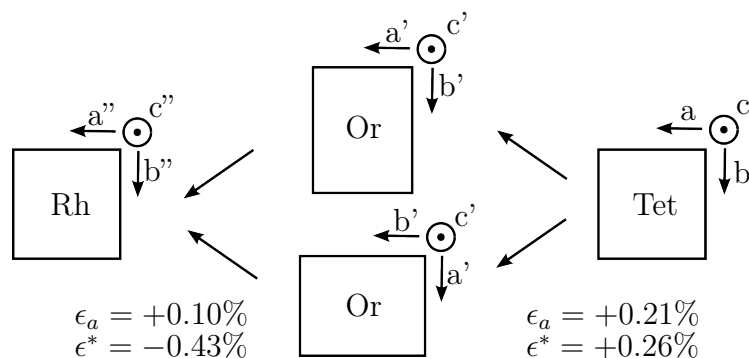


Figure 8.1: Schematically temperature dependent in-plane lattice distortion of (001)  $\text{BaTiO}_3$ . It is assumed that the  $\text{La}_{(1-x)}\text{Sr}_x\text{MnO}_3$  in-plane lattice parameter are clamped to the  $\text{BaTiO}_3$  substrate [125].  $\epsilon_a$  and  $\epsilon^*$  denote the in-plane area change and the in-plane distortion away from square symmetry.

Mn atoms. It was shown that LSMO films on cubic substrates show biaxial magnetic anisotropy while LSMO has uniaxial anisotropy on orthorhombic substrates [128]. Different type of substrate symmetries are present here due to the structural phases of the  $\text{BaTiO}_3$  substrate. The change of the magnetic anisotropy is directly observable in the magnetic hysteresis loops at different temperatures. For both doping levels of LSMO the shape of the  $m(H)$  curve changes for the different phases of the substrate, but also within the Or phase. The squareness ( $m_r/m_s$ ) of the hysteresis loops were evaluated from the measurements presented in Chapter 6 and 7. The resulting squarenesses are shown in Fig. 8.2 as a measure of the anisotropy. It clearly indicates the change of the magnetic anisotropy of the LSMO layer for each phase of the  $\text{BaTiO}_3$  substrate. The squareness is high in the Rh phase and decreases within the Or for increasing temperatures. The squareness again increases next to the Or  $\mapsto$  Tet phase transition.

Additionally, the influence of the strain induced change of structural parameter (bond length and bonding angles) on the exchange interaction can be seen in the evolution of the magnetization steps in  $m(T)$  with respect to the external magnetic field (see inset of Fig. 6.8). The steps in the magnetization decrease with increasing magnetic field but do not vanish in a saturation field as expected if those were purely related to the change of the anisotropy. Hence, the lattice distortions alter the exchange interaction, e.g. DE and SE of the  $\text{La}_{(1-x)}\text{Sr}_x\text{MnO}_3$  layer, which influence is independent of the external magnetic field.

Nevertheless, we have to keep in mind that the  $\text{BaTiO}_3$  is not in a single domain state, as XRD measurements show (see Fig. 6.4). Structural domains are present in (001)  $\text{BaTiO}_3$  e.g. a-type domains with elongated direction of the unit cell parallel to the interface in the tetragonal phase. Structural domains are present in each phase. In particular, those domains are responsible for the non-reproducible measurement of  $m(T)$  while warming at the Rh  $\mapsto$  Or phase transition, since these structural domains are not necessarily formed equally in every repetition and thus they induce different strain into the LSMO layer. In

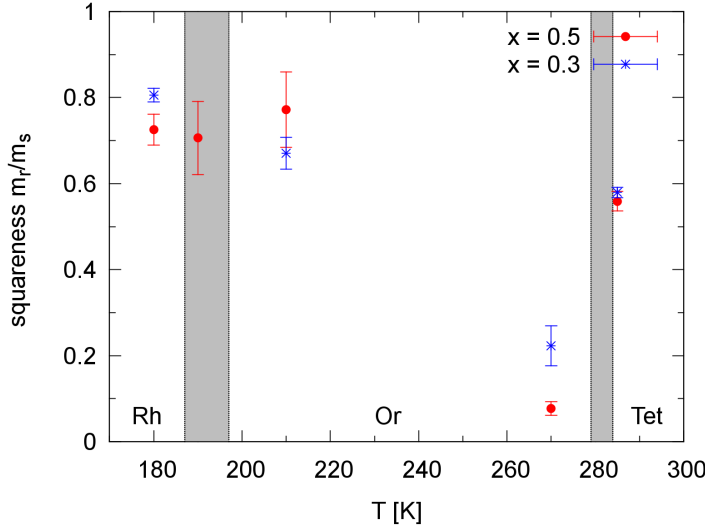


Figure 8.2: Squareness of the hysteresis loops as measure of the anisotropy for  $\text{La}_{0.5}\text{Sr}_{0.5}\text{MnO}_3$  and  $\text{La}_{0.7}\text{Sr}_{0.3}\text{MnO}_3$  depicted in red and blue, respectively. The gray boxes illustrate the region of the phase transitions of the substrate.

the Or phase, two twinning states are present in  $\text{BaTiO}_3$  [129]. In order to get a full picture of the strain induced into the LSMO layer, X-ray diffraction measurements to probe all lattice parameters in each  $\text{BaTiO}_3$  phases are necessary. Additionally angle-dependent magnetization measurements to probe the anisotropy of the LSMO/BTO system in each phase of substrate would clarify the change of the anisotropy as well as measurements of the out-of-plane direction. Vaz *et al.* [130] observed similar steps in the magnetization of  $\text{Fe}_3\text{O}_4/\text{BaTiO}_3(100)$  which show opposite jumps in the magnetization for the in-plane and out-of-plane direction.

So far the structural properties in the sense of strain and the influence thereof on the magnetism were discussed. Even more fascinating is the possibility to tune the magnetization by the application of electric fields. Measurements of the temperature dependent change of the magnetization  $\Delta m_{H,E_{AC}}(T)$  performed by the new MEC option show quite similar behavior for both doping levels of  $\text{La}_{(1-x)}\text{Sr}_x\text{MnO}_3$ . The possibility to alter the magnetization by electric fields is pronounced in proximity to the structural phase transition temperatures of the  $\text{BaTiO}_3$  substrate. It follows the behavior of the temperature dependent piezoelectric coefficient ( $d_{33}$ ) [131] of  $\text{BaTiO}_3$  as shown in Fig. 8.3 a). Thus, certainly the change of the magnetization is related to the strain induced to the LSMO layer by application of the AC electric field. As the piezoelectric coefficient quantifies the volume change of a piezoelectric material under the application of an electric field and the fact that it scales with the change of the magnetization of the LSMO layer, we address it as strain induced. Additionally, the domain mobility is increased near the phase transitions of  $\text{BaTiO}_3$  due to multiple domain orientations. Nevertheless, a charge carrier-mediated magneto-electric effect could also explain the observed effects. The change of the magnetization should be proportional to the charge carrier concentration at the in-

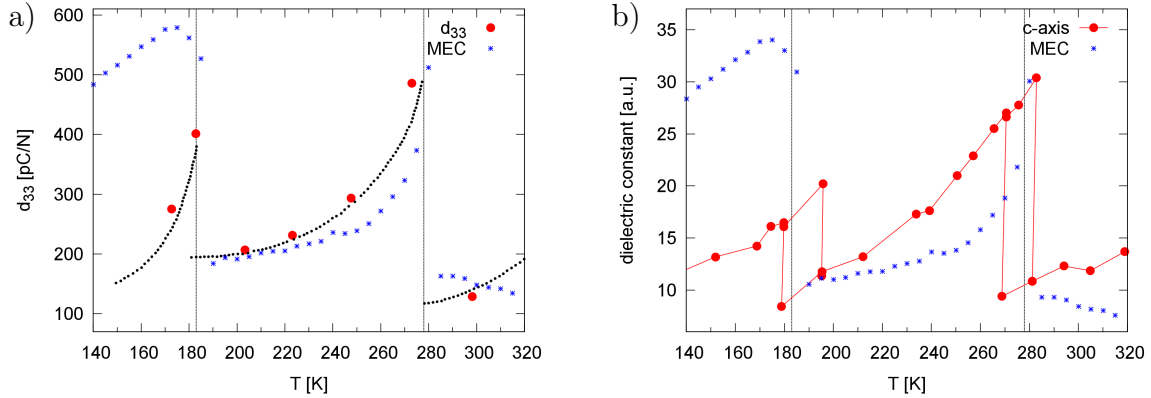


Figure 8.3: a) Piezoelectric coefficient  $d_{33}$  for (001)-oriented  $\text{BaTiO}_3$  as function of temperature adapted from [131]. Dashed line indicate calculated values for single-domain  $\text{BaTiO}_3$  crystals. b) Dielectric constant as function of temperature adapted from [132]. Vertical lines indicate phase transition temperatures of  $\text{BaTiO}_3$ . For comparison a scaled  $\Delta m$  measurement is shown.

interface. The LSMO/BTO heterostructure can be described as plate capacitor. Thus the carrier concentration is linear proportional to the dielectric constant  $\epsilon_r$  of the  $\text{BaTiO}_3$  under otherwise constant parameters. The initial dielectric constant of  $\text{BaTiO}_3$  is depicted in Fig. 8.3 b) [132]. The temperature dependent dielectric constant follows a similar behavior as the observed change of the magnetization  $\Delta m_{H,EAC}(T)$ . Thus, also the carrier concentration scales with the observed effect which suggests a charge carrier-mediated MEC. The effect could be easily proofed by using a non ferroelectric substrate where the effect of electrically induced strain could be eliminated.

The negative signal for  $\text{La}_{0.7}\text{Sr}_{0.3}\text{MnO}_3$  (Fig. 7.4) in the orthorhombic phase of the substrate is related to the change of the direction in which the magnetization is modified, as shown by the electric hysteresis measurements  $m_{H,T}(E)$ . The change of the direction can be explained by the existing of two twinning states in the Or phase of the  $\text{BaTiO}_3$  substrate [129]. The proportion of the states depends on the history of the sample and their orientation.

The electrical hysteresis loops  $m_{H,T}(E)$  show the influence of the electric field on the magnetization in detail. The observed change of the magnetization nicely corresponds to the  $\Delta m_{H,EAC}(T)$  measurements. The electric field dependent magnetization behaves different in each temperature region which is related to the structural phases of the substrate. Not just the structure of the substrate lattice is different, but also the ferroelectric polarization is pointing in a different direction. In the tetragonal phase the polarization points in [001] direction, while in the orthorhombic and the rhombohedral phase in [011] and [111] direction, respectively. Thus, the effect of the applied electric field on the ferroelectric polarization like the electric coercivity field of the  $\text{BaTiO}_3$  is different for each phase [133]. Also the electric field mediated strain in the  $\text{BaTiO}_3$  depends on the structural phase as

shown in Ref. [131].

In the Tet phase of the substrate no change of the magnetization is observed for the  $\text{La}_{0.5}\text{Sr}_{0.5}\text{MnO}_3$  (Fig. 6.11). The substrate is in a single domain state due to the applied electric field, but the field is not sufficient to alter the lattice parameter in a noticeable magnitude, following Ref. [134]. Also no other magneto-electric effect is present. Surprisingly, a change in the magnetization with respect to the electric field is observed for  $\text{La}_{0.7}\text{Sr}_{0.3}\text{MnO}_3$  (Fig. 7.5). It is unlikely that in this stoichiometry the magnetization is more sensitive to the strain since it is close to the maximum of the "FM dome" (Fig. 2.3). More likely is an asymmetric response of the  $\text{BaTiO}_3$  substrate to the electric field which is not sufficient to tune the ferroelectric polarization by  $180^\circ$  leading to an enhanced strain into the LSMO.

In the Or and Rh phase of the substrate an asymmetric behavior of the magnetization with respect to the electric field is observed (see Fig. 6.11 and 7.5). It suggests that the direction of the ferroelectric polarization is crucial for the mechanism of the magneto-electric coupling. Thus, purely electrically driven magneto-electric effects have to be discussed since those depend on the polarization direction of the ferroelectric. A possible explanation could be the predicted effect by Burton *et al.* [1], since it depends on the orientation of the electrical polarization. However that contradicted by the fact that a magneto-electric coupling is also observed for the  $\text{La}_{1-x}\text{Sr}_x\text{MnO}_3$  doping level of  $x=0.3$ , which is far away from any magnetic transition. Thus, it is unlikely to explain the observed effects. Especially, this could not be observed by PNR measurements. Also the carrier-mediated magneto-electric effect is unlikely, since a symmetrical altering of the magnetization is expected with respect to the applied electric field. Both directions of the electric field lead to a modification of the carrier concentration (accumulation or reduction) resulting in a variation of the exchange interaction. Furthermore, a purely electrically driven effect would be expected to be maximum in the Tet phase, since there, the spontaneous electrical polarization is biggest. Thus a charge driven effect is also unlikely for the Or and Rh phases of the substrate because almost no effect is observed in the Tet phase. The most likely explanation for the asymmetric response to the electric field can be understood by the polarization direction of the ferroelectric within the corresponding phase. The polarization axis orients in one of the twelve  $[110]$  directions in the Or phase. Neighboring ferroelectric domains are arranged with an angle of  $60^\circ$ ,  $90^\circ$ ,  $120^\circ$  and  $180^\circ$  (see. Fig.8.4). For the Rh phase, the polarization point in one of the eight  $[111]$  direction with adjacent oriented domains of  $71^\circ$ ,  $109^\circ$  and  $180^\circ$ . This can lead to an asymmetric response of the the  $\text{BaTiO}_3$  to the applied electric field. Additionally, the domain structure depends on the history of the sample and can change from substrate to substrate, even if those substrates are of the same orientation. This effect can even explain that in one sample the magnetization is altered for positive applied electric fields and in the other for negative fields. In total, this considerations underline the suggestion of a magneto-electric coupling effect via the elastic channel.

Furthermore, with the asymmetric response of the substrate to the electric field the observed effects in the magnetic field dependent magnetization  $m(H)$  can be explained. The

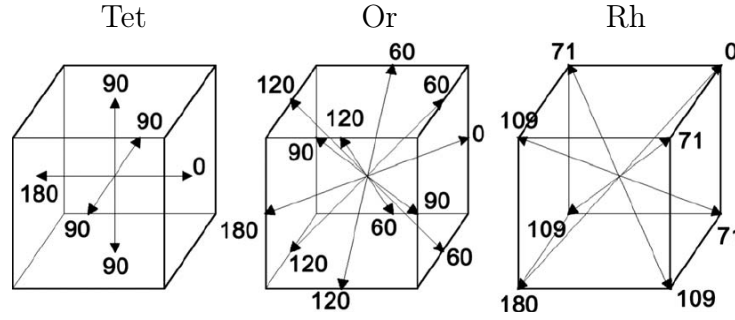


Figure 8.4: *Spontaneous polarization directions in the ferroelectric phases of  $\text{BaTiO}_3$ , taken from [135]. The angles between symmetry equivalent directions and direction "0" are given.*

magnetic hysteresis loops were already discussed regarding the change of anisotropy for the three different structural phases of the substrate. Now, the influence of the applied electric field on the hysteresis loops will be discussed. Most noticeable is the shift of the coercivity field with respect to the applied electric field, especially in the Or and Rh phase of the substrate. These shifts can be explained by the reorientation of ferroelectric domains in the substrate which are accompanied by a change in the lattice structure. This alters the magnetic ordering. Thus, the anisotropy is not just changed by temperature as discussed before, but also by the electric field. The shift of the coercivity field is observed just in one direction of the electric field. As mentioned before the complex ferroelectric domain structure and their response to the applied electric field is probably asymmetric. Similar asymmetric behavior was observed in  $\text{Fe}/\text{BaTiO}_3$  [115, 116]. Since, the ferroelectric domain structure is very important for the observed effects, it has to be analyzed. Polarized light microscopy could be used as quite simple technique to visualize the ferroelectric domains. Furthermore, a way to create a reproducible domain state in the  $\text{BaTiO}_3$  has to be found. This would simplify an interpretation and the comparison between several samples, especially since it is of interest to compare effects in magnetic layers of different stoichiometries.

The magnetic field dependency of the possibility to manipulate the magnetization was investigated by MEC measurements (see Fig. 6.13 and Fig. 7.7). The different lattice structure and electric polarization direction in each phase of the substrate leads to different behavior of  $\Delta m_{T,E_{AC}}(H)$  in those phases. The change in  $\Delta m_{T,E_{AC}}(H)$  is not zero for magnetic saturation fields, but converges to a constant value. This suggests that not just a change of the anisotropy is the driving force for the altering of the magnetization. It could be related to the modification of the exchange interaction, oxygen diffusion or carrier-concentration at the interface. The increased  $\Delta m_{H,E_{AC}}(T)$  for higher fields in most measurements can be explained by the rotation of magnetic domains into the measurement direction. Thus, more and more magnetic domains, like out-of-plane components, contribute to the measured  $\Delta m_{T,E_{AC}}(H)$ . The hysteretic shape of the  $\Delta m_{T,E_{AC}}(H)$  curve indicates a stabilization of those domains. An inverse magneto-electric effect is also possible to be responsible for the shape of the  $\Delta m_{T,E_{AC}}(H)$  curve, where the magnetic field

stabilizes the ferroelectric domains via the elastic channel. Surprisingly, zero crossing points or maxima in the  $\Delta m_{T,E_{AC}}(H)$  curves do not correspond to the magnetic coercivity fields obtained by the magnetic hysteresis loops. One could expect such a coincidence since the mobility of magnetic domains is highest at the magnetic coercivity field. On the other hand, it shows that the application of the electric field is not directly coupled to the magnetic domains, but to a different cross-coupling mechanism. The different behavior for the two stoichiometries under investigation might be related to the different doping level of  $\text{La}_{(1-x)}\text{Sr}_x\text{MnO}_3$  which might act differently due to the present coupling mechanisms. But as mentioned before, the ferroelectric domain state and the respond to the electric field might be different for different  $\text{BaTiO}_3$  substrates. Hence, its not possible to distinguish between the influence of the substrate and the stoichiometry. Again, further investigations of the substrates are required.

The analysis of the magnetic profile was performed to clarify a possible limitation of the magnetic effects to the interface. A difference in the polarized reflectivity was observed for  $\text{La}_{0.5}\text{Sr}_{0.5}\text{MnO}_3$  on  $\text{BaTiO}_3$  at room temperature in the Tet phase of the substrate. Unfortunately, the measurement at positive electric field had to be remeasured at the end of the beamtime, since the electric contact at the sample was broken in the first measurement. Thus, it is challenging to conclude which mechanism could be responsible for the observed difference in the reflectivity. The sample was in the cryostat under vacuum conditions for several days which could lead to increased oxygen vacancies within the LSMO layer and in the  $\text{BaTiO}_3$  substrate. Additionally, the domain structure of the substrate could be completely different since it went through several phase transitions in between the measurements. We have to assume that it is in a single domain state due to the applied electric field. Aging effects due to several electric switching processes lead to a drastic variation of the properties of  $\text{BaTiO}_3$  even for single crystals as shown by Ren *et al.* [136]. Furthermore, no change in the magnetization is expected regarding the magnetization measurement performed by MPMS. Hence, a discussion of the observed change in the intensity with respect to the applied electric field for this measurement cannot be done.

The reflectivity for the measurements performed in the Or and Rh phase of the substrate is the same for the different electric field directions. The MSLD profiles show a reduced magnetization at the LSMO/BTO interface for the sample produced by the OMBE. This reduction of the magnetization at the interface can be explained by strain. Regarding the strain vs. magnetization phase diagram in Chapter 2.2, tensile strain leads to an antiferromagnetic ground state in  $\text{La}_{0.5}\text{Sr}_{0.5}\text{MnO}_3$  [34, 35]. In contrast, no reduction of the interface magnetization is observed in the case of the sample produced by the HOPSS. Most probably, here, the influence of strain is much less for sputtered samples. The sputtering process is much faster compared to the growth by the OMBE system, leading to a different influence of strain induced into LSMO layer. The MSLD is dropping for increasing film thickness suggesting oxygen vacancies. Those vacancies might already occur during the growth process and can be different for the two preparation techniques.

The reduced magnetization for higher film thicknesses is even more pronounced for the  $\text{La}_{(1-x)}\text{Sr}_x\text{MnO}_3$  film with doping level of  $x=0.3$  produced by the HOPSS (see Fig. 7.12).

---

The MSLD profile shows an enhanced magnetization for the first  $\sim 130$  Å which drastically drops from  $\sim 1.5_{-0.2}^{+0.2} \mu_B/\text{Mn}$  to  $\sim 0.2_{-0.1}^{+0.1} \mu_B/\text{Mn}$  at 285 K. A similar drop of the magnetization was found at 210 K. The observed difference in the polarized neutron reflectivity for different directions of the applied electric field at 285 K (Tet) can mostly be related to an enhanced roughness of the sample surface accompanied with a reduction of the NSLD thereof. This reduction can be related to an oxygen deficient top layer, since the application of an electric field can lead to the diffusion of oxygen ions. The best FOM was achieved by using Model 0, with a slightly varied MSLD in comparison to the negative electric field state. The difference in the simulated intensity resulting from the models with varied magnetization profile are very small. Therefore, a clear decision, if the magnetic profile changes and in which way is difficult. Nevertheless, the consideration of a small magnetic moment induced into the Ti atoms of the BaTiO<sub>3</sub> at the interface as predicted for Fe/BaTiO<sub>3</sub> [124] is unlikely, since the FOM is degraded for this model. In addition, a zero magnetic moment is obtained in the BaTiO<sub>3</sub>, if it is considered as free fit parameter. The simulations show that, if there is a change in the magnetization, then it is most probably located at the interface. All the mechanisms which are possible to explain the observed effects, measured by MPMS, are somehow related to the interface, whether it is strain or a purely electric coupling mechanism.

Burton *et al.* predicted a switching from FM to AFM alignment at the interface for different polarization directions of the ferroelectric BaTiO<sub>3</sub> pointing to half doped La<sub>(1-x)</sub>Sr<sub>x</sub>MnO<sub>3</sub> [1]. First-principle calculations indicate a limitation of the effect to the first two unit cells. In general, there are some weaknesses in the approach of Burton *et al.*. They assume ideally flat interfaces in their calculations, however real interfaces have steps which lead to frustration, if different magnetic structures are present. Moreover different strain state are neglected and a ferroelectric single domain is assumed. Both lead to a change of magnetic anisotropy and of the exchange interaction, which will have bigger effects on the magnetic properties of the system. Furthermore, the presence of oxygen vacancies in real systems and the distribution thereof within the samples is also neglected. It is well known that the accumulation of oxygen vacancies is different for the interface and further away from it leading to a modification of various properties of the system e.g. magnetic or electric properties. While the first-principles calculations of Burton *et al.* give a nice physical model, real systems are much more complex and other mechanisms than the proposed one obviously are dominant.



# Chapter 9

## Summary and Outlook

The aim of this thesis was to investigate a possible magneto-electric coupling in an artificial multiferroic heterostructure of  $\text{La}_{(1-x)}\text{Sr}_x\text{MnO}_3$  and  $\text{BaTiO}_3$ . It was possible to grow single crystalline  $\text{La}_{(1-x)}\text{Sr}_x\text{MnO}_3$  films on  $\text{BaTiO}_3$  substrates by using a state-of-the art OMBE and HOPSS. The stoichiometry of the  $\text{La}_{(1-x)}\text{Sr}_x\text{MnO}_3$  films is confirmed by RBS measurements and a growth process for the OMBE was developed by an iterative refinement of the growth parameters. Structural properties of these films were investigated by X-ray scattering methods, which indicate a good film quality in terms of roughness and crystalline structure. Diffraction measurements at room temperature with applied electric fields proof the possibility to change the polarization of  $\text{BaTiO}_3$  and alter the proportion of c-type and a-type domains. Temperature dependent diffraction measurements provide an insight into the strain within the structural phases of the  $\text{BaTiO}_3$  substrate. They show that the LSMO film is clamped to the  $\text{BaTiO}_3$  substrate and that tensile strain is present in the whole investigated temperature range.

It could be shown that the magnetization of  $\text{La}_{(1-x)}\text{Sr}_x\text{MnO}_3$  on  $\text{BaTiO}_3$  substrates can be influenced by the variation of temperature as well as the application of electric fields. The temperature dependent magnetization shows steps at the phase transition temperatures of the  $\text{BaTiO}_3$  substrate. Those are related to strain effects in the different structural phases which can lead to a change in the magnetic anisotropy and a change of the exchange interaction. The change of the magnetic anisotropy is evidenced by magnetic hysteresis loops in the different phases of the substrate and the resulting squareness as function of the temperature. Additionally, the application of an electric field also leads to a change of the magnetic anisotropy indicated by the shift of the coercivity field in the hysteresis loops.

Even more fascinating is the possibility to directly alter the magnetization by an electric field. The magnetic response to an applied electric field could be determined by using a newly established measurement option as function of temperature and magnetic field. The modification of the magnetization with respect to the electric field is pronounced near the structural phase transitions. A more detailed view on the influence of the electric field on the magnetization could be given by electrical hysteresis loops. Particular, a present difference in the magnetization of  $\text{La}_{0.7}\text{Sr}_{0.3}\text{MnO}_3$  at 180 K and 285 K at zero electric field after the application of an electric field points to possible applications in non-volatile

data storage devices, when the magnetic state can be switched by a pulsed application of an electric voltage.

The magnetization profile of the LSMO/BTO heterostructure could be determined by polarized neutron reflectivity measurements. The samples grown by OMBE indicate a better epitaxial crystal structure, because of the strain induced lowered magnetization at the interface. Moreover, the magnetic profile of the samples produced by the HOPSS show a reduced magnetization for higher layer thicknesses related to oxygen vacancies. The observed differences in the polarized neutron reflectivity with respect to the applied electric field are mostly related to structural properties. A clear statement on a altering of the magnetization with respect to an applied electric field cannot be given, although it is most probably located at the interface.

The observed effects were discussed to find possible mechanisms for the observed magneto-electric coupling effects. In order to clarify the underlying coupling mechanism, further investigations are necessary. A more detailed investigation of the structural properties of the films and the substrate, especially of in-plane lattice parameters, is required for the complete understanding of how much strain is induced into the film. Furthermore, the change of lattice parameter with respect to applied electric fields in each phase would clarify the influence thereof onto structural distortions. Especially, the domain structure of the BaTiO<sub>3</sub> substrate has to be analyzed and engineered to be reproducible. Polarized light microscopy is a simple technique to investigate the domain structure of BaTiO<sub>3</sub>. In addition, the possibility to apply higher electric fields would guarantee a single domain state. The use of a different ferroelectric substrate such as lead zirconate titanate with a stable lattice structure can lead to a further understanding of the magneto-electric coupling. The effect predicted by Burten *et al.* [1] is unlikely to explain the observed effects. Nevertheless the investigation of La<sub>(1-x)</sub>Sr<sub>x</sub>MnO<sub>3</sub> with a doping level of  $x = 0.2$  would be interesting since there, the slope of the Curie temperature  $T_C$  vs. the doping level is very steep [32]. By the investigation of  $T_C$  with respect to an applied electric field one could easily proof the possibility to electrically shift the doping level.

# Acknowledgments

The work would not have been possible without the support of numerous people. I want to thank the following people who contributed to the outcome of this work:

**Prof. Dr. Thomas Brückel** for the opportunity to work on this very interesting subject with a rich pool of methods. I want to thank him for supporting me through the time and the possibility to travel to various places to participate at conferences and beamtimes.

**Prof. Dr. Larissa Juschkina** for the agreement to take the second revision of this thesis.

Especially, I would like to thank my supervisor **Dr. Alexander Weber** for all the support and the discussions we had during my thesis. I am very grateful for the way of supervising me with a nice balance between guidance and a lot of freedom in my research. I would like to thank you for the nice research trips we did together, whether to India or the United States.

**Dr. Arthur Glavic, Dr. Stefan Mattauch** and **Dr. Alexandros Koutsioumpas** for the scientific support during and after the neutron reflectivity measurements performed at the SNS and MLZ.

**Dr. Jürgen Schubert, Willi Zander** and **Dr. Bernd Holländer** for the help in the sample preparation and the investigation of the stoichiometry by RBS.

**Dr. Oleg Petravic** and **Liming Wang** for support at the MPMS.

**Markus Waschk** and **Paul Zakalek** for the good cooperation as the "OMBE team" with fruitful discussions, support in programming and the proofreading of my thesis.

It was a pleasure to share an office with **Johannes Reim** and **Ronnie E. Simon**. Thanks for all the unforgettable moments we had during the whole time and the joyful atmosphere. The mixture between a scientific surrounding and a lot of fun was always very motivating.

I want to thank all the members of the Institute for Scattering Methods in Jülich not only for the scientific discussions, but also for creating a lovely atmosphere.

Zum Schluss möchte ich mich bei meiner gesamten Familie bedanken. Meine Eltern haben den Grundstein gelegt, der mir meine wissenschaftliche Ausbildung und die Promotion überhaupt ermöglichte. Spezieller Dank geht an Kathi, die mich besonders während der stressigen Phasen meiner Promotion stets ertragen und vor allem unterstützt hat.



# Bibliography

- [1] J. D. Burton and E. Y. Tsymbal. Prediction of electrically induced magnetic reconstruction at the manganite/ferroelectric interface. *Physical Review B*, **80**(17):174406–1–174406–6, 2009.
- [2] J. Heber. Materials science: Enter the oxides. *Nature*, **459**:28–30, 2009.
- [3] Y. Tokura. Optical and magnetic properties of transition metal oxides. *Current Opinion in Solid State and Materials Science*, **3**(2):175–180, 1998.
- [4] J.G. Bednorz and K.A. Müller. Possible High  $T_c$  Superconductivity in the Ba-La-Cu-O System. *Zeitschrift für Physik B Condensed Matter*, **64**(2):189–193, 1986.
- [5] A-M Haghiri-Gosnet and J-P Renard. CMR manganites: physics, thin films and devices. *Journal of Physics D: Applied Physics*, **36**(8):R127–R150, 2003.
- [6] Manh-Huong Phan and Seong-Cho Yu. Review of the magnetocaloric effect in manganite materials. *Journal of Magnetism and Magnetic Materials*, **308**(2):325–340, 2007.
- [7] M. Fiebig. Revival of the magnetoelectric effect. *Journal of Physics D: Applied Physics*, **38**(8):R123–R152, 2005.
- [8] N. Izyumskaya, Ya. Alivov, and H. Morkoç. Oxides, Oxides, and More Oxides: High- $\kappa$  Oxides, Ferroelectrics, Ferromagnetics, and Multiferroics. *Critical Reviews in Solid State and Materials Sciences*, **34**(3-4):89–179, 2009.
- [9] F. Matsukura, Y. Tokura, and H. Ohno. Control of magnetism by electric fields. *Nature Nanotechnology*, **10**(3):209–220, 2015.
- [10] M. Gajek, M Bibes, S. Fusil, K. Bouzehouane, J. Fontcuberta, A. Barthelemy, and A. Fert. Tunnel junctions with multiferroic barriers. *Nature Materials*, **6**(4):296–302, 2007.
- [11] F. Yang, M. H. Tang, Z. Ye, Y. C. Zhou, X. J. Zheng, J. X. Tang, J. J. Zhang, and J. He. Eight logic states of tunneling magnetoelectroresistance in multiferroic tunnel junctions. *Journal of Applied Physics*, **102**(4):044504, 2007.
- [12] M. Bibes and A. Barthelemy. Multiferroics: Towards a magnetoelectric memory. *Nature Materials*, **7**(6):425–426, 2008.

- [13] Nicola A. Hill. Why Are There so Few Magnetic Ferroelectrics? *The Journal of Physical Chemistry B*, **104**(29):6694–6709, 2000.
- [14] U. Poppe, J. Schubert, R.R. Arons, W. Evers, C.H. Freiburg, W. Reichert, K. Schmidt, W. Sybertz, and K. Urban. Direct production of crystalline superconducting thin films of  $\text{YBa}_2\text{Cu}_3\text{O}_7$  by high-pressure oxygen sputtering. *Solid State Communications*, **66**(6):661–665, 1988.
- [15] D. G. Schlom, L. Chen, X. Pan, A. Schmehl, and M. A. Zurbuchen. A Thin Film Approach to Engineering Functionality into Oxides. *Journal of the American Ceramic Society*, **91**(8):2429–2454, 2008.
- [16] H. Y. Hwang, Y. Iwasa, M. Kawasaki, B. Keimer, N. Nagaosa, and Y. Tokura. Emergent phenomena at oxide interfaces. *Nature Materials*, **11**(2):103–113, 2012.
- [17] J. Chakhalian, A. J. Millis, and J. Rondinelli. Whither the oxide interface. *Nature Materials*, **11**(2):92–94, 2012.
- [18] N. Reyren, S. Thiel, A. D. Caviglia, L. Fitting Kourkoutis, G. Hammerl, C. Richter, C. W. Schneider, T. Kopp, A.-S. Rüetschi, D. Jaccard, M. Gabay, D. A. Muller, J.-M. Triscone, and J. Mannhart. Superconducting Interfaces Between Insulating Oxides. *Science*, **317**(5842):1196–1199, 2007.
- [19] A. Brinkman, M. Huijben, M. van Zalk, J. Huijben, U. Zeitler, J. C. Maan, W. G. van der Wiel, G. Rijnders, D. H. A. Blank, and H. Hilgenkamp. Magnetic effects at the interface between non-magnetic oxides. *Nature Materials*, **6**(7):493–496, 2007.
- [20] Hajo J. A. Molegraaf, Jason Hoffman, Carlos A. F. Vaz, Stefano Gariglio, Dirk van der Marel, Charles H. Ahn, and Jean-Marc Triscone. Magnetoelectric Effects in Complex Oxides with Competing Ground States. *Advanced Materials*, **21**(34):3470–3474, 2009.
- [21] M. A. Peña and J. L. G. Fierro. Chemical Structures and Performance of Perovskite Oxides. *Chemical Reviews*, **101**(7):1981–2018, 2001.
- [22] G. Rose. Beschreibung einiger neuen Mineralien des Urals. *Annalen der Physik*, **124**(12):551–573, 1839.
- [23] C. J. Howard and H. T. Stokes. Group-Theoretical Analysis of Octahedral Tilting in Perovskites. *Acta Crystallographica Section B*, **54**(6):782–789, 1998.
- [24] P. M. Woodward, T. Vogt, D. E. Cox, A. Arulraj, C. N. R. Rao, P. Karen, and A. K. Cheetham. Influence of Cation Size on the Structural Features of  $\text{Ln}_{1/2}\text{A}_{1/2}\text{MnO}_3$  Perovskites at Room Temperature. *Chemistry of Materials*, **10**(11):3652–3665, 1998.
- [25] H. A. Jahn and E. Teller. Stability of Polyatomic Molecules in Degenerate Electronic States. I. Orbital Degeneracy. *Proceedings of the Royal Society of London. Series A, Mathematical and Physical Sciences*, **161**(905):220–235, 1937.

- 
- [26] W. Heisenberg. Zur Theorie des Ferromagnetismus. *Zeitschrift für Physik*, **49**(9-10):619–636, 1928.
- [27] P. W. Anderson. Antiferromagnetism. Theory of Superexchange Interaction. *Physical Review*, **79**(2):350–356, 1950.
- [28] J. B. Goodenough. Theory of the Role of Covalence in the Perovskite-Type Manganites  $[\text{La},\text{M}(\text{II})]\text{MnO}_3$ . *Physical Review*, **100**(2):564–573, 1955.
- [29] J. B. Goodenough. An interpretation of the magnetic properties of the perovskite-type mixed crystals  $\text{La}_{(1-x)}\text{Sr}_x\text{CoO}_{(3-\lambda)}$ . *Journal of Physics and Chemistry of Solids*, **6**(2-3):287–297, 1958.
- [30] J. Kanamori. Superexchange interaction and symmetry properties of electron orbitals. *Journal of Physics and Chemistry of Solids*, **10**(2-3):87–98, 1959.
- [31] C. Zener. Interaction between the d-Shells in the Transition Metals. II. Ferromagnetic Compounds of Manganese with Perovskite Structure. *Physical Review*, **82**(3):403–405, 1951.
- [32] J. Hemberger, A. Krimmel, T. Kurz, H.-A. Krug von Nidda, V. Yu. Ivanov, A. A. Mukhin, A. M. Balbashov, and A. Loidl. Structural, magnetic, and electrical properties of single-crystalline  $\text{La}_{1-x}\text{Sr}_x\text{MnO}_3$  ( $0.4 < x < 0.85$ ). *Physical Review B*, **66**(9):094410–1–094410–8, 2002.
- [33] A. Urushibara, Y. Moritomo, T. Arima, A. Asamitsu, G. Kido, and Y. Tokura. Insulator-metal transition and giant magnetoresistance in  $\text{La}_{1-x}\text{Sr}_x\text{MnO}_3$ . *Physical Review B*, **51**(20):14103–14109, 1995.
- [34] K. Horiba, A. Maniwa, A. Chikamatsu, K. Yoshimatsu, H. Kumigashira, H. Wadati, A. Fujimori, S. Ueda, H. Yoshikawa, E. Ikenaga, J. J. Kim, K. Kobayashi, and M. Oshima. Pressure-induced change in the electronic structure of epitaxially strained  $\text{La}_{1-x}\text{Sr}_x\text{MnO}_3$  thin films. *Physical Review B*, **80**(13):132406–1–132406–4, 2009.
- [35] Y. Konishi, Z. Fang, M. Izumi, T. Manako, M. Kasai, H. Kuwahara, M. Kawasaki, K. Terakura, and Y. Tokura. Orbital-State-Mediated Phase-Control of Manganites. *Journal of the Physical Society of Japan*, **68**(12):3790–3793, 1999.
- [36] C. A. F. Vaz, J. A. Moyer, D. A. Arena, C. H. Ahn, and V. E. Henrich. Magnetic and electronic structure of ultrathin  $\text{La}_{1-x}\text{Sr}_x\text{MnO}_3$  films at half doping. *Physical Review B*, **90**(2):024414–1–024414–8, 2014.
- [37] A. von Hippel, R. G. Breckenridge, F. G. Chesley, and Laszlo Tisza. High dielectric constant ceramics. *Industrial & Engineering Chemistry*, **38**(11):1097–1109, 1946.
- [38] James W. Edwards, Rudolph Speiser, and Herrick L. Johnston. Structure of Barium Titanate at Elevated Temperatures. *Journal of the American Chemical Society*, **73**(6):2934–2935, 1951.

- [39] R. E. Cohen. Origin of ferroelectricity in perovskite oxides. *Nature*, **358**(6382):136–138, 1992.
- [40] H.F. Kay and P. Vousden. XCV. Symmetry changes in barium titanate at low temperatures and their relation to its ferroelectric properties. *Philosophical Magazine Series 7*, **40**(309):1019–1040, 1949.
- [41] Malcolm E. L. and A. M. Glass. *Principles and applications of ferroelectrics and related materials*. Oxford [Eng.] Clarendon Press, 1977.
- [42] Ph. Ghosez, J.-P. Michenaud, and X. Gonze. Dynamical atomic charges: The case of  $\text{ABO}_3$  compounds. *Physical Review B*, **58**(10):6224–6240, 1998.
- [43] R. E. Cohen and H. Krakauer. Electronic structure studies of the differences in ferroelectric behavior of  $\text{BaTiO}_3$  and  $\text{PbTiO}_3$ . *Ferroelectrics*, **136**(1):65–83, 1992.
- [44] W. Cochran. Crystal Stability and the Theory of Ferroelectricity. *Physical Review Letters*, **3**(9):412–414, 1959.
- [45] W. Cochran. Crystal stability and the theory of ferroelectricity. *Advances in Physics*, **9**(36):387–423, 1960.
- [46] R. Comes, M. Lambert, and A. Guinier. The chain structure of  $\text{BaTiO}_3$  and  $\text{KNbO}_3$ . *Solid State Communications*, **6**(10):715–719, 1968.
- [47] A. S. Chaves, F. C. S. Barreto, R. A. Nogueira, and B. Zēks. Thermodynamics of an eight-site order-disorder model for ferroelectrics. *Physical Review B*, **13**(1):207–212, 1976.
- [48] I.B. Bersuker. On the origin of ferroelectricity in perovskite-type crystals. *Physics Letters*, **20**(6):589–590, 1966.
- [49] R.E. Cohen. Theory of ferroelectrics: a vision for the next decade and beyond. *Journal of Physics and Chemistry of Solids*, **61**(2):139–146, 2000.
- [50] B. Ravel, E. A. Stern, R. I. Vedrinskii, and V. Kraizman. Local structure and the phase transitions of  $\text{BaTiO}_3$ . *Ferroelectrics*, **206**(1):407–430, 1998.
- [51] A.M. Quittet and M. Lambert. Temperature dependence of the Raman cross section and light absorption in cubic  $\text{BaTiO}_3$ . *Solid State Communications*, **12**(10):1053–1055, 1973.
- [52] Y. Yamada, G. Shirane, and A. Linz. Study of Critical Fluctuations in  $\text{BaTiO}_3$  by Neutron Scattering. *Physical Review*, **177**(2):848–857, 1969.
- [53] J. Harada, J. D. Axe, and G. Shirane. Neutron-Scattering Study of Soft Modes in Cubic  $\text{BaTiO}_3$  †. *Physical Review B*, **4**(1):155–162, 1971.
- [54] Y. Girshberg and Y. Yacoby. Ferroelectric phase transitions in perovskites with off-center ion displacements. *Solid State Communications*, **103**(7):425–430, 1997.

- 
- [55] W. Zhong, D. Vanderbilt, and K. M. Rabe. Phase-transitions In BaTiO<sub>3</sub> From First Principles. *Physical Review Letters*, **73**(13):1861–1864, 1994.
- [56] M. Sepliarsky, R.L. Migoni, and M.G. Stachiotti. Ab initio supported model simulations of ferroelectric perovskites. *Computational Materials Science*, **10**(1-4):51–56, 1998.
- [57] H. Krakauer, R. Yu, C.-Z. Wang, and C. Lasota. Precursor structures in ferroelectrics from first-principles calculations. *Ferroelectrics*, **206**(1):133–155, 1998.
- [58] H. Krakauer, R. Yu, C.-Z. Wang, K.M. Rabe, and U. V. Waghmare. Dynamic local distortions in KNbO<sub>3</sub>. *Journal of Physics: Condensed Matter*, **11**(18):3779–, 1999.
- [59] Q. Zhang, T. Cagin, and W. A. Goddard. The ferroelectric and cubic phases in BaTiO<sub>3</sub> ferroelectrics are also antiferroelectric. *Proceedings of the National Academy of Sciences*, **103**(40):14695–14700, 2006.
- [60] D. G. Schlom, L. Q. Chen, C. B. Eom, K. M. Rabe, S. K. Streiffer, and J. M. Triscone. Strain tuning of ferroelectric thin films. *Annual Review of Materials Research*, **37**:589–626, 2007.
- [61] K. J. Choi, M. Biegalski, Y. L. Li, A. Sharan, J. Schubert, R. Uecker, P. Reiche, Y. B. Chen, X. Q. Pan, V. Gopalan, L.-Q. Chen, D. G. Schlom, and C. B. Eom. Enhancement of Ferroelectricity in Strained BaTiO<sub>3</sub> Thin Films. *Science*, **306**(5698):1005–1009, 2004.
- [62] T. Suzuki, Y. Nishi, and M. Fujimoto. Analysis of misfit relaxation in heteroepitaxial BaTiO<sub>3</sub> thin films. *Philosophical Magazine A*, **79**(10):2461–2483, 1999.
- [63] C. H. Ahn, K. M. Rabe, and J.-M. Triscone. Ferroelectricity at the Nanoscale: Local Polarization in Oxide Thin Films and Heterostructures. *Science*, **303**(5657):488–491, 2004.
- [64] D. D. Fong, G. B. Stephenson, S. K. Streiffer, J. A. Eastman, O. Auciello, P. H. Fuoss, and C. Thompson. Ferroelectricity in Ultrathin Perovskite Films. *Science*, **304**(5677):1650–1653, 2004.
- [65] J. Junquera and Ph. Ghosez. Critical thickness for ferroelectricity in perovskite ultrathin films. *Nature*, **422**(6931):506–509, 2003.
- [66] Y. L. Li and L. Q. Chen. Temperature-strain phase diagram for BaTiO<sub>3</sub> thin films. *Applied Physics Letters*, **88**(7):072905, 2006.
- [67] Hans Schmid. Guest editorial. *Ferroelectrics*, **162**(1):xix–xxv, 1994.
- [68] N. A. Spaldin and M. Fiebig. The Renaissance of Magnetoelectric Multiferroics. *Science*, **309**(5733):391–392, 2005.
- [69] D. Khomskii. Multiferroics: Different ways to combine magnetism and ferroelectricity. *Journal of Magnetism and Magnetic Materials*, **306**(1):1–8, 2006.

- [70] D. Khomskii. Classifying multiferroics: Mechanisms and effects. *Physics*, **2**:20, 2009.
- [71] A.M. Kadomtseva, A.K. Zvezdin, Yu.F. Popov, A.P. Pyatakov, and G.P. Vorob'ev. Space-time parity violation and magnetoelectric interactions in antiferromagnets. **79**(11):571–581, 2004.
- [72] A. Moreira dos Santos, S. Parashar, A.R. Raju, Y.S. Zhao, A.K. Cheetham, and C.N.R. Rao. Evidence for the likely occurrence of magnetoferroelectricity in the simple perovskite, BiMnO<sub>3</sub>. *Solid State Communications*, **122**(1-2):49–52, 2002.
- [73] T. Kimura, S. Kawamoto, I. Yamada, M. Azuma, M. Takano, and Y. Tokura. Magnetocapacitance effect in multiferroic BiMnO<sub>3</sub>. *Physical Review B*, **67**(18):180401, 2003.
- [74] R. Seshadri and N. A. Hill. Visualizing the Role of Bi 6s "Lone Pairs" in the Off-Center Distortion in Ferromagnetic BiMnO<sub>3</sub>. *Chemistry of Materials*, **13**(9):2892–2899, 2001.
- [75] N. Ikeda, H. Ohsumi, K. Ohwada, K. Ishii, T. Inami, K. Kakurai, Y. Murakami, K. Yoshii, S. Mori, Y. Horibe, and H. Kito. Ferroelectricity from iron valence ordering in the charge-frustrated system LuFe<sub>2</sub>O<sub>4</sub>. *Nature*, **436**(7054):1136–1138, 2005.
- [76] M. Angst, R. P. Hermann, A. D. Christianson, M. D. Lumsden, C. Lee, M.-H. Whangbo, J.-W. Kim, P. J. Ryan, S. E. Nagler, W. Tian, R. Jin, B. C. Sales, and D. Mandrus. Charge Order in LuFe<sub>2</sub>O<sub>4</sub>: Antiferroelectric Ground State and Coupling to Magnetism. *Physical Review Letters*, **101**(22):227601, 2008.
- [77] S.-W. Cheong and M. Mostovoy. Multiferroics: a magnetic twist for ferroelectricity. *Nat Mater*, **6**(1):13–20, 2007.
- [78] T. Aoyama, K. Yamauchi, A. Iyama, S. Picozzi, K. Shimizu, and T. Kimura. Giant spin-driven ferroelectric polarization in TbMnO<sub>3</sub> under high pressure. *Nat Commun*, **5**:1–7, 2014.
- [79] I. A. Sergienko and E. Dagotto. Role of the Dzyaloshinskii-Moriya interaction in multiferroic perovskites. *Phys. Rev. B*, **73**:094434, 2006.
- [80] Bas B. Van Aken, Thomas T.M. Palstra, Alessio Filippetti, and Nicola A. Spaldin. The origin of ferroelectricity in magnetoelectric YMnO<sub>3</sub>. *Nature Materials*, **3**(3):164–170, 2004.
- [81] S. Geprägs, M. Opel, S. T. B. Goennenwein, and R. Gross. Multiferroic materials based on artificial thin film heterostructures. *Philosophical Magazine Letters*, **87**(3-4):141–154, 2007.
- [82] R. Ramesh, F. Zavaliche, Y. H. Chu, L. W. Martin, S. Y. Yang, M. P. Cruz, M. Barry, K. Lee, P. Yang, and Q. Zhan. Magnetoelectric complex-oxide heterostructures. *Philosophical Magazine Letters*, **87**(3-4):155–164, 2007.

- 
- [83] M. P. Singh and W. Prellier. Oxide superlattices for multiferroics: opportunities, issues, and challenges. *Philosophical Magazine Letters*, **87**(3-4):211–222, 2007.
- [84] Brückel Th., Heger G., Richter D., and Zorn R. (eds.). *Neutron Scattering*. Forschungszentrum Jülich GmbH, 2008.
- [85] J. Lekner. *Theory of Reflection of Electromagnetic and Particle Waves*. Springer, 1987.
- [86] L. G. Parratt. Surface Studies of Solids by Total Reflection of X-Rays. *Physical Review*, **95**(2):359–369, 1954.
- [87] G.L. Squires. *Introduction to the Theory of Thermal Neutron Scattering*. Dover Publications, 1978.
- [88] M. Björck and G. Andersson. GenX: an extensible X-ray reflectivity refinement program utilizing differential evolution. *Journal of Applied Crystallography*, **40**(6):1174–1178, 2007.
- [89] P. Zakalek. *Magnetic Interface Effects in Thin Film Heterostructures*. PhD thesis, RWTH Aachen, 2015.
- [90] R. Zhao, K. Jin, Z. Xu, L. Guo, H. and Wang, C. Ge, H. Lu, and G. Yang. The oxygen vacancy effect on the magnetic property of the  $\text{LaMnO}_{3-\delta}$  thin films. *Applied Physics Letters*, **102**(12):122402, 2013.
- [91] K. Oura, V. Lifshits, A. Saranin, A. Zotov, and M. Katayama. *Surface Science: An Introduction*. Springer, 2003.
- [92] J.B. Pendry. *Low Energy Electron Diffraction: The Theory and Its Application to Determination of Surface Structure*. Academic Press, 1974.
- [93] K. D. Childs, B. A. Carlson, L. A. LaVanier, and C. L. Hedberg. *Handbook of Auger electron spectroscopy : a book of reference data for identification and interpretation in Auger electron spectroscopy*. 1995.
- [94] A. Ichimiya and P.I. Cohen. *Reflection High-Energy Electron Diffraction*. Cambridge University Press, 2004.
- [95] W. Braun. *Applied RHEED: Reflection High-energy Electron Diffraction During Crystal Growth*. Springer, 1999.
- [96] J.H. Haeni, C.D. Theis, and D.G. Schlom. RHEED Intensity Oscillations for the Stoichiometric Growth of  $\text{SrTiO}_3$  Thin Films by Reactive Molecular Beam Epitaxy. *Journal of Electroceramics*, **4**(2-3):385–391, 2000.
- [97] Y. Yoneda, K. Sakaue, and H. Terauchi. RHEED observation of  $\text{BaTiO}_3$  thin films grown by MBE. *Surface Science*, **529**(3):283–287, 2003.

- [98] A. Glavic. *Multiferroicity in oxide thin films and heterostructures*. PhD thesis, RWTH Aachen, 2011.
- [99] M. McElfresh. *Fundamentals of Magnetism and Magnetic Measurements. Featuring Quantum Design's Magnetic Property Measurement System*. Quantum Design Inc., 1994.
- [100] Clarke John and Braginski Alex I., editors. *The SQUID Handbook: Fundamentals and Technology of SQUIDs and SQUID Systems*. Wiley-VCH, 2006.
- [101] Clarke John and Braginski Alex I., editors. *The SQUID Handbook: Applications of SQUIDs and SQUID Systems*. Wiley-VCH, 2006.
- [102] D. N. Astrov. The magnetoelectric effect in antiferromagnetic materials. *Sov. Phys.-JETP*, **11**:708, 1960.
- [103] P. Borisov, A. Hochstrat, V. V. Shvartsman, and W. Kleemann. Superconducting quantum interference device setup for magnetoelectric measurements. *Review of Scientific Instruments*, **78**(10):106105, 2007.
- [104] P. Borisov, A. Hochstrat, X. Chen, W. Kleemann, and C. Binek. Magnetoelectric Switching of Exchange Bias. *Physical Review Letters*, **94**:117203, 2005.
- [105] H. Ambaye, R. Goyette, A. Parizzi, and F. Klose. SNS Magnetism Reflectometer. *Neutron News*, **19**(3):11–13, 2008.
- [106] S. B. Mi, C. L. Jia, T. Heeg, O. Trithaveesak, J. Schubert, and K. Urban. Heterostructures of BaTiO<sub>3</sub> bilayer films grown on SrTiO<sub>3</sub> (001) under different oxygen pressures. *Journal of Crystal Growth*, **283**(3-4):425–430, 2005.
- [107] G. Koster, B. L. Kropman, G. J. H. M. Rijnders, D. H. A. Blank, and H. Rogalla. Quasi-ideal strontium titanate crystal surfaces through formation of strontium hydroxide. *Applied Physics Letters*, **73**(20):2920–2922, 1998.
- [108] Y. Yoneda, T. Okabe, K. Sakaue, H. Terauchi, H. Kasatani, and K. Deguchi. Structural characterization of BaTiO<sub>3</sub> thin films grown by molecular beam epitaxy. *Journal of Applied Physics*, **83**(5):2458–2461, 1998.
- [109] A. Barbier, C. Mocuta, D. Stanescu, P. Jegou, N. Jedrecy, and H. Magnan. Surface composition of BaTiO<sub>3</sub>/SrTiO<sub>3</sub>(001) films grown by atomic oxygen plasma assisted molecular beam epitaxy. *Journal of Applied Physics*, **112**(11):114116, 2012.
- [110] S. Miyake and R. Ueda. On phase transformation of BaTiO<sub>3</sub>. *Journal of the Physical Society of Japan*, **2**(5):93–97, 1947.
- [111] Y. S. Kim, D. H. Kim, J. D. Kim, Y. J. Chang, T. W. Noh, J. H. Kong, K. Char, Y. D. Park, S. D. Bu, J.-G. Yoon, and J.-S. Chung. Critical thickness of ultrathin ferroelectric BaTiO<sub>3</sub> films. *Applied Physics Letters*, **86**(10):102907, 2005.

- 
- [112] Katja Hirte. Optimierung der strukturellen Eigenschaften von gesputterten BaTiO<sub>3</sub>-Schichten, 2014.
- [113] S. Geprägs, A. Brandlmaier, M. Opel, R. Gross, and S. T. B. Goennenwein. Electric field controlled manipulation of the magnetization in Ni/BaTiO<sub>3</sub> hybrid structures. *Applied Physics Letters*, **96**(14):142509, 2010.
- [114] F. Tsui, M. C. Smoak, T. K. Nath, and C. B. Eom. Strain-dependent magnetic phase diagram of epitaxial La<sub>0.67</sub>Sr<sub>0.33</sub>MnO<sub>3</sub> thin films. *Applied Physics Letters*, **76**(17):2421–2423, 2000.
- [115] G. Venkataiah, Y. Shirahata, M. Itoh, and T. Taniyama. Manipulation of magnetic coercivity of Fe film in Fe/BaTiO<sub>3</sub> heterostructure by electric field. *Applied Physics Letters*, **99**(10):102506, 2011.
- [116] S. Brivio, D. Petti, R. Bertacco, and J. C. Cezar. Electric field control of magnetic anisotropies and magnetic coercivity in Fe/BaTiO<sub>3</sub>(001) heterostructures. *Applied Physics Letters*, **98**(9):092505, 2011.
- [117] S. Sahoo, S. Polisetty, C.-G. Duan, S. S. Jaswal, E. Y. Tsymbal, and C. Binek. Ferroelectric control of magnetism in BaTiO<sub>3</sub>/Fe heterostructures via interface strain coupling. *Physical Review B*, **76**:092108, 2007.
- [118] J. Blanc and D. L. Staebler. Electrocoloration in SrTiO<sub>3</sub>: Vacancy Drift and Oxidation-Reduction of Transition Metals. *Phys. Rev. B*, **4**:3548–3557, 1971.
- [119] X. Chen, N. Wu, J. Strozier, and A. Ignatiev. Spatially extended nature of resistive switching in perovskite oxide thin films. *Applied Physics Letters*, **89**(6):–, 2006.
- [120] Nicola Manca, Luca Pellegrino, and D Marré. Reversible oxygen vacancies doping in (La<sub>0.7</sub>,Sr<sub>0.3</sub>)MnO<sub>3</sub> microbridges by combined self-heating and electromigration. *Applied Physics Letters*, **106**(20):–, 2015.
- [121] C. A. F. Vaz, J. Hoffman, C. H. Ahn, and R. Ramesh. Magnetoelectric Coupling Effects in Multiferroic Complex Oxide Composite Structures. *Advanced Materials*, **22**(26-27):2900–2918, 2010.
- [122] James M. Rondinelli, Massimiliano Stengel, and Nicola A. Spaldin. Carrier-mediated magnetoelectricity in complex oxide heterostructures. *Nature Nanotechnology*, **3**(1):46–50, 2008.
- [123] X. Huang and S. Dong. Ferroelectric control of magnetism and transport in oxide heterostructures. *Modern Physics Letters B*, **28**(23):1430010–1–1430010–25, 2014.
- [124] C.-G. Duan, S. S. Jaswal, and E. Y. Tsymbal. Predicted magnetoelectric effect in Fe/BaTiO<sub>3</sub> multilayers: Ferroelectric control of magnetism. *Physical Review Letters*, **97**(4):047201, 2006.

- [125] M. K. Lee, T. K. Nath, C. B. Eom, M. C. Smoak, and F. Tsui. Strain modification of epitaxial perovskite oxide thin films using structural transitions of ferroelectric BaTiO<sub>3</sub> substrate. *Applied Physics Letters*, **77**(22):3547–3549, 2000.
- [126] A. J. Millis, T. Darling, and A. Migliori. Quantifying strain dependence in colossal magnetoresistance manganites. *Journal of Applied Physics*, **83**(3):1588–1591, 1998.
- [127] Z. Fang, I. V. Solovyev, and K. Terakura. Phase Diagram of Tetragonal Manganites. *Physical Review Letters*, **84**:3169–3172, 2000.
- [128] H. Boschker, M. Mathews, E. P. Houwman, H. Nishikawa, A. Vailionis, G. Koster, G. Rijnders, and D. H. A. Blank. Strong uniaxial in-plane magnetic anisotropy of (001)- and (011)-oriented La<sub>0.67</sub>Sr<sub>0.33</sub>MnO<sub>3</sub> thin films on NdGaO<sub>3</sub> substrates. *Physical Review B*, **79**:214425, 2009.
- [129] R. G. Rhodes. Barium titanate twinning at low temperatures. *Acta Crystallographica*, **4**(2):105–110, 1951.
- [130] C. A. F. Vaz, J. Hoffman, A.-B. Posadas, and C. H. Ahn. Magnetic anisotropy modulation of magnetite in Fe<sub>3</sub>O<sub>4</sub>/BaTiO<sub>3</sub>(100) epitaxial structures. *Applied Physics Letters*, **94**(2):022504, 2009.
- [131] S.-E. Park, S. Wada, L. E. Cross, and Th. R. ShROUT. Crystallographically engineered BaTiO<sub>3</sub> single crystals for high-performance piezoelectrics. *Journal of Applied Physics*, **86**(5):2746–2750, 1999.
- [132] W. J. Merz. The Electric and Optical Behavior of BaTiO<sub>3</sub> Single-Domain Crystals. *Physical Review Letters*, **76**:1221–1225, 1949.
- [133] H. H. Wieder. Ferroelectric Hysteresis in Barium Titanate Single Crystals. *Journal of Applied Physics*, **26**(12):1479–1482, 1955.
- [134] R. Tazaki, D. Fu, M. Itoh, M. Daimon, and S. Koshihara. Lattice distortion under an electric field in BaTiO<sub>3</sub> piezoelectric single crystal. *Journal of Physics: Condensed Matter*, **21**(21):215903, 2009.
- [135] P. Marton, I. Rychetsky, and J. Hlinka. Domain walls of ferroelectric BaTiO<sub>3</sub> within the Ginzburg-Landau-Devonshire phenomenological model. *Phys. Rev. B*, **81**:144125, 2010.
- [136] X. Ren. Large electric-field-induced strain in ferroelectric crystals by point-defect-mediated reversible domain switching. *Nature Materials*, **3**(2):91–94, 2004.

# List of Figures

2.1	<i>Crystal structure of <math>La_{(1-x)}Sr_xMnO_3</math> in the a) pseudocubic perovskite structure and in the b) tetragonal structure. The legend applies to both figures.</i>	4
2.2	<i>Electronic configuration in 3d-transition metal ions in a local picture. The crystal field and Jahn-Teller effect lead to a splitting in the energy levels.</i>	5
2.3	<i>Magnetic temperature-vs.-doping level phase diagram of <math>La_{(1-x)}Sr_xMnO_3</math> adapted from [32]. Ferromagnetic FM, antiferromagnetic AFM and paramagnetic PM regions are depicted as well as the electronic state (insulating: I, metallic: M) and the crystal structures (orthorhombic O, rhombohedral: R, tetragonal: T, monoclinic: Mc, and hexagonal H) . The stoichiometry used in this work is indicated by a red line.</i>	6
2.4	<i>Strain-vs.-doping level magnetic phase diagram of <math>La_{(1-x)}Sr_xMnO_3</math> adapted from [34, 35].</i>	7
2.5	<i>Typical ferroelectric hysteresis loop.</i>	9
2.6	<i>The shift of the Ti-ion with respect to the oxygen octahedron leads to a spontaneous electric polarization in <math>BaTiO_3</math>.</i>	9
2.7	<i>Temperature dependent lattice parameter of bulk <math>BaTiO_3</math> adapted from [40]. <math>BaTiO_3</math> undergoes phase transitions from cubic to tetragonal at <math>\approx 393</math> K, tetragonal to orthorhombic at <math>\approx 278</math> K and orthorhombic to rhombohedral at <math>\approx 183</math> K.</i>	9
2.8	<i>Control of order parameter in ferroics and multiferroics. The stress <math>\sigma</math>, electric field <math>E</math> and magnetic field <math>H</math> controls strain <math>\varepsilon</math>, magnetization <math>M</math> and electric polarization <math>P</math>, respectively. Additional interaction occur at the coexistence of at least two ordering parameter (multiferroicity) adapted from [68].</i>	11
3.1	<i>Schematic representation of a scattering experiment within the Fraunhofer approximation. Adapted from [84]</i>	13
3.2	<i>Geometry to derive the scattering cross-section.</i>	14
3.3	<i>Plot of the Laue function for <math>P=5</math> and <math>P=10</math>.</i>	17
3.4	<i>Typical scattering geometry under grazing incidence.</i>	18
3.5	<i>Schematic geometry of a PNR experiment. Neutrons are polarized parallel or antiparallel to the external magnetic field <math>\vec{H}</math>. This field leads to a magnetic induction <math>\vec{B} = \mu_0(\vec{H} + \vec{M})</math> in the sample with two in plane components <math>\vec{B}_\perp</math> and <math>\vec{B}_\parallel</math>.</i>	19

---

3.6	<i>Illustration to describe the modeling of the SLDs. Nuclear and magnetic profiles are separated. The final SLDs to simulate the <math>R_{++}</math> and <math>R_{--}</math> reflectivities are calculated by the addition and subtraction of the nuclear and magnetic SLDs, respectively.</i>	21
4.1	<i>Setup of the High Oxygen Pressure Sputtering System. The mass flow controller and the pumps ensures a stable oxygen pressure in the chamber. Five targets can be mounted on the movable target arm.</i>	24
4.2	<i>Newly designed sputter target holder/electrode head to avoid target cracking. The electrode ring is enlarged and the use of an additional insulation ring prevents dropping of the target.</i>	25
4.3	<i>Schematic setup of the Oxide Molecular Beam Epitaxy system adapted from [89].</i>	26
4.4	<i>a) typical LEED setup. b) LEED pattern of a good quality <math>\text{La}_{0.5}\text{Sr}_{0.5}\text{MnO}_3</math> layer on a <math>\text{SrTiO}_3</math> substrate measured at 100 eV.</i>	27
4.5	<i>Schematic explanation of the origin of Auger electrons.</i>	28
4.6	<i>Schematic geometry of RHEED. The electron beam hits the sample under grazing incidence. The surface sensitivity of this technique leads to rods in reciprocal space, since just two Laue equations are valid. The scattering pattern becomes visible on the detector screen. Here a typical pattern for a clean <math>\text{SrTiO}_3</math> substrate is shown.</i>	28
4.7	<i>Schematic setup of the X-ray diffractometer D8 Advanced. It operates with a copper X-ray source. The flight path is defined by Göebelmirrors and slits. The vacuum sample stage provides a temperature range from 70 to 700 K. Adapted from [98].</i>	30
4.8	<i>a) shows the Lennard-Jones Potential which describes the interaction between the measurement tip and the sample surface. b) shows the AFM-setup, the oscillation of the cantilever is probed by a laser beam which is detected by a 4-quadrant detector.</i>	31
4.9	<i>a) Diagram of the electrical connections, which are required for the operation of a commercial SQUID magnetometer for MEC measurements. b) Electrical connection to the sample which is fixed at a Vespel rod and covered by a straw. Around the straw the second-order gradiometer pick-up coils are depicted.</i>	33
4.10	<i>a) shows the comparison of a measurement performed by the new installed MEC option (<math>\omega = 1</math> Hz) and manually taken data points. It shows the change of the magnetization by the application of electric fields with respect to the external magnetic field. Both measurements are in a good agreement. b) shows the temperature dependent MEC measurement for a <math>\text{Au}/\text{BaTiO}_3/\text{Au}</math> system. No signal is observed, as expected. This gives evidence that no magnetic signal is measured by any flowing currents within the substrate due to application of the electric field.</i>	34
4.11	<i>MEC measurement on a <math>\text{Cr}_2\text{O}_3</math> crystal vs. temperature at <math>\omega = 1</math> Hz and <math>E = 65.2</math> kV/m. Reference data points taken from [103] are in good agreement with the measurement performed with the local setup at the JCNS.</i>	35

4.12	<i>Schematic setup of the polarized neutron reflectometer MARIA. The wavelength can be chosen by the use of a velocity selector. The beam is collimated by a slit system and can be polarized/analyzed by neutron optics. Electric and magnetic fields can be applied at the sample stage. . . . .</i>	36
4.13	<i>Sample holder used during the scattering experiments, to reduce background and allow connection of the electrodes for application of external electric fields. . . . .</i>	36
4.14	<i>Typical detector image taken at MARIA. The left peak 1) corresponds to the tail of the almost blocked direct beam, the peak in the middle of the detector is the reflected beam 2) and 3) shows the background. . . . .</i>	37
4.15	<i>Schematic setup of the time-of-flight reflectometer MR. . . . .</i>	38
4.16	<i>The detector image a) at MR shows the reflected and the tail of the direct beam. Red and green lines indicate the region of interest. b) shows the intensities separated to the flight time of the neutrons. . . . .</i>	38
5.1	<i>a) Topography of a prepared SrTiO<sub>3</sub> (001) substrate measured with AFM. Atomic flat terraces can be seen indicating a TiO<sub>2</sub> termination of the surface as expected. b) Line profile of the prepared SrTiO<sub>3</sub> substrate measured by AFM. The miscut is 0.3°. . . . .</i>	42
5.2	<i>a) AES of a SrTiO<sub>3</sub> substrate after the preparation treatment. The carbon peak vanishes due to the process indicating a clean surface. LEED pattern of a b) untreated and c) prepared SrTiO<sub>3</sub> substrate at an energy of 100 eV. The pattern gets much sharper with a lowered background due to the substrate preparation confirming the clean surface. . . . .</i>	42
5.3	<i>Lanthanum to manganese ratio within the samples measured by RBS. The factor <math>x</math> corresponds to the ratio of the weighted frequency changes <math>x = \frac{\Delta f_{La}}{\Delta f_{Mn}} \frac{m_{Mn}}{m_{La}}</math>. The dotted line is a guide to the eye. . . . .</i>	44
5.4	<i>RBS analysis of the final stoichiometry of La<sub>0.53</sub>Sr<sub>0.47</sub>MnO<sub>3</sub>. The gray area correspond to the RBS signal of the substrate and the green, yellow and blue to lanthanum, strontium and manganese of the layer, respectively. . . . .</i>	44
5.5	<i>Structural analysis of La<sub>0.53</sub>Sr<sub>0.47</sub>MnO<sub>3</sub> film on SrTiO<sub>3</sub>. a) Shows the XRR data and simulation with a thickness of <math>367 \pm 6</math> Å and a roughness of <math>5.7 \pm 0.6</math> Å. The (100) reflex b) of the layer corresponds to a lattice parameter of 3.83 Å. Thickness oscillations indicate a very smooth surface. The Bremsberg is not simulated. The inset in a) and b) shows the RHEED and LEED pattern, respectively, indicating a good sample quality. . . . .</i>	45
5.6	<i>RBS analysis of the stoichiometry of La<sub>0.5</sub>Sr<sub>0.5</sub>MnO<sub>3</sub> on MgO. The signal caused by the substrate is colored in gray. Lanthanum, strontium and manganese are colored in green, yellow and blue, respectively. . . . .</i>	47
5.7	<i>XRR measurement of La<sub>0.5</sub>Sr<sub>0.5</sub>MnO<sub>3</sub> on SrTiO<sub>3</sub> with a layer thickness of 264 Å and a roughness of 5 Å. The inset shows the XRD data of the (001) Bragg-peak. Thickness oscillations are present confirming a smooth layer. . . . .</i>	47
5.8	<i>RHEED study with respect to the deposition time of BaTiO<sub>3</sub>. The layer-by-layer growth mode a)-c) changes by the deposition time to a 3D like island growth d), indicated by the arising of additional peaks and the high background signal. . . . .</i>	48

5.9	<i>a) shows the XRR measurement of a grown Ba:Ti:O layer on SrTiO<sub>3</sub> including the fit of the data. The resulting SLD with respect to the layer thickness is shown in b). A drastically reduction of the density is observed after a thickness of 47 Å corresponding to a deposition time of about 950 s.</i>	49
5.10	<i>Analysis of stoichiometry: a) Comparison of Auger spectra of a grown Ba:Ti:O layer to the reference measurement of a BaTiO<sub>3</sub> substrate. The Ba peak of the sample is enlarged, while the Ti peak is too small. This suggests a Ba rich top layer. b) RBS analysis of a grown Ba:Ti:O layer on MgO substrate with a Ba:Ti ratio of 3:2.</i>	49
5.11	<i>RBS measurement including simulation of the data of a BaTiO<sub>3</sub> sample on MgO substrate showing a perfect stoichiometry.</i>	50
5.12	<i>Diffraction scan of BaTiO<sub>3</sub> layer on SrTiO<sub>3</sub> substrate. The observable (004)-BaTiO<sub>3</sub> reflection indicates a good layer quality.</i>	50
5.13	<i>a) shows the XRR measurement of a grown BaTiO<sub>3</sub> layer on SrTiO<sub>3</sub> including the fit of the data. The resulting SLD with respect to the layer thickness is shown in b). A small top layer with reduced SLD has to be taken into account.</i>	51
5.14	<i>a) Topography of a 600 Å BaTiO<sub>3</sub> layer produced by HOPSS and b) a line profile. The position of the extracted line profile is indicated by the green line in a).</i>	52
5.15	<i>a) Topography of a 80 Å BaTiO<sub>3</sub> layer produced by HOPSS and b) a line profile. The position of the extracted line profile is indicated by the green line in a). The surface is not homogeneous flat, but shows islands.</i>	52
6.1	<i>a) LEED pattern of the La<sub>0.53</sub>Sr<sub>0.47</sub>MnO<sub>3</sub> film on BaTiO<sub>3</sub> substrate, taken at 100 eV. The reflexes indicate epitaxial growth. b) The RHEED pattern taken after the growth process shows stripes indicating a smooth layer. Spots at the first Laue ring suggest a good crystalline quality.</i>	56
6.2	<i>a) Topography of the LSMO layer on BaTiO<sub>3</sub> measured by AFM and b) the Gaussian height distribution with a rms roughness of less than three unit cells.</i>	56
6.3	<i>a) XRR measurement of the 228 Å La<sub>0.53</sub>Sr<sub>0.47</sub>MnO<sub>3</sub> layer on BaTiO<sub>3</sub> substrate. The SLD profile obtained from the fit is shown b). The substrate is indicated by the gray color and the LSMO layer by blue color.</i>	57
6.4	<i>XRD measurement on the LSMO/BTO sample at room temperature with and without applied voltage of 400 V. Without electric field the second order BaTiO<sub>3</sub> Bragg peak splits due to structural domains within the substrate. The (002)/(020) a-type substrate peak vanishes due to the application of the voltage. A slight shift of the (002) LSMO Bragg peak is observed. Additional peaks are visible due to a wavelength contamination of the primary beam.</i>	58
6.5	<i>a) Contacted sample without applied voltage. The surface of the sample shows a stripe like pattern. b) Sample with applied electric field of 8 kV/cm. The surface becomes completely flat at the critical voltage of about 200 V. c) and d) show the corresponding reflection of a laser beam reflected from the sample.</i>	59

- 
- 6.6 *Rocking scan on a) the total plateau of reflection ( $2\Theta = 0.6$ ) with and without applied electric field. The application of the electric field leads to a sharpening of the reflection. b) rocking scan on the  $\text{BaTiO}_3$  (002) Bragg Peak. The stripe like pattern is oriented parallel and perpendicular to the scattering plane, both without electric field. . . . . 60*
- 6.7 *Diagram of the magnetization measurements. The blue lines indicate magnetic hysteresis loops for different applied electric fields. Electrical hysteresis loops at different magnetic field are depicted in red and the magnetization change  $\Delta m_H(T, E)$  performed by the MEC option is drawn in violet. Black dots indicate measurement points. A temperature range from  $T = 5$ -350 K can be probed. . . . . 62*
- 6.8 *Temperature dependent magnetization measurement at  $\mu_0 H = 10$  mT. Steps in the magnetizations are observed at the structural phase transitions of the  $\text{BaTiO}_3$  substrate. The gray boxes illustrate the temperature region of the phase transitions. The numbers 1. and 2. indicates the repetition of the measurement. The magnetization is additionally given in  $\mu_B$  per Mn atom with an error of approximately 5%. The inset shows the evolution of the magnetization step at the Or  $\mapsto$  Rh phase transition with respect to the external magnetic field. For a better visibility, the magnetization is normalized to that at 180 K. . . . . 63*
- 6.9 *Magneto-electric coupling measured with the MPMS. The temperature dependent change of the magnetizations  $\Delta m_{H, E_{AC}}(T)$  with respect to the applied AC electric field is observed at  $\mu_0 H = 3$  mT. A coupling is observed with maximum values near the phase transitions of the  $\text{BaTiO}_3$  substrate. Arrows indicate temperatures where data points are taken manually (see next section) . . . . . 64*
- 6.10 *Direction of the applied electric field. For negative applied voltages the electric field points towards and for positive fields away from the  $\text{La}_{(1-x)}\text{Sr}_x\text{MnO}_3$  layer. . . . . 65*
- 6.11 *Magnetization depending on the applied electric field at various temperatures at  $\mu_0 H = 3$  mT. The arrows show the direction of the increasing or decreasing electric field. An enlarged magnetization is observed for negative electric fields shown in b)-e). The magnetization for positive fields and at 285 K stays almost constant. . . . . 66*
- 6.12 *Magnetization as function of the electric field for various external magnetic fields at  $T = 270$  K. The application of negative electric field leads to an increase of the magnetization. The shape and size of the modification of the magnetization changes with the external magnetic field. . . . . 68*
- 6.13 *Measurement of  $\Delta m_{T, E_{AC}}(H)$  with respect to the external magnetic field for various temperatures. The shape of the curve changes with respect to the temperature. The curve at 180 K completely differs from the others, showing a hysteresis like behavior. The errorbars are smaller than the size of the data points. . . . . 70*

6.14	<i>Magnetic hysteresis loops at 285 K for different applied electric fields. No change of the loops can be observed with respect to the applied electric field. The black dashed lines indicate the coercivity field. . . . .</i>	71
6.15	<i>Hysteresis loops of the <math>\text{La}_{0.53}\text{Sr}_{0.47}\text{MnO}_3</math> layer for different electric fields, taken within the orthorhombic phase of the <math>\text{BaTiO}_3</math> substrate at a) 270 K and b) 210 K. A shift of the coercivity field is indicated by gray boxes. . . .</i>	72
6.16	<i>Hysteresis loops of the <math>\text{La}_{0.53}\text{Sr}_{0.47}\text{MnO}_3</math> layer, performed in the rhombohedral phase of the <math>\text{BaTiO}_3</math> substrate at a) 180 K and b) 190 K. The gray boxes indicate the shift of the coercivity field. . . . .</i>	73
6.17	<i>a) PNR measurement of the <math>\text{La}_{0.53}\text{Sr}_{0.47}\text{MnO}_3</math> film at 300 K with an applied electric field of +8 kV/cm . b) asymmetry to visualize the order of the magnetization. . . . .</i>	75
6.18	<i>Polarized neutron reflectivity data of the <math>\text{La}_{0.53}\text{Sr}_{0.47}\text{MnO}_3/\text{BaTiO}_3</math> sample at 300 K. The <math>R_{--}</math> reflectivity is divided by 10 for a better visibility. The reflectivity for electric field of +8 kV/cm and -8 kV/cm including the fit of the data are shown in a) and b), respectively. d) shows both data sets to visualize the difference in the reflectivity with respect to the applied electric field. The SLD profiles obtained by the fits are depicted in c). . . . .</i>	76
6.19	<i>Diagram to illustrate the model of the magnetization profile of the LSMO layer. The edges of the magnetization in the LSMO layer are described by two Fermi-Dirac distributions with variable positions <math>p_{\text{left}}</math> and <math>p_{\text{right}}</math> and widths <math>\sigma_{\text{left}}</math> and <math>\sigma_{\text{right}}</math>. . . . .</i>	77
6.20	<i>Polarized neutron reflectivity at 150 K, no difference with respect to the electric field direction is observed. b) shows the SLD corresponding to the best fit of the data. The NSLD regarding the substrate is depicted in grey, while the LSMO layer is colored in green. The magnetic SLD is drawn in blue. . . . .</i>	78
6.21	<i>Polarized neutron reflectivity data of the <math>\text{La}_{0.5}\text{Sr}_{0.5}\text{MnO}_3/\text{BaTiO}_3</math> sample at 210 K, in the orthorhombic phase. The <math>R_{--}</math> reflectivity is divided by 10 for a better visibility. The reflectivity for electric field of <math>\pm 8</math> kV/cm including the fit are shown in a). b) shows the SLD obtained by the fit of the data. . . . .</i>	79
6.22	<i>For comparison: Magnetization profiles at various temperatures. The profile thickness is given in units relative to the nuclear layer thickness <math>d_{\text{nucl.}}</math>. . . . .</i>	80
6.23	<i>a) Simulation of the polarized neutron reflectivity using the b) magnetization profile for FM and AFM alignment at the interface as predicted by Burton et al. Structural parameters of the <math>\text{La}_{0.53}\text{Sr}_{0.47}\text{MnO}_3/\text{BTO}</math> sample are used. . . . .</i>	80
7.1	<i>a) XRR measurement of the <math>\text{La}_{0.7}\text{Sr}_{0.3}\text{MnO}_3</math> layer on <math>\text{BaTiO}_3</math>. The SLD obtained by the fit is shown in b). A top layer with reduced SLD has to be taken into account. The substrate is marked in gray, LSMO in green and the top layer in blue. . . . .</i>	82

7.2	<i>a) shows the <math>\omega/2\Theta</math>-scan of the <math>\text{La}_{0.7}\text{Sr}_{0.3}\text{MnO}_3/\text{BaTiO}_3</math> sample. The second order Bragg peak of the <math>\text{BaTiO}_3</math> substrate is split into c-type and a-type domains. The Bragg peak at <math>Q = 3.26 \text{ \AA}^{-1}</math> corresponds to the lattice parameter of <math>c_{\text{LSMO}} = 3.85 \text{ \AA}</math> of the crystalline LSMO film. The temperature dependent out-of-plane lattice parameters of the substrate and the LSMO film are depicted in b) and c), respectively.</i>	83
7.3	<i>Temperature dependent magnetization measurement at <math>\mu_0 H = 10 \text{ mT}</math>. Also for the <math>\text{La}_{0.7}\text{Sr}_{0.3}\text{MnO}_3</math> stoichiometric film, steps in the magnetizations are observed at the structural phase transitions of the <math>\text{BaTiO}_3</math> substrate. The gray boxes illustrate the temperature region of the supposed phase transitions. The magnetization is additionally given in <math>\mu_B</math> per Mn atom with an error of approximately 5%.</i>	84
7.4	<i>Magneto-electric coupling of <math>\text{La}_{0.7}\text{Sr}_{0.3}\text{MnO}_3/\text{BaTiO}_3</math> measured by MPMS. The temperature dependent change of the magnetizations <math>\Delta m</math> with respect to the applied AC electric field is observed at <math>\mu_0 H = 3 \text{ mT}</math>. A clear coupling is observed with maximum values near the phase transitions of the <math>\text{BaTiO}_3</math> substrate. A negative change of the magnetization is observed within the orthorhombic phase.</i>	85
7.5	<i>Magnetization of the <math>\text{La}_{0.7}\text{Sr}_{0.3}\text{MnO}_3</math> film depending on the applied electric field at various temperatures at <math>\mu_0 H = 3 \text{ mT}</math>. It is clearly possible to manipulate the magnetization by an electric field. The effect is maximal at 180 K within the rhombohedral phase of the substrate and at 270 K (orthorhombic). A difference of the magnetization is present also without electric field after polarizing the sample with <math>E = +4 \text{ kV/cm}</math> and <math>E = -4 \text{ kV/cm}</math>, at 180 and 285 K.</i>	87
7.6	<i>Comparison of the relative magnetization of both doping levels depending on the applied electric field at various temperatures.</i>	88
7.7	<i>MEC measurements of <math>\text{La}_{0.7}\text{Sr}_{0.3}\text{MnO}_3</math> with respect to the external magnetic field for various temperatures. The arrows indicate the direction of increasing or decreasing magnetic field.</i>	90
7.8	<i>For comparison: MEC measurements of <math>\text{La}_{0.7}\text{Sr}_{0.3}\text{MnO}_3</math> and <math>\text{La}_{0.53}\text{Sr}_{0.47}\text{MnO}_3</math> with respect to the external magnetic field for various temperatures.</i>	91
7.9	<i>Hysteresis loops of <math>\text{La}_{0.7}\text{Sr}_{0.3}\text{MnO}_3</math> on <math>\text{BaTiO}_3</math> for different applied electric fields at 285 K. The magnetization slightly increases with positive applied electric field and <math>\mu_0 H &gt; 5 \text{ mT}</math>. For a better visibility b) shows the hysteresis plotted in a smaller scale. The gray boxes indicate the modification of the coercivity field.</i>	92
7.10	<i>Magnetic field dependent magnetization for different applied electric fields at a) 270 K and b) 210 K. At 210 K the shift of the coercivity field is indicated by the gray boxes.</i>	93
7.11	<i>Hysteresis loops performed at 180 K for different applied electric fields. No change in the magnetic behavior is found for the different electric fields at this temperature.</i>	94

7.12	<i>Polarized neutron reflectivity data of the <math>\text{La}_{0.7}\text{Sr}_{0.3}\text{MnO}_3/\text{BaTiO}_3</math> sample at 285 K. The <math>R_{--}</math> reflectivity is divided by 10 for a better visibility. The reflectivities for electric fields of <math>\mathbf{E} = \pm 4</math> kV/cm including the fit of the data are shown in a) and b), respectively. d) shows both data sets to visualize the difference in the reflectivity with respect to the applied electric field. The SLD profiles obtained by the fits are depicted in c).</i> . . . . .	96
7.13	<i>a) PNR data of <math>\text{La}_{0.7}\text{Sr}_{0.3}\text{MnO}_3</math> on <math>\text{BaTiO}_3</math> at 285 K with the simulated intensities according to different models. The SLDs of the models are presented in b)-g).</i> . . . . .	97
7.14	<i>Polarized neutron reflectivity data of the <math>\text{La}_{0.7}\text{Sr}_{0.3}\text{MnO}_3/\text{BaTiO}_3</math> sample in the Or phase of the substrate at 210 K. The <math>R_{--}</math> reflectivity is divided by 10 for a better visibility. The Q-dependent reflectivity for electric field of 0 kV/cm and -4 kV/cm and the fits are shown in a) and b). The SLD profiles obtained by the fits are depicted in c). d) shows both data sets to visualize the difference in the reflectivity with respect to the applied electric field.</i> . . . . .	99
8.1	<i>Schematically temperature dependent in-plane lattice distortion of (001) <math>\text{BaTiO}_3</math>. It is assumed that the <math>\text{La}_{(1-x)}\text{Sr}_x\text{MnO}_3</math> in-plane lattice parameter are clamped to the <math>\text{BaTiO}_3</math> substrate [125]. <math>\epsilon_a</math> and <math>\epsilon^*</math> denote the in-plane area change and the in-plane distortion away from square symmetry.</i> . . . .	103
8.2	<i>Squareness of the hysteresis loops as measure of the anisotropy for <math>\text{La}_{0.5}\text{Sr}_{0.5}\text{MnO}_3</math> and <math>\text{La}_{0.7}\text{Sr}_{0.3}\text{MnO}_3</math> depicted in red and blue, respectively. The gray boxes illustrate the region of the phase transitions of the substrate.</i> . . . . .	104
8.3	<i>a) Piezoelectric coefficient <math>d_{33}</math> for (001)-oriented <math>\text{BaTiO}_3</math> as function of temperature adapted from [131]. Dashed line indicate calculated values for single-domain <math>\text{BaTiO}_3</math> crystals. b) Dielectric constant as function of temperature adapted from [132]. Vertical lines indicate phase transition temperatures of <math>\text{BaTiO}_3</math>. For comparison a scaled <math>\Delta m</math> measurement is shown.</i>	105
8.4	<i>Spontaneous polarization directions in the ferroelectric phases of <math>\text{BaTiO}_3</math>, taken from [135]. The angles between symmetry equivalent directions and direction "0" are given.</i> . . . . .	107

# List of Tables

5.1	<i>Optimal parameters for the growth of <math>La_{0.53}Sr_{0.47}MnO_3</math> films by the OMBE.</i>	44
5.2	<i>Optimal parameters for the growth of <math>La_{0.5}Sr_{0.5}MnO_3</math> films by the HOPSS.</i>	46
6.1	<i>Change of magnetization with respect to the applied electric field at <math>\mu_0 H=3</math> mT and various temperatures. Additionally, the relative change <math>\Delta m_{\text{man.}}</math> of the absolute moment is given.</i>	67
6.2	<i>Summary of the magnetization with respect to the electric field for a series of measurements at 270 K and various magnetic fields.</i>	69
6.3	<i>Coercivity field and remanent magnetization at 210 K including relative changes compared to <math>E = 0</math> kV/cm. The hysteresis loop with <math>E = +4</math> kV/cm shows a shift of the coercivity field of 3.2 mT and a reduced remanent magnetization of 45.5% compared to the hysteresis at <math>E = 0</math> kV/cm. The squareness <math>m_r/m_s</math> is a measure for the anisotropy.</i>	72
6.4	<i>Summarized results of the coercivity field, the remanent magnetization and the relative changes compared to <math>E = 0</math> kV/cm at 180 K and 190 K. Coercivity fields are highly enlarged by the application of positive applied electric fields. The squareness slightly changes.</i>	74
7.1	<i>Magnetization of <math>La_{0.7}Sr_{0.3}MnO_3</math> with respect to the applied electric field at <math>\mu_0 H=3</math> mT and various temperatures. Additionally, the absolute <math>\Delta m</math> and relative changes of the magnetization <math>\Delta m_{\text{rel.}}</math> are given.</i>	86
7.2	<i>Shift of the center of the hysteresis loops in MEC measurement with respect to the external magnetic field.</i>	89
7.3	<i>Coercivity field and the remanent magnetization at 270 K and 210 K, both within the orthorhombic phase of the <math>BaTiO_3</math> substrate. Additionally the squareness and the deviation of <math>\mu_0 \Delta H_C</math> from the neutral state without applied electric field is given.</i>	93
7.4	<i>Differences of the compared models to simulate the PNR data at <math>E = +4</math> kV/cm.</i>	98
1	<i>XRR fit parameter of the <math>La_{0.53}Sr_{0.47}MnO_3</math>, prepared by the OMBE.</i>	135
2	<i>XRR fit parameter of the <math>La_{0.7}Sr_{0.3}MnO_3</math>, prepared by the HOPSS.</i>	136
3	<i>PNR fit parameter of <math>La_{0.53}Sr_{0.47}MnO_3</math> at 300 K for <math>E = +8</math> kV/cm and <math>E = -8</math> kV/cm.</i>	137
4	<i>PNR fit parameter of <math>La_{0.5}Sr_{0.5}MnO_3</math> at 150 K for <math>E = +8</math> kV/cm and <math>E = -8</math> kV/cm.</i>	138

List of Tables

---

5	<i>PNR fit parameter of <math>La_{0.5}Sr_{0.5}MnO_3</math> at 210 K for <math>E = +8</math> kV/cm and <math>E = -8</math> kV/cm. . . . .</i>	139
6	<i>PNR fit parameter of <math>La_{0.7}Sr_{0.3}MnO_3</math> at 285 K for <math>E = +4</math> kV/cm and <math>E = -4</math> kV/cm. . . . .</i>	140
7	<i>PNR fit parameter of <math>La_{0.7}Sr_{0.3}MnO_3</math> at 210 K for <math>E = 0</math> kV/cm and <math>E = -4</math> kV/cm. . . . .</i>	141

# Fit parameter

## XRR

**La<sub>0.53</sub>Sr<sub>0.47</sub>MnO<sub>3</sub>/BaTiO<sub>3</sub> prepared by OMBE:**

LSMO layer thickness	+228 <sup>+1</sup> <sub>-4</sub>
LSMO layer SLD real	+4.67 (fixed)
LSMO layer SLD imaginary	-0.43 (fixed)
LSMO layer roughness	+5.50 <sup>+0.03</sup> <sub>-0.07</sub>
BTO SLD real	+4.47 (fixed)
BTO SLD imaginary	-0.48 (fixed)
BTO roughness	+6.84 <sup>+0.09</sup> <sub>-0.31</sub>
FOM	2.38

Table 1: *XRR fit parameter of the La<sub>0.53</sub>Sr<sub>0.47</sub>MnO<sub>3</sub>, prepared by the OMBE.*

**La<sub>0.7</sub>Sr<sub>0.3</sub>MnO<sub>3</sub>/BaTiO<sub>3</sub> prepared by HOPSS:**

LSMO top layer thickness	+15.29 <sup>+0.64</sup> <sub>-0.14</sub>
LSMO top layer SLD real	+3.94 <sup>+0.06</sup> <sub>-0.06</sub>
LSMO top layer SLD imaginary	-0.41 <sup>+0.01</sup> <sub>-0.01</sub>
LSMO top layer roughness	+2.98 <sup>+0.06</sup> <sub>-0.09</sub>
LSMO layer thickness	+349.89 <sup>+5.31</sup> <sub>-4.94</sub>
LSMO layer SLD real	+4.85 (fixed)
LSMO layer SLD imaginary	-0.51 (fixed)
LSMO layer roughness	+6.63 <sup>+0.29</sup> <sub>-0.77</sub>
BTO SLD real	+4.47 (fixed)
BTO SLD imaginary	-0.48 (fixed)
BTO roughness	+6.96 <sup>+1.58</sup> <sub>-0.86</sub>
FOM	3.91

Table 2: *XRR fit parameter of the La<sub>0.7</sub>Sr<sub>0.3</sub>MnO<sub>3</sub>, prepared by the HOPSS.*

## PNR

The parameter of the PNR fits are presented in the following tables. Fixed parameters are marked as well as constrained parameters.

### PNR 300 K:La<sub>0.53</sub>Sr<sub>0.47</sub>MnO<sub>3</sub>/BaTiO<sub>3</sub> prepared by OMBE

	E = +8kV/cm	E = -8kV/cm
<b>Magnetic</b>		
$p_{\text{right}}$	$+232_{-9}^{+11}$	$+257_{-11}^{+21}$
$\sigma_{\text{right}}$	$+25_{-4}^{+3}$	$+30_{-6}^{+12}$
$m_{\text{LSMO}}$	$+0.9_{-0.2}^{+0.2}$	$+0.6_{-0.2}^{+0.1}$
$p_{\text{left}}$	$+79_{-3}^{+1}$	$+87_{-15}^{+3}$
$\sigma_{\text{left}}$	$+22_{-8}^{+12}$	$+20_{-10}^{+10}$
<b>Nuclear</b>		
toplayer thickness	$+14_{-4}^{+9}$	$+13_{-9}^{+6}$
toplayer NSLD	$+1.7_{-2}^{+1}$	$+1.7_{-.2}^{+0.1}$
toplayer roughness	$+46_{-1}^{+1}$	$+31_{-2}^{+2}$
LSMO thickness	$+254_{-2}^{+2}$	$+252_{-3}^{+3}$
LSMO NSLD	+3.44 (fixed)	+3.44 (fixed)
LSMO roughness	$+11_{-1}^{+1}$	$+12_{-1}^{+1}$
BTO NSLD	+2.88 (fixed)	+2.88 (fixed)
BTO roughness	$+9_{-1}^{+3}$	$+5_{-1}^{+4}$
FOM	5.46	5.46

Table 3: PNR fit parameter of La<sub>0.53</sub>Sr<sub>0.47</sub>MnO<sub>3</sub> at 300 K for E = +8 kV/cm and E = -8 kV/cm.

**PNR 150 K:La<sub>0.53</sub>Sr<sub>0.47</sub>MnO<sub>3</sub>/BaTiO<sub>3</sub> prepared by OMBE**

	E = +8kV/cm	E = -8kV/cm
<b>Magnetic</b>		
$p_{\text{right}}$	$+237_{-2}^{2+}$	$\leq E = +8\text{kV/cm}$
$\sigma_{\text{right}}$	$+12_{-3}^{+4}$	$\leq E = +8\text{kV/cm}$
$m_{\text{LSMO}}$	$+1.98_{-0.04}^{+0.1}$	$\leq E = +8\text{kV/cm}$
$p_{\text{left}}$	$+77_{-9}^{+8}$	$\leq E = +8\text{kV/cm}$
$\sigma_{\text{left}}$	$+12_{-1}^{+2}$	$\leq E = +8\text{kV/cm}$
<b>Nuclear</b>		
toplayer thickness	$+26_{-2}^{+4}$	$\leq E = +8\text{kV/cm}$
toplayer NSLD	$+1.8_{-0.2}^{+0.2}$	$\leq E = +8\text{kV/cm}$
toplayer roughness	$+25_{-3}^{+4}$	$\leq E = +8\text{kV/cm}$
LSMO thickness	$+248_{-2}^{+2}$	$\leq E = +8\text{kV/cm}$
LSMO NSLD	$+3.57_{-0.2}^{+0.1}$	$\leq E = +8\text{kV/cm}$
LSMO roughness	$+15.5_{-0.4}^{+0.6}$	$\leq E = +8\text{kV/cm}$
BTO NSLD	+2.88 (fixed)	$\leq E = +8\text{kV/cm}$
BTO roughness	$+10_{-1}^{+1}$	$\leq E = +8\text{kV/cm}$
FOM	8.72	$\leq E = +8\text{kV/cm}$

Table 4: PNR fit parameter of  $\text{La}_{0.5}\text{Sr}_{0.5}\text{MnO}_3$  at 150 K for  $E = +8 \text{ kV/cm}$  and  $E = -8 \text{ kV/cm}$ .

---

**PNR 210 K:La<sub>0.5</sub>Sr<sub>0.5</sub>MnO<sub>3</sub>/BaTiO<sub>3</sub> prepared by HOPSS**

	E = +8kV/cm	E = -8kV/cm
<b>Magnetic</b>		
$p_{\text{right}}$	$+79_{-14}^{+5}$	$\leq E = +8\text{kV/cm}$
$\sigma_{\text{right}}$	$+195_{-1}^{+7}$	$\leq E = +8\text{kV/cm}$
$m_{\text{LSMO}}$	$+1.6_{-0.1}^{+0.1}$	$\leq E = +8\text{kV/cm}$
$p_{\text{left}}$	$+30_{-16}^{+3}$	$\leq E = +8\text{kV/cm}$
$\sigma_{\text{left}}$	$+69_{-1}^{+6}$	$\leq E = +8\text{kV/cm}$
<b>Nuclear</b>		
toplayer thickness	$+39_{-2}^{+1}$	$\leq E = +8\text{kV/cm}$
toplayer NSLD	$+3.16_{-0.1}^{+0.2}$	$\leq E = +8\text{kV/cm}$
toplayer roughness	$+12.9_{-1.5}^{+0.8}$	$\leq E = +8\text{kV/cm}$
LSMO thickness	$+270_{-4}^{+2}$	$\leq E = +8\text{kV/cm}$
LSMO NSLD	+3.67 (fixed)	$\leq E = +8\text{kV/cm}$
LSMO roughness	$+31_{-6}^{+1}$	$\leq E = +8\text{kV/cm}$
BTO NSLD	+2.85 (fixed)	$\leq E = +8\text{kV/cm}$
BTO roughness	$+23_{-3}^{+4}$	$\leq E = +8\text{kV/cm}$
FOM	2.48	$\leq E = +8\text{kV/cm}$

Table 5: *PNR fit parameter of La<sub>0.5</sub>Sr<sub>0.5</sub>MnO<sub>3</sub> at 210 K for E = +8 kV/cm and E = -8 kV/cm.*

**PNR 285 K:La<sub>0.7</sub>Sr<sub>0.3</sub>MnO<sub>3</sub>/BaTiO<sub>3</sub> prepared by HOPSS**

	E = +4kV/cm	E = -4kV/cm
<b>Magnetic</b>		
MAG 3 thickness	remaining thickness	remaining thickness
MAG 3 moment per unit cell	+0.2 <sup>+0.1</sup> <sub>-0.1</sub>	+0.2 <sup>+0.2</sup> <sub>-0.1</sub>
MAG 3 roughness	LSMO roughness	LSMO roughness
MAG 2 thickness	+101 <sup>+7</sup> <sub>-8</sub>	+108 <sup>+9</sup> <sub>-8</sub>
MAG 2 moment per unit cell	+1.5 <sup>+0.1</sup> <sub>-0.1</sub>	+1.5 <sup>+0.2</sup> <sub>-0.2</sub>
MAG 2 roughness	+31 <sup>+4</sup> <sub>-3</sub>	+25.6 <sup>+0.3</sup> <sub>-5</sub>
MAG 1 thickness	MAG 1 roughness	MAG 1 roughness
MAG 1 moment per unit cell	+0.65 <sup>+0.2</sup> <sub>-0.3</sub>	+0.2 <sup>+0.4</sup> <sub>-0.2</sub>
MAG 1 roughness	+10 <sup>+15</sup> <sub>-1</sub>	+17 <sup>+11</sup> <sub>-13</sub>
<b>Nuclear</b>		
toplayer thickness	+74 <sup>+8</sup> <sub>-2</sub>	
toplayer NSLD	+3.24 <sup>+0.03</sup> <sub>-0.03</sub>	
toplayer roughness	+12.5 <sup>+1.2</sup> <sub>-0.3</sub>	
LSMO thickness	+306 <sup>+1</sup> <sub>-7</sub>	+381 <sup>+5</sup> <sub>-4</sub>
LSMO NSLD	+3.74 (fixed)	+3.74 (fixed)
LSMO roughness	+9.70 <sup>+0.74</sup> <sub>-0.95</sub>	+16 <sup>+1</sup> <sub>-1</sub>
BTO NSLD	+2.85 (fixed)	+2.85 (fixed)
BTO roughness	+39.54 <sup>+2.30</sup> <sub>-7.52</sub>	+30 <sup>+5</sup> <sub>-5</sub>
FOM	5.70	5.60

Table 6: PNR fit parameter of La<sub>0.7</sub>Sr<sub>0.3</sub>MnO<sub>3</sub> at 285 K for E = +4 kV/cm and E = -4 kV/cm.

---

**PNR 210 K:La<sub>0.7</sub>Sr<sub>0.3</sub>MnO<sub>3</sub>/BaTiO<sub>3</sub> prepared by HOPSS**

	E = 0 kV/cm	E = -4 kV/cm
<b>Magnetic</b>		
MAG 3 thickness	remaining thickness	remaining thickness
MAG 3 moment per unit cell	+0.98 <sup>+0.07</sup> <sub>-0.07</sub>	+1.1 <sup>+0.1</sup> <sub>-0.1</sub>
MAG 3 roughness	LSMO roughness	LSMO roughness
MAG 2 thickness	+107.43 <sup>+16.02</sup> <sub>-16.92</sub>	+74 <sup>+14</sup> <sub>-10</sub>
MAG 2 moment per unit cell	+2.46 <sup>+0.20</sup> <sub>-0.17</sub>	+2.7 <sup>+0.2</sup> <sub>-0.3</sub>
MAG 2 roughness	+43.91 <sup>+5.16</sup> <sub>-8.13</sub>	+44 <sup>+5</sup> <sub>-1</sub>
MAG 1 thickness	MAG 1 roughness	MAG 1 roughness
MAG 1 moment per unit cell	+0.86 <sup>+0.05</sup> <sub>-0.65</sub>	+1.1 <sup>+0.5</sup> <sub>-0.3</sub>
MAG 1 roughness	+26.27 <sup>+3.51</sup> <sub>-5.7</sub>	+28 <sup>+2</sup> <sub>-4</sub>
<b>Nuclear</b>		
LSMO thickness	+379 (fixed)	+379 <sup>+4</sup> <sub>-4</sub>
LSMO NSLD	+3.74 (fixed)	+3.74 (fixed)
LSMO roughness	+10 <sup>+1</sup> <sub>-1</sub>	+3.1 <sup>+2.6</sup> <sub>-0.1</sub>
BTO NSLD	+2.85 (fixed)	+2.85 (fixed)
BTO roughness	+40 <sup>+2</sup> <sub>-8</sub>	+26 <sup>+6</sup> <sub>-4</sub>
FOM	4.06	3.72

Table 7: *PNR fit parameter of La<sub>0.7</sub>Sr<sub>0.3</sub>MnO<sub>3</sub> at 210 K for E = 0 kV/cm and E = -4 kV/cm.*